Interfacing DNA Nanotechnology with Biological Systems

By

Justin William Conway

A thesis submitted to McGill University in partial fulfillment of the requirements for the degree of Doctor of Philosophy

Department of Chemistry, McGill University

Montreal, Quebec, Canada

April 2015

I dedicated this thesis to my family for all the laughs, love and support they showed me through my post-graduate studies; my mother Linda, my father Peter, my little sister and brother, Andrea and Gregory, my brother-in-law Ben and my girlfriend Jessica. It is also dedicated to my grandparents, Claire and Peter, Rolande and Robert for giving me the unique opportunity to experience both farm and forest, which I know planted the seed of curiosity that shaped my journey here.

Abstract

Deoxyribonucleic acid (DNA) has evolved in nature to store and transfer the genetic information of all life on earth. The fidelity of information processing relies on the precise pairing through non-covalent interactions of a molecular code consisting of four unique nucleobases. By using this programmability DNA can be taken of a biological context and used as building material for the programmable assembly of nanostructures. The routine automated synthesis of DNA has allowed researchers to explore many different DNA architecture designs and applications leading to the creation of the diverse field now termed DNA nanotechnology. DNA nanotechnology has generated many examples of scaffolds, cages, and networks able to precisely position molecules for applications in therapeutics, diagnostics, light harvesting devices, nanopatterning and even molecular computing. The objective of this thesis is to expand the interface between DNA nanotechnology and biological systems. In this way, DNA nanostructures can be used as modular platforms for the design of cellular probes and drug delivery vehicles. We focus our efforts on examining DNA and lipid bilayer interactions as well as increasing DNA nanostructure serum stability.

Chapter 1 of this thesis discusses the origins and evolution of the field of DNA nanotechnology and focuses on specific examples within all three major divisions of this field. Chapter 2 describes our work investigating spherically supported bilayers as a platform to land and reversibly assemble DNA cages. This work examines the dynamic addressability of the cages on bilayers, their diffusion properties and depth of anchored cages, and the bilayer templated assembly of DNA structures. Chapter 3 investigates the selective deposition of DNA tile networks on saturated and unsaturated supported lipid bilayers using three structurally different hydrophobic anchors. It is shown that correct network assembly only occurs with compatible packing between the DNA-anchor and the lipid alkyl chains. The variation of the anchor and bilayer chemistry generates switchable network morphologies and filamentous materials. Chapter 4 describes our research towards improving the serum stability of DNA nanostructures, using a combination of folding topology and small synthetic end modifications to the DNA. This work uses a DNA triangular prism cage formed from three DNA strands. It is shown that the folded architecture of these cages and small chemical modifications on the DNA ends significantly stabilize the single stranded DNA and the final cages from fetal bovine serum degradation. We also show how this cage can be fully

ligated to create a closed structure with the highest observed serum stability. These projects intend to demonstrate new ways in which DNA nanotechnology can be applied to biological systems for both medicinal and material based applications.

Résumé

L'acide désoxyribonucléique (ADN) a évolué dans la nature afin de stocker et transférer l'information génétique de toute vie sur terre. La fidélité du traitement de l'information dépend de la précision de l'appariement, par interactions non-covalentes, d'un code moléculaire consistant de quatre bases azotées uniques. L'utilisation de cette programmation permet à l'ADN d'être sorti de son contexte biologique et d'être utilisé en tant que matériau de construction pour l'assemblage programmé de nanostructures. La synthèse automatisée de l'ADN, maintenant routinière, a permis aux chercheurs d'explorer différents designs architecturaux en ADN et leurs applications, ce qui a mené à la création du domaine de recherche très diversifié maintenant appelé nanotechnologie en ADN. La nanotechnologie en ADN a généré de nombreux exemples de structures, cages, objets en trois dimensions et réseaux, capables de positionner précisément des molécules ayant des applications thérapeutiques, diagnostiques, comme dispositifs de collecte de lumière, en « nanopatterning » et même comme ordinateurs moléculaires. L'objectif de cette thèse est l'expansion des méthodes par lesquelles la nanotechnologie en ADN peut être interfacée avec des systèmes biologiques. De cette façon, la nanotechnologie en ADN peut être utilisée en tant que plateforme modulaire pour le design de sondes cellulaires et de véhicules de livraison. Nous concentrerons nos efforts sur l'examen des interactions entre l'ADN et les bicouches lipidiques de même que sur l'amélioration de la stabilité dans le sérum des nanostructures d'ADN.

Le chapitre 1 de cette thèse discute des origines et de l'évolution du domaine d'étude de la nanotechnologie en ADN et se concentre sur des exemples spécifiques contenus dans les trois divisions majeures de ce domaine de recherche. Le chapitre 2 décrit notre travail d'investigation sur les bicouches sphériques supportées en tant que plateformes pour faire atterrir et assembler de façon réversible des cages d'ADN. Ce travail examine l'adressage dynamique des cages sur les bicouches, leurs propriétés de diffusion et la profondeur de l'ancrage des cages et l'assemblage guidé par les bicouches de structures d'ADN. Le chapitre 3 investigue la déposition sélective de réseaux de tuiles d'ADN sur des bicouches lipidiques supportées saturées et insaturées en utilisant

trois ancres hydrophobiques structurellement différents. Il est démontré que l'assemblage correct des réseaux se produit seulement lors de remplissages compatibles entre l'ADN-ancre et les chaînes alkyles lipidiques. Le changement de l'ancre et de la bicouche génère aussi des morphologies en réseaux changeables et des matériaux filamenteux. S'éloignant des bicouches, le chapitre 4 décrit notre recherche sur l'amélioration de la stabilité dans le sérum des nanostructures en ADN en utilisant une combinaison de topologies de pliement et de petites insertions synthétiques à la fin des brins d'ADN. Ce travail utilise un prisme triangulaire en ADN formé de trois brins d'ADN pour toutes les investigations. Il est aussi démontré que les petites modifications à la fin des brins d'ADN stabilisent de façon significative l'ADN simple-brin et l'architecture assemblée finale de la dégradation par sérum bovin fœtal. Nous montrons aussi comment cette cage peut être complètement liée afin de créer une structure fermée avec la plus grande stabilité observée dans le sérum. Ces projets ont pour intention de faire avancer les technologies existantes et de démontrer de nouvelles façons par lesquelles la nanotechnologie en ADN peut être appliquée avec des systèmes biologiques pour des applications basées en médecine et en matériaux.

Translated by Katherine Bujold

Acknowledgements

First and foremost I would like to thank my family. My parents for encouraging and supporting me to pursue my university studies all the way to the end; little did they know it would take this long. I was given every opportunity to push myself as far as I could go along any path of my choice, I will always be grateful for this. I would like to thank my sister (and Ben) and brother for all their encouragement. I would like to thank Jessica for always supporting, believing in me and laughing at all my jokes (wolf pack on!). Also, I would like to thank my extended family, Les Richards and Les Cyrs for all their support and encouragement.

I would like to thank my supervisor Prof. Hanadi Sleiman for her mentorship and creating an environment where creativity and new ideas are encouraged and can be brought to the table for discussion. I would also like to thank Prof. Sleiman for always pushing me to achieve my full potential, it has made me a better scientist. I also need to say thank you for hiring all the right people to make my time in the lab such a great experience!

I would like to thank all the faculty and professors in the McGill Chemistry Department that have helped me along way and that I have had a chance to work with over the years.

One thing to be said for the McGill Chemistry Department is that once you have joined, you are now part of an amazing community of people, with an incredible diversity of activities and just not enough time to try them all. From the Black Shuck hockey to summer softball, basketball to touch football, BDP to Moondog, bagel hour or the winter classic, defense parties and Thomspon House, or Robbie Burns Day, there is a lot going on. I would like to take the opportunity to thank some of the friends I made along the way.

Chris, the journey through the rabbit hole was indeed quite epic, thanks for helping me through it all and showing me how to stay afloat in grad school. Working together taught me a lot about good research work ethic and how to be critical about results. The lab saying, “If a gel looks bad, run it again. If a gel looks good, run it again,” appropriately describes out mind-set. Whether on an epic bike ride (and walking home with a flat tire!), a late night jam session in St. Bruno, guest appearances with Moondog, at Black Shuck playoff runs or simply chasing Boomicorns and

Dragons, I am glad I had a solid partner in crime. I would like to say you were a voice of reason, I would be lying. Thanks.

Kai, you are like the little brother I already have! I have complete confidence that one day you will reach your target deadlift weight and make your parents very proud. You always appreciate my most ridiculous of jokes and our conversations are, literally, mind numbing. Thanks for all the encouragement; coming to the band shows for photo ops, giving me back great Christmas presents, hat parties, getting me addicted to protein supplements and translating all those Mandarin menus. You are definitely my boy! I wish you all the dirty beards you could want. In all seriousness, I could not have made it through without good friends, thank you.

Tom, the Scottsman, whether it was hockey, music, or brewing we gave everything the "Viking Hammer". Thanks for having my back (literally) while we worked together on some great projects. I will never forget our quest for the ultimate IPA, our "research safaris", your brother's funny names, the Chambly bike ride (I have the scars), the arcane science of temporal exploration and most importantly our highly experimental, research driven brew sessions. I am still amazed at how Canadian Scottsmen turn out to be when you spend five years getting to know them.

Jo, not sure who I should thank more, you or Bismark, since you brought him everywhere we went! It was worth it though since he is so good at making friends. Your refined palate led us on many adventures, all the way to Burlington and Weinstein and Gambinos. I most of all would thank you for your quick sense of humour and positive attitude, even when the lab was a dark place for me. Your initiation of Evans room or pic-nick table "think tank" discussions have clarified all of life's mysteries for us, #yolo. Your opinion is always unique and interesting, and it's all yours.

Graham, Garry and Katie, from campfire sing-alongs, to the Russian party, to the Hiberville rink, cottage weekends and the summer reservoir games (no head injuries though!), thanks for all the great memories.

Nicole and John, thanks for believing in my ideas and helping me accomplish what was truly a sprint to the finish for my thesis. I could not have done it without either of you. I think John and I owe Nicky a music party!

Kevin, my best friend since kindergarten, regardless whatever was happening in our lives, thanks for being able to sit back with me and watch the Habs game and not talk science!

Although not everyone is here at the finish line, I would like to thank all of the people that were there from the start and those just passing through. Carolin my friend since undergrad, Rolf my first mentor, Karina, the Brazilian dance storm, Andrea and her Ducky, Katherine, and her awesomeness, Ilton and his speedo, Kim the calm at the center of the storm (unless were at Johan's), Janane our fearless ambassador, Donnie our French connection, Aurelie my protégé, Pongphak who never shies away from one more project, Amani with her new Canadian spirit, Dowina and Anita. I would also like to thank the boys from Black Shuck for some great hockey moments at McConnel and BDP afterwards and also Sam and Doc Rock for welcoming me into many guest appearances with Moondog at the No Tell.

Well on a final note, as the official lab DJ, I have created a final tribute to my lab mates. Below is attached the Ultimate PhD Playlist; the songs that got me there and back again with a solid group of friends. Best of luck to all of you, go with the Force!

PhD Ultimate Playlist

Song 1: A-Ok-Face to Face

Song 2: When the levee breaks-Led Zeppelin

Song 3: Hey Joe-Jimmy Hendrix

Song 4: Summertime-Sublime

Song 5: Feels so good-Jamiroquai

Song 6: The Day-The Roots

Song 7: Beercan-Beck

Song 8: Jailbreak-Thin Lizzy

Song 9: This is a call-Foo Fighters

Song 10: Highschool lover-Cayucas

Song 11: Snakes are charmed-Torche

Song 12: Blow up the outside-Soundgarden

Song 13: Homebrew-311

Song 14: Everybody loves the sunshine-Seu Jorge

Song 15: White noise-Dispatch

Song 16: Ziggy Stardust-David Bowie

Song 17: Always on time-Ja Rule

Song 18: Man or mouse-Millencollin

Song 19: Astronaut-G Love

Song 20: The Rhythm-The Cat Empire

Table of Contents

List of Figures

List of Tables

List of Abbreviations

µL: microliter

µm: micrometer

µM: micromolar

1D: one dimensional

2D: two dimensional

$3C_{12}$: dodecane diol trimer

3D: three dimensional

3PS: three point star

5'OH: 5' hydroxyl

A: adenine

ACN: acetonitrile

AFM: atomic force microscopy

AuNPs: gold nanoparticles

bp: base pair

C: cytosine

C6: hexane diol

Chol: cholesterol

CPG: controlled pore glass

cryoEM: cryogenic electron microscopy

Cy3: Cyanine 3

Cy5: Cyanine 5

DCM: dichloromethane

DLS: dynamic light scattering

DMT: dimethoxy trityl

DNA: deoxyribonucleic acid

DOPC: 1,2-dioleoyl-sn-glycero-3-phosphocholine

DPPC: 1,2-dipalmitoyl-sn-glycero-3-phosphocholine

DS: displacement strands

ds: double stranded

DX: double crossover

em: emission

ex: excitation

FBS: fetal bovine serum

FFT: Fast Fourier transform

FRAP: fluorescence recovery after photobleaching

FRET: fluorescent resonant energy transfer

G: guanine

GUV: giant unilamellar vesicle

H-bond: hydrogen bond

HEG: hexaethylene glycol

HG: head group

HPLC: high-performance liquid chromatography

hr: hour

L: ligated

M : molar

min: minute

mL: milliliter

mM : millimolar

MMT: monomethoxy trityl

MS: mass spectrometry

ms: millisecond

mW: milliwatts

NC_{16}: palmitoyl analog

NH: amine

nm: nanometer

NNI: National Nanotechnology Initiative

NP: nanoparticle

nt: nucleotide

P: phosphate

PAGE: polyacrylamide gel electrophoresis

PD: polydispersity

RP-HPLC: reverse-phase high-performance liquid chromatography

RT: room temperature

s: second

ss: single stranded

SSLBM: spherically supported lipid bilayer membrane

STM: scanning tunneling microscope

STV: streptavidin

SUV: small unilamellar vesicle

SWNT: single walled carbon nanotube

T: thymine

TEM: transmission electron microscopy

TP: triangular prism

Tr: trityl

TX: triple crossover

UV: ultraviolet

Vis: visible

Contributions of Authors

Chapter 2:

SSLBM preparation, fluorescence imaging, FRAP experiments and editing were performed by Caroline Madwar. Synthesis of the original hydrophobic anchors and system design was done in part by Thomas Edwardson and Christopher McLaughlin. Johans Fahkoury assisted in editing and figure design.

Chapter 3:

Nicole Ayakyan performed AFM imaging and editing. John Chu Chia Hsu performed AFM, native gel analysis and figure editing. Donatien de Rochambeau performed the coupling and HPLC analysis of the palmitoyl analog phosphoramidite. Maciej Barlog synthesized and characterized using NMR the palmitoyl analog phosphoramidite precursor.

Chapter 4:

Christopher McLaughlin performed FBS assays, and assisted in synthesis of the DNA strands and editing. Katherine Castor performed and analyzed the thermal denaturing experiments.

Appendix 1:

Johans Fahkoury performed the fluorescence microscopy and assisted in the system design.

Chapter 1

Introduction

1.1 Nanotechnology

In recent years, the precise control of materials at the molecular level has been an increasingly important objective. This has paved the way for the creation of a new interdisciplinary field termed nanotechnology. Nanotechnology has been defined by the National Nanotechnology Initiative (NNI) as the manipulation of matter where at least one of the size dimensions is 1-100 nm, and where new properties emerge as a result of this length scale. Its applications are seen in medicine such as imaging, targeting, and drug delivery, in material fabrication such as nanocircuitry, nanopatterning and light harvesting devices or even in day to day applications such as sun screens, currency authentication and towards cleaning the environment[1-4]. These diverse applications of nanomaterials are linked to the intrinsic changes to the physical characteristics of matter when scaled down to the nanometer size level[5] such as its electronic state, physical structure, magnetic or optical properties[6].

As technological advancement drives the miniaturization of materials, top-down fabrication methods such as lithography, whereby material is removed to form a pattern, are approaching their limits. This era of nanotechnology was anticipated by Feynman in his 1959 lecture "Plenty of Room at the Bottom" in 1959, wherein he describes bottom-up assembly to meet emerging fabrication limitations. Although the invention of the scanning tunneling microscope (STM) has now allowed the fabrication of devices with atomic precision, this fabrication route is time consuming, expensive, and highly specialized. Furthermore, although chemical synthesis has created innumerable covalently linked molecular structures, the size range of most molecules is limited to several nanometers. The drive towards tailored nanostructures has driven chemists to look "beyond the molecule" for new construction strategies[7].

In 1978, Jean-Marie Lehn first coined the term supramolecular chemistry to define the non-covalent intermolecular assembly of molecules into higher-order structures. Supramolecular

chemistry employs these non-covalent interactions to organize smaller component molecules together in a predetermined, programmable fashion[7]. Some of the first examples of supramolecular assemblies include crown ethers and cryptands, (Figure 1.1A/B) which were shown to recognize and complex with metal cations in a predictable fashion. As the field expanded more complex supramolecular organizations emerged such as capsule forming structures (Figure 1.1C) and cavitands (Figure 1.1D) with chemical functionality. Developments in supramolecular chemistry led to a rapid expansion in the domains of molecular recognition and host-guest chemistry. Cram, Lehn and Pederson were awarded the Nobel Prize in chemistry in 1987 for their fundamental work which laid down the fundamental rules of supramolecular chemistry, such as the pre-organization of binding partners for binding affinity and selectivity and the use of simple, predictable interactions[8-10].

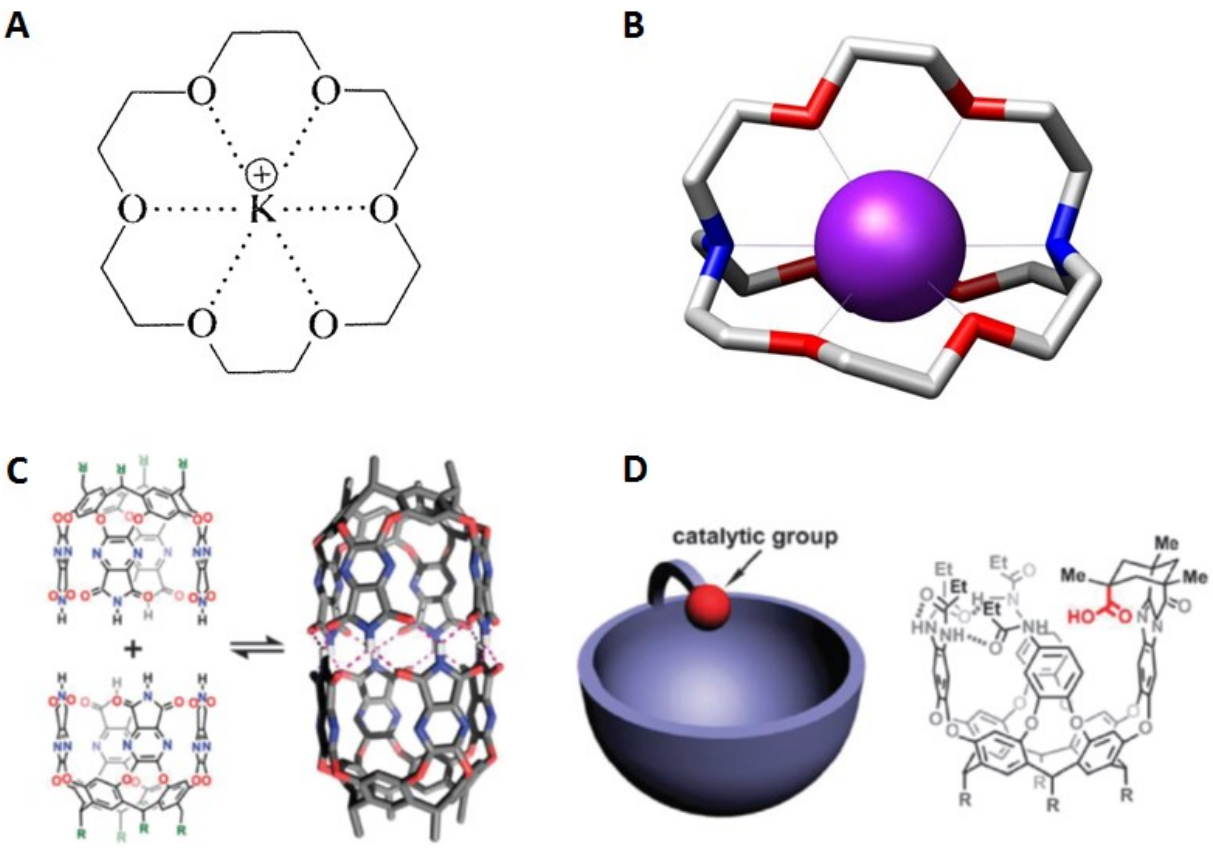

Figure 1.1: Several examples of supramolecular chemistry based on non-covalent molecular recognition and self-assembly. From the top left, the images depict: (A) a metal coordinating crown ether structure, (B) a cryptand containing a guest molecule, (C) a capsule formation[11], (D) a cavitand with a functional modification[11].

Today, researchers make use of weak, cooperative interactions such as hydrogen bonding (H-bonding), metal coordination, hydrophobic interactions, π-stacking, Van der Waals interactions or even electrostatics[8,10] to design "smart" nanoscale assemblies that self-assemble from their components with high yields. Supramolecular assemblies are held together through many cooperative, weak non-covalent interactions between molecular building blocks. Their relatively weak and reversible nature allows for error correction within misassembled structures. This can be carefully controlled by varying assembly conditions such as temperature, ionic strength, concentration or metal coordination states. As the understanding of different types of non-covalent

interactions grows, chemists have been able to create increasingly selective assemblies by varying the shape, size, charge or flexibility of the component molecules.

The development of functional intermolecular assemblies using carefully chosen chemical properties has several advantages over top-down assembly methods including error correction, high yields, parallel fabrication of billions of structures and reduced fabrication times. It should be noted that the design of such structures is by no means trivial and requires a significant investment of time for developing stable architectures, reproducible chemical synthetic routes and characterization methods before large scale use. Self-assembling systems as a means to create functional materials are drawing a considerable amount of scientific and economic attention and they have already revolutionized many present fabrication techniques.

Although supramolecular chemistry has yielded an extraordinary amount of new materials, it does have certain limitations, primarily the fact that these assemblies are constructed using symmetry and periodicity. The design and synthesis of novel functional molecular organizations will require selective asymmetric positioning of chemical modifications within these structures. Scientists have therefore turned to investigating other self-assembling molecules which may be used in conjunction with the supramolecular intermolecular systems described above.

1.2 DNA

Deoxyribonucleic acid (DNA) is one of the most remarkable examples of a self-assembling material and has been the focus of extensive research for over 30 years. It is commonly found as a double helical structure and is known to store the unique genetic information of biological life on earth. The structure of DNA was determined in 1953 by Watson and Crick[12] in collaboration with Franklin[13] (Figure 1.2). DNA consists of two individual strands aligned in an anti-parallel fashion, composed of a repeating deoxyribose sugar backbone connected through a phosphodiester bond between the 3' and 5' hydroxyl positions on the sugar ring. The deoxyribose sugar is covalently linked to the nucleobase at the C1 position of the ring. These bases can be divided into two categories, purines which consist of adenine (A) or guanine (G) and pyrimidines which consist of thymine (T) and cytosine (C) (Figure 1.2). Together the phosphate, deoxyribose sugar and a nucleobase comprise what is termed a nucleotide. Our genetic information is coded into long

strands of DNA by specific sequences of nucleotides, with some strands over 200 million units in length.

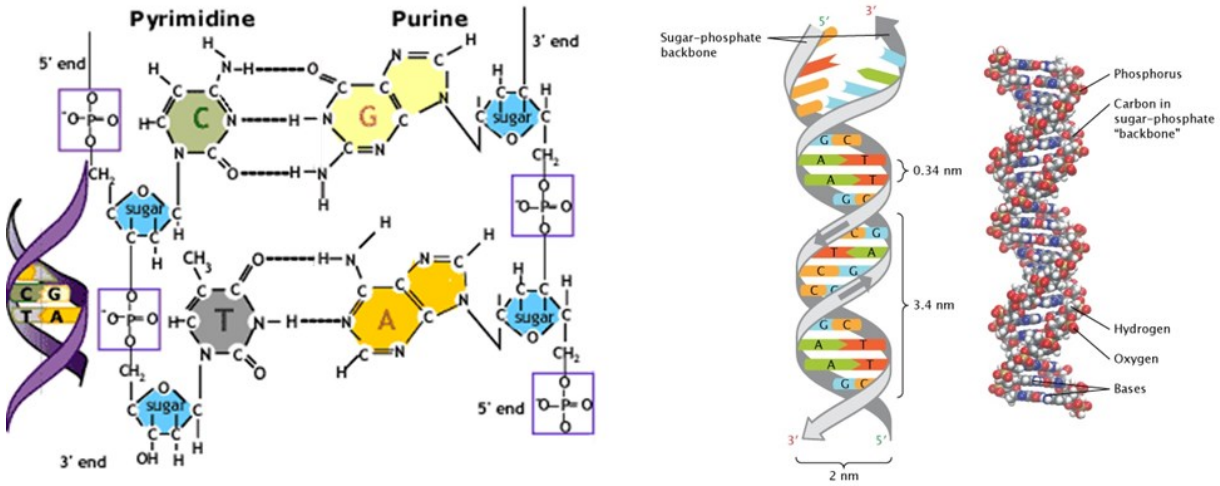

Figure 1.2: (Right) Chemical structure of DNA nucleotides, (Left) DNA helical structure[14,15].

The helical assembly of two strands of DNA is linked to the highly specific H-bonding patterns between the nucleobases, A with T and G with C. The A-T base pair (bp) is held through 2 H-bonds while the G-C base pairing is held through 3 H-bonds, leading to a stronger interaction between this bp (Figure 1.2). Furthermore, the alignment into a helical structure places the conjugated rings of the bps such that favorable π-stacking occurs. It is the combination of many weak non-covalent interactions that lead to the cooperative zipping in the double stranded (ds) helical structure.

The structural parameters of the DNA helix have been extensively examined; it has been shown that a double helix behaves as a rigid rod up to 10 nm with a persistence length of 50 nm. The DNA helix can be found in several forms, but under physiological conditions it is in the B-form helical structure, has a width of 2 nm and a pitch of 3.4 nm, or 10.5 bps per turn (Figure 1.2)[16,17]. Other helical forms include A-form helices found under dehydrated conditions and Z-form helices, which are a result of high salt concentrations (Figure 1.3A). There are also several examples of modified base pairing such as Høøgsteen base pairing (Figure 1.3B) which leads to structures such as the *i*-motif (Figure 1.3C), and G-quadruplex (Figure 1.3D) structures. It should be stressed that under normal conditions the highly discriminate collective interactions between bps lead to precise strand recognition and programmable assembly.

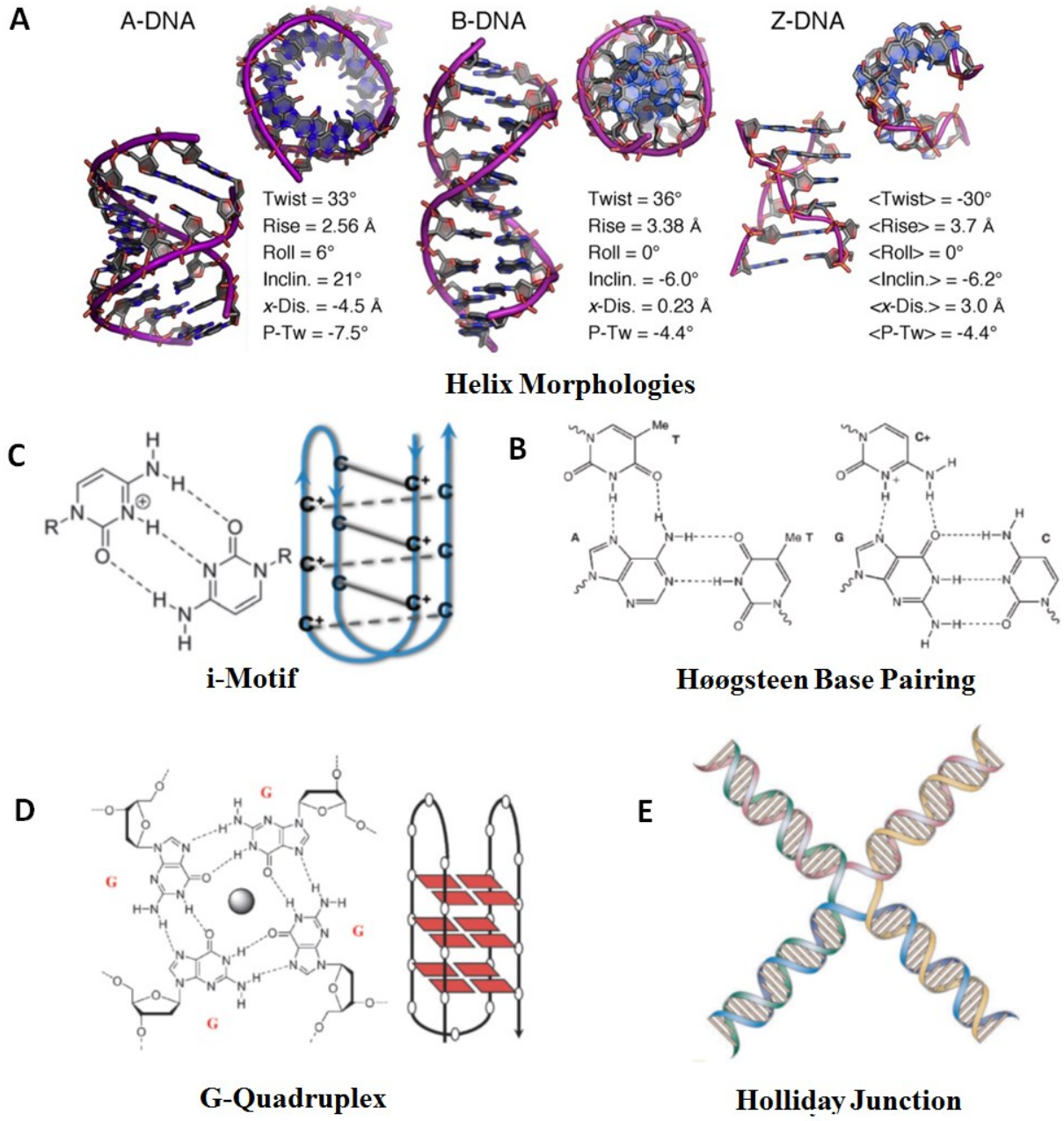

Figure 1.3: (A) Different helical morphologies of DNA. (B) Høogsteen base pairing motif. [16,17], (C) i-motif folding pattern[18], (D) G-quadruplex folding pattern[19], (E) Holliday Junction structure[20].

The present explosion of DNA related research is linked to the significant advancements that have been made in the synthesis of the biopolymer itself. In the 1950s work by Khorana showed that DNA synthesis was possible using solution phase phosphodiester chemistry. The next major step

in DNA synthesis was accomplished by Letsinger (1960s) who developed the method of phosphotriester oligonucleotide synthesis[21]. The main improvements here being use of orthogonal protecting groups to prevent some of the side reactions found in earlier chemistries. Although originally developed as a solution phase synthesis method, it eventually was used in combination with a solid support. Work by Caruthers (1970s) further improved the efficiency of the coupling reactions by taking advantage of phosphitetriester synthesis to create the stable nucleoside phosphoramidites commonly used today (Figure 1.4)[22]. Synthetic DNA synthesis at this point became a cycle of reactions whereby nucleotides are coupled sequentially to a solid support as reagents are flowed through. Recognizing the potential for automation of this process, Ogilvie et al developed the first commercially available automated DNA synthesizer[23].

Automated DNA synthesis consists of four steps: (1) deprotection, (2) activation and coupling, (3) capping, and (4) oxidation (Figure 1.4A). In general, the first base of a DNA sequence is anchored to a solid support through an ester 3' linkage and contains a protecting group for the 5' hydroxyl (5'OH) (trityl (Tr), dimethoxy trityl (DMT) or monomethoxy trityl (MMT) group) – most often DMT. The solid support is typically small grains of silica containing pores with a defined size and packed into a column. The first step of the synthesis is the deprotection of the 5'OH. Second, the next nucleotide is added as a 3'-phosphoramidite derivative, along with an activator which favours coupling with the 5'OH. Next the uncoupled strands are capped with an acetyl group to minimize the growth of oligonucleotides with failed coupling. Finally, the base is oxidized with iodine to the stable phosphorous(V) oxidation state. The cycle is then ready for the next base addition. Once completed the strand is cleaved from the solid support and the nucleotides are deprotected using ammonium hydroxide. Presently, there exist several companies that sell DNA synthesizers compatible with standard solid-phase phosphotriester chemistry, as well as companies specializing in the synthesis of ready to couple phosphoramidite versions of bps and non-natural molecules (Bioautomation, ChemGenes or Glen Research).

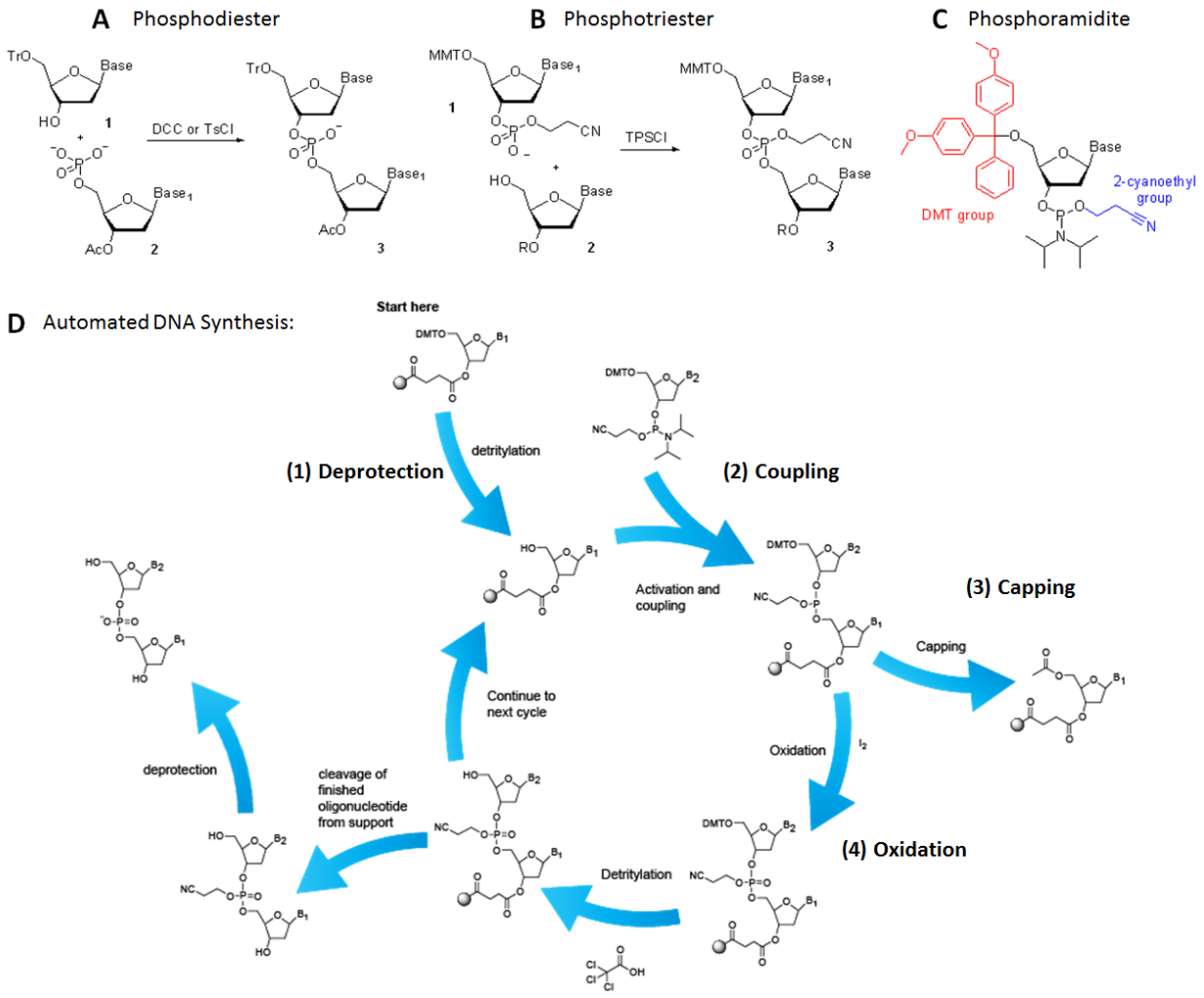

Figure 1.4: Chemical structures illustrating the historical evolution of DNA synthesis. (A) The synthetic scheme of Khorana for solution phase phosphodiester synthesis, (B) the synthetic scheme of Letsinger for solid phase synthesis of phosphotriester synthesis, (C) the present day phosphoramidite developed by Caruthers, (D) Schematic representation of the chemical steps during automated DNA synthesis.

1.3 DNA Nanotechnology

The programmability and simple base pairing rules of DNA were first recognized as a tool for creating self-assembled materials in the 1980s by Seeman and co-workers. Seeman was interested in the field of biological crystallography and intended to use DNA as a programmable scaffold to

form 3D crystalline networks, for biomolecular crystallography applications. This marked the first instance of DNA used as a building material, outside its normal biological context, and the beginning of the field of DNA Nanotechnology. As the potential of DNA to precisely organize materials was demonstrated and applied to a variety of fields, the strategies for assembling DNA nanostructures have been classified into three main groups: (1) Structural DNA Nanotechnology, (2) DNA Origami and (3) Supramolecular DNA Nanotechnology.

1.3.1 Structural DNA Nanotechnology

Structural DNA Nanotechnology focuses on the design of DNA structures from pre-assembled tile units or individual complementary strands, as building blocks to form one-, two- and three-dimensional (3D) objects or networked materials. The initial work by Seeman focused on using the naturally occurring four-way Holliday junction as a starting point for the structural motif of his tile-network assembly (Figure 1.5)[24,25]. In this study the junction motif was re-designed to include unpaired nucleotides or "sticky-ends" at the end of each arm. The junction was also designed using asymmetric strands to prevent branch migration found in naturally occurring Holliday junctions. The pre-organized sticky-ends are programmed to be complementary and drive the self-assembly of the Holliday junction tiles into a network or nanostructure. This was the first example showing how DNA could be used as a building block by breaking its normal 1D structure.

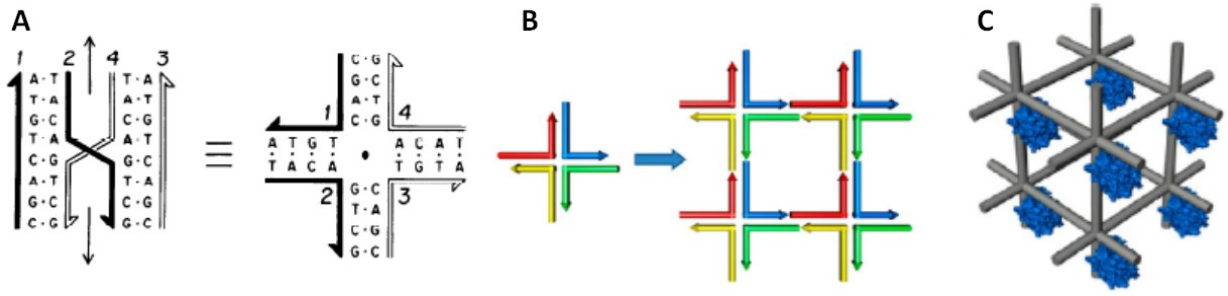

Figure 1.5: (A) The naturally occurring Holliday junction, showing reversible branch migration due to strand symmetry. (B) Seeman's modified Holliday junction for construction of lattices. Each junction consists of 4 unique strands. (C) Representations of potential crystal matrix organization for biological crystallography using a Holliday junction based tile [17,24].

The drive towards higher-order DNA structures using tile assembly methods was limited by the problem of flexibility within the branch points of the DNA building blocks. This led to the design of the first double crossover (DX) tile using two parallel interwoven helices as a more rigid primary building block[26] for construction of larger DNA structures (Figure 1.6A). Many research groups have developed a wide variety of different tile based assemblies through folding crossover variations and branched designs, however all such examples share the concept of pre-organized sticky-ends to direct specific structural features. Presently, there exist several variations of the DX tile motif used to direct different connectivities: multi-junction tiles[27], triple cross-over motifs[28], double-double DX tiles[29], and rectangular tiles 4, 6, 8 or 12 helices in width[30,31] (Figure 1.6B). These different assemblies will be discussed as specific examples in the following section.

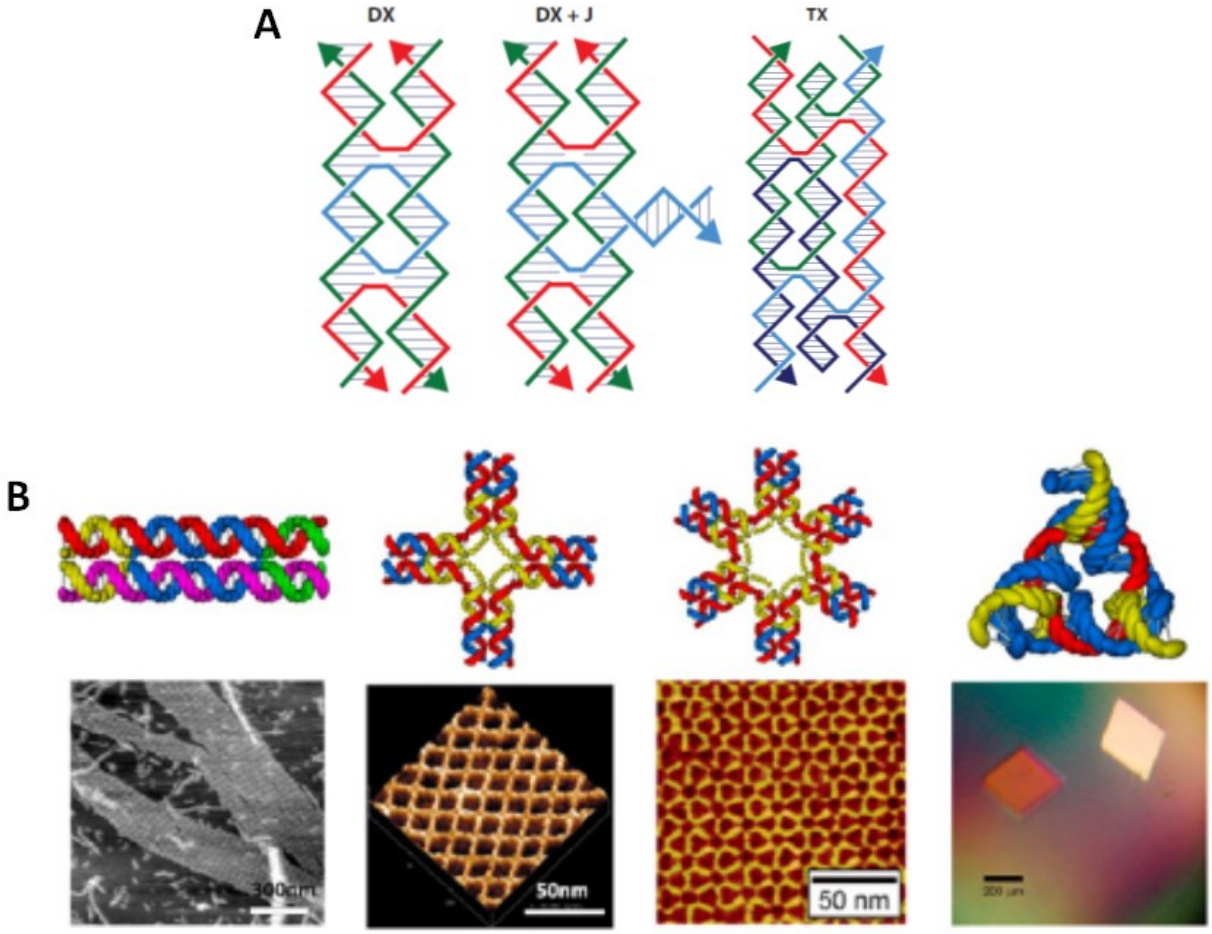

Figure 1.6: (Left) Design showing the original DX motif, the modified DX+ J for altered assembly, and the triple cross-over (TX) motif. (Right) Several examples of

networks that are generated using DX-based DNA tiles and visualized using AFM and light microscopy[17,32].

1.3.1.1 2D Tile Based Networks

Large extended 2D tile DNA networks have been shown to assemble in solution and readily deposit on a solid substrate surface such as mica for characterization and imaging using atomic force microscopy (AFM) and other microscopy techniques. One of the first examples of DNA visualized using AFM was in 1992, by a group who imaged plasmid DNA (Figure 1.7)[33]; they postulated that the technique of AFM may be applied to studying protein-DNA interactions as well as chromosome mapping. Some of the first images of 2D DX tile networks using AFM were reported in work by Seeman *et al*. in the late 1990s (Figure 1.7)[34,35]. AFM has since become one of the standard characterization techniques for visualizing DNA nanomaterials, and generating unambiguous evidence for correct molecular organization.

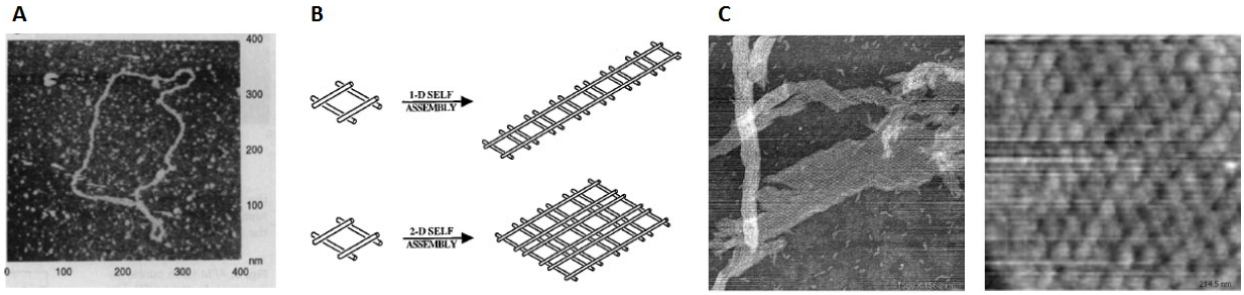

Figure 1.7: (A) First reported AFM image of plasmid DNA. (B) Assembly strategy to create 1D/2D networks using the original DX tile. (C) Early AFM images of 2D DX tile networks [33,35].

Research into these structures has focused on demonstrating the ability of DNA to organize molecules into controlled arrays towards the creation of sensors, microdevice components, molecular motors, logic gates or reaction cascades[32,36]. This is accomplished by covalent modification of one of the tile forming strands to create a handle for the docking of guest molecules. 2D tile networks can then be assembled as usual and anchored guest molecules will be templated into a controllable, periodic arrangement. Extended 2D tile motifs have typically been

used to organize materials such as proteins[37], aptamers[38](targeting oligonucleotides), nanoparticles (NPs)[39-41], or antibodies[42].

One of the first examples of the directed organization of biomolecules using 2D tile networks, made use of biotin functionalized tiles to position streptavidin (Figure 1.8A)[37]. Researchers were able to deposit streptavidin onto the 2D networks and control its periodic placement by varying the position of the biotin functionality embedded within the 2D network. Similar 2D tile networks have also been engineered to organize linear arrays of aptamers (Figure 1.8B)[38] or antibodies[42] for protein-binding and show periodic positioning using AFM. Inspired by the original idea of Seeman to use DNA as a scaffold to organize proteins for imaging, it has been shown that 2D arrays can be used for single molecule imaging of templated proteins using cryo-transmission electron microscopy (cryo-TEM) (Figure 1.8C)[43]. These examples demonstrate the power of DNA for precise positioning of material across long-range 2D networks, however the undefined extended nature these scaffolds limited their addressability as asymmetric platforms. This was solved by introducing increased asymmetry into the tile networks themselves, and creating a set of unique tiles programmed to assemble into a specific shape such as a 3x3 peg-board[44,45].

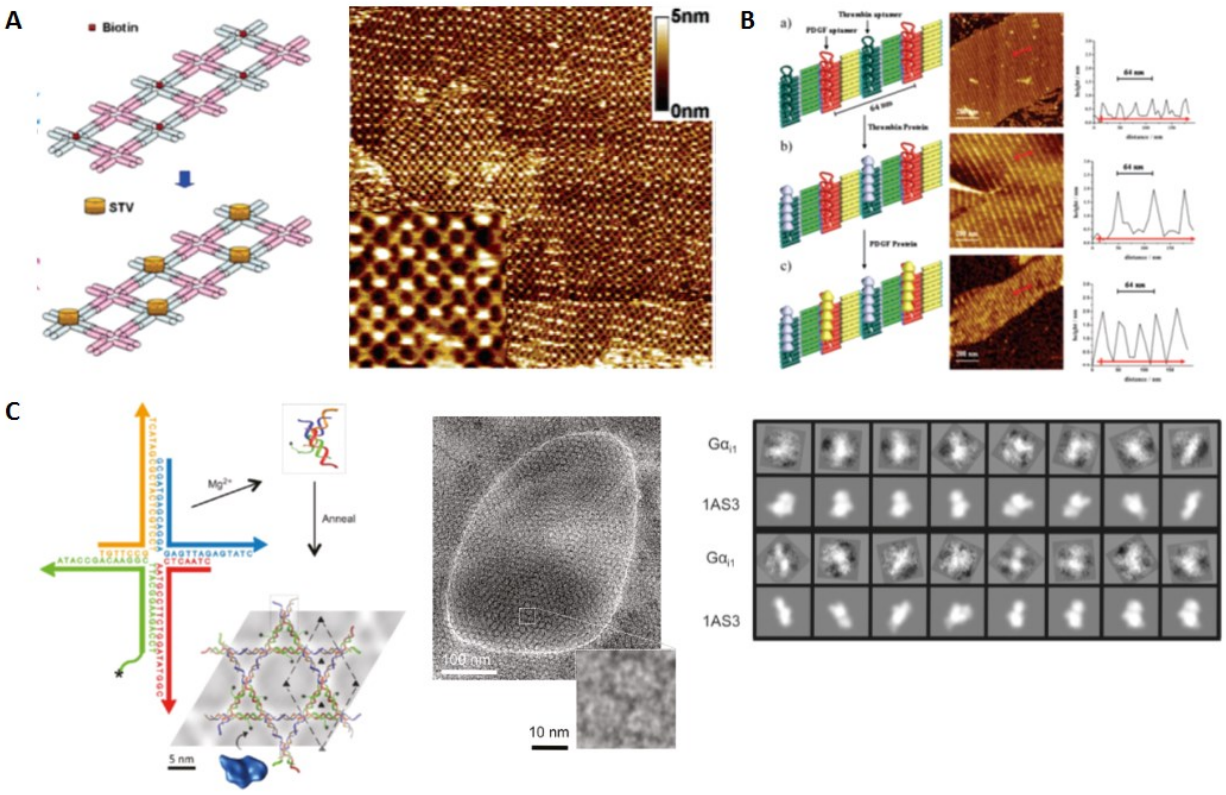

Figure 1.8: (A) Biotin labeled DNA tiles have been shown to form 2D networks that can organize streptavidin (STV). (B) An extended tile network has been formed using alternating tile rows functionalized with different protein binding aptamers. (C) A modified Holliday junction motif was used as a scaffold to organize proteins for cryogenic electron microscopy (cryoEM) imaging[37,38,43].

Finite 2D tile networks have been examined as a platform for asymmetric placement of biomolecules. One example makes use of a programmed mixture of 9 unique tiles to form a 3x3 tile based peg-board with each tile designed to be addressable by a specific biotin modified DNA strand (Figure 1.9A). When the peg-boards are incubated with streptavidin, labeling only occurred at designated positions[44]. Similar work was done to create a 4x4 peg-board that was then appropriately labeled to create a topological pattern spelling 'DNA' (Figure 1.9B)[45].

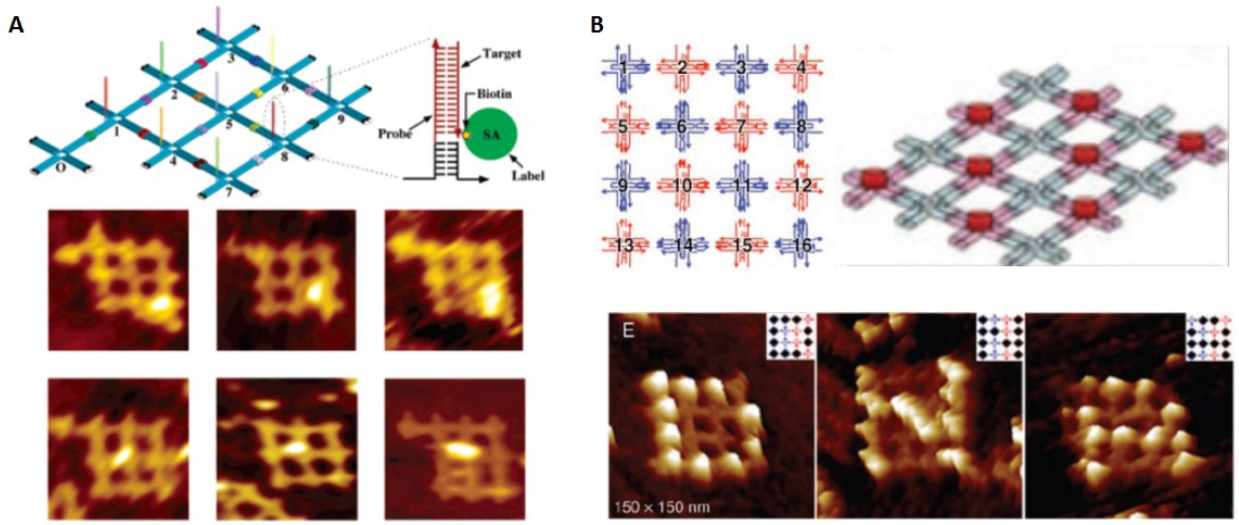

Figure 1.9: (A) Design of the 3x3 tile peg-board for controlled placement of STV. (B) Design of the 4x4 tile-pegboard used to spell DNA through programmed binding of STV[44,45].

DNA tile networks have been used to organize inorganic materials as well. Precise 2D arrays of nanoparticles have been created with potential applications in plasmonic or nanoelectronic devices. Early examples of this strategy were demonstrated by organizing a periodic network of tiles displaying open hybridization sites followed by the landing of DNA functionalized gold nanoparticles (AuNPs) (Figure 1.10A/B)[39,40]. A tensegrity triangle tile motif[46] was used to organize different sized AuNPs into repeating 2D arrays. In this work two populations of tiles were pre-assembled with different sized AuNPs and then combined to form 2D networks, and imaged using TEM (Figure 1.10C)[41]. These strategies demonstrate that AuNP labeling can be performed post 2D network formation or during formation, without hindering the DNA hybridization.

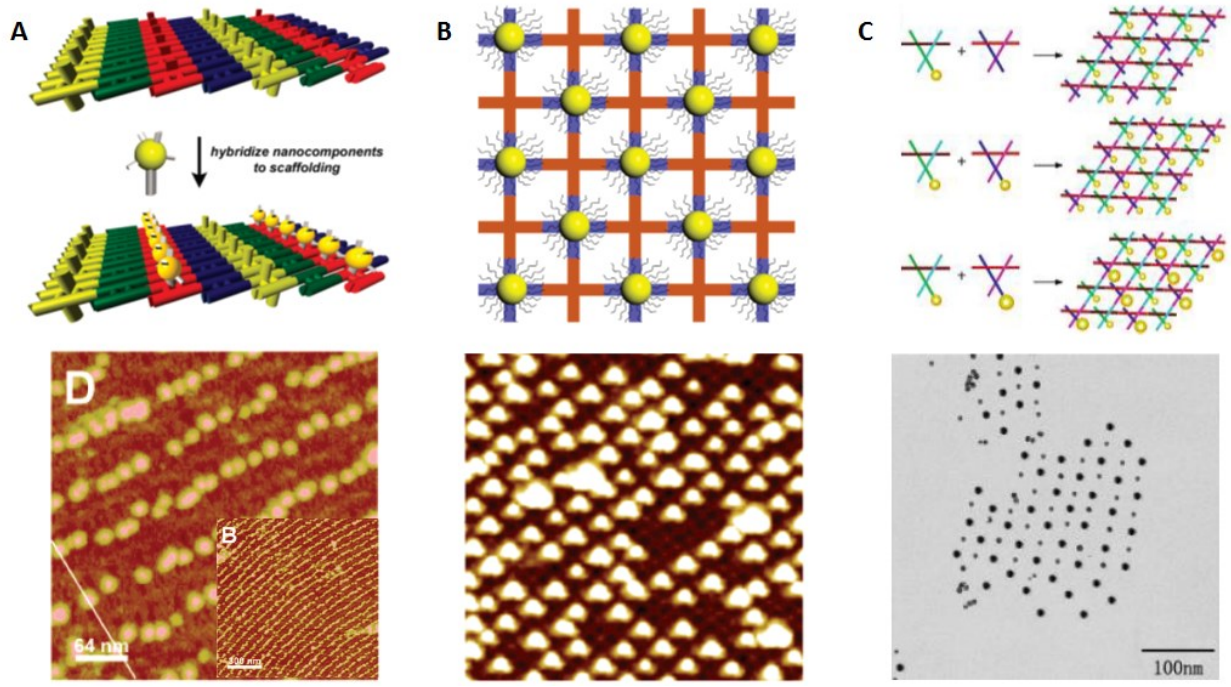

Figure 1.10: (A) 2D tile network used to pattern AuNPs in linear arrays. (B) 2D tile network used to pattern AuNPs in periodic arrangements. (C) Tensegrity triangle tile used to create patterns of alternating sized AuNPs[39-41].

1.3.1.2 Single-Stranded DNA Tiles

The tile motifs discussed up to this point are examples of individual tile units comprised of several strands, designed to pre-assemble into primary building blocks which then self-assemble into a macromolecular structure. In pushing the limits of tile based assemblies researchers have asked the question of what is the minimum number of strands required to create a "tile" unit for construction of well-defined nanostructures[47,48]. This challenge was first achieved by Mao in 2006 using a design that employs a self-complementary single strand tile unit (Figure 1.11A). This design, based on a DX tile, was shown to self-assemble into extended nanotube structures which were then used to template the formation of Pd nanowires[47].

Using the previously developed T-junction[49], Mao et al has also shown similar single strand tile motifs, the Z-tile and the C-tile, which are able to direct the self-assembly into long filaments or a 2D grid pattern respectively (Figure 1.11B)[48].

A major limiting factor of tile assembly is the lack of strand asymmetry to control a defined shape. The discrete peg-board examples previously discussed meet the criteria using a set of up to 12 unique tiles. However, each tile requires its own sub-set of unique strands which quickly becomes difficult to manage experimentally. The use of an asymmetric single stranded (ss) tile would greatly overcome this limitation.

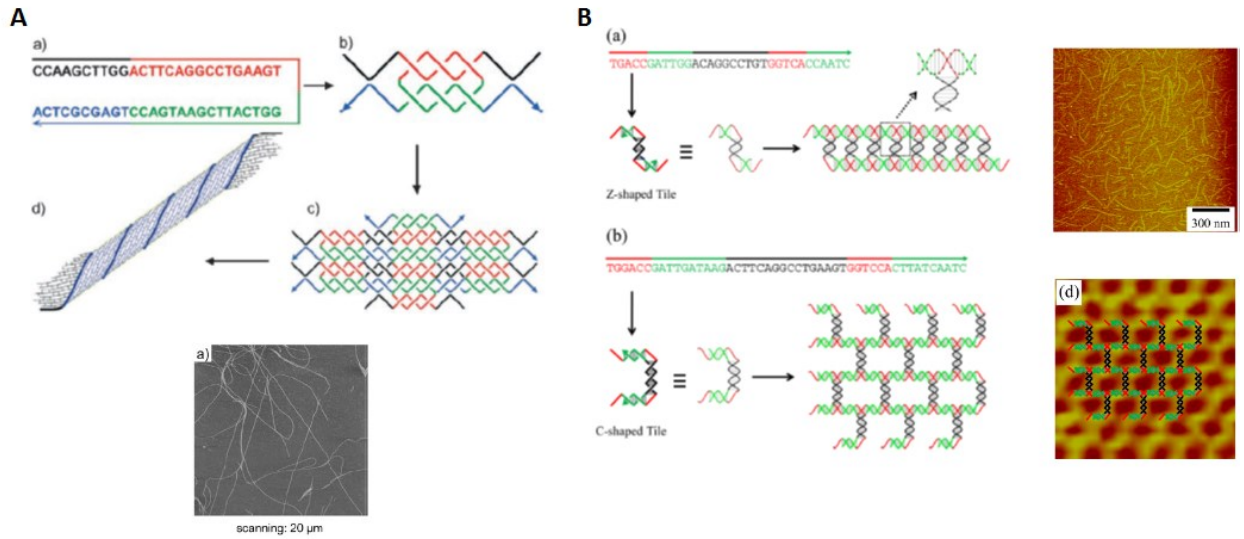

Figure 1.11: (A) Single-stranded DNA tiles assemble into a self-complementary building block that undergoes further assembly into a rolled 2D network nanotube structure. (B) Structure and self-assembly of the Z-tile which forms linear networks and the C-tile which assembles into a 2D extended network[47,48].

The first example of extending the single-stranded (ss) symmetric tile assembly towards discrete object formation used a pool of 4 to 20 ssDNA tiles that assemble width-wise through asymmetric hybridization and symmetrically length-wise to create controlled width nanotubes (Figure 1.12A)[50]. Recognizing that symmetric assembly could be completely eliminated, a unique set of DNA "bricks" was designed as a pre-defined canvas or "brick-wall" (Figure 12B). This ss tile canvas could be variably assembled into 2D structures by leaving out certain bricks, analogous to removing pixels from a canvas. Conceptually each single DNA strand was considered as a unique tile comprised of 4 distinct binding regions with which it can hybridize to four neighboring strands. This technique was extended to a larger canvas size that included over 300 unit bricks or pixels

with which they were able to assemble over 100 different 2D shapes using subsets of the master brick collection[51].

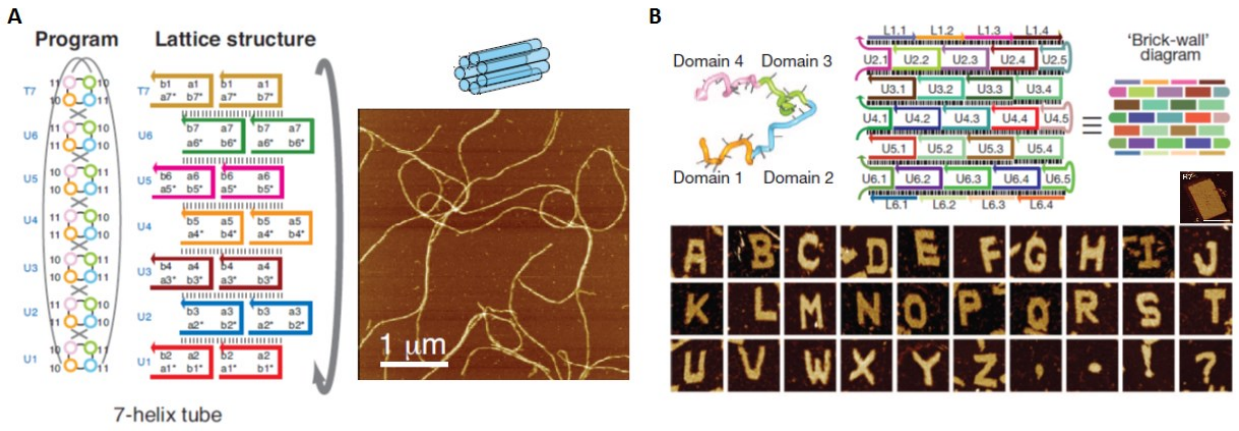

Figure 1.12: (A) ssDNA tiles with width-wise asymmetry and length-wise symmetric self-assembly patterns to form a nanotube with variable width. (B) First example of a large pool of unique ssDNA tiles used to create a 2D network canvas that can form over 300 different shapes[50,51].

1.3.1.3 3D Tile Structures

Using a slight modification of how these individual tiles self-assemble, Yin et al were able to extend this methodology to create 3D self-assembling structures (Figure 1.13). As these structures become more complex and the number of unique strand pixels increases, the manual assembly and design methods also increase in their difficulty. These challenges were met by using robotic pipetting and computer design programs to generate the subset of strands required to make each desired object[52]. The 3D molecular canvas tile strategy is an excellent example of exploiting DNA's programmability for the design of complex nanostructures. However, the major disadvantage of this scheme is that it requires the design and synthesis of a huge library of DNA strands, as well as automated sample preparation and sequence design.

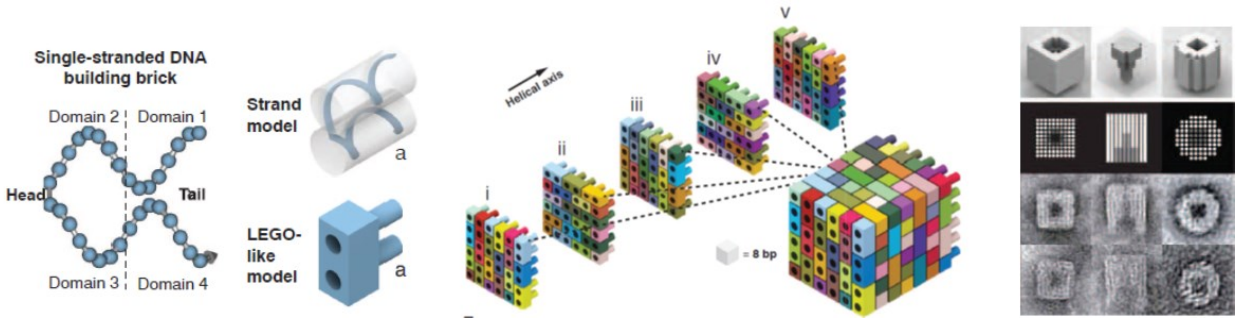

Figure 1.13: Design and assembly strategy for 3D ssDNA tile construction[52].

Traditional DX tile-like structures have also been used to create 3D DNA networks by variation of assembly conditions and through careful modifications to introduce flexibility and curvature into the tiles. The three point star motif (3PS) was shown to self-assemble into a series of geodesic spheres simply by varying assembly concentrations from 50-500 nM and by introducing controlling flexibility in the center of the tile structure (Figure 1.14A)[53]. Previously, the 3PS was shown to assemble into long range 2D networks[54] by alternating the tile connectivity in an up and down fashion to minimize the overall network curvature. The 3D closed networking relies on tiles assembling with the same face directed upwards thereby favouring curvature and driving the network into a closed structure. Work by the same group in collaboration with Seeman has led to the use of a tensegrity triangle tile motif, programmed in such a way as to self-assemble into a 3D network of crystalline material (Figure 1.14B)[55]. This required the use of very short sticky-ends (2 bases). Indeed, as was the original goal of Seeman, the tensegrity tile motif is designed to assemble into a closed packed crystal structure which could be potentially used to scaffold large biological molecules for crystallographic structure determination.

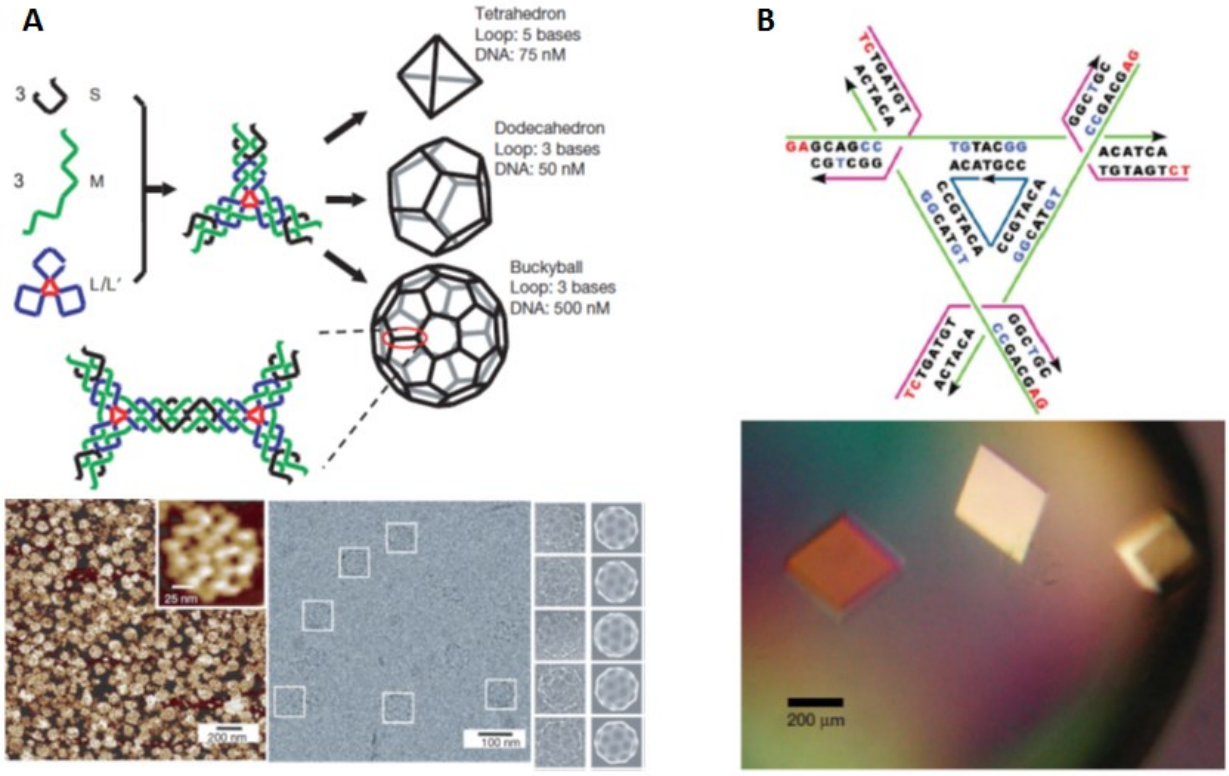

Figure 1.14: (A) The 3PS motif can form 3 different geodesic spheres through variation of assembly conditions and tile flexibility. Structures were well characterized with AFM and Cryo-EM. (B) The 3D network forming tensegrity triangle, which forms well defined crystalline structures[53,55].

1.3.1.4 Alternative Designs for 3D DNA Nanostructures

Many groups are also interested in programming linear strands of DNA to form small discrete 3D objects using alternative assembly schemes from the tiles based designs. Work by Joyce et al showed that rather than using individual tiles to construct prismatic objects, a single continuous strand could be employed as a backbone. This strategy used a continuous 1.7 kilobase single strand of DNA held together through linking strands to form an octahedron (Figure 1.15A)[56] (Shih, Joyce-Nature 2004). This strategy may have been part of the inspiration for DNA origami which will be discussed in the following section. Work by Sleiman et al has used a variable clip-by-clip methodology to design a series of prismatic cages where each prism face is a continuous strand of

DNA (Figure 1.15B), and contains multiple addressable ss binding regions[57]. Other examples of discrete DNA structures include a ligated cube (Figure 1.15C)[58], a tetrahedron (Figure 1.15C)[59,60] and an icosohedron based cage structure (Figure 1.15D)[61].

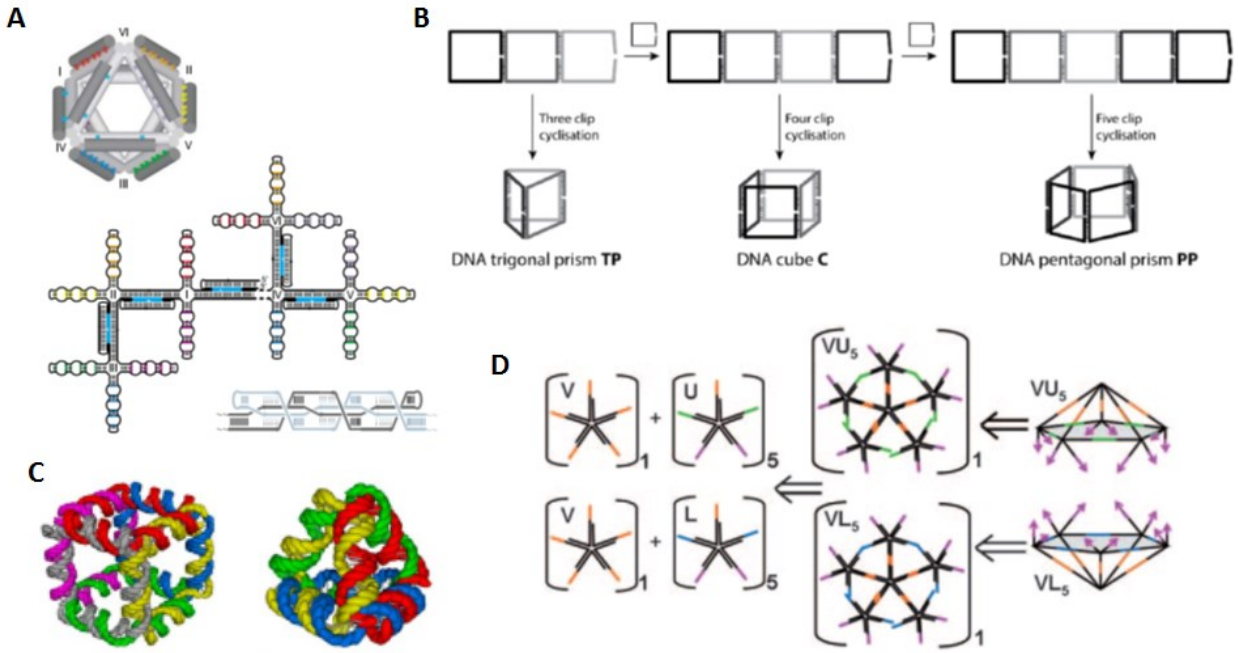

Figure 1.15: (A) A DNA octahedron structure formed using a continuous central strand held together with stappling strands. (B) The clip-by-clip assembly scheme using 96mer DNA strands to form a series of prismatic scaffolds. (C) The original ligated cube design and the tetrahedron structure. (D) An icosohedron formed using a small pool of unique DNA tiles[32,56,57,61].

Discrete 3D DNA structures have also been used to position protein components and other multivalent components such as fluorophores and aptamers. Protein encapsulation within a DNA tetrahedron was also accomplished[62] by varying the positioning of the point of attachment along the helical axis. The organization of proteins along the edges of a tetrahedron scaffold was used to increase antibody response and create a platform for vaccine construction[63]. Work by Sleiman et al showed that a modular prismatic cage can be used to precisely position polymer conjugated DNA in 3D[64].

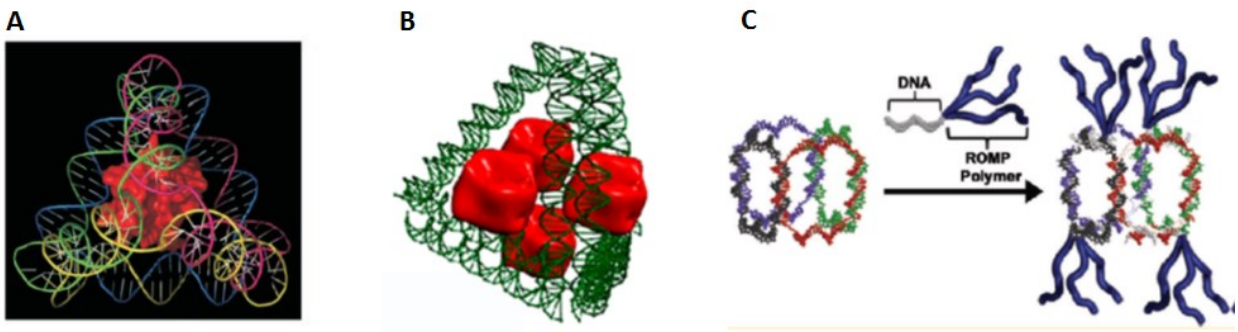

Figure 1.16: (A) The DNA tetrahedron was shown to be able to encapsulate a protein guest molecule. (B) The tetrahedron scaffold was used to organize protein components for increased antibody response towards better vaccine platforms. (C) The DNA cube structure used to organized polymer conjugates with specific 3D arrangements[62-64].

1.3.2 DNA Origami

In 2006, Rothemund demonstrated an alternative method to create robust, asymmetric nanostructures using a long single strand of DNA folded into a precise shape using staple strands[65]. This technique is termed DNA origami and has been used extensively to create many different functional materials as will be discussed. DNA origami uses a long single strand (>1000 nucleotides) of circular genomic DNA as a backbone for the assembly of hundreds of small "staple" strands (16-20 nts) which fold the backbone using a crossover motif, into a pre-determined shape (Figure 1.17A). Using a long strand of DNA and computer software (e.g., Cadnano), a user can vary the arrangement of the asymmetric staple strands to manipulate the backbone into virtually any design. DNA origami has the particular advantage of using short unpurified staple strands in a huge excess relative to the backbone strand to favour product formation. Most significantly, DNA origami scaffolds are an ideal substrate for the precise positioning of materials that need only be conjugated to a staple strand for incorporation into the structure. In the following section we will discuss advances in DNA origami design and applications.

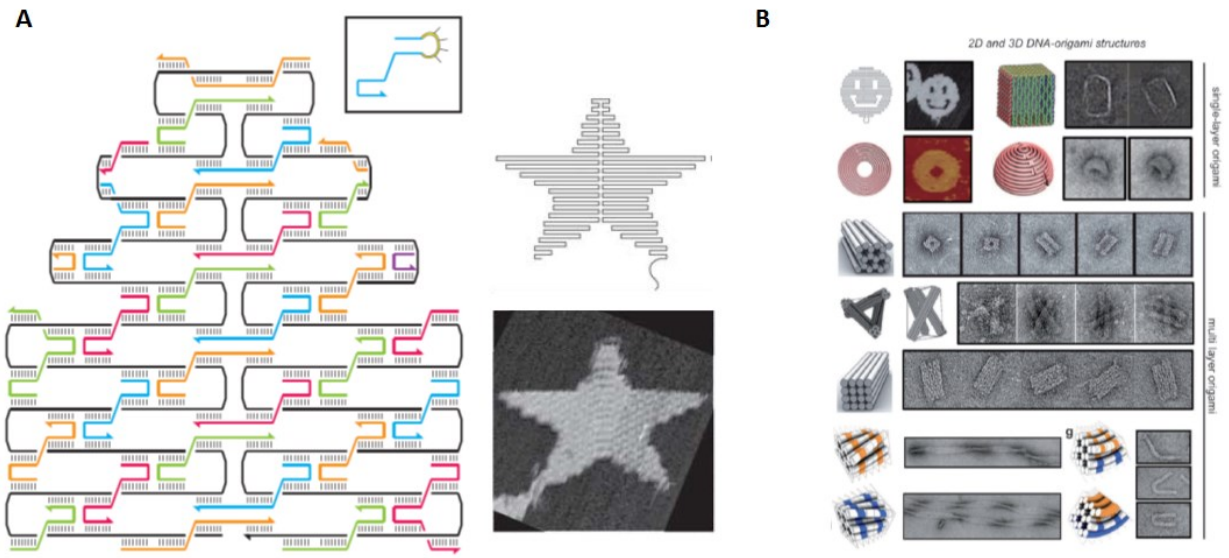

Figure 1.17: (A) Schematic representation of DNA origami showing a single continuous strand held together with many staple strands. (B) Examples of various 2D/3D shapes that have been constructed using DNA origmi[65,66].

1.3.2.1 2D DNA Origami for the Organization of Molecules

DNA origami has been used to position material in 2D arrays for applications in sensors, confined reaction studies, light harvesting, templated metal growth, and assembly into higher order structures. One of the most powerful features of DNA origami is that each strand in the assembly has a specific "address" indicating its position, in this way DNA origami tiles are inherently applicable for asymmetric peg-board organizations. In 2008 Yan et al published one of the first examples of using 2D DNA origami to position arrays of aptamers for single molecule detection of multiple RNA sequences (Figure 1.18A)[67,68]. The DNA origami tile used in these experiments was designed with three rows of ssDNA, each one being complementary to three different RNA targets. The tiles were incubated with a mixture of cell derived RNA and hybridization occurs only for the targeted RNA sequences detectable using AFM. An origami tile with two rows of pre-positioned biotins covalently attached to the DNA strands through different orthogonally cleavable chemical bonds was developed by Gothelf et al (Figure 1.18B)[69]. Researchers were able to demonstrate selective positioning and chemical cleavage of the biotin-streptavidin complexes from the substrate surface using AFM.

Other examples using DNA origami to organize and study proteins have investigated the effects of crowding on protein binding[70] as well as demonstrating the controlled deposition of viral capsid proteins[71]. Zinc-finger proteins with high affinity for specific DNA sequences have also been shown to predictably interact with origami tiles labeled with the respective protein binding sequences[72].

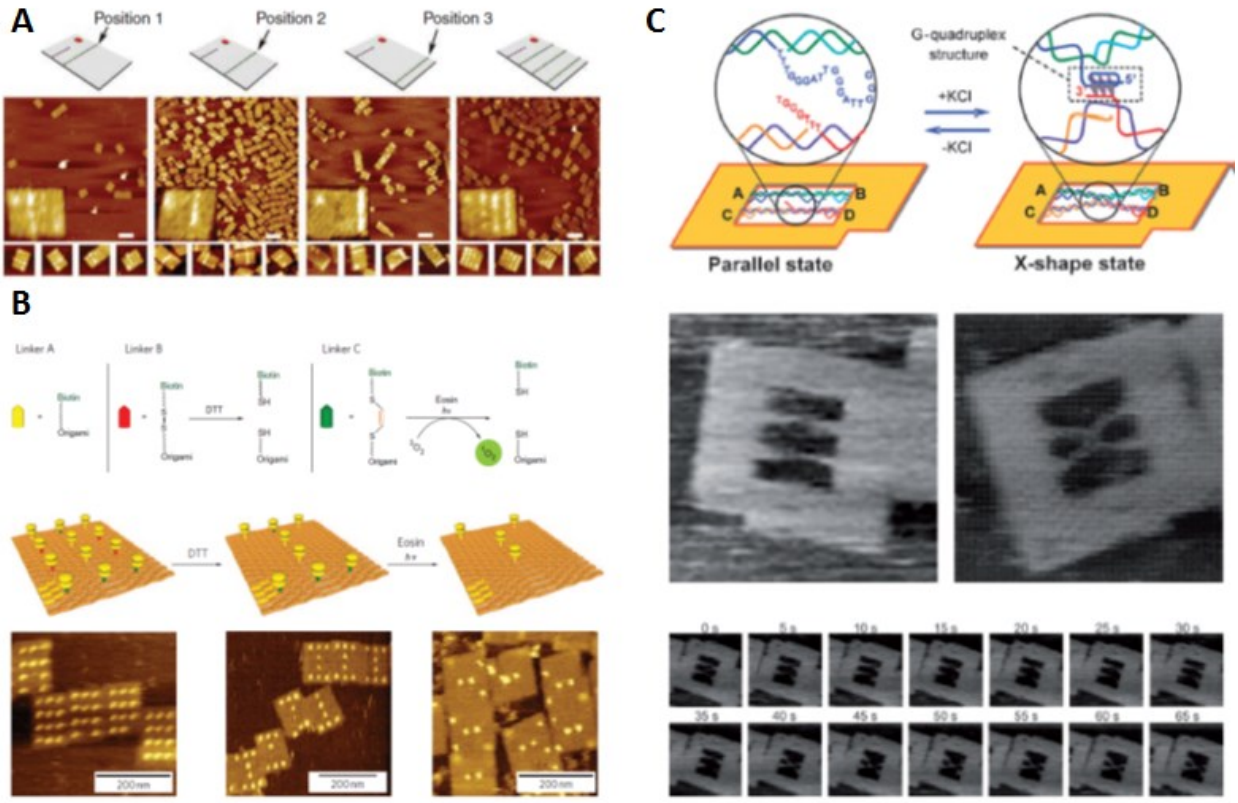

Figure 1.18: Examples of a DNA origami tile used to: (A) detect the binding of different RNA targets, (B) selectively remove biotin-STV using orthogonal cleavage reactions, (C) monitor the reversible formation of a single G-quadruplex structures[67,69,73].

A DNA origami tile was used to scaffold and visualize the reversible formation of a single G-quadruplex structure with-in the origami tile itself (Figure 1.18C)[73]. The origami tile was designed with a central cavity spanned by two helices in an anti-parallel orientation that contain unpaired single stranded DNA (overhangs) located in the middle of each helix. These overhangs contained G-quadruplex forming strands, which switchably assemble into a crossed (G-quadruplex) or

parallel (helix) pattern as KCl was added or removed from the solution. Fast-scanning AFM was used to visualize the real-time folding and unfolding of the central G-quadruplex structure.

1.3.2.2 Construction of Higher Order Architectures Using 2D Origami

As described above, 2D DNA origami tiles have been shown to precisely pattern a wide variety of biomolecules. Research has also focused on assembling DNA origami tiles into higher-order structures using blunt end stacking[74,75]. In this work, rectangular origami tiles were designed with blunt ends along particular edge lengths and a structural marker on the surfacing for indexing (Figure 1.19). It was shown that tiles predictably assemble into linear configurations. This methodology was extended to create tiles with specific "bar-coded" blunt end presentation in a variety of shapes that allowed precise pairing between selected tiles to create several higher order structures.

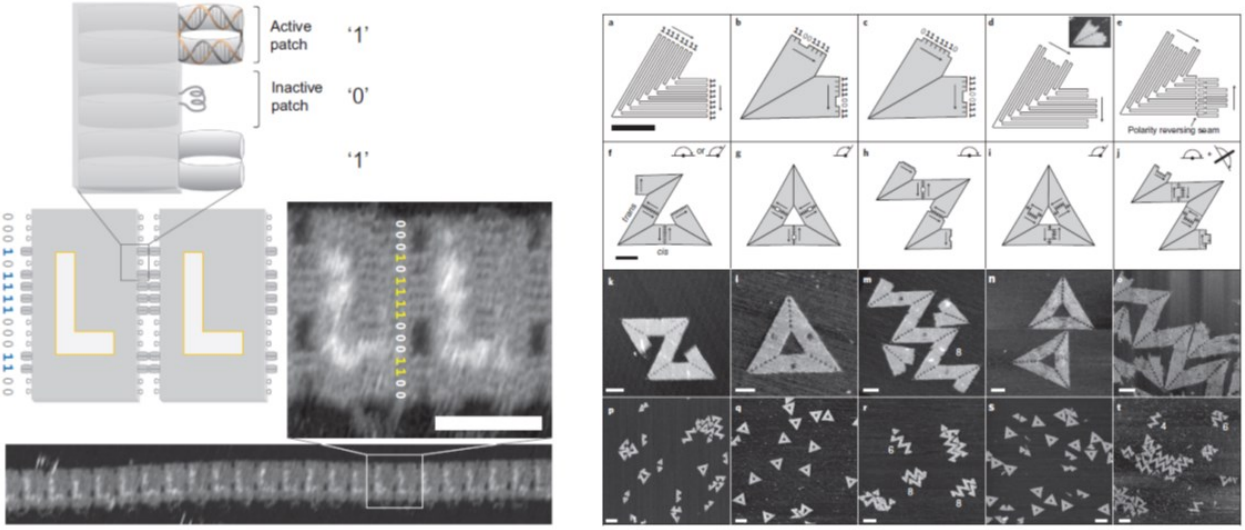

Figure 1.19: The strategy and self-assembly of DNA origami tiles using blunt-end stacking[75]. Blunt ended motifs can be added as a barcoded self-assembly. Using this methodology DNA origami tiles can be organized into different higher assemblies.

Many DNA folding design techniques have now been developed to introduce curvature, rigidity and 3D structural motifs into DNA origami structures. These strategies can be viewed as two

distinct construction approaches: (1) using 2D DNA origami tiles as building blocks themselves and (2) weaving the genomic backbone itself into a dense 3D object.

One of the first examples of a 3D origami construct was a cube structure formed using a single stranded backbone, folded into six square domains for each cube face (Figure 1.20A). These square domains were then folded into the cube structure using edge staple strands to fold the 3D prism[76]. The group was able to visualize the parallel alignment of the open square domains and the closed cubic morphology using AFM. The opening of the lid using "toehold" strand displacement[77] was monitored with a FRET pair positioned along the two edges that meet when the lid is closed. This work was proposed to find applications in logic gated sensors or as drug delivery vehicles. Komiyama et al showed formation of a DNA origami box using a slightly varied folding pattern[78] yielding the same cube product (Figure 1.20B), and Yan et al demonstrated the formation of a tetrahedron structure using similar strategies (Figure 1.20C)[79].

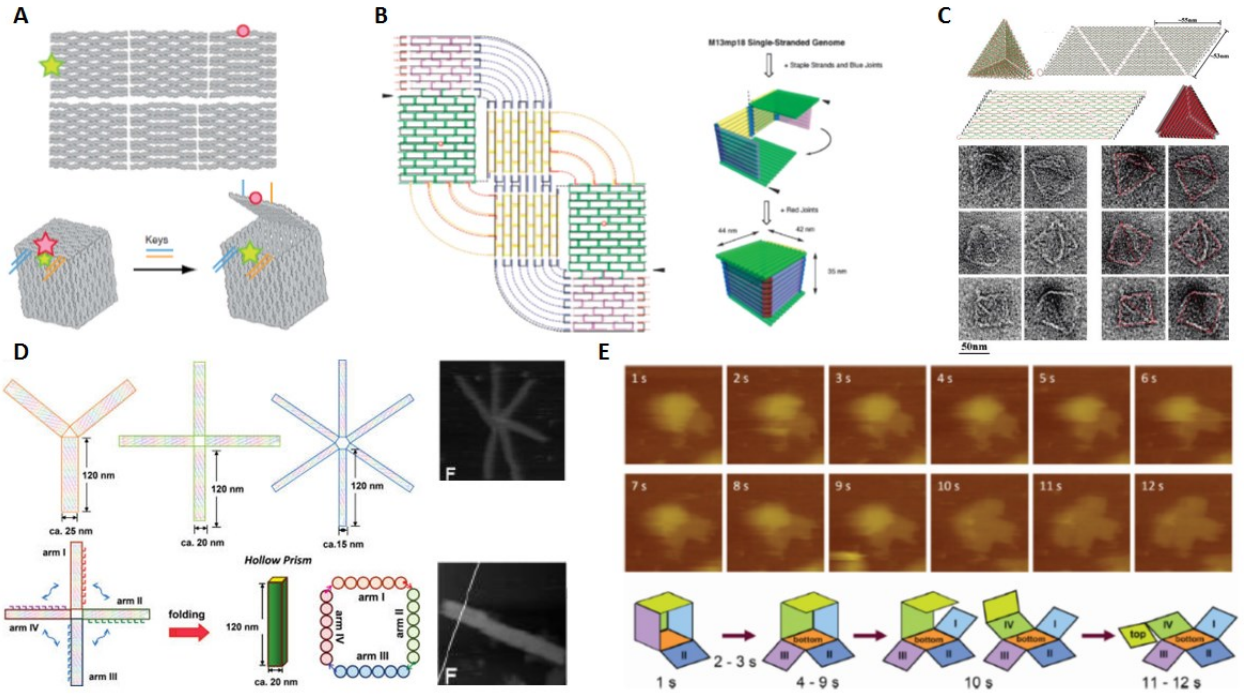

Figure 1.20: (A) DNA origami used to create a box with a toehold gated lid. (B) An alternative folding pattern to for a DNA origami box. (C) DNA origami tiles folded into a tetrahedron geometry. (D) Formation of elongated prismatic structures using the

pre-formed domain strategy. (E) Fast-scan AFM was used to image the unfolding of a DNA box structure[76,78-81].

Using this same domain pre-fabrication strategy Sugiyama et al demonstarted a similar scheme to form elongated triangular, rectangular, or hexagonal prisms from DNA origami tiles (Figure 1.20D)[81]. This design approach consisted of the creation of a central geometric shape with extended arms from each of the edges to generate the walls of the prismatic structure. The extended arms were brought together using edge staple strands and the constructs were characterized using AFM. In a follow-up publication Sugiyama et al were able to show the real-time unfolding of the prismatic structure using fast-scan AFM (Figure 1.20E)[80,81].

1.3.2.3 3D Origami Using Space Filling Helices

DNA origami was applied towards creating 3D objects by folding the origami backbone into a series of space filling helical bundles. One of the first groups to demonstrate this strategy was Shih et al using pleated layers of helices constrained to a honey-comb lattice to form a series of 3D objects (Figure 1.21A)[82]. Shih et al showed that by varying the mono/divalent cation ratios and annealing times, 3D objects ranging from 10-100 nm could be readily formed, purified and imaged using TEM. Threading the backbone into an asymmetric continuous 3D object has facilitated the creation of increasingly complex objects that may be useful in creating nanodevice components.

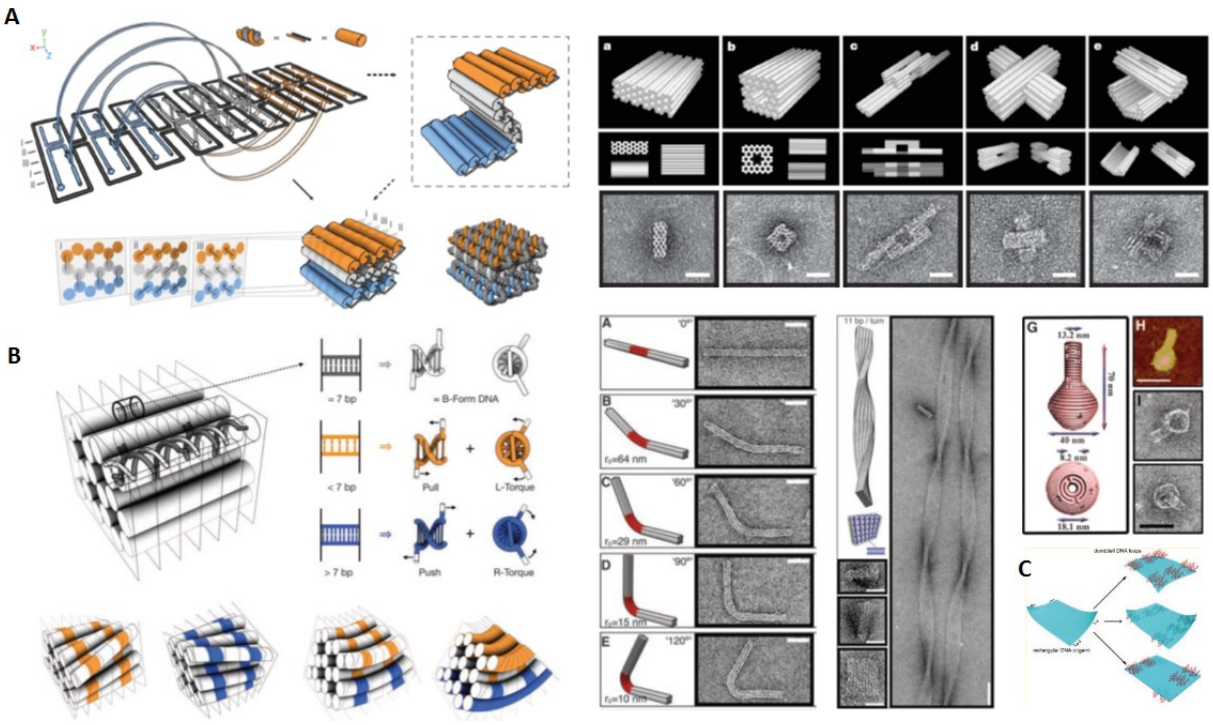

Figure 1.21: (A) One of the first examples using space filling helical organizations to form 3D objects using DNA origami. (B) Schematic representation of how curvature was introduced into helical bundles. (C) Precise control of tunable curvature was demonstrated using a rod formed through helical bundles. (D) The curvature of 2D origami tiles was controlled using adjustments of hairpin loops[82-85].

Expanding upon the previous method, it was found that by including insertions or deletions of specific base pairs within a DNA origami helical bundle, the helix could be controllably curved (Figure 1.21B)[83]. Using this principle, a DNA origami rod comprised of a bundle of several helices was designed. Researchers were able to precisely curve and twist the DNA-rod structure following a simple set of design rules. Work by Yan et al also examined structural requirements to generate in-plane curvature within a series concentric helical bundles by using increasing amounts of cross-overs between helices (Figure 1.21C)[84]. Out of plane curvature to form curved 3D objects was achieved by adjusting the position of inter-helix cross-overs and was used to create a series of curved 3D objects. This same group also examined relieving and controlling curved stress in 2D DNA origami sheets through specific placement of hairpin loops (Figure 1.21D)[85]. Many of these design principles for 3D DNA origami as well as specific examples and application are discussed in several review articles[66,86-88].

1.3.2.4 DNA Origami for Drug Delivery

Due to the versatility of 3D DNA origami design and functionalization, a wide range of structures have been used for organizing proteins (viruses, enzymes), nanoparticles, drug delivery vehicles, light harvesting complexes as well as carbon nanotubes with a spatial resolution of approximately 6 nm. This following section will discuss several variations of these applications.

DNA origami structures have been investigated as a delivery vehicle for therapeutic agents through encapsulation or intercalation within the highly dense helical bundles. Similar to the controlled opening of the DNA origami box[76], a delivery vehicle was designed consisting of two curved DNA origami tiles hinged together along one edge and closed via toeholds to form a gated DNA pocket (Figure 1.22A)[89]. The toeholds are designed with aptamers for specific protein targets that upon binding trigger the opening of the structure and cargo release. The structure was shown to readily open upon addition of the proper chemical queue and was successfully loaded with both AuNPs and fluorescently labeled antibodie fragments components. Cell culture experiments were performed by loading the DNA robot with fluorescently labeled antibodies targeted to specific cellular components. Using this methodology, the researchers were able to show predictable antibody fragment release and labeling of several of the cell lines. This strategy could be applied to a wide variety of drug cargoes simply by modifying the internal pocket loading strands. DNA origami structures have also been used to delivery drug payloads via intercalation of the therapeutics within the helices (Figure 1.22B)[90]. This work found a strong shape dependence on the release of intercalated drug, favouring a linear rod motif compared to a planar triangular tile. These DNA tiles were found to increase the internalization of the therapeutic agent and have the advantage of being able to load a high concentration of drug molecule.

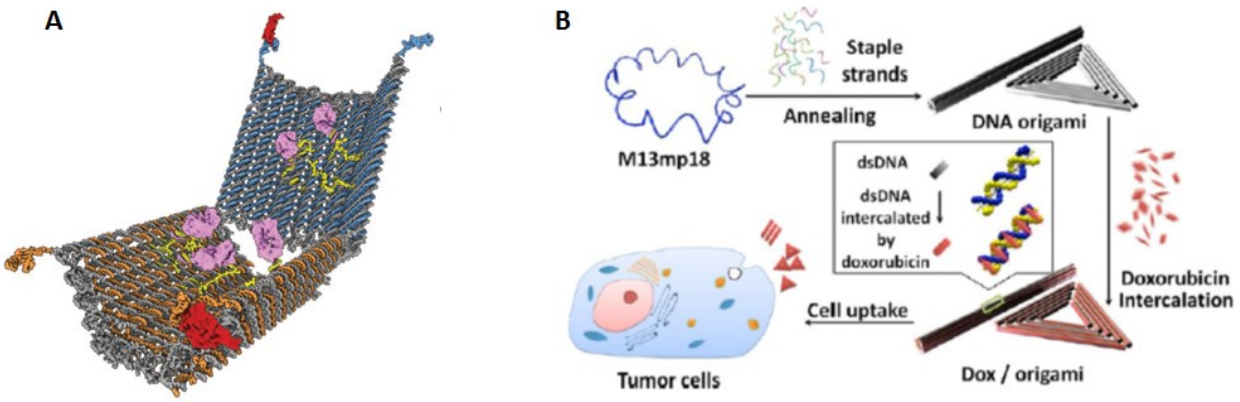

Figure 1.22: (A) Design of a gated DNA pocket able to selectively release cargo in the presence of the proper chemical trigger. (B) DNA origami used as a drug delivery vehicle through intercalation[89,90].

1.3.2.5 DNA Origami for Investigating Biological Reactions

The precise placement of molecules on 2D DNA origami tiles has allowed researchers to tether chemically reactive components in programmable arrays to investigate localized diffusion limited reactions. Several examples have used DNA scaffolds to study biological systems such as enzyme cascade reactions involving localized shuffling of reactive chemical intermediates. DNA nanotechnology has been used to demonstrate distance dependence relationships in enzyme cascades reactions using extended DNA scaffolds[91]. However expansion of DNA based techniques for further enzymatic cascade studies would be well served by a rigid, fully programmable scaffold such as DNA origami tiles. Similar to Willner et al, glucose oxidase and horseradish peroxidase were modified with a DNA strand, allowing for their controlled positioning at increasing distances on the surface of the origami tile (Figure 1.23A)[92]. The enzyme activity was then measured by absorbance at 410 nm, and was found to drop significantly at distances greater than 20 nm. This same group has also used rolled DNA origami tiles to further investigate enzyme cascade dependence on the scaffold structure[92]. These examples also demonstrate how DNA can begin to be interfaced with biological systems to create complex protein arrays for model systems or functional molecular devices.

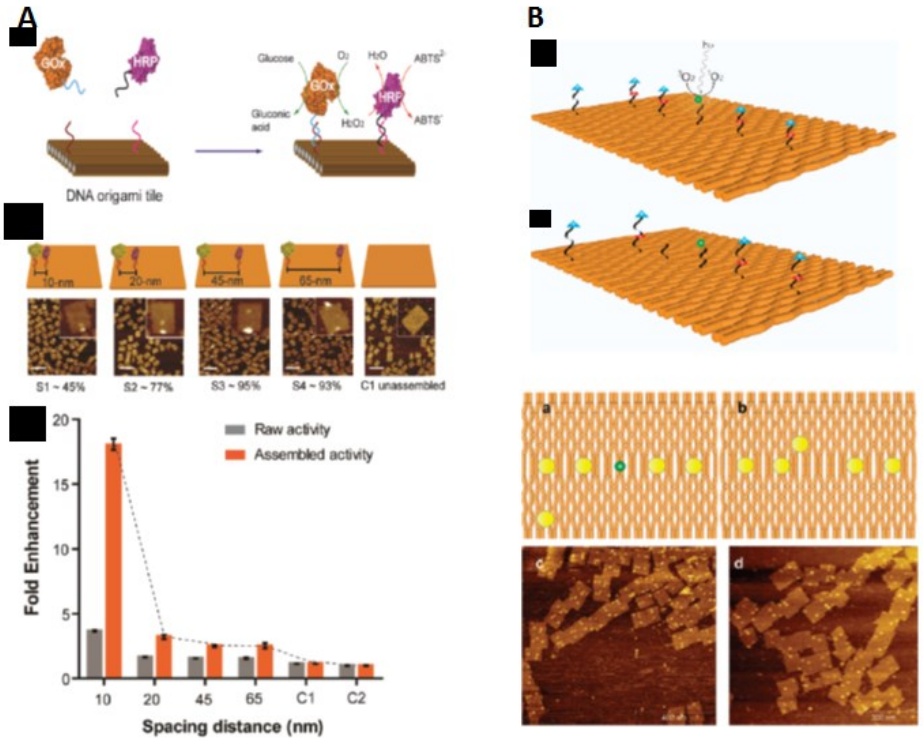

Figure 1.23: Examples of a DNA origami tile used to: (A) position two enzymes and study their cascade reaction distance dependence, (B) study local diffusion of reactive chemical species[93-95].

The diffusion dependence of *in situ* produced reactive chemical species has also been examined using DNA origami tiles containing a central singlet oxygen photosensitizer, surrounded by biotin modified DNA strands containing singlet oxygen cleavable bonds (Figure 1.23B)[94]. Figure 1.23B bottom panels a and b show the position of cleavable biotinylated DNA strands, and panels c and d show before and after the cleavage event respectively. Biotin-streptavidin molecules were cleaved by singlet oxygen in a distance dependent fashion as observed by monitoring the removal of biotinylated strands using AFM.

1.3.2.6 DNA Origami for Super-resolution Microscopy

DNA origami has been used in the field of super-resolution microscopy. This technique involves labeling of the object of focus with transiently emitting fluorophores and computer analysis of the fluorescent "blinking" which generates a high resolution image[96]. Each blinking event is recorded

and the software can isolate the foci of emission, after collecting sufficient data the image is digitally reconstructed for observation. One of the first super-resolution images of a DNA origami tetrahedron was generated using a technique termed "DNA PAINT". The origami structure is designed such that short, transiently binding DNA-fluorophores reversibly bind to the scaffold, tracing the structure (Figure 1.24A)[97]. One of the challenges of super-resolution microscopy is the creation of a proper measurement standard with a well-defined size and number of fluorescent molecules. DNA origami structures are particularly advantageous to use as standards for these experiments due to their tailored size and controlled number of hybridized fluorophores. Work by the same group developed a DNA origami rod with transiently labeled ends as a standard for super-resolution measurements (Figure 1.24B/C) [98,99]. Super-resolution microscopy applications will be discussed further in the supramolecular DNA nanotechnology section.

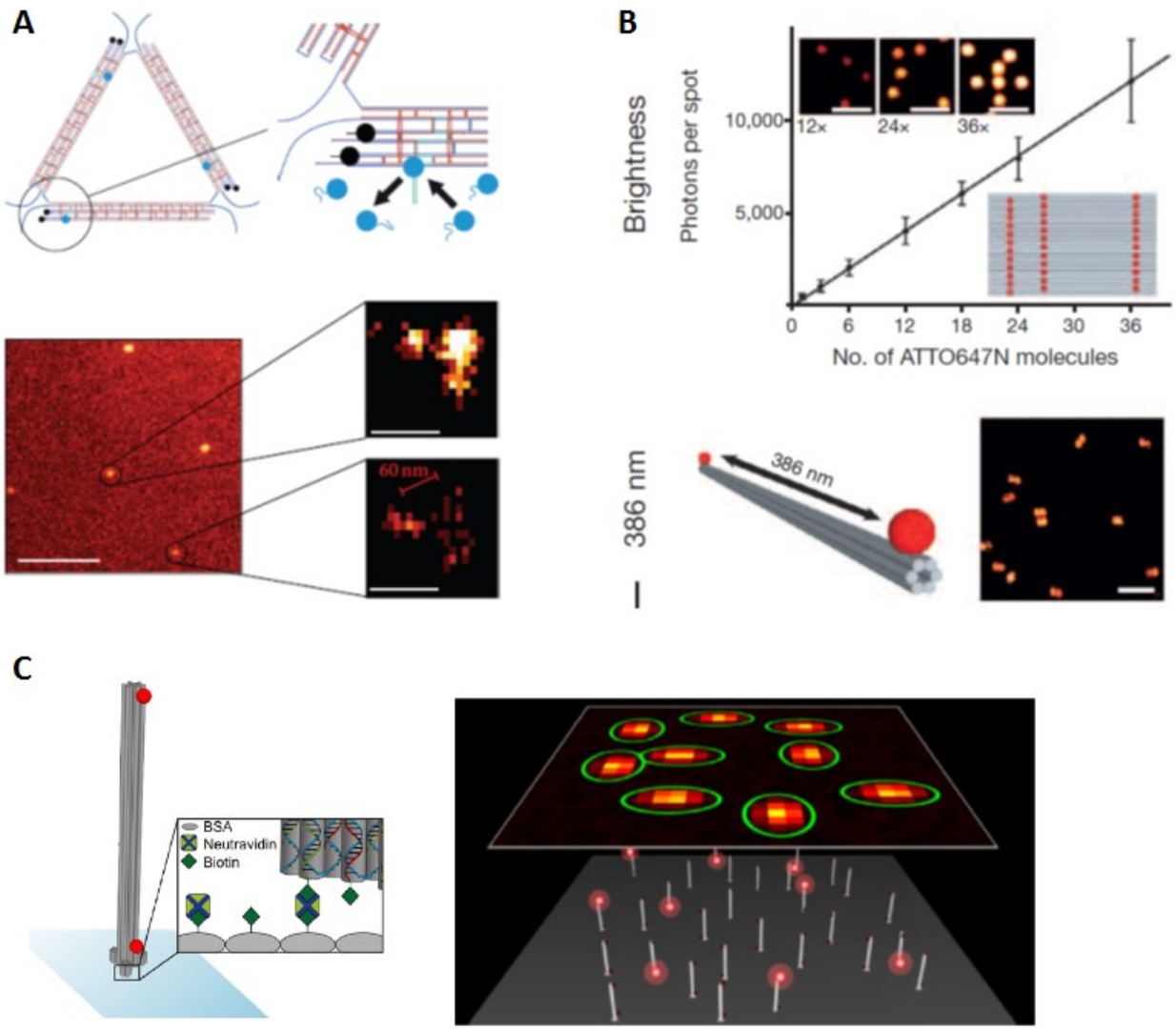

Figure 1.24: (A) DNA paint technique applied to imaging a DNA tetrahedron. (B) A DNA origami rod used as a standard for fluorescence intensity and size. (C) A DNA rod attached to an origami tile and imaged using super-resolution microscopy to determine surface orientation[97-99].

1.3.2.7 DNA Origami and Molecular Machines

The inspiration for Rothemund's original development of DNA origami was to create molecular computing devices similar to the system proposed by Adleman[100]. The field of DNA computing has emerged from this original idea and there are now many examples of DNA logic gates and

walkers[101]. In many of the examples DNA origami tiles serve as a programmable substrate for the specific placement of DNA strands which can direct various molecular processing. It has been shown that a "DNA walker" can be programmed to progress across a DNA origami tile in predetermined pathway (Figure 1.25A). Along this route, the walker is able to pick up and assemble specific AuNP cargoes,[102] through the correct input and pre-assembly of toehold displacement strands. Although quite complex in design, the AFM and TEM images show correct sequenced assembly, creating one of the first examples of a molecular assembly line demonstrating a true bottom-up approach for the creation of functional nanomaterials.

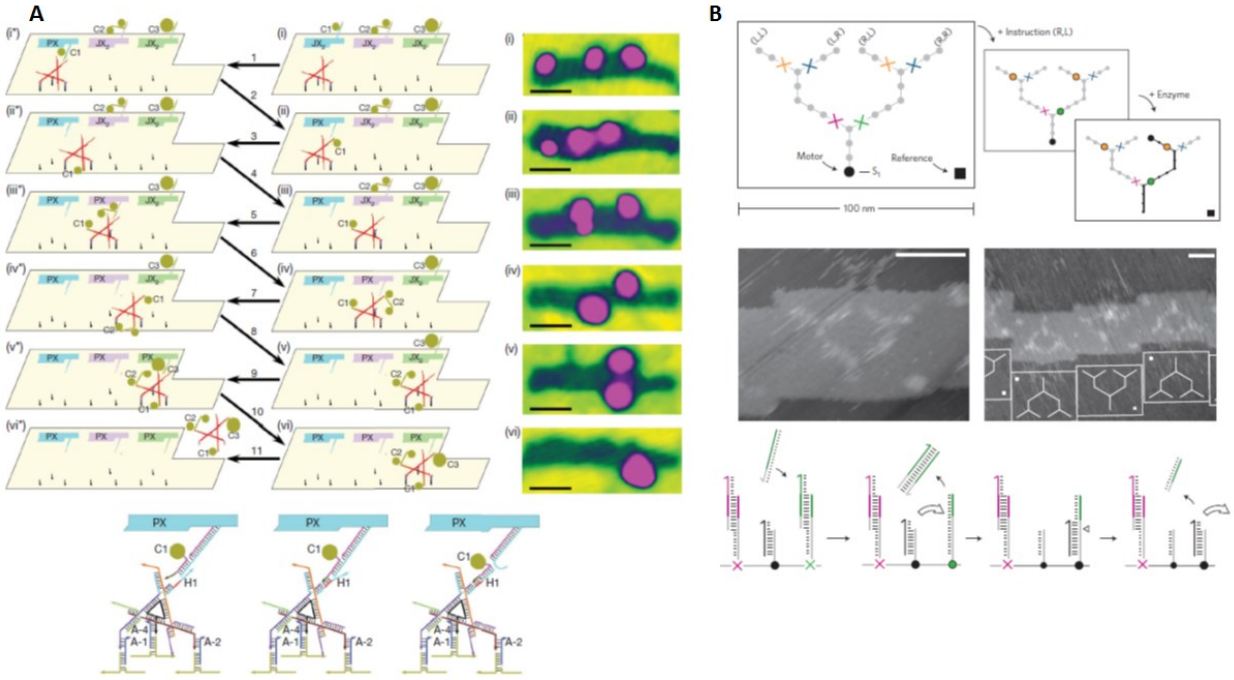

Figure 1.25: (A) Diagram showing the DNA walker pathway and programmed assembly. (B) A DNA motor with programmable pathways of motion based on specific strand inputs[102,103].

A second example of a programmable motor was shown to be directed into one of four pathways laid out as DNA tracks on a DNA origami tile (Figure 1.25B)[103]. This strategy employed the sequential displacement of blocking "stator" strands to direct the DNA motor, a single DNA strand along a predetermined path. Researchers engineered the system such that upon removal of a particular stator strand, the DNA motor progresses forward one step along a chosen pathway by

hybridizing to the next part of the track. This binding creates a cleavable restriction enzyme site, which following enzymatic digestion leaves the DNA motor with single stranded toehold that interacts with the next position when the following stator is again removed. These methods show that molecular computing can be expanded for creation of increasingly complex functional materials able to self-assemble precise molecules or sort particular cargos.

The creation of molecular computational devices will require precise fabrication of electronic components through self-assembly. In pursuit of this long-term goal, Rothemund et al have used DNA origami tiles to orient carbon nanotubes and create conductive circuits (Figure 1.26)[104]. In this work single walled carbon nanotubes (SWNT) are non-covalently functionalized with DNA strands through physisorption of the strands to the tube surface (Figure 1.26A). These strands contain a complementary sequence to a specific region of a DNA origami tile. Cross-junctions of DNA positioned SWNT were positioned on silica wafers and connected to platinum/gold electrodes, and exhibited electrical conductance (Figure 1.26B). This work demonstrates the feasibility of using DNA scaffolds to organize electrical device components. However, many challenges remain such as covalent modification of the SWNT with DNA as well as preventing tile aggregation from non-specific interactions with SWNT.

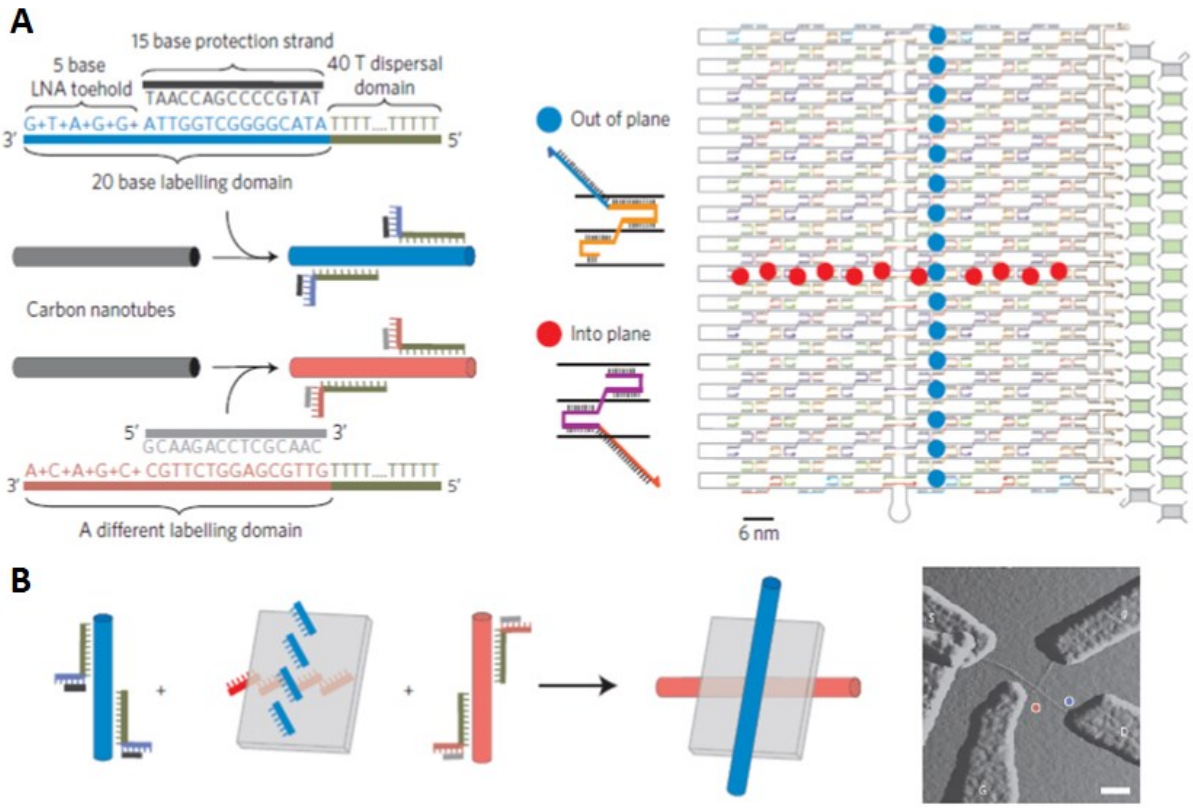

Figure 1.26: Schematic representation of DNA origami used to organize SWNT and measure their electrical conductance[104,105]. (A) Architecture of the DNA origami tile showing the sticky ends positioned for landing the SWNT. (B) Illustration of positioned SWNT for electrical conductance measurements.

1.3.3 Supramolecular DNA Nanotechnology

Although both structural DNA nanotechnology and DNA origami have been used to assemble a number of modified DNA strands, the scaffold designs are limited to DNA hybridization rules and assembly schemes. These design strategies also require a large number of different DNA strands for assembled structures, although as costs of DNA synthesis decrease this will be less problematic. Supramolecular self-assembling materials on the other hand, have employed a wide variety of directed, tunable interactions, such as metal coordination or amphiphilic aggregation, to form discrete objects of predetermined shape[10,106,107]. Supramolecular DNA nanotechnology aims to combine programmable DNA self-assembly with synthetic molecules and principles commonly

used in supramolecular chemistry (Figure 1.27)[107,108], to generate new materials formed through hierarchal interactions. Supramolecular DNA nanotechnology offers a more DNA economic route for structure diversity, and also tends to increase product yields as the assemblies require fewer strand components. Many synthetic components can be readily coupled to DNA, such as metal-complexing ligands, redox centers, photoswitches, polymers and magnetic particles, which will greatly expand the applications for DNA nanotechnology as functional materials.

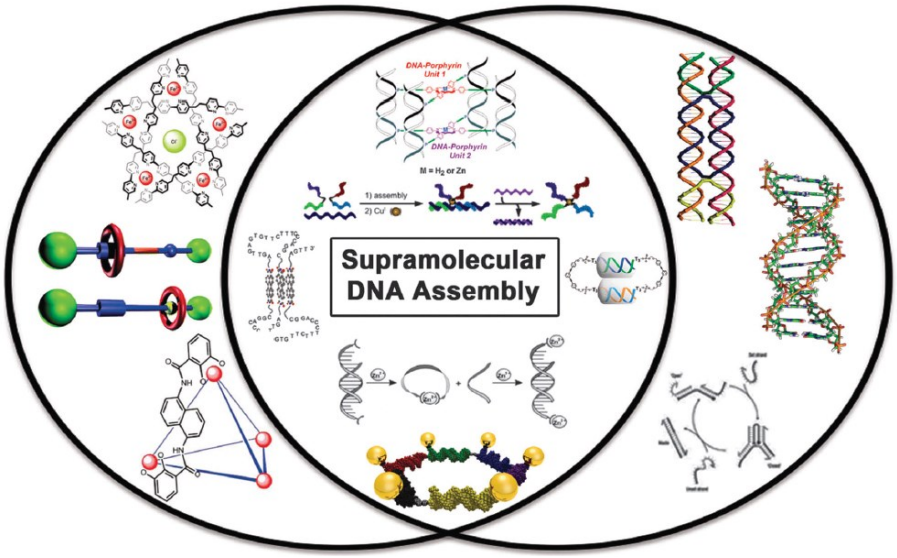

Figure 1.27: A diagram showing the overlap of compatible self-assembly strategies for Supramolecular chemistry and DNA nanotechnology[107].

1.3.3.1 Synthetic Insertions for Pre-Organization

Expanding supramolecular chemistry designs for complex, multifunctional applications will require the precise placement of molecular building blocks into higher order structures. Towards this goal many research groups have covalently linked synthetic organic molecules which impart specific geometries to uniquely coded strands of DNA for programmed assembly. One early example of this strategy used a rigid vertex insertion within a self-complementary ssDNA to orient the strand into a specific angle which directs the DNA hybridization pattern into a series of closed macrocycles (Figure 1.28A)[109]. Non-pairing Ts were inserted for increased flexibility and it was found that fewer larger macrocycles were formed. Sleiman et al have generated a fully asymmetric

DNA hexagon using a rigid vertex to favour macrocycle formation and used this strategy to organize conjugated AuNPs in a hexagonal crown structure (Figure 1.28B)[110]. The group has also used a rigid vertex to create a small dynamic library of closed macrocycles from pre-oriented self-complementary DNA strands (Figure 1.28C)[111]. It was found that by using a small molecule that weakly binds DNA, the products could be directed into a single macrocycle population. Further work demonstrated the synthesis of ligated single stranded closed macrocycles, such as triangles and squares[112]. These macrocycles were used as templates to organize gold nanoparticles (AuNPs) into defined 2D-structures. They are fully addressable, and AuNP functionalized strands that can be reversibly bound and released from the scaffold using toehold strand displacement (Figure 1.28D).

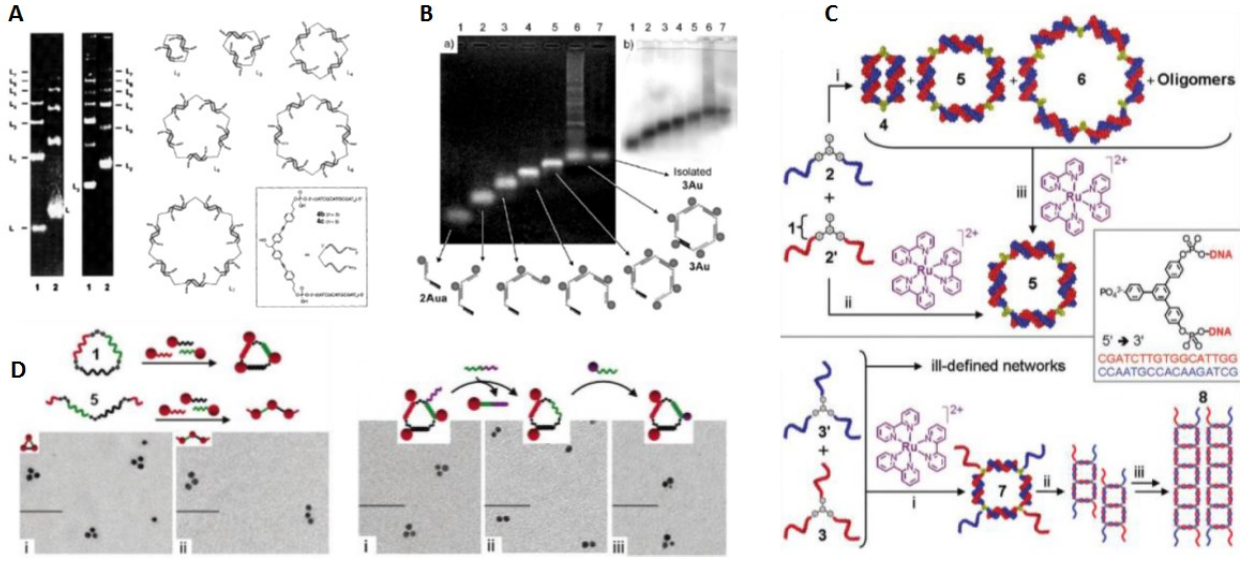

Figure 1.28: (A) The symmetric self-assembly of a pool of macrocycles formed using an angled rigid vertex insertion with the DNA strand. (B) The asymmetric self-assembly of a DNA hexagon using a rigid vertex insertion, and labeled with AuNPs. (C) An example showing how a guest molecule can drive the formation of a pool of macrocycles into a single favoured product. (D) A triangular DNA cycle that can be reversibly addressed with AuNPs[109-112].

Sleiman et al extended macrocycle formation into 3D object construction using linking strands to bridge two ligated macrocycles. In this work a series of polygon faces were synthesized and used to generate a variety of caged 3D DNA structures (Figure 1.29A). These cages were designed with

addressable ss edges which were used to dynamically compress or extend the 3D structure[113]. An alternative method for cage construction was shown by the same group using a flexible C6 alkyl chain insertion as the vertex to generate 2D/3D shapes and cages (Figure 1.29B)[114].

The method of using a planar DNA cycle to define the geometry in 2D was also applied to the formation of extended nanotubes (Figure 1.29C)[115]. In this work the 2D DNA polygon was assembled into a "rung" structure with sticky-ends extending up and down for longitudinal assembly via linking strands. The nanotube was designed using both triangular and square polygon-shaped rungs and was shown to assemble into long filamentous material as imaged by AFM. A follow up paper by the group was able to show AuNP encapsulation and controlled release from within the periodic cage structures forming the tube scaffold (Figure 1.29D)[116]. The success of synthetic insertions, such as rigid and flexible vertices to pre-organize DNA strands has generated interest in other structure modifications such as branching units.

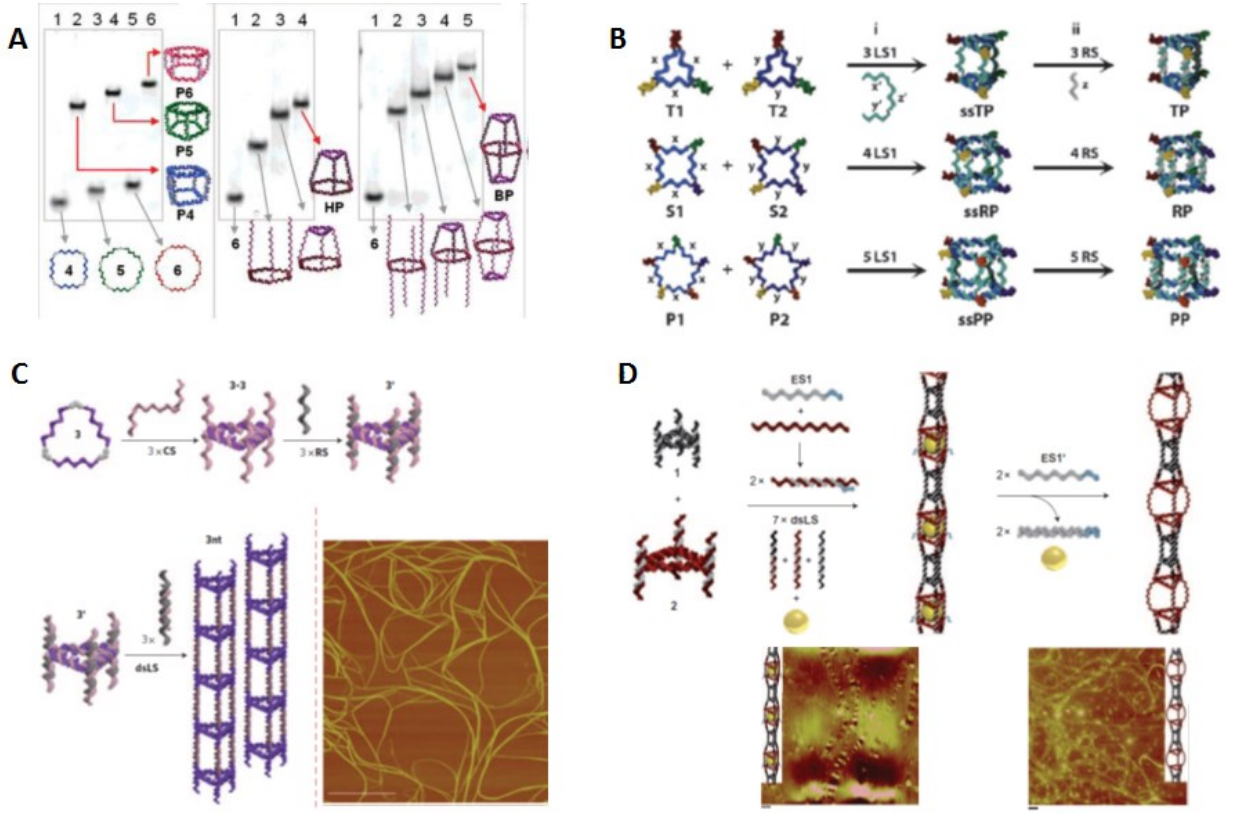

Figure 1.29: (A) A series of DNA cages formed using planar polygon macrocylcles. (B) A series of DNA prisms formed using a flexible vertex in the planar polygon

cycles. (C) DNA nanotube formation using a polygon cycle as a rung. (D) Controlled loading/release of AuNPs from a nanotube[113-116].

1.3.3.2 Synthetic Branching Units

Synthetic branching units have been covalently coupled to DNA to further expand the connectivity of DNA from its normal linear duplex, towards multi-junction architectures. Early work by Kiedrowski et al showed the synthesis of a pair of complementary trifunctional linkers connected to 3 symmetric DNA strands. These structures hybridize into a cage structure resembling a cryptand[117]. When combined in equimolecular amounts a product distribution was observed by gel electrophoresis with the favoured assembly being a dimer (Figure 1.30A).

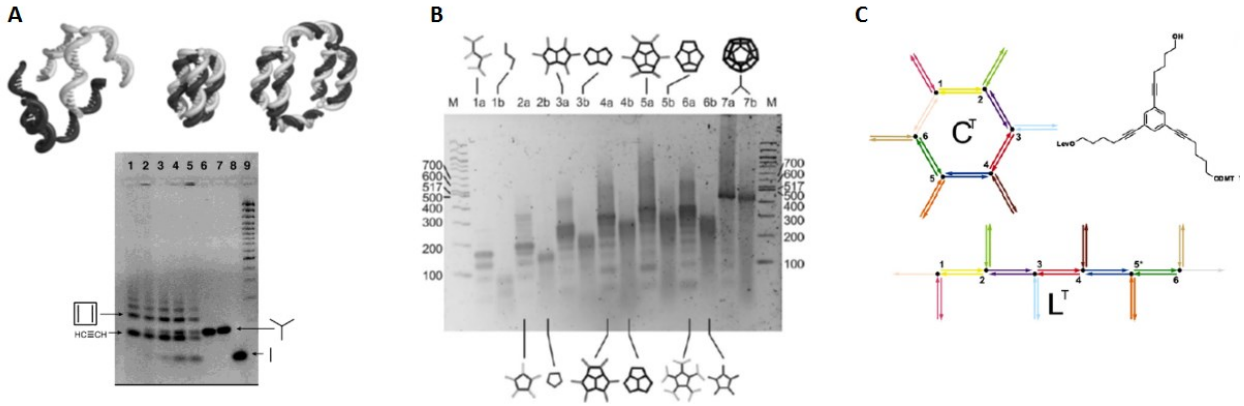

Figure 1.30: (A) Design and native gel electrophoresis assembly analysis of a symmetric 3 way junction. (B) Design of a set of 20 asymmetric tri-linker motifs programmed to assemble into a dodecahedron. (C) A series of 6 asymmetric tri-linkers used to form an addressable hexagon shaoe[117-120].

Other groups have created trifunctionalized branching units that self-assemble into a spherical dodecahedron (Figure 1.30B)[118]. This design required the synthesis of a set of 20 asymmetric branched DNA units, synthesized using a 3 step process. Initially the first of three DNA strands is grown using reverse phase phosphoramidite chemistry in the 5' to 3' direction, this strand is then terminated with a tri-linker. Following this coupling step, the tri-linker contains two hydroxyl groups, one DMT protected and one free for coupling which is used to grow the second strand (3'

to 5'). Finally, the third strand can be synthesized upon cleavage of the DMT protecting group. Similarly, a trigonal linking unit was used to create an asymmetrically designed hexagon with each vertex containing an addressable third strand directed away from the center (Figure 1.30C)[119]. Seeman et al also showed that a 4 way DNA branch can drive the curvature of structural DNA tile based 2D networks into tubular structures[120].

1.3.3.3 DNA Stability and Synthetic Insertions

As synthetic insertions and modification strategies have expanded to use many different structural motifs, research groups began to examine the consequent effects on DNA stability. Many of these studies were motivated by experimentally observed sharp melting transitions in densely linked DNA nanostructures, explained by neighboring duplex and effective ion concentrations effects[121,122]. One study[122] has examined the dimer cage structure formed through complementary trifunctionalized junctions similar to cages developed by Kiedrowski et al.[117]. This cage structure places 3 helices within close proximity and was found to have switch-like cooperativity for dehybridization (Figure 1.31A). The structures were determined to have a >10˚C increase in their melting point as well as displaying a narrowed melting transition relative to duplex controls. The observed cooperativity was determined to be linked to the recruitment of shared counterion clouds between the negatively charged phosphate back bone. A second study used computational methods to examine a similar system comparing a trigonal DNA dimer and a normal DNA duplex and found results in good agreement with the experimental data (Figure 1.31B)[123].

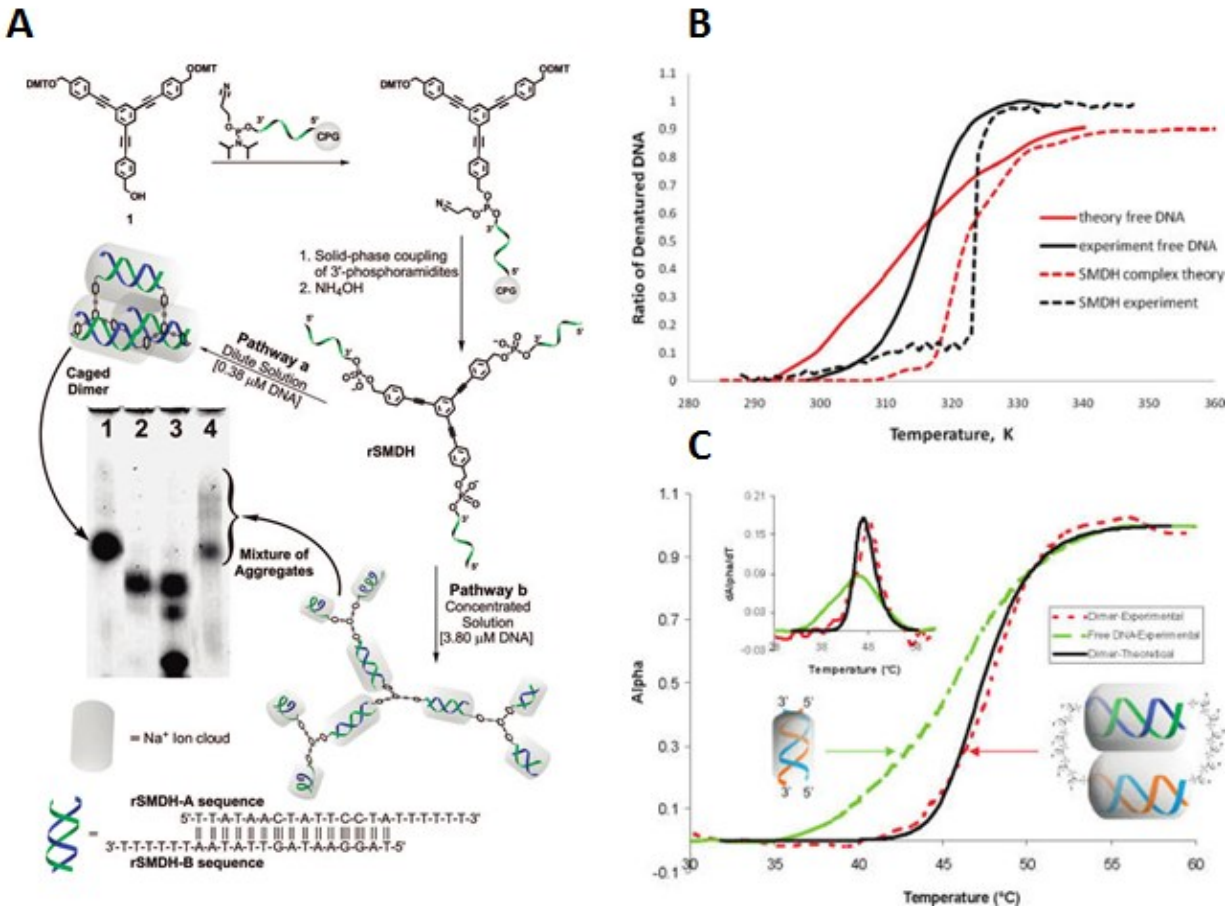

Figure 1.31: (A) Design of two complementary tri-linker DNA units which exhibit increased thermal stability and sharper melting curves, attributed to ion cloud sharing between the duplexes. (B) A graphical representation of thermal denaturing computational studies indicating good agreement with experimental data. (C) A two duplex system to study the effects of ion cloud sharing towards increasing cooperative DNA hybridization[122-124].

Simplified dimer duplexes that incorporate synthetic vertices have also been used to examine the neighboring duplex and effective concentration model, using both computational and experimental results (Figure 1.31C)[124]. Sleiman et al have also examined the effects of three different synthetic vertices on a DNA dimer duplexes in terms of stabilization[125]. These studies will serve to develop alternate ways of tuning self-assembly products through variable synthetic insertions that favour cooperative hybridization[121].

1.3.3.4 Metal Coordinating Ligands Conjugated to DNA

The junctions and rigid vertices used in the supramolecular DNA work presented so far impart specific structural motifs to generate a desired product however, the synthetic insertions and the DNA itself do not possess any active function. Inspired by biological molecules that rely on catalytic metal sites, supramolecular chemistry has explored the incorporation of metal coordinating ligands for both geometric manipulation and potential functionalities[126]. These principles can be used to design DNA structures with new geometries previously inaccessible with purely carbon based planar vertices discussed above, which may lead to chemically active materials[127].

One of the first examples of a DNA functionalized with a transition metal center was work by Sleiman *et al.* in 2001. This work successfully inserted a luminescent and redox active metal center within a sequence of DNA. Metal-DNA ligand research was also focused on using inert metals to direct assemblies into a variety of metal coordinated geometries. Early work by Han and McLaughlin respectively, in 2004 demonstrated the synthesis of a 2 (Figure 1.32A), 4 (Figure 1.32B), and 6-arm (Figure 1.32C) DNA branching motifs using a metal coordinated geometry [128-130]. These symmetric constructs were shown to be fully addressable with ssDNA and able to self-assemble into macroscopic crystal-like networks.

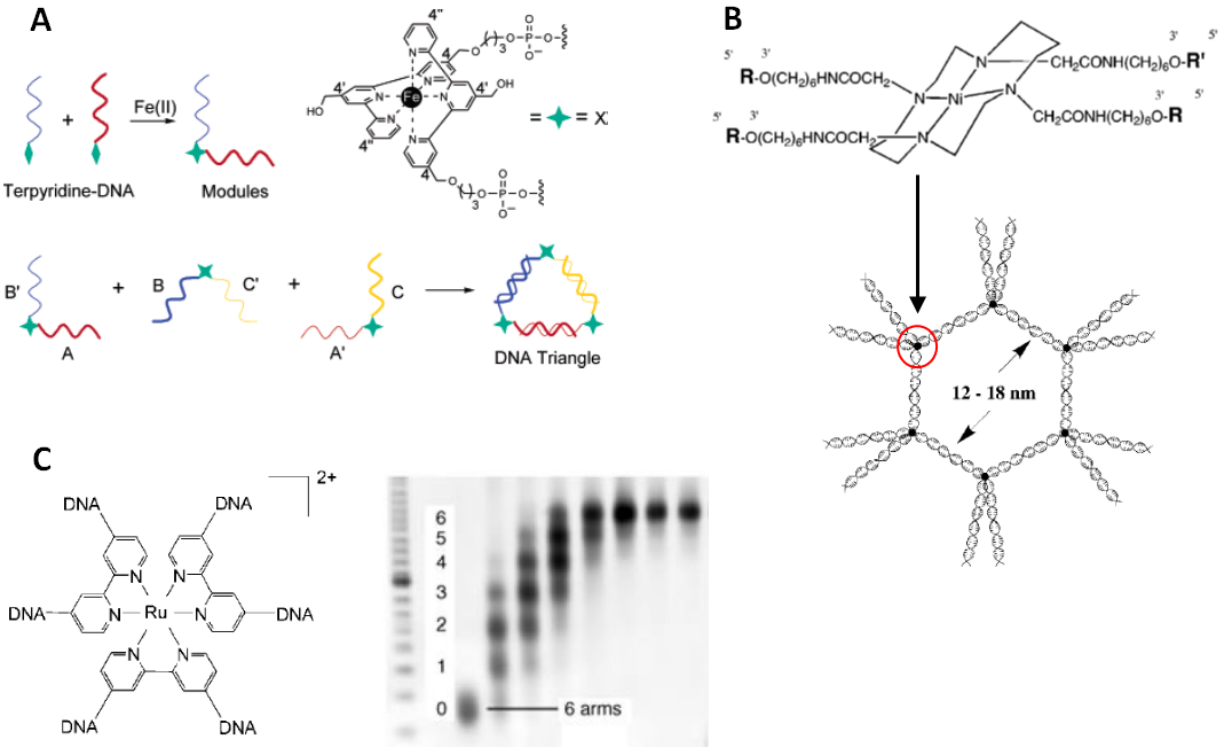

Figure 1.32: Examples of different organizations created using metal-ligand insertions within DNA [128-130]. (A) Formation of a metal coordinated two arm junction used to form a triangular shape. (B) Formation of a metal coordinated four arm junction used to create a hexagonal pattern. (C) Formation of a metal coordinated six arm junction with addressable DNA arms.

One of the challenges to creating catalytic metal ligands with DNA is the incompatibility of the harsh DNA synthesis conditions for chemically active metals that may be present during preparation. Alternatively, DNA can be synthesized with uncoordinated ligands and DNA hybridization can be used to template the metal ligand pockets for metal loading post-synthesis. Sleiman et al have shown that this method can generate well defined structures with significantly increased thermal stability relative to non-metalated controls (Figure 1.33A)[131,132]. Work by this same group was able to demonstrate selective incorporation of metals through modification of the ligand unit as well as error-correction for mismatched metal and ligand combinations (Figure 1.33B). Using the metal-to-ligand selectivity, this method could be used to extend DNA programmability with a new coding motif for self-assembly[132]. Metal-DNA ligands were also used to construct extended DNA nanotubes (Figure 1.33C)[133] and linearly patterned 2 or 3 arm DNA

junctions[134]. These methods hold the potential for creating artificial photosynthesis, metal catalysts, or nanoelectronic devices[135].

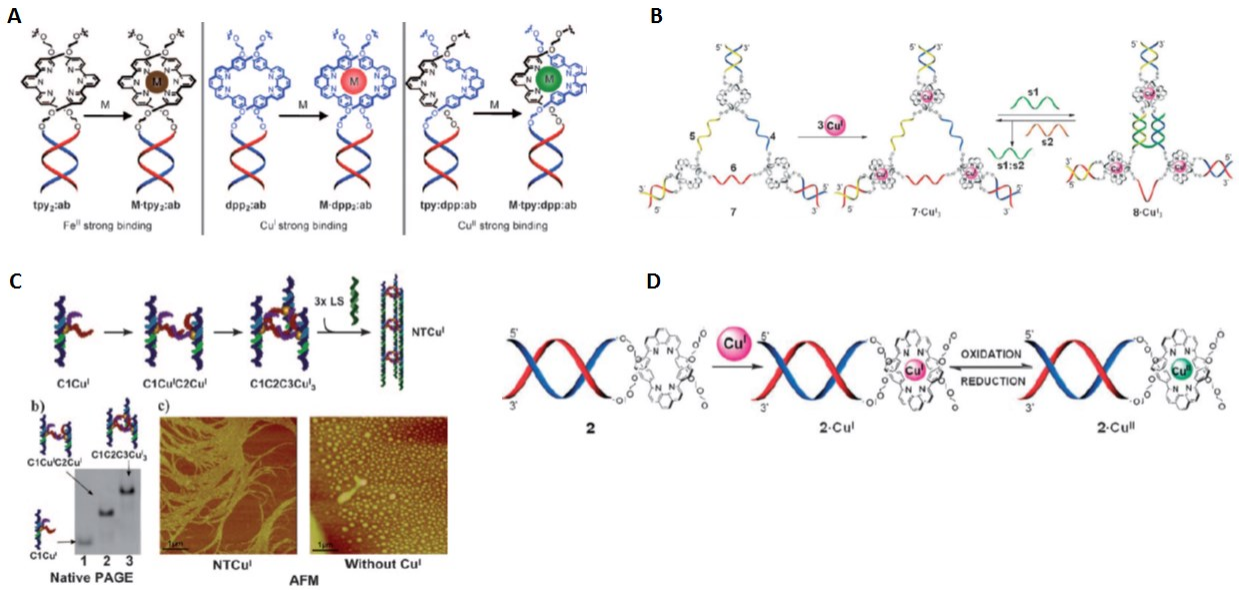

Figure 1.33: (A) Design of a triangular cycle which self-assembles to template 3 metal binding pockets. (B) Design of selective and error-correcting metal binding pockets templated by DNA hybridization. (C) DNA nanotube formation using a metal ligand insertion for switchable long range morphologies[131-133,135].

An early example of functional metal ligand insertion into DNA sequences for the formation of discrete cyclic metal-DNA structures was demonstrated by Sleiman et al. This work utilized a redox and photo active $[Ru(bipyridine)_3]^{2+}$ (Ru) molecule to add both function and geometric constraint to metal-DNA cycles[136]. It was found that the Ru vertex retained its fluorescent properties and favoured the formation of closed duplexed helix dimers. It was also shown that a redox active Cu ligand retains functionality when inserted within a DNA nanostructure (Figure 1.33D)[131]. More recently it was shown that charge transfer through DNA can be mediated through incorporation of metal-ligands and mismatched base pairing, this will be useful for developing DNA nanowires.

Metal ligands have also been incorporated into artificial oligonucleotides designed to assemble periodic arrays of metal particles within the interior of the DNA helix with potential applications to create nanowires or molecular magnets[137-139]. This work has shown incorporation of two

different metal binding oligonucleotides which can be periodically arranged as desired. Readers are directed to two review articles for further information on metal binding DNA nucleotides[126,139].

1.3.3.5 DNA and Synthetic Polymers

One of the greatest advantages of DNA is that it can be covalently coupled to a variety of molecules. These can give access to orthogonal self-assembling strategies, such as those used in block copolymer chemistry[140]. In general, block copolymers assemble into morphologies such that they minimize the intrinsic energy constraints for each polymer component. The classic example of this situation is an amphiphilic block polymer composed of both hydrophobic and hydrophilic polymers (analogous to a lipid structure). When placed in an aqueous medium the polymers are driven to self-assemble such that contact between the hydrophobic polymer block and the aqueous medium is minimized. Other energetic terms, such as the entropic cost of chain straightening of the polymers in the core and chain-chain interactions within the micelle core and periphery play a determinant role in the resulting morphology.

The covalent modification of DNA strands with hydrophobic polymers has led to the creation of new synergistically self-assembled DNA nanostructures. Polymer components have been coupled to DNA strands to create new addressable block co-polymers that take advantage of DNA programmability to impart dynamic structure variations[141]. Work by the Hermann and Gianneschi groups has designed DNA block co-polymers with spherical to rod/filament morphologies using a combination of DNA addressability (Figure 1.34A/B), restriction enzymes (Figure 1.34A), and/or annealing conditions (Figure 1.34C)[142-144]. Such switchable nanostructures have potential applications as drug carriers with controlled release.

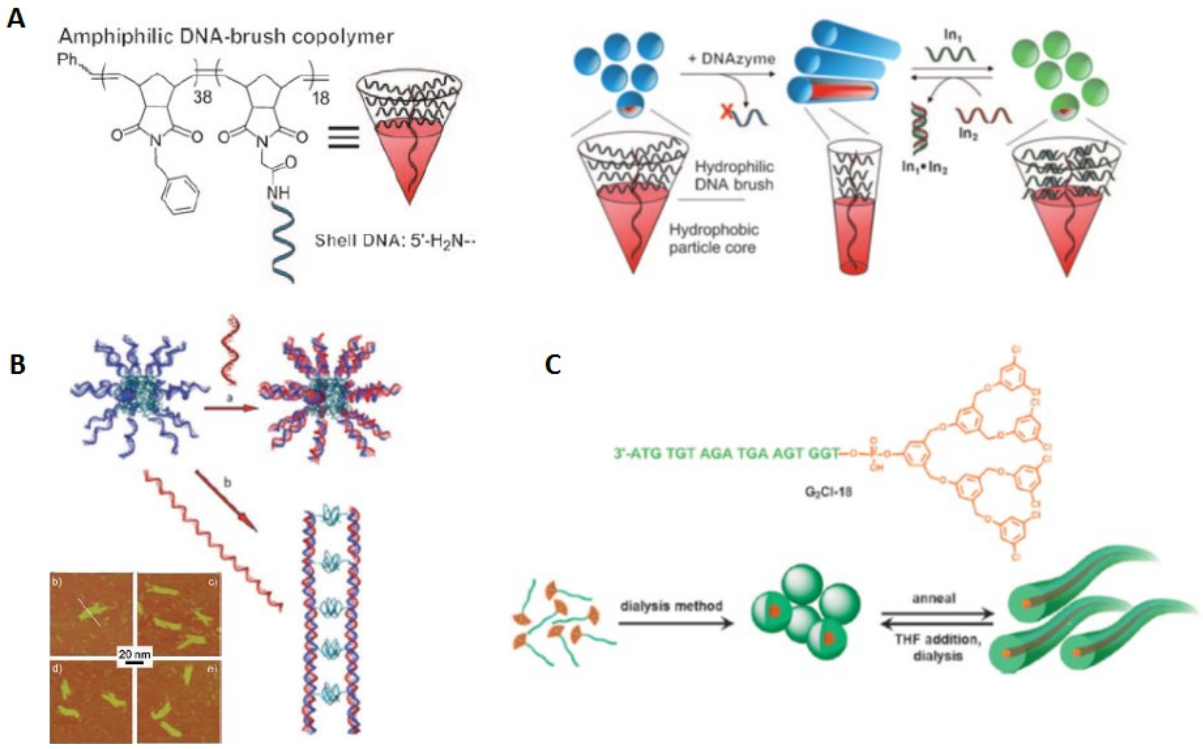

Figure 1.34: (A) DNA-polymer conjugates show reversible formation of spherical micelles to rod-like structures using enzymatic cleavage and DNA hybridization. (B) Schematic representation of ssDNA-polymer conjugates which can be assembled into micelles or filaments by using short or long complementary strands respectively. (C) Dendritic polymers have been coupled to DNA and show switchable morphologies using dialysis and annealing conditions[142-144].

Work by Sleiman *et al.* has focused on the multivalent placement of DNA-polymer conjugates on DNA scaffolds as means of creating hybrid materials exhibiting morphological control[145] , increased serum stability[64] and small hydrophobic molecule encapsulation[146]. Early work by this group designed a dendritic polymer covalently linked to complementary DNA strands that assemble into a duplexed tri-block co-polymer arrangement (Figure 1.35A)[145]. This building unit then undergoes secondary self-assembly into filaments driven by the microphase separation of the 2 polymer components when mixed with different ratios of organic solvents. Further work by this group was able to demonstrate the multivalent placement of brush-polymer DNA conjugates on a cubic scaffold which generated significantly increased serum stability from nuclease degradation[64] compared to unmodified DNA scaffolds (Figure 1.35B). The cubic scaffold was also used for the

placement of hydrophobic dendritic polymers with variable higher order morphologies depending on the number of loaded DNA-polymers (Figure 1.35C)[146]. When four DNA-polymer conjugates were positioned on opposing faces of the cube scaffold, the polymer units were found to orient and aggregate internally within the scaffold, creating a "mini-micelle" environment. It was shown that the hydrophobic core could be loaded with compatible small molecules for drug delivery applications.

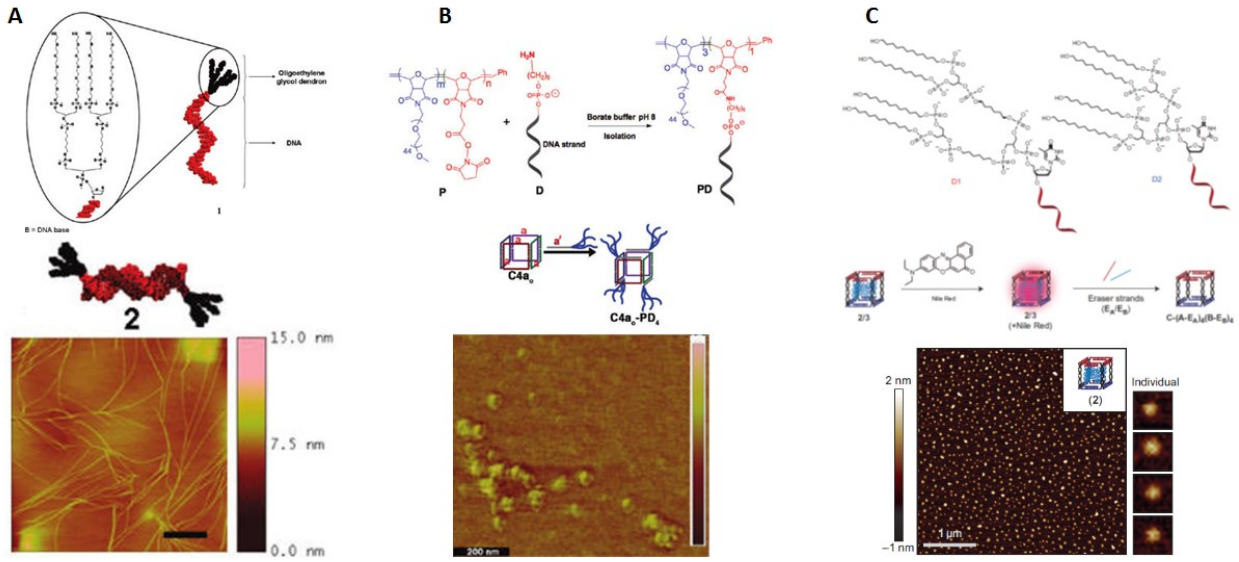

Figure 1.35: (A) Design of duplexed DNA-polymer conjugates which generate a filament like self-assembled morphology. (B) A cubic scaffold was used to position DNA-polymers in 3D. (C) Hydrophobic polymer were scaffolded on a cubic scaffold and showed formation of a "mini-micelle"[64,145,146].

As the synthesis of oligonucleotides has become increasingly routine in many labs, so too has the variety of commercially available non-nucleotide phosphoramidites. There presently exists on the market several oligomer based units generally used as spacing units for DNA structure design that contain hydrophobic/philic chains. Phosphoramidite chemistry can therefore be used to introduce sequence-defined polymer units to DNA strands through standard DNA synthesis. Moreover, by using phosphoramidite solid-phase methods, DNA block copolymer synthesis can potentially be fully automated. Sleiman et al has shown one of the first examples of this strategy for creating precision DNA-block copolymers, where the polymer block is sequence-controlled and monodisperse (Figure 1.36A)[147]. Using oligoethylene glycol and dodecane phosphoramidites,

variable hydrophilic/phobic character can be systematically introduced into polymer units. It was found that DNA strands coupled to a hydrophobic block can form micelles capable of encapsulating small hydrophobic molecules. A follow-up study of this system demonstrated that the micelle structures can be further addressed using the exposed ssDNA corona to hybridize and anchor multiple 3D cubic scaffolds to the surface of the micelle (Figure 1.36B)[57]. It was found that by varying the length of the hydrophobic polymer block the micelle size and number of closed packed DNA prisms could be controlled. The scaffolds themselves were shown to hybridize a series of asymmetrically binding fluorophores which undergo FRET, indicating that DNA cubes remain fully addressable in the close-packed orientation and could potentially serve as light-harvesting complexes.

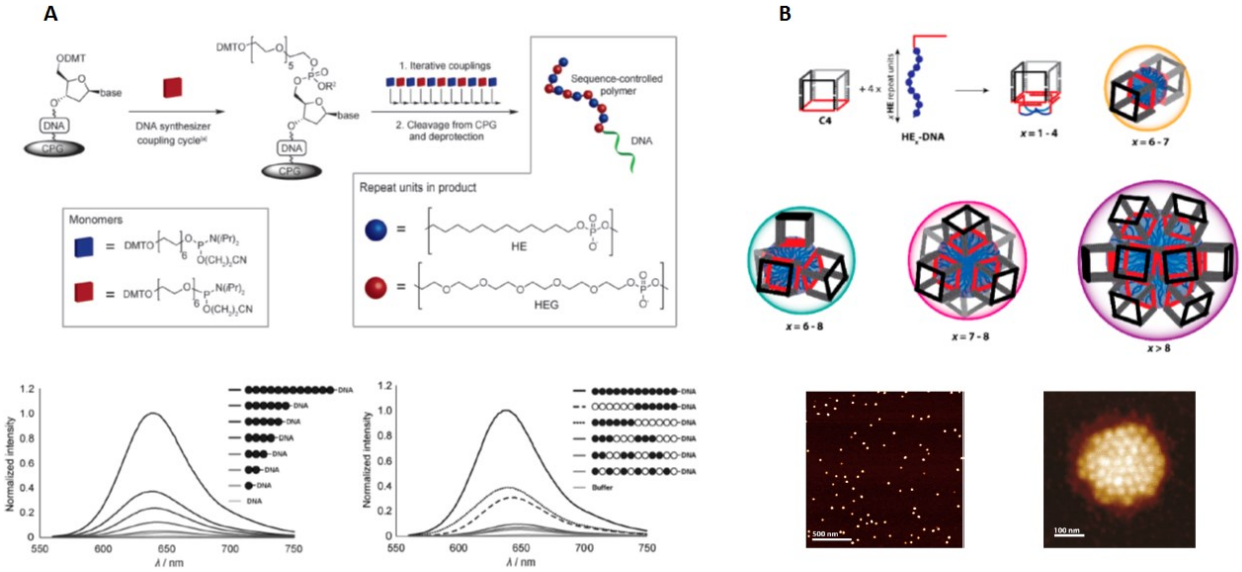

Figure 1.36: (A) Design of sequence specific polymers assembled using phosphoramidite chemistry. Absorbance measurements correlate well with micelle size and encapsulation measurements. (B) DNA-polymer micelles were used to create size-controlled aggregates able to organize DNA cubic scaffolds[57,147].

1.3.4 DNA and Lipidic Modifications

DNA scaffolds provide access to virtually any nanometer-sized shape on the scale of proteins, however they lack the functionality and long-range assembly often mediated by proteins and other

cellular components. Cellular membranes are composed of a mixture of lipids and proteins with a hydrophobic domain, and are another example of a self-assembling material. Although not as programmable as DNA, self-assembled cellular membranes composed of a mixture of liquids and proteins, are able to form large extended molecular structures[148]. Membrane self-assembly drives large scale spatial organization and directs cellular compartmentalization, which is important for separating functional domains and localization of enzymes cascade reactions. There is therefore significant interest in the application of DNA nanotechnology to mimic or control the lipid based assemblies and combine the high precision interactions of DNA with the dynamic, long range assembly scale of lipid membranes. Lipid membranes are also an interesting environment for DNA-lipid directed assemblies as they represent the barrier for all cellular communication and drug delivery. As the demand for biologically relevant lipidic components has increased, the availability of these chemical modifications as phosphoramidites for easy coupling to DNA strands has increased. As will be discussed in the following section, DNA-lipidic conjugates can now be readily synthesized and have been applied to a variety of lipid bilayer studies.

1.3.4.1 Lipid Bilayer Membranes

Phospholipids are amphiphilic molecules composed of three distinct regions; (1) the hydrophobic tail groups, which consist of long alkyl chains with different degrees saturation, (2) the linker component, which is typically a short molecule such as glycerol, and (3) the polar head group (HG), which can be charged or zwitterionic (Figure 1.37A). The main groups of lipids that are used in biological membranes are glycerophospholipids, sphingophospholipids and stearols, such as cholesterol[148]. Due to the biophysical properties of the distinct chemical regions, lipids are generally insoluble in water and will aggregate together to satisfy the opposing minimum energy requirements for the hydrophobic (alkyl chains) and hydrophilic (HG) portions. The final structure that forms from aggregation is determined by several molecular parameters such as alkyl chain hydrophobicity/saturation, electrostatics (HG), and steric hindrance[149]. In an aqueous environment, the HG and alkyl chains of lipids spontaneously aggregate to form different spherical structures such as micelles, or bilayers with the HGs directed outward in contact with water and the alkyl chains buried in the center (Figure 1.37B).

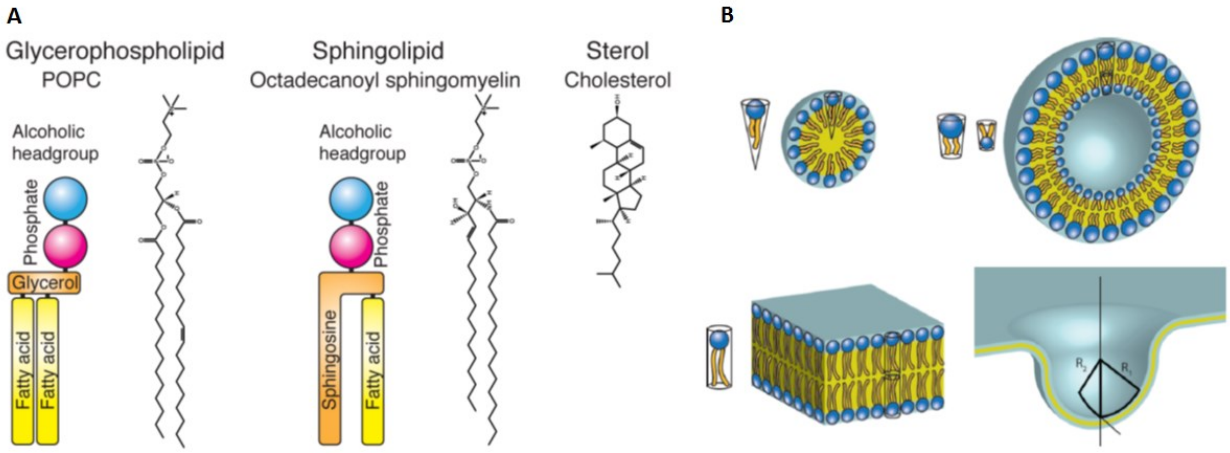

Figure 1.37: (A) Lipid structure. (B) General lipid self-assemblies[148].

The organization of lipids within bilayer membranes is referred to as their phase behaviour and is analogous in some ways to liquid-solid state transitions. Lipids that are packed densely together form a liquid-ordered (lo) gel phase, favoured by low temperatures. Similarly, lipids which are unable to efficiently pack together within a comparable surface area form liquid-disordered (ld) phases, favoured by increased temperature. A classic example of the relationship between structure and lipid phase is 1,2-dioleoyl-sn-glycero-3-phosphocholine (DOPC) compared to 1,2-dipalmitoyl-sn-glycero-3-phosphocholine (DPPC). The structure of DOPC contains two 18 carbon unsaturated alkyl chains and a zwitterionic HG, while DPPC contains two 16 carbon saturated chains and the same HG. When mixed together into vesicle bilayers at room temperature DOPC and DPPC phase separate into ld and lo phases respectively, based on the steric restrictions of their alkyl chain interactions[150,151]. Phase transitions between these states can be readily controlled using temperature variations, and are a unique biophysical property inherent to a specific phospholipid chemical structure.

When lipids with different phase transition temperatures are mixed, the packing constraints of self-assembled bilayers generate co-existence of liquid-ordered and liquid-disordered phase separated domains, enriched in a particular lipid (Figure 1.38). Although cholesterol cannot form a bilayer on its own, it is readily incorporated into bilayers with marked effects on the original phase behaviour. Cholesterol is known to have a strong preference for incorporation into liquid-ordered phases but, can interact within both saturated/unsaturated lipid mixtures, leading to variable phase co-existence or even 3 distinct phase domains (ld, lo and liquid-crystaline)[149,152]. Membrane

proteins have particular preference for different phase domains, therefore using these biophysical properties allows cells to compartmentalize into asymmetric functional domains.

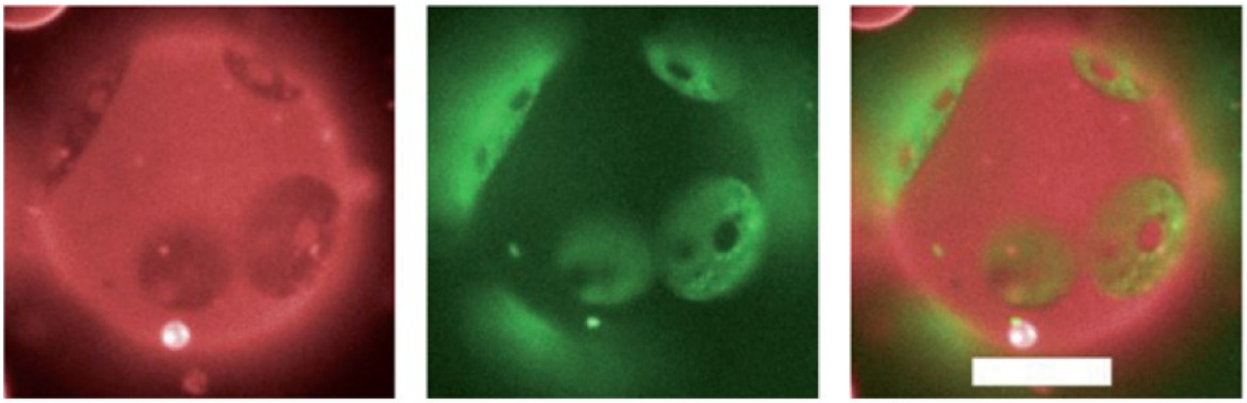

Figure 1.38: Images of phase separated fluorescently labeled lipid domains[148].

1.3.4.2 DNA Nanostructures and Lipid Membrane Interactions

There are several general ways in which DNA can interact with lipid bilayers: (1) non-specific electrostatic interactions (Figure 1.39A), (2) hydrophobic functionalization of DNA (Figure 1.39B), and (3) using protein specific interactions (Figure 1.39C). DNA is composed of a negatively charged backbone, it will therefore interact with charged lipid head groups through electrostatic interactions. It has been shown that DNA can interact with positively charged lipids to form DNA-lipid complexes that can be used for transfecting DNA into cells[153]. DNA has also been shown to bind to zwitterionic lipids in the presence of buffer salts which neutralize the negative charge, as monitored using surface area- pressure isotherms[154] and visually using fast-scan AFM[155]. There are many studies focused on the interactions of DNA with lipids, however the mechanism of interaction has yet to be fully understood[148,156].

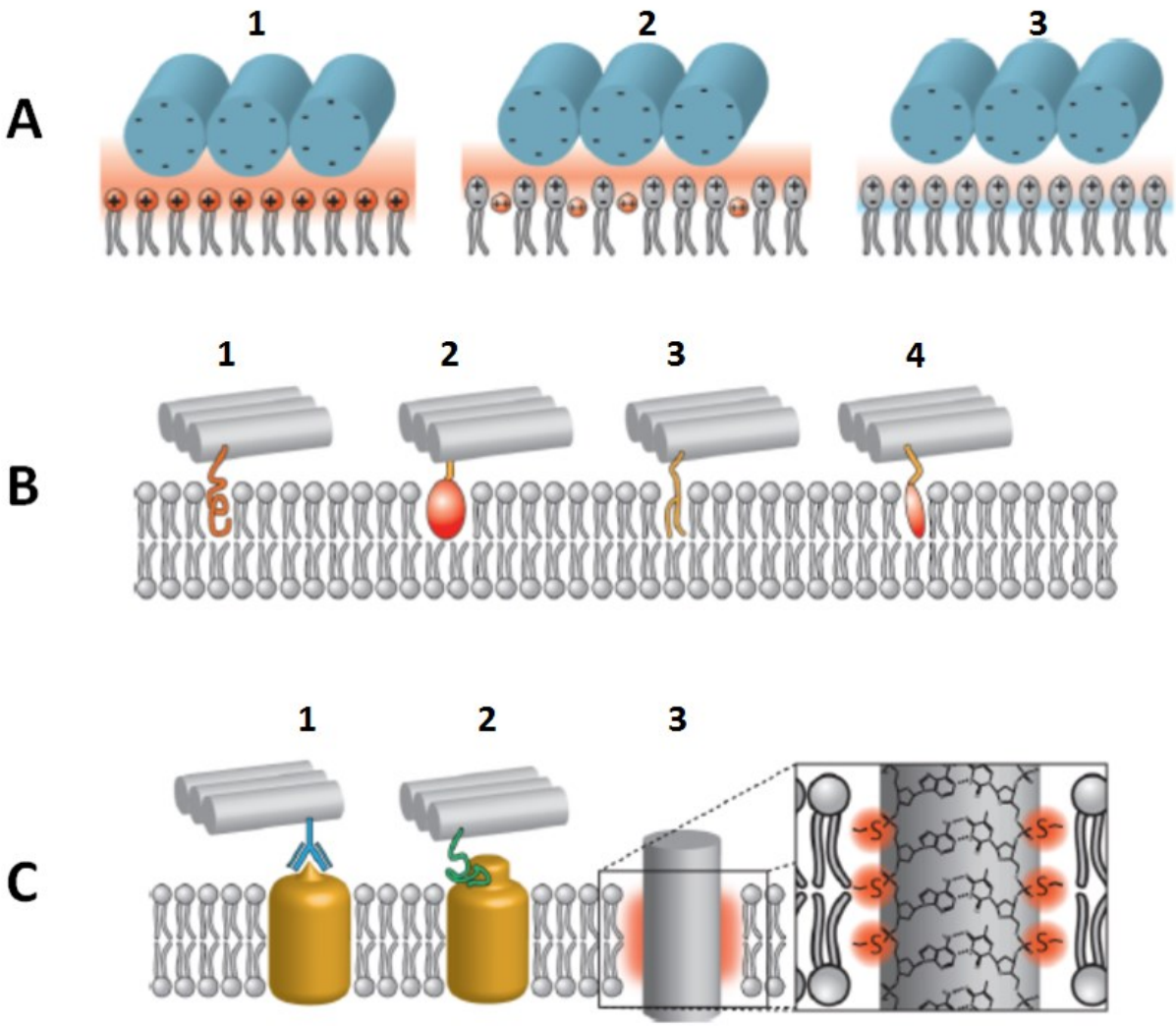

Figure 1.39: Schematic representation of different interactions between DNA and lipids[148]. (A) Non-specific interactions DNA-lipid interactions: (A1)-DNA with cationic lipids, (A2)-DNA with zwitterionic lipids and electrostatic neutralizing buffer salts, (A3)-DNA with zwitterionic lipids. (B) DNA-lipidic conjugates as anchoring motifs: (B1) hydrophobic polymers, (B2) porphyrin, (B3) alkyl chains, and (B4) cholesterol. (C) Membrane protein based DNA-bilayer anchoring: (C1) antibodies, (C2) aptamers, (C3), ethyl-thiophosphate backbone for hydrophobic insertion.

The second most commonly used mechanism to direct DNA constructs onto lipid bilayers is through covalent modification of the DNA with a lipidic moiety. Modifications such as cholesterol[157], porphyrin[158], or tocopherol[157] are readily available as phosphoramidites.

Furthermore, there are many other hydrophobic modifications that have been examined and coupled post-DNA synthesis using activated ester or thiol-based couplings[159]. Many groups have extensively studied the binding properties of lipidic and stearol conjugates such as palmitoyl and cholesterol with conflicting results. For example, it was found that in a three component lipid mixture of DOPC/sphingomyelin (SM)/Cholesterol, that DNA-cholesterol conjugates partitioned equally into the lo and ld phases[160]. Conversely, it was shown that using a similar mixture of DOPC/DPPC/cholesterol DNA-cholesterol conjugates partition almost exclusively into the ld phase[161]. Although some results may differ, it was found that multiple cholesterol anchors are required for irreversible bilayer binding and that the linker unit connecting the cholesterol with the DNA also influences the phase partitioning of the DNA construct[160-162]. Other groups found that they were able to completely direct the DNA conjugate to the lo phase using a double palmitoyl modification[157,163].

1.3.4.3 Phase Targeted DNA-Lipidic Conjugates

It has been shown that DNA nanostructures can be selectively partitioned into either lo or ld phase separated bilayer domains by choosing the appropriate DNA-lipidic anchor (Figure 1.40A)[157]. In this work, the DNA construct was designed with both a dipalmitoyl and a di-tocopherol anchoring moiety, which partition to lo and ld phases respectively. When incorporated into a single DNA construct and loaded on a bilayer, the scrambled anchor combination generates a partitioning preference favouring the ld phase as visualized using fluorescence microscopy. The DNA structure is designed with a restriction site for enzymatic cleavage, which separates the two anchors, allowing their re-distribution within the bilayer into their preferred phase separated domains.

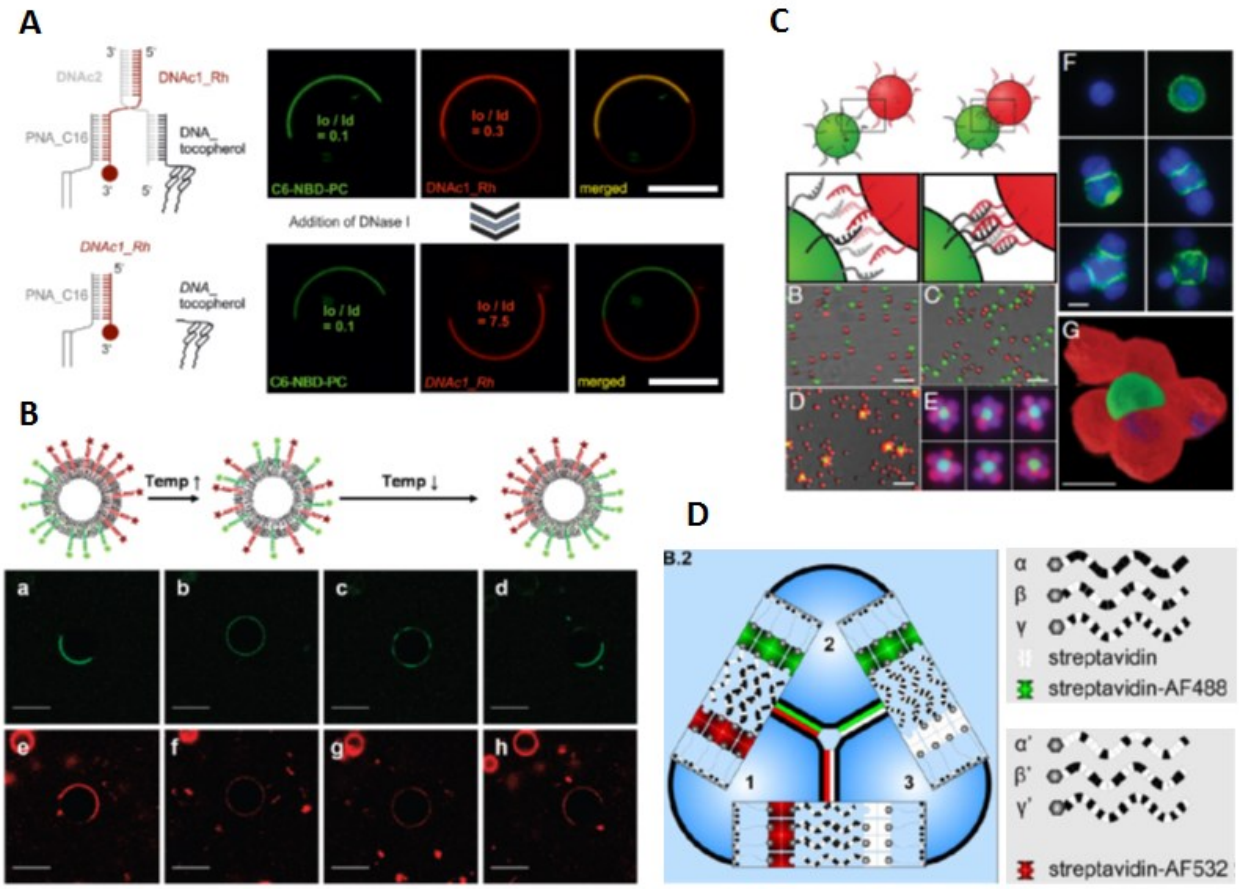

Figure 1.40: (A) Switchable phase partitioning using different DNA-lipidic conjugates. (B) Reversible phase separation using temperature control. (C) Functionalization of Jurkat cell membranes with complementary DNA strands for controlled aggregation. (D) Vesicles are shown to be organized using DNA hybridization and biotin-STV interactions[157,163,164].

Further studies, examining phase partitioning of labeled DNA-lipid conjugates found that at room temperature di-palmitoylated DNA, phase separates into the lo phase of a 1:1:1 mixture of DOPC/ sphingomyelin/cholesterol[163]. Using a second labeled DNA-tocopherol molecule, known to preferentially partition into the ld phase[165], the authors were able to visualize the phase separation of the two DNA-lipidic conjugates to their respective ld and lo domains. This phase separation can be scrambled by heating to temperatures above the known phase transition, leading to a homogenous re-distribution of the DNA-lipid throughout the entire vesicle bilayer (Figure 1.40B). Upon cooling the respective DNA-lipidic conjugates again phase separated into their respective

domains. Bilayer anchored DNA origami rods have also been shown to exhibit selective and reversible phase partitioning using different ionic salt additives[166].

One of the main goals of combining DNA scaffolds and lipid bilayer systems is the development of a modular methodology to control membrane compartmentalization and to organize cells themselves into microtissues. Work by Bertozzi et al has shown that isolated Jurkat cells can be efficiently functionalized with different complementary DNA strands that allow their controlled aggregation by varying the cell stoichiometry (Figure 1.40C)[164]. In this way cells were found to aggregate in a predictable fashion based on how they were modified with complementary lipid modified DNA strands. It was found that three main variables affected cell assembly, cell density, surface density of DNA, and DNA sequence complexity. Similar studies have also shown variable vesicle organization based on loading vesicles with complementary DNA-lipidic conjugates or dimerizing protein interactions (Figure 1.40D) (biotin-streptavidin)[167-169]. This control over cellular organization may be used to engineer asymmetric vesicle assemblies and microtissues as model research systems or in the construction of artificial organs.

1.3.4.4 Biophysical Studies of DNA Hybridization on Bilayer

The biophysical properties of DNA nanostructures embedded within lipid bilayers have been extensively studied in terms of templated hybridization, interfacial duplex destabilization/orientation, surface density and in-bilayer diffusion rates[156,170]. One of the first groups investigating DNA-lipidic conjugates determined that 20mer ssDNA regions anchored to a bilayer through a tocopherol anchor remained fully addressable for their complementary unmodified DNA sequence[165]. Further study of interfacial DNA hybridization by Herrmann and Arbuzova et al revealed that the base pairing closest to the hydrophobic anchor is partially disrupted generating a slight decrease in thermal stability (Figure 1.41A)[156]. Although hybridization may be hindered in the region closest to the lipidic anchor, DNA structures can be assembled through bilayer templation. It was shown that a closed DNA hexagon can be sequentially assembled at the membrane surface (Figure 1.41B)[171].

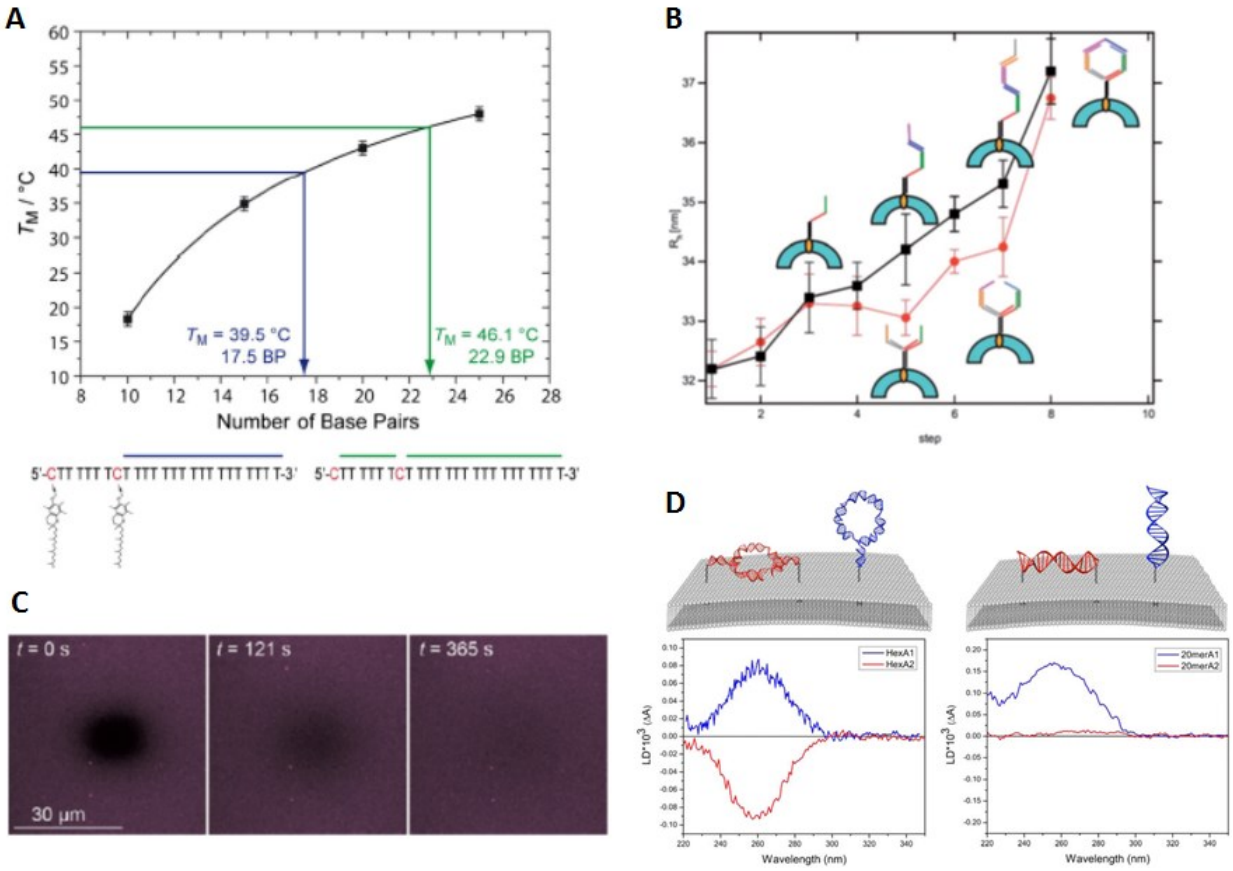

Figure 1.41: (A) Thermal stability in lipidic modified DNA duplexes is slightly lowered due to disrupted hybridization between base pairing closest to the bilayer. (B) Strategy for the on-bilayer construction of a DNA hexagon. The increase in particle size as the DNA construct is built on the bilayer surface is monitored using DLS. (C) FRAP experiments of fluorescently labeled bilayer showing the bleaching event followed by recovery. (D) Bilayer tethered DNA constructs show preferential orientations with respect to the bilayer and variable anchor points using linear dichroism spectroscopy[156,171-173].

The diffusion of DNA nanostructures within bilayer environments has been examined using fluorescence recovery after photobleaching (FRAP). This fluorescence microscopy technique monitors a fluorescent bilayer area before, during and after a localized photobleaching event. It was found that upon the bleaching event a dark (non-fluorescent) region was observed which slowly recovered its initial fluorescence as neighboring fluorephores diffuse into the target area

(Figure 1.41C)[173,174]. The rate of fluorescence recovery was found to be significantly reduced as the DNA structure was tethered to the bilayer through 1 to 3 cholesterol anchor points[173].

Another study has examined DNA duplex orientation on-bilayer, using a DNA hexagon construct that can be anchored to the bilayer by either 1 or 2 DNA-lipid conjugates (Figure 1.41D)[172]. It was found that when a single anchor was used the hexagon assumed a perpendicular orientation relative to the bilayer, while when two anchors were used a parallel orientation was observed. It was shown that a minimum of 2 DNA-lipidic conjugates are need to orient a structure parallel to the membrane[175].

Work by Brown and Baglioni et al demonstrated that the DNA-lipid conjugate surface density influences the conformation of the oligonucleotide portion above the bilayer. The structures were observed to shift from a quasi-random coil to a more rigid configuration as surface density increases. A labeled DNA origami nanorod anchored to a bilayer was used to probe mobility within the lipid environment as the surface concentration was increased. As expected, as the packing density of nanorods increased there was a marked decrease in their translational and rotational freedom[176]. Collectively the biophysical parameters discussed will allow researchers to combine DNA and lipid self-assembly for many novel biological applications.

1.3.3.5 DNA Nanotechnology and Bilayer Applications

The hybridization, orientation, and packing of DNA-lipidic conjugates within a bilayer have been shown to be highly modular, allowing for greater control as DNA nanotechnology is developed towards specialized functional applications. The following section will discuss several recent developments that interface DNA nanotechnology with lipid bilayer membranes.

Work by Sugiyama et al has used DNA origami hexagon tiles anchored to supported bilayers to demonstrate their diffusion properties and reversible dimerization (Figure 1.42A)[155]. The hexagon tiles were designed with photoswitchable hybridization along a single edge, allowing reversible dimerization upon irradiation with UV/visible light. Fast-scanning AFM was used to visualize the dimerization and dissociation event on bilayer in real-time within a 60 s timespan. The Yan group has demonstrated how this method can be applied for high resolution imaging of cellular membranes using DNA "paint" (Figure 1.42B)[177]. Using a similar bilayer landing design,

rectangular DNA origami tiles were engineered to transiently bind multiple fluorophores on the face furthest from the membrane. This allows landed DNA "barges" to diffuse within a lipid membrane environment, and be used to perform super resolution microscopy of imaging surface features.

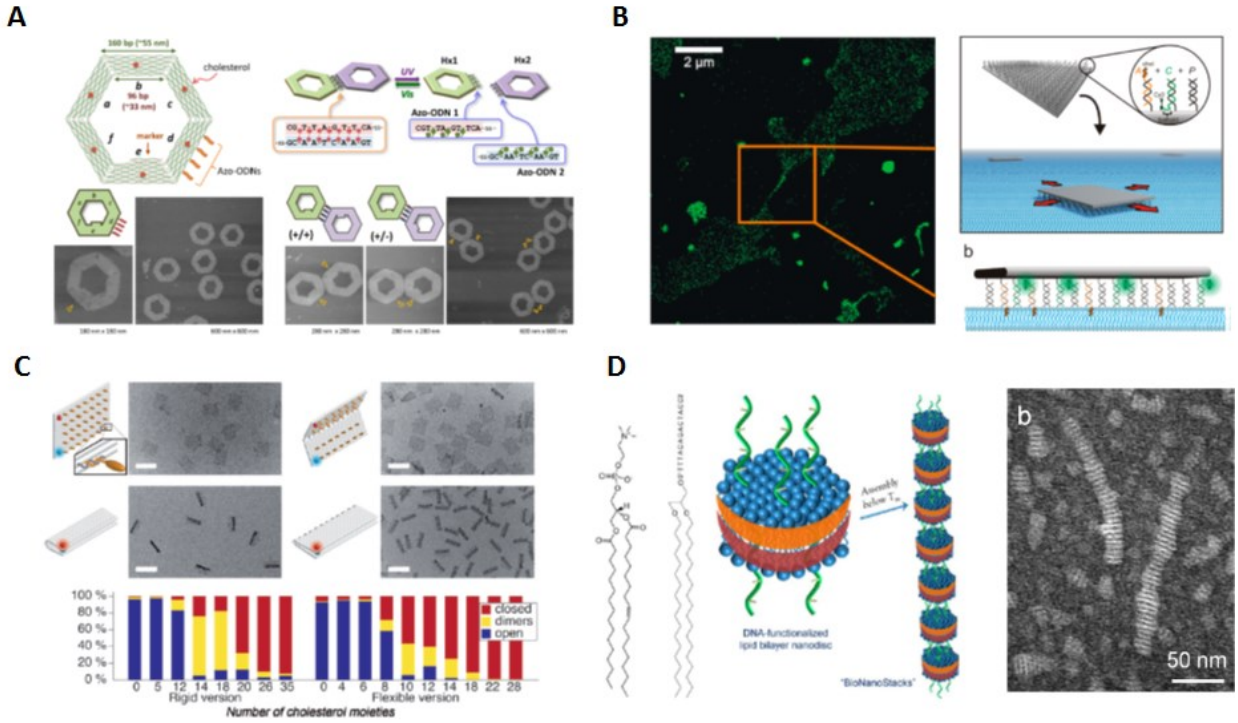

Figure 1.42: (A) Hexagonal DNA origami tiles are shown to reversibly dimerize upon UV-vis radiation. (B) A DNA origami barge has been used to perform DNA-paint on a bilayer membrane. (C) A folded DNA origami tile used to create a hydrophobic sandwich structure via bound cholesterols. (D) Lipid nanodisks were linearly organized using complementary DNA-lipid conjugates[155,177-179].

In other work, a DNA origami bilayer "sandwich" structure designed as a folded rectangular tile was functionalized with multiple DNA-cholesterol conjugates on the same face that aggregate to bend the tile in half (Figure 1.42C)[178]. It was found that a minimum of 26 cholesterol modifications were required to drive the formation of the bilayer-like structure. The origami bilayer was found to open and land on lipid bilayer membranes, which would be useful for drug delivery applications

Although not an extended bilayer, work by Sligar *et al.*[180] has shown the formation of nano-disks composed of an amphiphilic protein scaffold belt which holds together a circular bilayer of lipids. Using these mini bilayers another group created complementary DNA-lipid conjugates which were used to linearly stack the disks (Figure 1.42D)[179]. It was shown that the periodicity of the disk stacking could be readily controlled by adjusting the length of the complementary linking strands. This work demonstrates the combination of lipid, protein and DNA self-assembly.

Biological processes such as vesicle fusion normally induced by SNARE proteins, have also been mimicked using DNA hybridization[181]. The Boxer group developed a system for studying vesicle fusion into lipid bilayers using vesicles prepared with fluorescent lipid dyes that can be deposited on a bilayer using DNA-lipid conjugates[182]. As the vesicles fuse with the bilayer their fluorescent lipids merge and diffuse within the membrane leading to a measureable decrease in fluorescence (Figure 1.43A). It was found that only about 5% of vesicles that land on the bilayer undergo full fusion, and that the sequence and density of fusion-inducing DNA anchors does not significantly affect this outcome. The arrested hemi-fusion conformation is being further investigated.

A second study has used complementary DNA-cholesterol conjugates to investigate the fusion of vesicles of varying lipid composition (Figure 1.43B)[183]. This work relied on monitoring FRET pairing between appropriately labeled vesicles as they are driven to fuse by the DNA hybridization. It was determined that at least 1/3 of all DNA-induced fusion events correspond to full mixing of the outer and inner lipid bilayer leaflets.

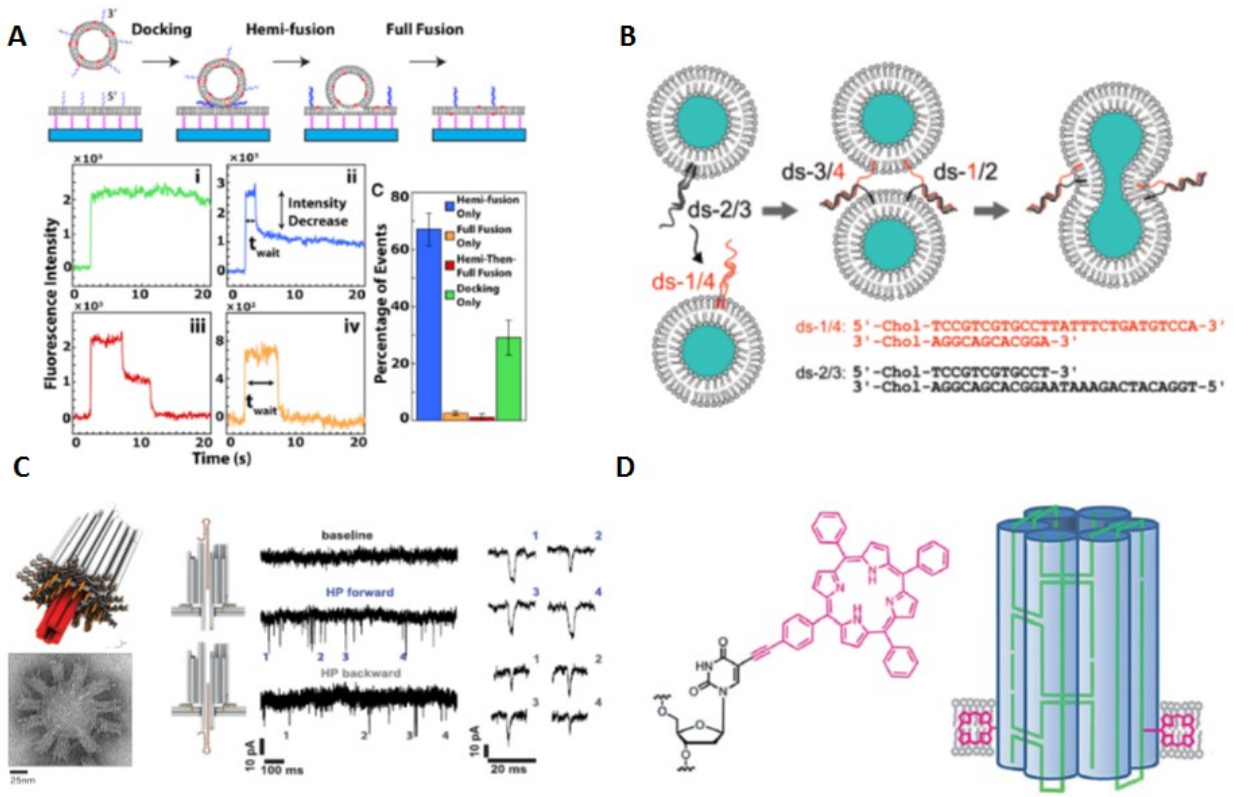

Figure 1.43: (A) Diagram of the set-up used to examine vesicle to bilayer fusion. (B) Vesicle-vesicle fusion has been examined using complementary DNA-lipid conjugates. (C) Design of a DNA origami pore, anchored to a bilayer using 26DNA-cholesterols. It was also used to detect translocation of DNA through the pore. (D) A second DNA origami pore design, comprised of a smaller structure and two porphyrin anchors, which serve a second role as fluophores[182-185].

DNA nanotechnology has been used in the development of nanopores designed to insert within lipid bilayer membranes. In nature membrane pores generally allow selective molecules to enter and exit the cell in a controlled fashion. Inspired by these designs, DNA has been recognized in being particularly useful for the construction of nanopores as the structure and size can be precisely controlled thereby determining its size exclusion properties. Nanopores have been applied for single molecule detection within these systems by applying a voltage across a single pore separating two electrolyte solution and measuring the current. When individual molecules translocate through the pore, there is a measurable change in the current as the flow of ions is disrupted[186].

One recent example of DNA nanopore formation has used a DNA origami scaffold to construct a barrel like structure containing a bilayer spanning hollow stem (2 nm diameter, 42 nm in length), anchored to the membrane via 26 DNA-cholesterol modifications (Figure 1.43C)[184]. TEM imaging indicates that the pore is directed to the bilayer in the correct orientation. Single-channel electrophysical experiments were performed and successfully detected and differentiated the translocation of hairpin/G-quadruplex forming DNA. Another group has developed a simplified nanopore design that uses two porphyrin based anchors to land a six-helix bundle DNA origami construct, with a 2 nm interior channel and 14 nm in length, on a membrane (Figure 1.43D)[185]. Not only can the structure be anchored using fewer DNA-lipidic conjugates, but the porphyrin molecules also behave a fluorescent tags. It is proposed that DNA nanopores may be used to create synthetic ion pumps to power molecular devices or even used as antimicrobial agents.

1.3.5 DNA Serum Stability

As has been discussed, many DNA nanotechnology strategies are being developed for diagnostic and therapeutic applications *in vivo* [88,107,187]. The challenge all such applications will need to address will be serum stability. The serum environment poses two particular difficulties for DNA self-assemblies, first being the serum's non-optimal ionic composition and pH for DNA assembly, and second being the presence of nucleases which are specifically evolved to target and degrade foreign oligonucleotides[188]. DNA nanostructures are typically assembled in a buffer solution containing ideal concentrations of Na^+ and Mg^{2+} ions as counter ions to decrease the electrostatic repulsion within the negatively charged phosphate backbone. The buffer solution is also adjusted to a pH of 8, while that of human plasma is approximately pH 7.4. The non-buffered serum conditions may therefore lead to fraying and consequent disassembly of a DNA construct, severely limiting its lifetime and usefulness. Serum stability of DNA constructs is generally assessed using fetal bovine serum (FBS), which is known to contain a mixture of exo/endonucleases. DNA nanostructures are incubated with FBS and the DNA is collected and analyzed to determine the extent of degradation and in serum lifetimes [189-191].

Perhaps even more challenging for the use of DNA nanotechnology *in vivo* is the targeted degradation of foreign DNA by nucleases. Nuclease enzymes are classified into two general

groups: (1) endonucleases, which degrade DNA from an internal strand location and (2) exonucleases which degrade DNA from the 3'/5' end. Oligonucleotide nuclease resistance has been extensively researched, largely driven by gene silencing therapeutics, and there presently exist several commonly used chemical modifications to stabilize nucleotides. These modifications can be introduced into the phosphate backbone, the sugar molecule or within the nucleobase and block nuclease recognition and degradation. Common protection schemes include phosphothioated backbones, 2´-O-methyl groups, as well as peptide and locked nucleic acids[192]. Many of these modifications can be used in combination; other groups have used the modified nucleotides at specific end positions rather than throughout the entire strand to create was have been termed 'gapmers'[193-195]. Although these protection strategies have shown significant improvement for oligonucleotide serum stability, they are synthetically challenging to make and are therefore quite expensive relative to unmodified DNA.

A lesser developed strategy for increasing nuclease resistance is the folding topology of DNA nanostructures[196-198]. In this approach, the DNA folded topology is shown to hinder nuclease recognition and consequent digestion. Moreover, this strategy is particularly attractive as it only uses unmodified DNA strands. Although there exist several examples indicating that small, dense DNA structures have improved serum lifetimes[196-198], the designs have limited modularity for the incorporation of additional DNA-functionalized strands and cage size. As will be discussed in Chapter 4, work in this thesis[199] has shown that a combination of folding topology and small 5'/3' end modifications can significantly stabilize DNA nanostructures in serum.

1.4 Context and Scope of Thesis Research

DNA nanotechnology has demonstrated an unprecedented ability to scaffold materials at the nanometer scale allowing for many innovative applications. The research presented in this thesis has focused on how DNA nanotechnology can be interfaced with biological environments by using a combination of structure design, synthetic insertions, and dynamic addressability. Our research has focused on two biological environments, phospholipid bilayers and serum media. Phospholipid bilayers represent the barrier for all cellular communication and are themselves a long-range self-assembling structure. DNA nanotechnology can be applied to this system for both the creation of

modular membrane models for cell signal behaviour and to provide a secondary scaffold that extends the organization limits of present DNA strategies.

DNA nanotechnology has also gained considerable interest as a drug delivery strategy, for its ability to organize multivalent components and be readily chemically modified. In order for these drug vehicles to effectively deliver a therapeutic payload they must remain intact as they travel *in vivo* to a target. We have therefore focused on examining how DNA serum stability towards nucleases can be increased using a combination of folding topology and small modified base insertions.

In Chapter two, we will begin by discussing research aimed at examining the dynamic addressability of DNA embedded within a spherically supported lipid bilayer membrane (SSLBM). This project uses a DNA based triangular prism to variably scaffold DNA-cholesterol conjugates which orient the scaffold on the bilayer surface with single-stranded edges facing outwards. A series of three complementary DNA-fluorophores are then reversibly hybridized to the scaffold using toehold displacement strategies, and visualized using fluorescence microscopy. The diffusion behaviour of the prism structures is investigated using FRAP experiments. The accessibility of bilayer loaded DNA cages is also examined using nuclease degradation experiments while varying the position and number of DNA-cholesterol anchors. The results of this research suggest that the SSLBM-DNA platform can be readily used to create dynamic model systems for organizing sensors, photo-receptors or cellular communication.

Chapter three examines how hydrophobic lipid and polymer modifications can be used in combination with DNA tile networks to achieve both selective deposition and modified morphology. This project uses a three-point star DNA motif modified at a central 3' or 5' position to introduce one of three possible hydrophobic anchoring units: (1) Cholesterol, (2) a modified palmitoyl based structure, and (3) a polymeric dodecane diol. The tiles are made with both sticky-ends for hybridization and blunt ends to investigate the interplay of DNA directing hydrogen bonding and hydrophobic aggregation. Tiles networks are pre-formed and deposited on DOPC and DPPC bilayers with selective deposition depending on the nature of the anchoring unit. Furthermore, the network is shown to undergo re-arrangements of tile packing based on bilayer and anchor character. This work shows promise for the extending the long-range ordering of DNA

into the micrometer range, which will be useful in technologies such as micro-circuitry, that require large patterned surfaces.

In Chapter four, we will examine how the serum stability of DNA cages can be improved to increase their usefulness as drug delivery vehicles. We investigate the use of three small, commercially available synthetic nucleotide insertions at the 5'/3' ends to prevent nuclease digestion: (1) hexathylene glycol, (2) hexane diol, and (3) a phosphate group. As a benchmark, a fully ligated triangular prism was synthesized and isolated for use in the degradation studies, and showed significant serum resistance. All modifications were investigated in terms of how they affect the thermal stability of the final assembled 3D cage. We use closed DNA cage structures, as well as structures that are unable to fold into cages, to demonstrate the nuclease protection conferred by closure into a discrete object. This research will be useful for the creation of serum stabilized drug delivery vehicles created using simple, commercially available chemical modifications.

In the Appendix 1, progress towards the creation multivalent aptamer-loaded scaffolds and siRNA synthesis will be discussed. The first part of this section will discuss the use of a cubic scaffold to load up to eight aptamer units. The precise 3D placement of aptamers will be compared to control samples consisting of a covalently connected linear repeat of the aptamer unit. In this way we have investigated how the 2D/3D presentation of targeting aptamers affects their target recognition.

1.5 References

(1) Chong, T. C.; Hong, M. H.; Shi, L. P. *Laser Photonics Rev.* **2010**, *4*, 123-143.

(2) Gondal, M. A.; Dastageer, M. A.; Khalil, A. *Catal. Commun.* **2009**, *11*, 214-219.

(3) Pollini, M.; Paladini, F.; Licciulli, A.; Maffezzoli, A.; Nicolais, L.; Sannino, A. *J. Appl. Polym. Sci.* **2012**, *125*, 2239-2244.

(4) Shuklin, S. G.; Buzilov, S. V.; Shuklin, D. S. *Inorg. Mater. Appl. Res.* **2011**, *2*, 160-163.

(5) Hobson, D. W. *WIRE: Nanomed. Nanobiotechnol.* **2009**, *1*, 189-202.

(6) Hashimoto, M.; Tong, R.; Kohane, D. S. *Mol. Pharmaceutics* **2013**, *10*, 2127-2144.

(7) Lehn, J.-M. *Supramolecular Chemistry: Concepts and Perspectives*; Weiham, 1995.

(8) Diederich, F. *Angew. Chem., Int. Ed.* **2007**, *46*, 68-69.

(9) Pedersen, C. J. *J. Am. Chem. Soc.* **1967**, *89*, 7017-7036.

(10) Lehn, J.-M. *Chem. Soc. Rev.* **2007**, *36*, 151-160.

(11) Dong, Z.; Luo, Q.; Liu, J. *Chem. Soc. Rev.* **2012**, *41*, 7890-7908.

(12) Watson, J. D.; Crick, F. H. C. *Nature* **1953**, *171*, 709-756.

(13) Franklin, R. E.; Gosling, R. G. *Nature* **1953**, *172*, 156-157.

(14) Structure of DNA. URL: http://bootstrike.com/Genetics/DNA/dna_structure.php (accessed 03/03/2015).

(15) Pray, L. *Nature Education* **2008**, *1*, 37.

(16) Ho, P. S.; Carter, M. *DNA Structure: Alphabet Soup for the Cellular Soul*, 2011.

(17) Seeman, N. C. *Annu. Rev. Biochem.* **2010**, *79*, 65-87.

(18) Day, H. A.; Huguin, C.; Waller, Z. A. E. *Chem. Commun.* **2013**, *49*, 7696-7698.

(19) Murat, P.; Singh, Y.; Defrancq, E. *Chem. Soc. Rev.* **2011**, *40*, 5293-5307.

(20) Reynolds, J. *Nat Cell Biol* **2004**, *6*, 184-184.

(21) Efimov, V. A.; Buryakova, A. A.; Reverdatto, S. V.; Chakhmakhcheva, O. G.; Ovchinnikov, Y. A. *Nucleic Acids Res.* **1983**, *11*, 8369-8387.

(22) Beaucage, S. L.; Caruthers, M. H. *Tetrahedron Lett.* **1981**, *22*, 1859-1862.

(23) Alvarado-Urbina, G.; Sathe, G.; Liu, W.; Gillen, M.; Duck, P.; Bender, R.; Ogilvie, K. *Science* **1981**, *214*, 270-274.

(24) Seeman, N. C. *J. Theor. Biol.* **1982**, *99*, 237-247.

(25) Kallenbach, N. R.; Ma, R.-I.; Seeman, N. C. *Nature* **1983**, *305*, 829-831.

(26) Fu, T. J.; Seeman, N. C. *Biochemistry* **1993**, *32*, 3211-3220.

(27) He, Y.; Tian, Y.; Ribbe, A. E.; Mao, C. *J. Am. Chem. Soc.* **2006**, *128*, 15978-15979.

(28) LaBean, T. H.; Yan, H.; Kopatsch, J.; Liu, F.; Winfree, E.; Reif, J. H.; Seeman, N. C. *J. Am. Chem. Soc.* **2000**, *122*, 1848-1860.

(29) Reishus, D.; Shaw, B.; Brun, Y.; Chelyapov, N.; Adleman, L. *J. Am. Chem. Soc.* **2005**, *127*, 17590-17591.

(30) Mathieu, F.; Liao, S.; Kopatsch, J.; Wang, T.; Mao, C.; Seeman, N. C. *Nano Lett.* **2005**, *5*, 661-665.

(31) Ke, Y.; Liu, Y.; Zhang, J.; Yan, H. *J. Am. Chem. Soc.* **2006**, *128*, 4414-4421.

(32) Zhang, F.; Nangreave, J.; Liu, Y.; Yan, H. *J. Am. Chem. Soc.* **2014**, *136*, 11198-11211.

(33) Hansma, H. G.; Vesenka, J.; Siegerist, C.; Kelderman, G.; Morrett, H.; Sinsheimer, R. L.; Elings, V.; Bustamante, C.; Hansma, P. K. *Science* **1992**, *256*, 1180-1184.

(34) Winfree, E.; Liu, F.; Wenzler, L. A.; Seeman, N. C. *Nature* **1998**, *394*, 539-544.

(35) Mao, C.; Sun, W.; Seeman, N. C. *J. Am. Chem. Soc.* **1999**, *121*, 5437-5443.

(36) Lin, C.; Liu, Y.; Yan, H. *Biochemistry* **2009**, *48*, 1663-1674.

(37) Park, S. H.; Yin, P.; Liu, Y.; Reif, J. H.; LaBean, T. H.; Yan, H. *Nano Lett.* **2005**, *5*, 729-733.

(38) Chhabra, R.; Sharma, J.; Ke, Y.; Liu, Y.; Rinker, S.; Lindsay, S.; Yan, H. *J. Am. Chem. Soc.* **2007**, *129*, 10304-10305.

(39) Le, J. D.; Pinto, Y.; Seeman, N. C.; Musier-Forsyth, K.; Taton, T. A.; Kiehl, R. A. *Nano Lett.* **2004**, *4*, 2343-2347.

(40) Zhang, J.; Liu, Y.; Ke, Y.; Yan, H. *Nano Lett.* **2006**, *6*, 248-251.

(41) Zheng, J.; Constantinou, P. E.; Micheel, C.; Alivisatos, A. P.; Kiehl, R. A.; Seeman, N. C. *Nano Lett.* **2006**, *6*, 1502-1504.

(42) He, Y.; Tian, Y.; Ribbe, A. E.; Mao, C. *J. Am. Chem. Soc.* **2006**, *128*, 12664-12665.

(43) Selmi, D. N.; Adamson, R. J.; Attrill, H.; Goddard, A. D.; Gilbert, R. J. C.; Watts, A.; Turberfield, A. J. *Nano Lett.* **2011**, *11*, 657-660.

(44) Lund, K.; Liu, Y.; Lindsay, S.; Yan, H. *J. Am. Chem. Soc.* **2005**, *127*, 17606-17607.

(45) Park, S. H.; Pistol, C.; Ahn, S. J.; Reif, J. H.; Lebeck, A. R.; Dwyer, C.; LaBean, T. H. *Angew. Chem., Int. Ed.* **2006**, *118*, 749-753.

(46) Liu, D.; Wang, M.; Deng, Z.; Walulu, R.; Mao, C. *J. Am. Chem. Soc.* **2004**, *126*, 2324-2325.

(47) Liu, H.; Chen, Y.; He, Y.; Ribbe, A. E.; Mao, C. *Angew. Chem., Int. Ed.* **2006**, *45*, 1942-1945.

(48) Tian, C.; Zhang, C.; Li, X.; Hao, C.; Ye, S.; Mao, C. *Langmuir* **2014**, *30*, 5859-5862.

(49) Hamada, S.; Murata, S. *Angew. Chem., Int. Ed.* **2009**, *121*, 6952-6955.

(50) Yin, P.; Hariadi, R. F.; Sahu, S.; Choi, H. M. T.; Park, S. H.; LaBean, T. H.; Reif, J. H. *Science* **2008**, *321*, 824-826.

(51) Wei, B.; Dai, M.; Yin, P. *Nature* **2012**, *485*, 623-626.

(52) Ke, Y.; Ong, L. L.; Shih, W. M.; Yin, P. *Science* **2012**, *338*, 1177-1183.

(53) He, Y.; Ye, T.; Su, M.; Zhang, C.; Ribbe, A. E.; Jiang, W.; Mao, C. *Nature* **2008**, *452*, 198-201.

(54) He, Y.; Mao, C. *Chem. Commun.* **2006**, 968-969.

(55) Zheng, J.; Birktoft, J. J.; Chen, Y.; Wang, T.; Sha, R.; Constantinou, P. E.; Ginell, S. L.; Mao, C.; Seeman, N. C. *Nature* **2009**, *461*, 74-77.

(56) Shih, W. M.; Quispe, J. D.; Joyce, G. F. *Nature* **2004**, *427*, 618-621.

(57) Serpell, C. J.; Edwardson, T. G. W.; Chidchob, P.; Carneiro, K. M. M.; Sleiman, H. F. *J. Am. Chem. Soc.* **2014**, *136*, 15767-15774.

(58) Chen, J.; Seeman, N. C. *Nature* **1991**, *350*, 631-633.

(59) Goodman, R. P.; Schaap, I. A. T.; Tardin, C. F.; Erben, C. M.; Berry, R. M.; Schmidt, C. F.; Turberfield, A. J. *Science* **2005**, *310*, 1661-1665.

(60) Goodman, R. P.; Heilemann, M.; Doose, S.; Erben, C. M.; Kapanidis, A. N.; Turberfield, A. J. *Nat. Nanotechnol.* **2008**, *3*, 93-96.

(61) Bhatia, D.; Mehtab, S.; Krishnan, R.; Indi, S. S.; Basu, A.; Krishnan, Y. *Angew. Chem., Int. Ed.* **2009**, *48*, 4134-4137.

(62) Erben, C. M.; Goodman, R. P.; Turberfield, A. J. *Angew. Chem., Int. Ed.* **2006**, *118*, 7574-7577.

(63) Liu, X.; Xu, Y.; Yu, T.; Clifford, C.; Liu, Y.; Yan, H.; Chang, Y. *Nano Lett.* **2012**, *12*, 4254-4259.

(64) McLaughlin, C. K.; Hamblin, G. D.; Hänni, K. D.; Conway, J. W.; Nayak, M. K.; Carneiro, K. M. M.; Bazzi, H. S.; Sleiman, H. F. *J. Am. Chem. Soc.* **2012**, *134*, 4280-4286.

(65) Rothemund, P. W. K. *Nature* **2006**, *440*, 297-302.

(66) Saccà, B.; Niemeyer, C. M. *Angew. Chem., Int. Ed.* **2012**, *51*, 58-66.

(67) Ke, Y.; Lindsay, S.; Chang, Y.; Liu, Y.; Yan, H. *Science* **2008**, *319*, 180-183.

(68) Rajendran, A.; Endo, M.; Sugiyama, H. *Angew. Chem., Int. Ed.* **2012**, *51*, 874-890.

(69) Voigt, N. V.; Torring, T.; Rotaru, A.; Jacobsen, M. F.; Ravnsbaek, J. B.; Subramani, R.; Mamdouh, W.; Kjems, J.; Mokhir, A.; Besenbacher, F.; Gothelf, K. V. *Nat. Nanotechnol.* **2010**, *5*, 200-203.

(70) Rinker, S.; Ke, Y.; Liu, Y.; Chhabra, R.; Yan, H. *Nat. Nanotechnol.* **2008**, *3*, 418-422.

(71) Stephanopoulos, N.; Liu, M.; Tong, G. J.; Li, Z.; Liu, Y.; Yan, H.; Francis, M. B. *Nano Lett.* **2010**, *10*, 2714-2720.

(72) Nakata, E.; Liew, F. F.; Uwatoko, C.; Kiyonaka, S.; Mori, Y.; Katsuda, Y.; Endo, M.; Sugiyama, H.; Morii, T. *Angew. Chem., Int. Ed.* **2012**, *124*, 2471-2474.

(73) Sannohe, Y.; Endo, M.; Katsuda, Y.; Hidaka, K.; Sugiyama, H. *J. Am. Chem. Soc.* **2010**, *132*, 16311-16313.

(74) Maffeo, C.; Luan, B.; Aksimentiev, A. *Nucleic Acids Res.* **2012**, *40*, 3812-3821.

(75) Woo, S.; Rothemund, P. W. K. *Nature Chem.* **2011**, *3*, 620-627.

(76) Andersen, E. S.; Dong, M.; Nielsen, M. M.; Jahn, K.; Subramani, R.; Mamdouh, W.; Golas, M. M.; Sander, B.; Stark, H.; Oliveira, C. L. P.; Pedersen, J. S.; Birkedal, V.; Besenbacher, F.; Gothelf, K. V.; Kjems, J. *Nature* **2009**, *459*, 73-76.

(77) Zhang, D. Y.; Seelig, G. *Nature Chem.* **2011**, *3*, 103-113.

(78) Kuzuya, A.; Komiyama, M. *Chem. Commun.* **2009**, 4182-4184.

(79) Ke, Y.; Sharma, J.; Liu, M.; Jahn, K.; Liu, Y.; Yan, H. *Nano Lett.* **2009**, *9*, 2445-2447.

(80) Endo, M.; Hidaka, K.; Sugiyama, H. *Org. Bioorg. Chem.* **2011**, *9*, 2075-2077.

(81) Endo, M.; Hidaka, K.; Kato, T.; Namba, K.; Sugiyama, H. *J. Am. Chem. Soc.* **2009**, *131*, 15570-15571.

(82) Douglas, S. M.; Dietz, H.; Liedl, T.; Hogberg, B.; Graf, F.; Shih, W. M. *Nature* **2009**, *459*, 414-418.

(83) Dietz, H.; Douglas, S. M.; Shih, W. M. *Science* **2009**, *325*, 725-730.

(84) Han, D.; Pal, S.; Nangreave, J.; Deng, Z.; Liu, Y.; Yan, H. *Science* **2011**, *332*, 342-346.

(85) Li, Z.; Wang, L.; Yan, H.; Liu, Y. *Langmuir* **2012**, *28*, 1959-1965.

(86) Castro, C. E.; Kilchherr, F.; Kim, D.-N.; Shiao, E. L.; Wauer, T.; Wortmann, P.; Bathe, M.; Dietz, H. *Nat. Methods* **2011**, *8*, 221-229.

(87) Nangreave, J.; Han, D.; Liu, Y.; Yan, H. *Curr. Opin. Chem. Biol.* **2010**, *14*, 608-615.

(88) Torring, T.; Voigt, N. V.; Nangreave, J.; Yan, H.; Gothelf, K. V. *Chem. Soc. Rev.* **2011**, *40*, 5636-5646.

(89) Douglas, S. M.; Bachelet, I.; Church, G. M. *Science* **2012**, *335*, 831-834.

(90) Jiang, Q.; Song, C.; Nangreave, J.; Liu, X.; Lin, L.; Qiu, D.; Wang, Z.-G.; Zou, G.; Liang, X.; Yan, H.; Ding, B. *J. Am. Chem. Soc.* **2012**, *134*, 13396-13403.

(91) Wilner, O. I.; Weizmann, Y.; Gill, R.; Lioubashevski, O.; Freeman, R.; Willner, I. *Nat. Nanotechnol.* **2009**, *4*, 249-254.

(92) Fu, Y.; Zeng, D.; Chao, J.; Jin, Y.; Zhang, Z.; Liu, H.; Li, D.; Ma, H.; Huang, Q.; Gothelf, K. V.; Fan, C. *J. Am. Chem. Soc.* **2013**, *135*, 696-702.

(93) Fu, J.; Liu, M.; Liu, Y.; Woodbury, N. W.; Yan, H. *J. Am. Chem. Soc.* **2012**, *134*, 5516-5519.

(94) Helmig, S.; Rotaru, A.; Arian, D.; Kovbasyuk, L.; Arnbjerg, J.; Ogilby, P. R.; Kjems, J.; Mokhir, A.; Besenbacher, F.; Gothelf, K. V. *ACS Nano* **2010**, *4*, 7475-7480.

(95) Stein, I. H.; Steinhauer, C.; Tinnefeld, P. *J. Am. Chem. Soc.* **2011**, *133*, 4193-4195.

(96) Betzig, E.; Patterson, G. H.; Sougrat, R.; Lindwasser, O. W.; Olenych, S.; Bonifacino, J. S.; Davidson, M. W.; Lippincott-Schwartz, J.; Hess, H. F. *Science* **2006**, *313*, 1642-1645.

(97) Smith, D. M.; Sch; #252; ller, V.; Forthmann, C.; Schreiber, R.; Tinnefeld, P.; Liedl, T. *J. Nucleic Acids* **2011**, *2011*, 9.

(98) Schmied, J. J.; Gietl, A.; Holzmeister, P.; Forthmann, C.; Steinhauer, C.; Dammeyer, T.; Tinnefeld, P. *Nat. Methods* **2012**, *9*, 1133-1134.

(99) Schmied, J. J.; Forthmann, C.; Pibiri, E.; Lalkens, B.; Nickels, P.; Liedl, T.; Tinnefeld, P. *Nano Lett.* **2013**, *13*, 781-785.

(100) Adleman, L. *Science* **1994**, *266*, 1021-1024.

(101) Krishnan, Y.; Simmel, F. C. *Angew. Chem., Int. Ed.* **2011**, *50*, 3124-3156.

(102) Gu, H.; Chao, J.; Xiao, S.-J.; Seeman, N. C. *Nature* **2010**, *465*, 202-205.

(103) Wickham, S. F. J.; Bath, J.; Katsuda, Y.; Endo, M.; Hidaka, K.; Sugiyama, H.; Turberfield, A. J. *Nat. Nanotechnol.* **2012**, *7*, 169-173.

(104) Maune, H. T.; Han, S.-p.; Barish, R. D.; Bockrath, M.; Goddard, I. I. A.; Rothemund Paul, W. K.; Winfree, E. *Nat. Nanotechnol.* **2010**, *5*, 61-66.

(105) Acuna, G. P.; Möller, F. M.; Holzmeister, P.; Beater, S.; Lalkens, B.; Tinnefeld, P. *Science* **2012**, *338*, 506-510.

(106) Vicens, J.; Vicens, Q. *J. Incl. Phenom. Macrocycl. Chem.* **2011**, *71*, 251-274.

(107) McLaughlin, C. K.; Hamblin, G. D.; Sleiman, H. F. *Chem. Soc. Rev.* **2011**, *40*, 5647-5656.

(108) Aldaye, F. A.; Palmer, A. L.; Sleiman, H. F. *Science* **2008**, *321*, 1795-1799.

(109) Shi, J.; Bergstrom, D. E. *Angew. Chem., Int. Ed.* **1997**, *36*, 111-113.

(110) Aldaye, F. A.; Sleiman, H. F. *Angew. Chem., Int. Ed.* **2006**, *45*, 2204-2209.

(111) Aldaye, F. A.; Sleiman, H. F. *J. Am. Chem. Soc.* **2007**, *129*, 10070-10071.

(112) Aldaye, F. A.; Sleiman, H. F. *J. Am. Chem. Soc.* **2007**, *129*, 4130-4131.

(113) Aldaye, F. A.; Sleiman, H. F. *J. Am. Chem. Soc.* **2007**, *129*, 13376-13377.

(114) McLaughlin, C. K.; Hamblin, G. D.; Aldaye, F. A.; Yang, H.; Sleiman, H. F. *Chem. Commun.* **2011**, *47*, 8925-8927.

(115) Aldaye, F. A.; Lo, P. K.; Karam, P.; McLaughlin, C. K.; Cosa, G.; Sleiman, H. F. *Nat. Nanotechnol.* **2009**, *4*, 349-352.

(116) Lo, P. K.; Karam, P.; Aldaye, F. A.; McLaughlin, C. K.; Hamblin, G. D.; Cosa, G.; Sleiman, H. F. *Nature Chem.* **2010**, *2*, 319-328.

(117) Scheffler, M.; Dorenbeck, A.; Jordan, S.; Wüstefeld, M.; von Kiedrowski, G. *Angew. Chem., Int. Ed.* **1999**, *38*, 3311-3315.

(118) Zimmermann, J.; Cebulla, M. P. J.; Mönninghoff, S.; von Kiedrowski, G. *Angew. Chem., Int. Ed.* **2008**, *47*, 3626-3630.

(119) Tumpane, J.; Kumar, R.; Lundberg, E. P.; Sandin, P.; Gale, N.; Nandhakumar, I. S.; Albinsson, B.; Lincoln, P.; Wilhelmsson, L. M.; Brown, T.; Nordén, B. *Nano Lett.* **2007**, *7*, 3832-3839.

(120) Endo, M.; Seeman, N. C.; Majima, T. *Angew. Chem., Int. Ed.* **2005**, *44*, 6074-6077.

(121) Jin, R.; Wu, G.; Li, Z.; Mirkin, C. A.; Schatz, G. C. *J. Am. Chem. Soc.* **2003**, *125*, 1643-1654.

(122) Boman, F. C.; Gibbs-Davis, J. M.; Heckman, L. M.; Stepp, B. R.; Nguyen, S. T.; Geiger, F. M. *J. Am. Chem. Soc.* **2009**, *131*, 844-848.

(123) Prytkova, T. R.; Eryazici, I.; Stepp, B.; Nguyen, S.-B.; Schatz, G. C. *J. Phys. Chem. B* **2010**, *114*, 2627-2634.

(124) Eryazici, I.; Prytkova, T. R.; Schatz, G. C.; Nguyen, S. T. *J. Am. Chem. Soc.* **2010**, *132*, 17068-17070.

(125) Greschner, A. A.; Bujold, K. E.; Sleiman, H. F. *J. Am. Chem. Soc.* **2013**, *135*, 11283-11288.

(126) Leininger, S.; Olenyuk, B.; Stang, P. J. *Chem. Rev.* **2000**, *100*, 853-908.

(127) Lippard, S. J. *Nature Chem. Biol* **2006**, *2*, 504-507.

(128) Choi, J. S.; Kang, C. W.; Jung, K.; Yang, J. W.; Kim, Y.-G.; Han, H. *J. Am. Chem. Soc.* **2004**, *126*, 8606-8607.

(129) Stewart, K. M.; McLaughlin, L. W. *J. Am. Chem. Soc.* **2004**, *126*, 2050-2057.

(130) Stewart, K. M.; Rojo, J.; McLaughlin, L. W. *Angew. Chem., Int. Ed.* **2004**, *43*, 5808-5811.

(131) Yang, H.; Sleiman, H. F. *Angew. Chem., Int. Ed.* **2008**, *47*, 2443-2446.

(132) Yang, H.; Rys, A. Z.; McLaughlin, C. K.; Sleiman, H. F. *Angew. Chem., Int. Ed.* **2009**, *48*, 9919-9923.

(133) Yang, H.; Altvater, F.; de Bruijn, A. D.; McLaughlin, C. K.; Lo, P. K.; Sleiman, H. F. *Angew. Chem., Int. Ed.* **2011**, *50*, 4620-4623.

(134) Gothelf, K. V.; Thomsen, A.; Nielsen, M.; Cló, E.; Brown, R. S. *J. Am. Chem. Soc.* **2004**, *126*, 1044-1046.

(135) Yang, H.; Metera, K. L.; Sleiman, H. F. *Coord. Chem. Rev.* **2010**, *254*, 2403-2415.

(136) Mitra, D.; Di Cesare, N.; Sleiman, H. F. *Angew. Chem., Int. Ed.* **2004**, *43*, 5804-5808.

(137) Tanaka, K.; Tengeiji, A.; Kato, T.; Toyama, N.; Shionoya, M. *Science* **2003**, *299*, 1212-1213.

(138) Tanaka, K.; Clever, G. H.; Takezawa, Y.; Yamada, Y.; Kaul, C.; Shionoya, M.; Carell, T. *Nat. Nanotechnol.* **2006**, *1*, 190-194.

(139) Clever, G. H.; Kaul, C.; Carell, T. *Angew. Chem., Int. Ed.* **2007**, *46*, 6226-6236.

(140) Mai, Y.; Eisenberg, A. *Chem. Soc. Rev.* **2012**, *41*, 5969-5985.

(141) Kwak, M.; Herrmann, A. *Chem. Soc. Rev.* **2011**, *40*, 5745-5755.

(142) Ding, K.; Alemdaroglu, F. E.; Börsch, M.; Berger, R.; Herrmann, A. *Angew. Chem., Int. Ed.* **2007**, *46*, 1172-1175.

(143) Chien, M.-P.; Rush, A. M.; Thompson, M. P.; Gianneschi, N. C. *Angew. Chem., Int. Ed.* **2010**, *49*, 5076-5080.

(144) Wang, L.; Feng, Y.; Yang, Z.; He, Y.-M.; Fan, Q.-H.; Liu, D. *Chem. Commun.* **2012**, *48*, 3715-3717.

(145) Carneiro, K. M. M.; Aldaye, F. A.; Sleiman, H. F. *J. Am. Chem. Soc.* **2010**, *132*, 679-685.

(146) Edwardson, T. G. W.; Carneiro, K. M. M.; McLaughlin, C. K.; Serpell, C. J.; Sleiman, H. F. *Nature Chem.* **2013**, *5*, 868-875.

(147) Edwardson, T. G. W.; Carneiro, K. M. M.; Serpell, C. J.; Sleiman, H. F. *Angew. Chem., Int. Ed.* **2014**, *53*, 4567-4571.

(148) Langecker, M.; Arnaut, V.; List, J.; Simmel, F. C. *Acc. Chem. Res.* **2014**, *47*, 1807-1815.

(149) Veatch, S. L.; Keller, S. L. *Biophys. J.* **2003**, *85*, 3074-3083.

(150) Connell, S. D.; Smith, D. A. *Mol. Membr. Biol.* **2006**, *23*, 17-28.

(151) Lawrence, J. C.; Saslowsky, D. E.; Michael Edwardson, J.; Henderson, R. M. *Biophys. J.* **2003**, *84*, 1827-1832.

(152) Veatch, S. L.; Keller, S. L. *Phys. Rev. Lett.* **2005**, *94*, 148101.

(153) Felgner, P. L.; Gadek, T. R.; Holm, M.; Roman, R.; Chan, H. W.; Wenz, M.; Northrop, J. P.; Ringold, G. M.; Danielsen, M. *PNAS* **1987**, *84*, 7413-7417.

(154) Gromelski, S.; Brezesinski, G. *Langmuir* **2006**, *22*, 6293-6301.

(155) Suzuki, Y.; Endo, M.; Yang, Y.; Sugiyama, H. *J. Am. Chem. Soc.* **2014**, *136*, 1714-1717.

(156) Schade, M.; Berti, D.; Huster, D.; Herrmann, A.; Arbuzova, A. *Adv. Colloid Interface Sci.* **2014**, *208*, 235-251.

(157) Schade, M.; Knoll, A.; Vogel, A.; Seitz, O.; Liebscher, J.; Huster, D.; Herrmann, A.; Arbuzova, A. *J. Am. Chem. Soc.* **2012**, *134*, 20490-20497.

(158) Woller, J. G.; Börjesson, K.; Svedhem, S.; Albinsson, B. *Langmuir* **2012**, *28*, 1944-1953.

(159) Scheidt, H. A.; Müller, P.; Herrmann, A.; Huster, D. *J. Biol. Chem.* **2003**, *278*, 45563-45569.

(160) Bunge, A.; Loew, M.; Pescador, P.; Arbuzova, A.; Brodersen, N.; Kang, J.; Dähne, L.; Liebscher, J.; Herrmann, A.; Stengel, G.; Huster, D. *J. Phys. Chem. B* **2009**, *113*, 16425-16434.

(161) Beales, P. A.; Vanderlick, T. K. *J. Phys. Chem. B* **2009**, *113*, 13678-13686.

(162) Banchelli, M.; Betti, F.; Berti, D.; Caminati, G.; Bombelli, F. B.; Brown, T.; Wilhelmsson, L. M.; Nordén, B.; Baglioni, P. *J. Phys. Chem. B* **2008**, *112*, 10942-10952.

(163) Loew, M.; Springer, R.; Scolari, S.; Altenbrunn, F.; Seitz, O.; Liebscher, J.; Huster, D.; Herrmann, A.; Arbuzova, A. *J. Am. Chem. Soc.* **2010**, *132*, 16066-16072.

(164) Gartner, Z. J.; Bertozzi, C. R. *PNAS* **2009**, *106*, 4606-4610.

(165) Kurz, A.; Bunge, A.; Windeck, A.-K.; Rost, M.; Flasche, W.; Arbuzova, A.; Strohbach, D.; Müller, S.; Liebscher, J.; Huster, D.; Herrmann, A. *Angew. Chem., Int. Ed.* **2006**, *45*, 4440-4444.

(166) Czogalla, A.; Petrov, E. P.; Kauert, D. J.; Uzunova, V.; Zhang, Y.; Seidel, R.; Schwille, P. *Faraday Discuss.* **2013**, *161*, 31-43.

(167) Beales, P. A.; Vanderlick, T. K. *J. Phys. Chem. A* **2007**, *111*, 12372-12380.

(168) Beales, P. A.; Nam, J.; Vanderlick, T. K. *Soft Matter* **2011**, *7*, 1747-1755.

(169) Hadorn, M.; Hotz, P. E. *PLoS One* **2010**, *5*, e9886.

(170) Beales, P. A.; Vanderlick, T. K. *Adv. Colloid Interface Sci.* **2014**, *207*, 290-305.

(171) Baldelli Bombelli, F.; Betti, F.; Gambinossi, F.; Caminati, G.; Brown, T.; Baglioni, P.; Berti, D. *Soft Matter* **2009**, *5*, 1639-1645.

(172) Lundberg, E. P.; Feng, B.; Saeid Mohammadi, A.; Wilhelmsson, L. M.; Nordén, B. *Langmuir* **2013**, *29*, 285-293.

(173) Börjesson, K.; Lundberg, E. P.; Woller, J. G.; Nordén, B.; Albinsson, B. *Angew. Chem., Int. Ed.* **2011**, *50*, 8312-8315.

(174) van der Meulen, S. A. J.; Leunissen, M. E. *J. Am. Chem. Soc.* **2013**, *135*, 15129-15134.

(175) Börjesson, K.; Wiberg, J.; El-Sagheer, A. H.; Ljungdahl, T.; Mårtensson, J.; Brown, T.; Nordén, B.; Albinsson, B. *ACS Nano* **2010**, *4*, 5037-5046.

(176) Czogalla, A.; Kauert, D. J.; Seidel, R.; Schwille, P.; Petrov, E. P. *Nano Lett.* **2015**, *15*, 649-655.

(177) Johnson-Buck, A.; Jiang, S.; Yan, H.; Walter, N. G. *ACS Nano* **2014**, *8*, 5641-5649.

(178) List, J.; Weber, M.; Simmel, F. C. *Angew. Chem., Int. Ed.* **2014**, *53*, 4236-4239.

(179) Beales, P. A.; Geerts, N.; Inampudi, K. K.; Shigematsu, H.; Wilson, C. J.; Vanderlick, T. K. *J. Am. Chem. Soc.* **2013**, *135*, 3335-3338.

(180) Denisov, I. G.; Grinkova, Y. V.; Lazarides, A. A.; Sligar, S. G. *J. Am. Chem. Soc.* **2004**, *126*, 3477-3487.

(181) Jahn, R.; Lang, T.; Südhof, T. C. *Cell* **2003**, *112*, 519-533.

(182) van Lengerich, B.; Rawle, Robert J.; Bendix, Poul M.; Boxer, Steven G. *Biophys. J.* **2013**, *105*, 409-419.

(183) Stengel, G.; Zahn, R.; Höök, F. *J. Am. Chem. Soc.* **2007**, *129*, 9584-9585.

(184) Langecker, M.; Arnaut, V.; Martin, T. G.; List, J.; Renner, S.; Mayer, M.; Dietz, H.; Simmel, F. C. *Science* **2012**, *338*, 932-936.

(185) Burns, J. R.; Göpfrich, K.; Wood, J. W.; Thacker, V. V.; Stulz, E.; Keyser, U. F.; Howorka, S. *Angew. Chem., Int. Ed.* **2013**, *52*, 12069-12072.

(186) Bell, N. A. W.; Keyser, U. F. *FEBS Lett.* **2014**, *588*, 3564-3570.

(187) Fu, J.; Liu, M.; Liu, Y.; Yan, H. *Acc. Chem. Res.* **2012**, *45*, 1215-1226.

(188) Uhlmann, E.; Ryte, A.; Peyman, A. *Antisense Nucleic Acid Drug Dev.* **1997**, *7*, 345-350.

(189) Wahlestedt, C.; Salmi, P.; Good, L.; Kela, J.; Johnsson, T.; Hökfelt, T.; Broberger, C.; Porreca, F.; Lai, J.; Ren, K.; Ossipov, M.; Koshkin, A.; Jakobsen, N.; Skouv, J.; Oerum, H.; Jacobsen, M. H.; Wengel, J. *PNAS* **2000**, *97*, 5633-5638.

(190) Deleavey, G. F.; Watts, J. K.; Alain, T.; Robert, F.; Kalota, A.; Aishwarya, V.; Pelletier, J.; Gewirtz, A. M.; Sonenberg, N.; Damha, M. J. *Nucleic Acids Res.* **2010**, *38*, 4547-4557.

(191) Keum, J.-W.; Bermudez, H. *Chem. Commun.* **2009**, 7036-7038.

(192) Deleavey, Glen F.; Damha, Masad J. *Chem. Biol.* **2012**, *19*, 937-954.

(193) Kurreck, J. *Eur. J. Biochem.* **2003**, *270*, 1628-1644.

(194) Kauppinen, S.; Vester, B.; Wengel, J. *Drug Discovery Today: Technol.* **2005**, *2*, 287-290.

(195) Fluiter, K.; Mook, O. R. F.; Vreijling, J.; Langkjaer, N.; Hojland, T.; Wengel, J.; Baas, F. *Mol. BioSyst.* **2009**, *5*, 838-843.

(196) Keum, J. W.; Ahn, J. H.; Bermudez, H. *Small* **2011**, *7*, 3529-3535.

(197) Walsh, A. S.; Yin, H.; Erben, C. M.; Wood, M. J. A.; Turberfield, A. J. *ACS Nano* **2011**, *5*, 5427-5432.

(198) Li, J.; Pei, H.; Zhu, B.; Liang, L.; Wei, M.; He, Y.; Chen, N.; Li, D.; Huang, Q.; Fan, C. *ACS Nano* **2011**, *5*, 8783-8789.

(199) Conway, J. W.; McLaughlin, C. K.; Castor, K. J.; Sleiman, H. *Chem. Commun.* **2013**, *49*, 1172-1174.

Preface:

Chapter 2 discusses our work towards exploring the addressability of 3D DNA scaffolds when embedded within a lipid environment. These experiments allowed us to determine how proximity to the bilayer surface affects toehold displacement strategies on the upper and lower scaffold faces located further from or embedded within the bilayer. We examine the diffusion properties of the bilayer anchored DNA cages, their use as a template surface for higher order assembly, and controlling their depth within a bilayer by adding multiple bilayer directing anchors. Furthermore, the silica sphere-supported lipid bilayer membrane system itself has several advantages for combination with DNA nanotechnology over traditional lipid vesicles, such mechanical robustness, well controlled size, and easy separation from the supernatant via centrifugation.

Chapter 2

Dynamic Behavior of DNA Cages Anchored on Spherically Supported Lipid Bilayers

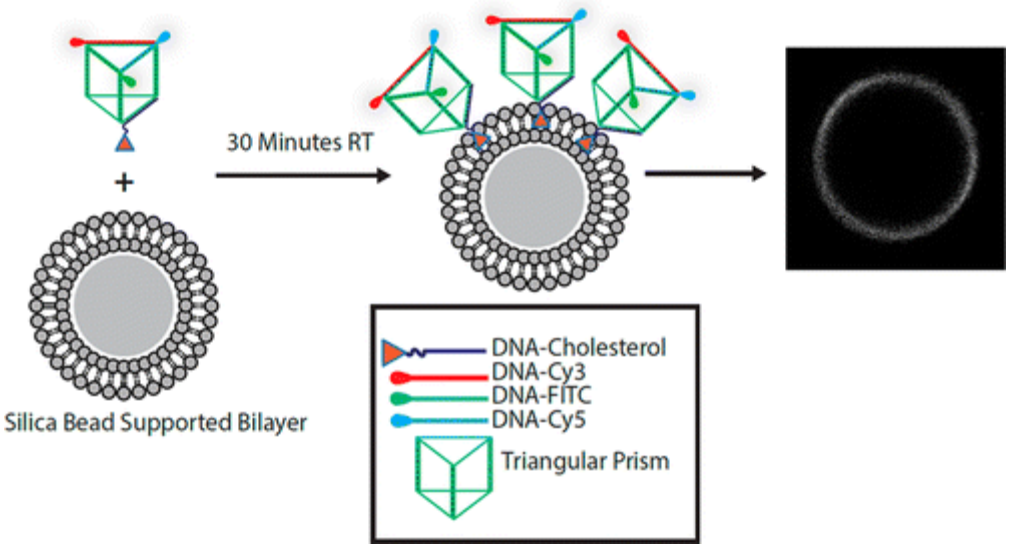

The majority of this chapter has been published as "Dynamic Behaviour of DNA Cages Anchored on Spherically Supported Lipid Bilayers", J. W. Conway, C. Madwar, T. G. Edwardson, C. K. McLaughlin, J. Fahkoury, R. B. Lennox, H. F. Sleiman J. Am. Chem. Soc., 2014, 2014, 136 (37), 12987-12997.

2.1 Abstract

We report the anchoring of 3D-DNA-cholesterol labeled cages on spherically supported lipid bilayer membranes (SSLBM) formed on silica beads, and their addressability through strand displacement reactions, controlled membrane orientation and templated dimerization. The bilayer-anchored cages can load three different DNA-fluorophores by hybridization to their 'top' face (furthest from bilayer) and unload each of them selectively upon addition of a specific input displacement strand. We introduce a method to control strand displacement from their less accessible 'bottom' face (closest to the bilayer), by adding cholesterol-substituted displacing strands that insert into the bilayer themselves in order to access the toehold region. The orientation of DNA cages within the bilayer is tunable by positioning multiple cholesterol anchoring units on the opposing two faces of the cage, thereby controlling their accessibility to proteins and enzymes. A population of two distinct DNA cages anchored to the SSLBMs exhibited significant membrane fluidity and have been directed into dimer assemblies on bilayer via input of a complementary linking strand. Displacement experiments performed on these anchored dimers indicate that removal of only one prism's anchoring cholesterol strand was not sufficient to release the dimers from the bilayer, however removal of both cholesterol anchors from the dimerized prisms via two displacement strands cleanly released the dimers from the bilayer. This methodology allows for the anchoring of DNA cages on supported lipid bilayers, the control of their orientation and accessibility within the bilayer, and the programmable dimerization and selective removal of any of their components. The facile coupling of DNA to other functional materials makes this an attractive method for developing stimuli-responsive protein or nanoparticle arrays, drug releasing biomedical device surfaces and self-healing materials for light harvesting applications, using a highly modular, DNA-economic scaffold.

2.2 Introduction

DNA nanostructures have shown tremendous promise for the precise organization of functional materials[1-4]. In order to integrate them into devices for diagnostic assays[5-8], optoelectronic[9], plasmonic circuitry[10-12] or biomedical applications[13-18], it will be important to transition these

structures from solution to solid surfaces. DNA structures have been typically immobilized on hard surfaces (such as gold or silicon)[2,19], but these rigid surfaces diminish or completely shut down the 2D-diffusion of tethered DNA and serve as a significant steric and diffusion barrier. On the other hand, lipid bilayers present a soft, fluid two-dimensional substrate that can effectively interface with numerous solid substrates[4,20,21]. Anchoring DNA nanostructures to these bilayers may preserve their dynamic character, and depending on the lipid composition and experimental conditions, would allow 2D-motion of these structures with tunable kinetics.

DNA strands positioned on lipid membranes have been used in a variety of contexts. They can act as tethers of lipid vesicles to planar bilayers[22], as mediators of vesicle fusion in analogy to SNARE proteins[23,24], as guides for the formation of 'designer' microtissues from DNA tagged cells[25], and as templates for the formation of supramolecular vesicle networks[23,24]. DNA nanostructures anchored in lipid membranes have been shown to mimic the behavior of nanopore forming proteins[26,27] and the properties of photosynthetic systems[1,28]. Peptide nucleic acid-DNA hybrid structures can cluster in specific lipid domains and this clustering can be changed to other domains with the addition of nucleases that degrade the DNA component[29]. Two studies have recently examined dynamic behavior of 2D-DNA origami structures on lipid bilayers, by photochemically switching the association of hexagonal origami tiles, or by hybridization of origami 'barges' that are held at a distance from the lipid bilayer membrane[30-32]. Another study using cholesterol functionalized DNA origami helical bundles examined the dynamics of these structures on free standing bilayers while varying the buffer salt concentrations, and the consequent domain partitioning[33].

We here report the association, dynamic behavior, hybridization and lift-off of cholesterol-labeled three-dimensional DNA cages on spherically supported lipid bilayer membranes (SSLBMs) formed on silica beads. The anchored cages present two faces: a 'top' accessible face furthest from the bilayer, and a 'bottom' face closest to the bilayer. They can readily load different DNA-fluorophores on their top face and selectively unload each of them upon addition of a specific displacing strand. On the other hand, the bilayer membrane provides a steric barrier for the bottom face of the DNA cages nearest the lipid environment. We introduce a method to control the less sterically accessible bottom face, by using displacing DNA strands that can partially insert into the

bilayer themselves via cholesterol modification. We show the ability to control the orientation of the cages within the bilayer by varying the position and number of cholesterol substituents, thereby tuning enzyme accessibility to the cages. In chemical terms, the spherical bilayer can serve as a versatile and tunable 'protecting group' for DNA nanostructures. Finally, we show the efficient on-bilayer diffusion of DNA cages, as well as their ability to dimerize by hybridization on the lipid bilayer. The resulting dimer prism is doubly anchored to the bilayer. Lifting off one of its two component prisms is not sufficient to release the dimer from the bilayer, however removing both anchored prisms with two displacement strands cleanly released the dimer from the bilayer. The 3D-structures used here are DNA-minimal, fully dynamic and appear to be intimately coupled to the lipid bilayer, rather than floating on its surface. Because of the ease of coupling DNA to other functional materials, this approach has the potential to produce stimuli-responsive protein arrays, molecule-responsive drug releasing biomedical device surfaces, and self-healing materials for optoelectronic or light harvesting applications.

2.3 Results and Discussion

2.3.1 Design of the DNA Cage and Assembly Strategy.

The DNA cages used in these experiments consist of three 96-base DNA strands or 'clips'. Each clip is designed so that it's two 10 base ends are complementary to the back of the next clip, and the third clip is complementary to the back of the first clip. The result is that hybridization of the three strands leads to a closed triangular prism (TP)[34], Figure 2.1 (see Experimental Section 2.5.3). This cage possesses 6 single stranded (ss) 20-base binding regions (green) with different sequences. The top ss regions are used to hybridize to DNA strands carrying fluorescent labels (Cy3, Cy5, and Alexa488), while the bottom face hybridizes to a DNA strand that carries a cholesterol anchor. The result is an amphiphilic 3D- architecture (Figure 2.2).

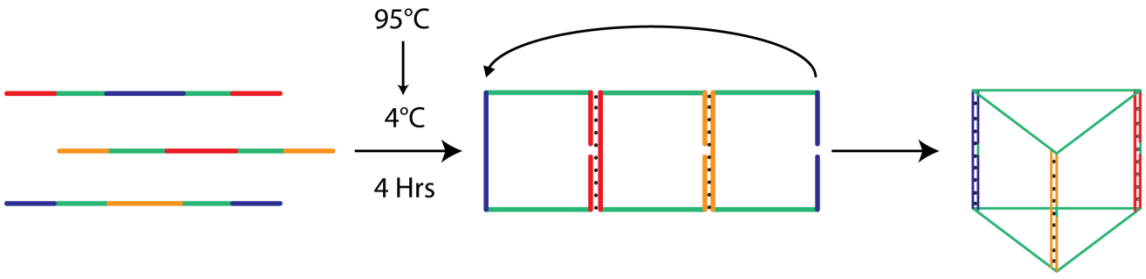

Figure 2.1: Clip-by-clip assembly of TP scaffold.

All short oligonucleotides designed to hybridize to the ss regions of the cage consist of the complementary 20 base region followed by a 6-base extension and chemical modification at either the 5'/3' end (Figure 2.2). The 6-base extension serves as a toehold initiation point for strand displacement of the 26mer DNA-conjugates from the scaffold. In this way, each of the modified DNA strands can be selectively displaced from the prism by the addition of a strand which is fully complementary to the 26-base stretch (Figure 2.2, Panel A).[17] Using this writing and erasing capability, we have compared the binding and removal of functional DNA-conjugates from a prismatic scaffold in solution and within a lipid bilayer environment.

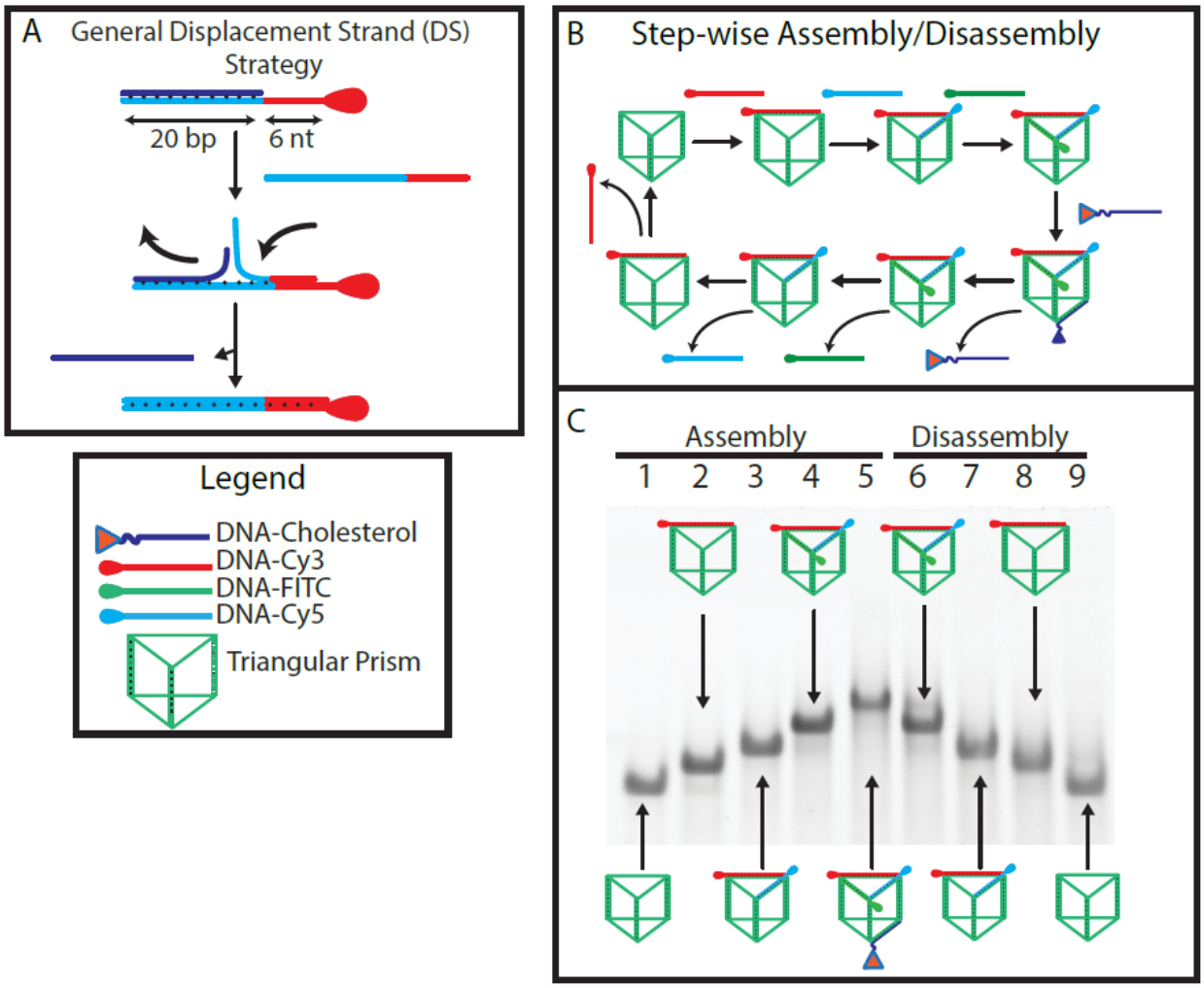

Figure 2.2: Panel A: Schematic representation of the displacement strategy. Panel B: Representation of the stepwise assembly/disassembly on a DNA triangular prism scaffold. Panel C: Non-denaturing polyacrylamide gel electrophoresis showing the stepwise addressability of the triangular DNA scaffold and its disassembly via strand displacement. Lane 1: TP scaffold, lane 2: previous + Cy3, lane 3: previous + Cy5, lane 4: previous + Alexa488 (A488), lane 5: previous + cholesterol anchor, lane 6: previous, displace cholesterol anchor, lane 7: previous, displace A488, lane 8: previous, displace Cy5, lane 9: previous, displace Cy3.

2.3.2 In Solution Hybridization and Displacement of Fluorescent Labels and Cholesterol Anchors on the DNA Cage.

To form the DNA cages, all strands are combined in one pot and annealed from 95 to 10°C, over 4 hours (see Experimental Section 2.5.3). Assembled structures are characterized by native polyacrylamide gel electrophoresis (Figure 2.2, Panel C). Lane 1 shows a single band corresponding to the assembled DNA cage formed using three 96mer strands, indicating that the prism structure is the single major product formed in near quantitative yield. Lanes 2-5 show the sequential hybridization of the ss regions to three fluorescently labeled DNA strands on the top face and a single cholesterol anchor-substituted strand on the bottom face. The band pattern indicates that the addition of each DNA-conjugate is accompanied by a corresponding decrease in gel mobility. This confirms the formation of the 3D triangular scaffold and successful loading of three different fluorescent tags and the cholesterol anchor unit.

Lanes 6-8 represent the sequential displacement of three bound fluorophore-DNA strands and the cholesterol-DNA in solution using four different displacement strands (DS). In each of these experiments, the fully loaded prism scaffold (lane 5) is used and the required DSs are added in three-fold excess relative to the target strand. The mixtures are incubated for 30 minutes at room temperature. The increase in gel mobility seen in lanes 6-9 corresponds to the stepwise formation of the initial ss DNA cage. In this way the fully functional DNA cage can be assembled and then disassembled using the correct series of chemical inputs[35].

2.3.3 Anchoring the DNA Cages on the Lipid Bilayer.

In this study, we use spherically-supported bilayer lipid membranes (SSLBMs) composed of the synthetic phospholipid 1,2-dioleoyl-sn-glycero-3-phosphocholine (DOPC) on 5 μm silica beads, as a model lipid bilayer membrane[36]. Similar lipid bilayer systems have been used as nanovectors[37], for protein screening[38,39], and as artificial supports for inducing functional neural synapse formation[40]. SSLBMs offer many desirable features as biomembrane model systems in comparison to their vesicle counterparts. They have increased mechanical stability and control of particle size and reproducibility. They can also be readily concentrated into a pellet by centrifugation and washed without compromising the membrane integrity. Such manipulations are

highly problematic with the related giant unilamellar vesicles (GUVs)[41]. In comparison to flat supported bilayer membranes, SSLBMs are considerably easier to manipulate and examine using a variety of microscopy and spectroscopy techniques that are not available for substrates with a planar geometry[42,43]. Silica beads are also ideal for interfacing with biological systems due to their chemical inertness and biocompatibility[37,40]. Finally, mesoporous silica particles have been used for finely controlled drug release and have been coupled to lipid bilayer membranes[39].

Solutions of annealed DNA cages with cholesterol anchors (Cholesterol anchor has 20 nucleotide (nt) prism binding region and 6 nt toehold (26 nt version)) are combined with the bilayer coated bead solution in buffer. In general, the sample preparation using a large excess of DNA cages ensures that the beads are completely covered in a homogenous layer of DNA cages as seen in Figure 2.5. After 15 min. of incubation, the beads/DNA are centrifugated to remove any unbound DNA cage or DNA-conjugate (see Experimental Section 2.5.4 for preparation details). The amount of functionalized DNA prism bound to the SSLBMs can be determined through fluorescence intensity quantification of the supernatant solution after prism release from the bilayer (see below, and Experimental Section 2.5.5).

It is determined that 5.9×10^{-13} ($\pm$ 0.2×10^{-13}) mols of labeled TP are lifted off and collected from the surface of the beads. This represents 4% of the initial amount of DNA cage that was incubated with the SSLBMs, therefore there is approximately 6.6×10^{5} labeled TP/bead or 8.4×10^{3} TP/μm^2, based on the size of the SSLBMs. Based on the approximate area of each prism, we predicted 4.7×10^{4} TP/μm^2. This data implies partial but homogenous coverage (see Figure 2.5) of the SSLBM with the DNA cages. The value indicates that the TP structures occupy about 6x more area than our initial prediction. Our calculation assumes a perfect fit of all TPs packed onto the surface; on the bilayer membrane the TPs likely behave as rigid constructs with a random packing which may account for the observed difference.

2.3.4 Confocal Fluorescence Imaging of 3D DNA Constructs and Membrane Mobility.

Figure 2.3 shows a typical confocal fluorescence image of a DNA prism functionalized with a single fluorophore and cholesterol anchor loaded on the DOPC SSLBM. The image shows a homogenous distribution of fluorescence intensity within the SSLBM. A series of control samples served to investigate possible off-target membrane interactions. These controls included partially assembled, fluorescently labeled DNA cages as well as the single-stranded fluorophore-labeled oligonucleotides. In all cases, a measurable and reproducible fluorescence signal is only observed for the fully assembled DNA cage containing both a hybridized fluorophore and cholesterol anchor.

It has been shown that DNA is able to bind to zwiterionic lipid mono/bilayers in the presence of divalent cations[31]. This work has compared the absorption of the DNA structures to a supported lipid bilayer with and without the cholesterol anchors and has determined that although there is some non-specific interactions between the DNA and the lipids, the addition of the cholesterol anchors significantly increases the amount of landed DNA structure. Non-specific binding may also be occurring in our system, but the washing steps during sample preparation minimize this binding. Furthermore, imaging conditions are kept constant for all samples to allow consistent comparison of fluorescent intensities. It should be noted that at higher laser power some residual fluorescence is observed in the bilayer, and that even after our lift-off experiments (Figure 2.5) there remains some residual fluorescence on the SSLBMs. Both of these observations may be attributed to the non-specific binding of DNA to the lipid bilayer.

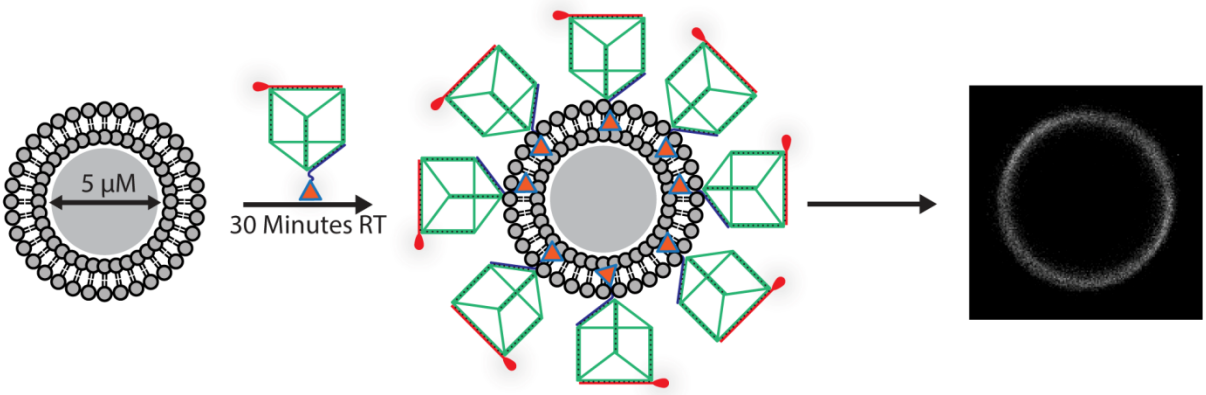

Figure 2.3: Representation of labeled system (left, not shown to scale), a confocal fluorescent image of an SSLBM (right).

The mobility of our prismatic scaffold within the bilayer environment is confirmed using FRAP. Comparative FRAP measurements allow quantification of 2D-diffusion of the DNA cages which are anchored (26 nt version) within the supported lipid bilayers. This involves determining the mobility of a fluorescently-labelled DNA cage anchored via cholesterol into a fluid SSLBM formed from DOPC phospholipids (melting point of −20 °C)[44] and comparing it to the mobility of a fluorescent lipid analog (BODIPY® FL-C5) in DOPC SSLBM (see Experimental Section 2.5.7).

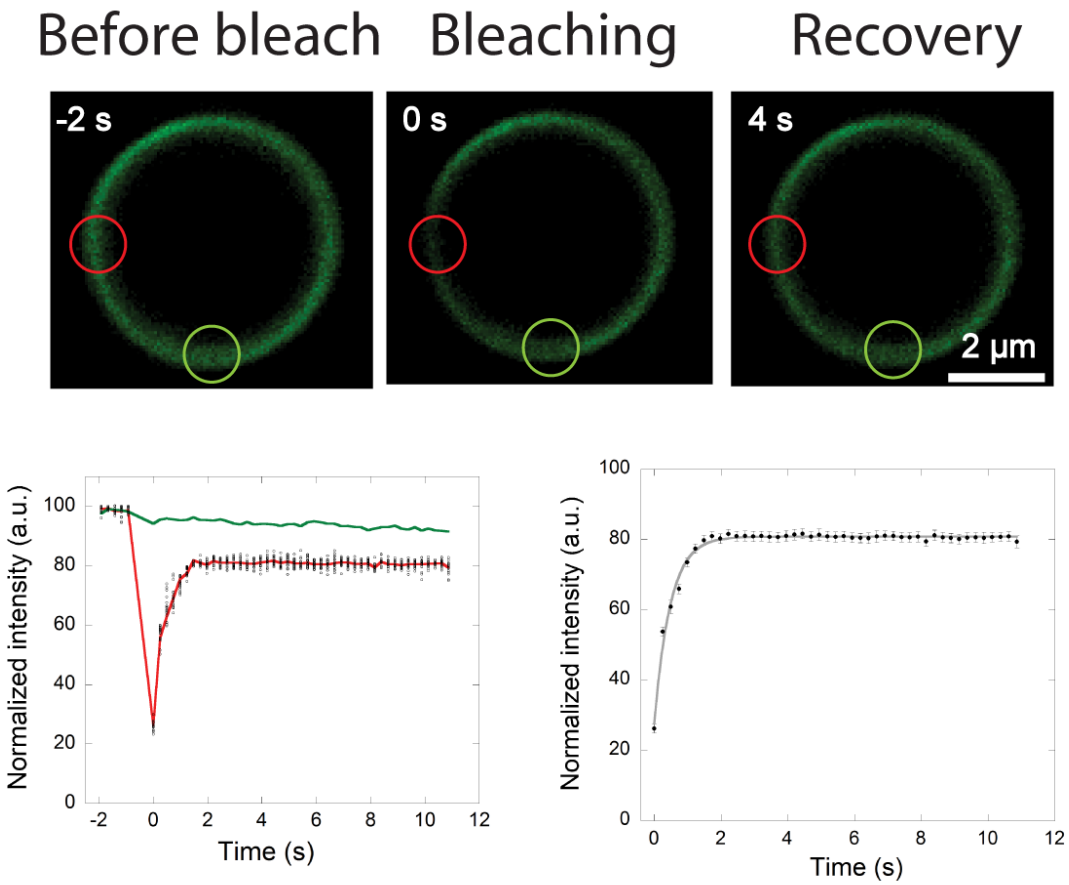

Figure 2.4: FRAP data. (Top) Images of DOPC SSLBMs containing Alexa488 functionalized DNA cages before and after photobleaching a 1.3 µm spot, indicated by the red circle. A reference spot of the same size indicated by the green circle is used to correct for bleaching caused by imaging. (Bottom left) Individual FRAP data from 20 separate experiments, the averaged FRAP curve of the complete data set of 50 separate experiments (red) and the mean reference curve (green). All FRAP data are normalized to the pre-bleaching fluorescence. (Bottom right) The averaged FRAP data (and standard error values) fit to a one diffusing component model (R value of 0.994).

Figure 2.4 shows a FRAP study for DOPC SSLBM containing Alexa488-functionalized DNA cages. Recovery of fluorescence intensity is evident, indicating that the DNA cages are mobile and able to diffuse in and out of the bleached spot on a time scale comparable to the control fluorescent lipid molecules (0.472 s for fluorescent DNA conjugates vs. 0.377 s for fluorescent lipid analogs).

Furthermore, this timescale for fluorescence recovery is in good agreement with previous measurements on labeled SSLBMs[4,43]. The values of diffusion coefficients (D), half-life of fluorescence recovery ($\tau_{1/2}$), as well as a ratio of mobile to immobile species are summarized in Table 2.1.

Table 2.1: Diffusion characteristics of Alexa 488 DNA prism and BODIPY® FL-C5 as measured by FRAP.

	Alexa488 DNA Chol	**BODIPY® FL-C_5**
$\tau_{1/2}$ (s)	0.472	0.377
D ($\mu m^2/s$)	0.802	1.00
Mobile fraction (%)	80.8 +/- 0.2	95.9 +/- 0.3

(1) $\tau_{1/2}$ is the half life of fluorescence recovery. (2) D is the diffusion coefficient. For details on fit model equations and calculations of diffusion coefficient refer to Experimental Section 2.5.7.

For the bleached DNA fluorescent conjugate, an average recovery maximum of 80% of the initial fluorescence intensity is observed (taking into account the bleaching caused by imaging). This could be explained by aggregated cholesterol-anchored DNA cages within the supported bilayers contributing to a population of immobile species. Although slightly lower than some values previously reported diffusion coefficient[4,43,45,46],which range from 0.6 to 3 $\mu m^2/s$ depending on the sample, our measurements of 0.8 and 1 $\mu m^2/s$ for the prism and lipids are very similar. The difference may be related to the supported bilayer system itself and was not the focus of this study. FRAP analysis was performed using the equation for a 2D diffusion model, which is an approximation for a spherical system. This is usually done for giant unilamellar vesicles as they are large enough that the surface is assumed to be close to planar at the molecular level. This assumption may not be the same for our system (5μm diameter beads). However these values are only used for a comparison rather than to report an absolute value. It is therefore more appropriate

to compare the half life of recovery for lipids to that of the DNA structures, because this value is measured directly from our FRAP curve analysis and is not extrapolated from using model equations. Overall, the similar diffusion characteristics of the fluorescent DNA conjugate to those of the fluorescent lipid analog in SSLBMs suggest that they undergo similar diffusion kinetics within the SSLBM system[4,43,45,46].

2.3.5 Stepwise On-Bilayer Hybridization and Strand Displacement from the Top Face of DNA Cages.

Many of the existing examples of DNA rearrangements on supported bilayers rely on temperature or enzymatically induced disassembly to initiate domain formation or component partitioning[3,29]. Strand displacement events on the supported bilayer provides a method to control DNA-mediated membrane interactions using a large number of strand stimuli of different sequences. We thus investigate whether the bilayer anchored DNA cages (26 nucleotide version) are able to undergo toehold-mediated displacement with added DNA strands. First, we examine lift-off of the strands hybridized to the prism face furthest from the bilayer.

To do this, we prepare SSLBMs and anchor the cholesterol substituted DNA prism as above. We add the three DNA-fluorophore strands (Cy3, Cy5, and Alexa488) sequentially to the bound prisms, each time incubating for 15 min, washing the beads and then collecting them by centrifugation. Figure 2.5 summarizes the confocal fluorescence images collected after each addition. Rows A to F in Figure 2.5 show that the DNA cage can be readily hybridized on the supported bilayer membrane to all three of the fluorescent DNA-labels in a stepwise fashion. Confocal images following each incubation step show a homogenous fluorescent distribution on the bilayer. Overlay images for the sequential labelling additions, show co-localization at each step for all fluorophores. This confirms that each prism is able to readily bind several components while associated with a lipid bilayer environment.

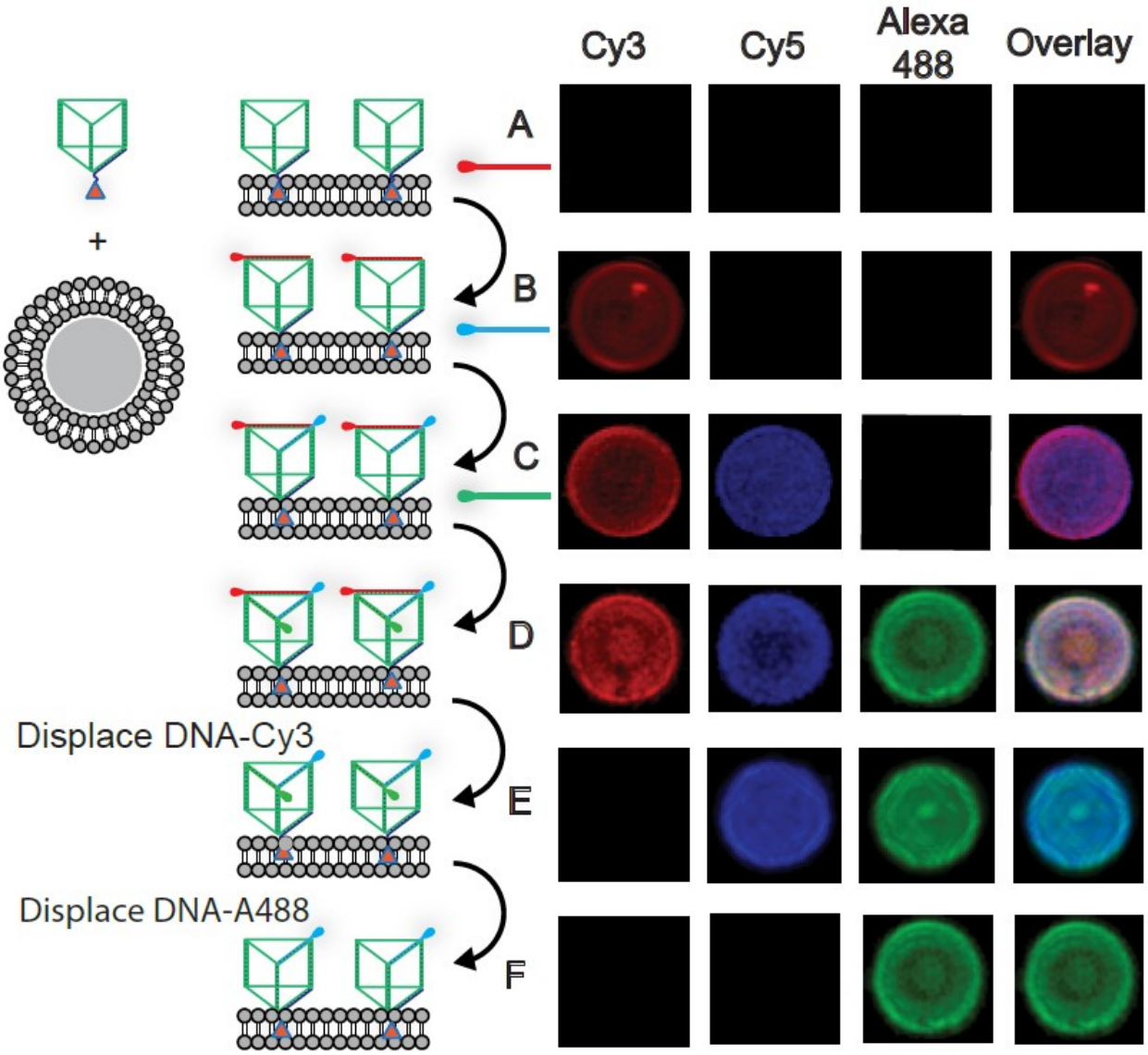

Figure 2.5: Confocal monitoring of the bilayer during the stepwise assembly and disassembly of the embedded triangular scaffold. Images are Z-stacked 2D images showing the 3D homogenous morphology of the SSLBMs. Row (A), addition of prism, row (B) Cy3 addition to anchored prisms, row (C) addition of Cy5, row (D) addition of Alexa488, row (E) addition Cy3 displacing strand, row (F) addition of Cy5 displacing strand. Steps A-D represent the assembly; steps E and F represent the disassembly.

We then add the displacement strands to remove the fluorophore labelled oligonucleotides sequentially from the embedded scaffold, as described above. Row E corresponds to the addition

of the displacement strand for the DNA-Cy3 component, to the Cy3/Cy5/Alexa488 labelled prisms on the bilayers, followed by washing and centrifugation cycles. Row F corresponds to the same experiment with the displacement strand for the DNA-Cy5 component. Addition of the displacement strand results in the removal of the fluorophore from the anchored DNA cage and complete loss of the fluorescence signal for each corresponding targeted DNA-label. Following removal of the two fluorophores Cy3 and Cy5, only the single Alexa488 fluorophore is observed on the SSLBM surface. This demonstrates that the top face of the DNA cage remains reversibly addressable while incorporated within a SSLBM. Thus, functional components can be organized and selectively lifted off DNA cages anchored on bilayer membrane surfaces.

2.3.6 Strand Displacement from the Bottom Face of DNA Cages.

Displacement of the cholesterol anchor and subsequent release of the entire DNA cage from the SSLBM surface is examined using a 6 bp toehold region on the DNA-cholesterol strand. This strand displacement would need to occur from the bottom face of the prism which is closest to bilayer, as shown in Figure 2.6. A triangular prism with a single DNA-Cy5 and a single DNA-cholesterol anchor was incorporated into the SSLBM as described above.

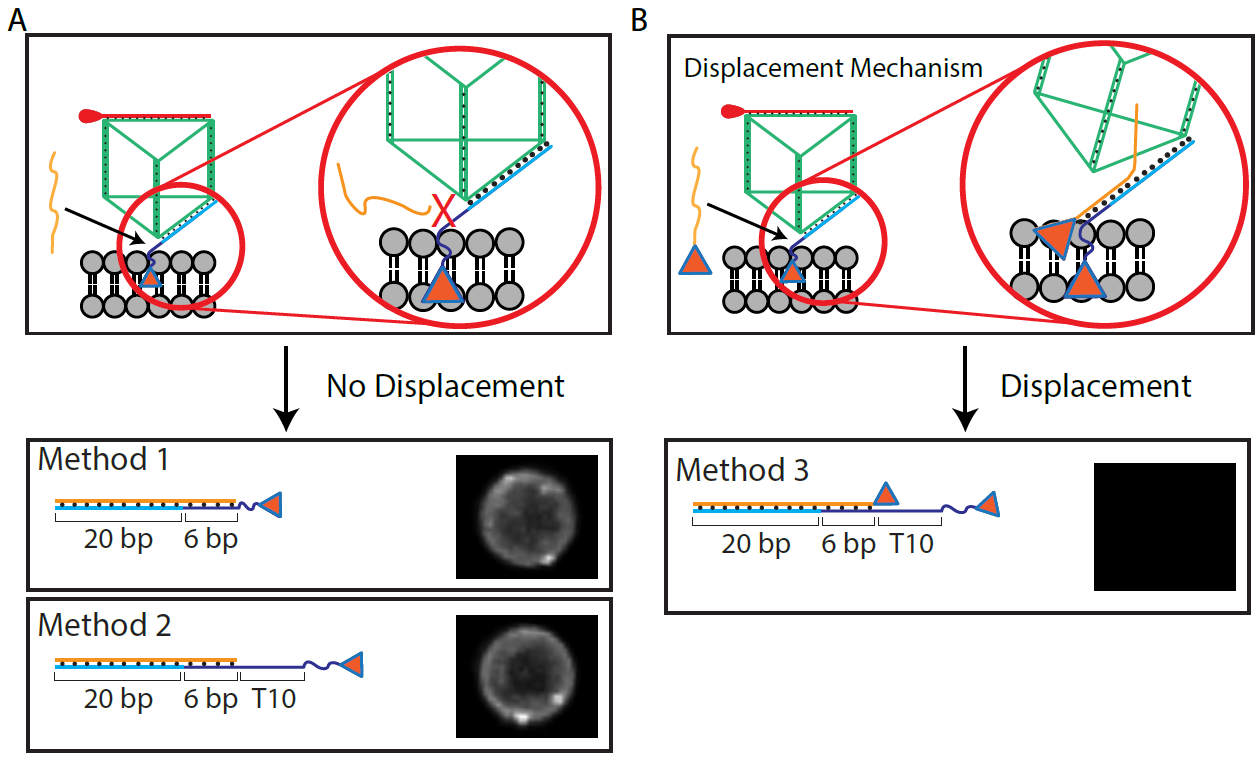

Figure 2.6: (A) Top, toehold displacement strategies for bottom face strand (triangle represents cholesterol molecule). Bottom, design of toeholds: Method 1, the cholesterol labeled strand has a 6 base toehold closest to the cholesterol molecule, Method 2, the cholesterol labeled strand has an additional polythymidine (T10 spacer version) between the toehold and cholesterol units. The erasing strand (orange) is unsubstituted. (B) Top, in-bilayer toehold displacement strategy for bottom face strand. The erasing strand (orange) has a cholesterol unit (triangle), allowing it to anchor itself in the bilayer and gain access to the bottom face. Bottom, composition of toehold and erasing strand.

Our initial strategy (method 1, Figure 2.6A) involves addition of an erasing strand fully complementary to the cholesterol-DNA (26nt version) strand for 30 min, followed by washing. However, confocal images of the beads following this step display unchanged fluorescence intensity. This suggests that the six-base toehold is inaccessible to the displacing strand as it is located directly on the cholesterol anchor, which is embedded within the lipid bilayer. The displacement strand itself can effectively remove the DNA-cholesterol from the prism in solution, as confirmed by native PAGE in Figure 2.2 lane 6.

In a second attempt, we use a DNA-cholesterol anchor containing a polythymidine (T10 version) spacer between the cholesterol unit, and the toehold/binding region (Fig. 2.6A, method 2), in order to distance the toehold from the membrane cholesterol anchor. This modification however yields similar results and the SSLBMs retained their original fluorescence intensity, indicating that the T10 extension is insufficient to increase the toehold accessibility.

A third strategy (Figure 2.6B method 3) proved to be successful. This involves the use of a displacing strand that is itself functionalized with cholesterol, such that it is able to bind to the bilayer, and possibly achieve closer access to the bottom face of the prism. After addition of this cholesterol-DNA strand and washing, SSLBMs with functionalized DNA prism exhibit near complete loss of fluorescence. This confirms that the erasing strand is now able to diffuse into the bilayer, find its complementary binding region and release the entire DNA assembly from the lipid bilayer surface (see below for analysis of the supernatant). Although displacement strategies have previously been used for removal of target strands in a DNA assembly, to our knowledge, this is the first example of a displacement strategy used within a lipid bilayer system to successfully release a 3D DNA cage. This strategy can not only be used for positioning and control of specific membrane components but could be extended to dynamically and selectively release any DNA macro-assemblies that are anchored on a lipid bilayer.

2.3.7 Enzyme Accessibility of DNA Cages on Bilayers.

Biological applications using DNA cages assembled on supported bilayers are most likely to involve membrane protein interactions. In order to determine if the DNA scaffolds embedded within the SSLBMs are accessible to enzymatic processing, DNase I, a non-specific nuclease is added to a solution of prisms anchored (T10 spacer version) on this bilayer (30 min followed by washing).

Figure 2.7 summarizes the results for this assay. Column 1 represents confocal microscopy images of a standard DNA-bead solution before the addition of the nuclease, to confirm homogenous fluorescent labeling. Column 2 is an image of the same DNA-bead solution containing prisms anchored via the T10 extended cholesterol anchor (see Figure 2.6), incubated with DNase I. This

image shows complete loss of the fluorescence signal, indicating that DNase I is able to interact and digest the membrane bound DNA cages. This is in good agreement with similar studies involving fluorescently labeled duplex DNA constructs.[27]

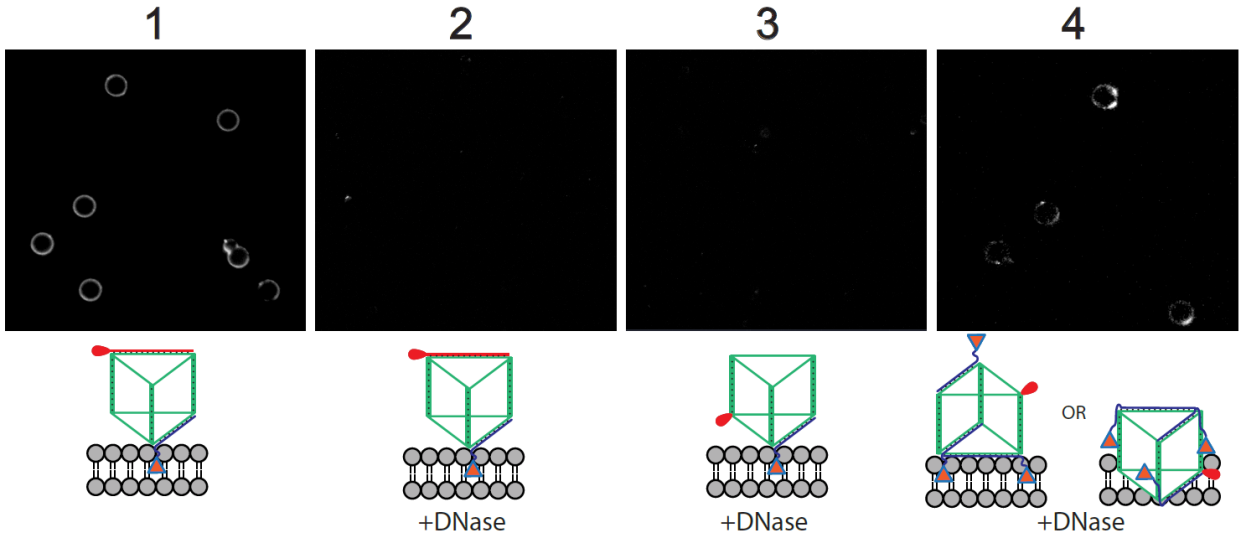

Figure 2.7: Confocal fluorescent images of the bilayer anchored triangular prism scaffold following DNase I incubation. Column: **1**-hybridized Cy3 label on top face of prism (no DNase I), **2**-hybridized Cy3 label on top face of prism + DNase I, **3**-Cy3 label as an internal strand modification on bottom face of prism + DNase I, **4**-Cy3 label as an internal strand modification + 3-Cholesterol anchors on the top and bottom faces of prism + DNase I. This last construct is expected to be more closely associated with the bilayer with variable morphologies (see above figure column 4), which limits its accessibility to nucleases.

To determine if only the topmost label binding region of the DNA scaffold is accessible for enzymatic degradation, we assemble a DNA prism containing an internalized Cy3 label, which is oriented on the bottom face of the prism and on the same side as the cholesterol-DNA anchor (T10 spacer version). Following the enzyme treatment, loss of fluorescence is also observed (Figure 2.7 column 3), which confirms that indeed the lower portion of scaffold (that is inaccessible to displacement strands, see Figure 2.6) is being digested and not just the hybridized top label.

Lastly (Fig. 2.7, column 4), the labeled scaffold was again used. However it is functionalized with 3 cholesterol anchoring units (T10 spacer version), two positioned on the bottom and one positioned on the top face. This arrangement of cholesterol units can potentially generate orientations which increasingly bury the DNA scaffold within the membrane, rendering it less accessible to nuclease degradation. There remains a significant amount of fluorescence intensity associated with the bilayer following enzyme incubation (Fig. 2.7, column 4), although it is slightly reduced when compared to the control sample. This indicates that the DNA construct is now only partially accessible to nuclease degradation. Future work will examine the orientation and penetration depth of the DNA cage within the bilayer.

The modular nature of the DNA cage construction demonstrated here allows for orientational control of the cholesterol units on this scaffold. In turn, this control can be used to tune the position of the DNA cage either on the bilayer surface or deeper within the bilayer. Thus, cages can be more or less accessible to proteins based on their substitution patterns. This may also affect their ability for cellular internalization, when used as drug or oligonucleotide delivery vehicles.

2.3.8 In Solution Dimerization of Prism Scaffolds.

To expand the DNA/SSLBM technology for biological and materials applications that require patterning or clustering of these cages on the bilayer, we investigate the reversible dimerization of the DNA cages associated with the bilayer environment. In this regard, we create two prisms (TP-A and TP-B), one functionalized with Cy3 and the second with Cy5 (Figure 2.8, Panel A). Each prism is designed to hybridize a strand containing a 15 nt overhang sticky-end, such that an added linking strand can dimerize the two prisms through the overhang components. The linking strand used hybridizes each 15 nt overhang, and contains a 5 nt toehold allowing for its dynamic removal from the assembly and consequent dimer dissociation. Each prism is labelled with a unique DNA-cholesterol anchor (T10 spacer version) on the opposite face, and these anchors also contain overhang sequences. Thus the prisms can individually be removed from the bilayer by using specific displacement strand inputs.

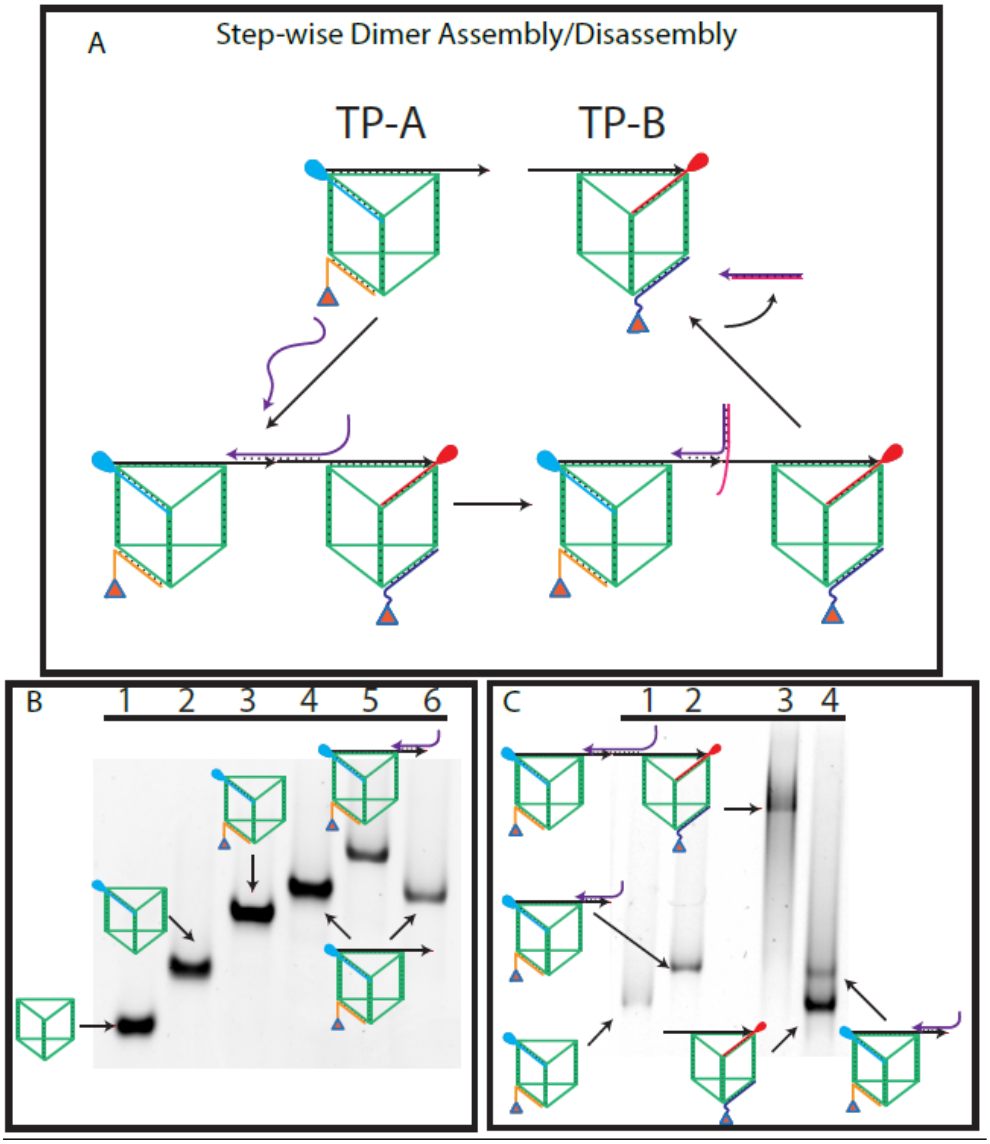

Figure 2.8: (A) Representation of the step-wise dimer assembly/disassembly. (B) Native PAGE results showing the stepwise loading of the scaffold; lane 1: TP, lane 2: previous + Cy5 (blue), lane 3: previous + cholesterol anchor (yellow), lane 4: previous + overhang sticky-end (black), lane 5: previous + linking strand (purple), lane 6: previous displace the linking strand. (C) Native PAGE showing step-wise dimer assembly/disassembly; lane 1: TP-A + Cy5 + cholesterol anchor + overhang, lane 2: TP-B + Cy5 + cholesterol anchor + overhang + linking strand, lane 3: samples in lane 1 and 2 are combined to form the dimer (12 hrs RT), lane 4: previous + linker displacement to recover monomers.

Figure 2.8, Panel B shows the stepwise assembly of all components on the DNA scaffold. Lanes 2, 3, and 4 show the corresponding decrease in gel mobility as the fluorescent tag, cholesterol anchor, and the overhang strand providing the sticky-end are assembled on one of the prisms (TP-A). Lanes 5 and 6 show the addition and consequent displacement of the final linking strand in solution on TP-A (TP-B assembles with the same efficiency, data not shown). In solution, dimerization of TP-A and TP-B is demonstrated in Figure 2.8, Panel C, in which TP-A, pre-functionalized with all components including the linking strand (lane 1), is combined with TP-B which is also pre-assembled with all necessary strands except the linking strand (lane 2). Lane 3 represents the dimerization of these two structures following 12 hours of incubation at room temperature and shows a band with a corresponding decrease in gel mobility. The linker displacement strand is then added to the assemblies in 2.5 equivalents leading to recovery of the initial starting components, as seen in lane 4 by the two bands with comparable mobility to lanes 1 and 2. The diffuse bands in this gel likely arise from lower dimerization efficiency of the two prisms in solution and/or partial dissociation of the TP dimer as it moves down the gel.

2.3.9 Dimerization and Lift-Off of the Prisms on the Bilayer.

SSLBMs in these experiments are prepared by combining a 1:1 mixture of TP-A (Cy5-labeled) and TP-B (Cy3-labeled) and anchoring them together on the beads. Figure 2.9B, row 1 shows representative confocal microscopy images of the beads in the two Cy3/Cy5 fluorescent channels.

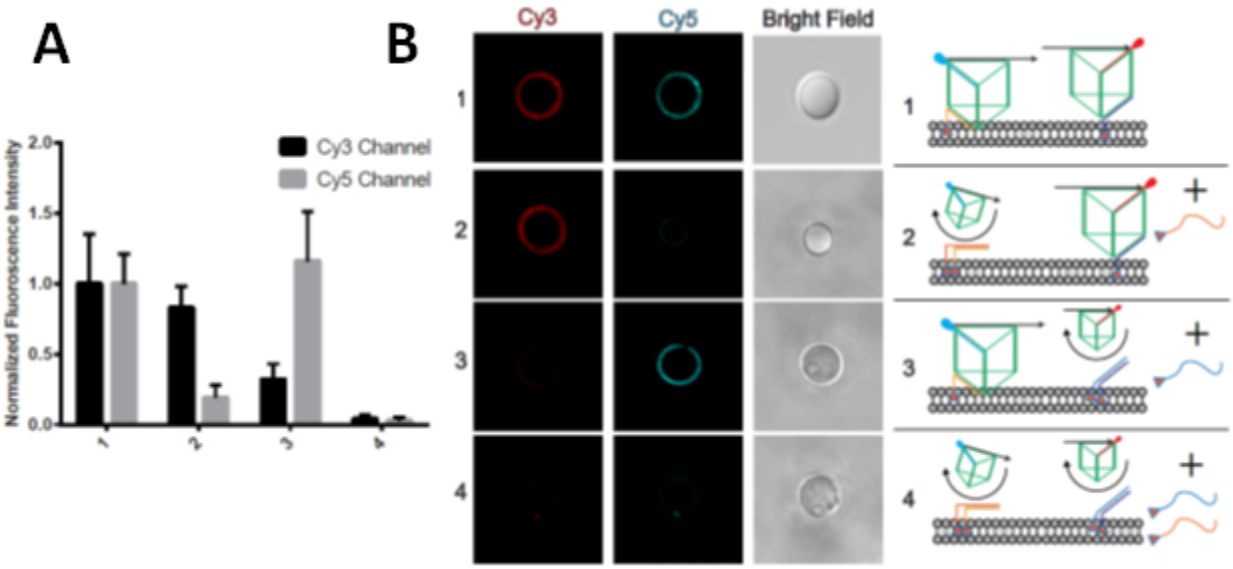

Figure 2.9: (A) Normalized fluorescence intensity measurements for rows 1 to 4 from Figure 2.9B. (B) Confocal fluorescent images of individual prism bilayer lift-off in a mixed prism population: Row 1-Control sample TP-A(Cy5) + TP-B(Cy3) no linker, Row 2-Displace TP-A (Cy5), Row 3-Displace TP-B (Cy3), Row 4-Displace both prisms.

Initial experiments confirm that each individual prism population can be addressed within this mixed prism bilayer. In Figure 2.9B row 2, the cholesterol-labeled displacement strand for prism TP-A is added, and the images show bead fluorescence only in the Cy3 channel, consistent with TP-A removal. Row 3 shows the selective lift-off of prism TP-B and disappearance of the Cy3 fluorescence. Finally in row 4 both of the displacement strands are added and we observe complete loss of fluorescence as both of the prism groups are released from the bilayer surface. Analysis of the fluorescence intensity of the beads, as monitored during the displacement and prism removal events are shown in Figure 2.9A, and correlate with the captured images.

We then add an equimolecular amount of linking strand to these SSLBMs in order to induce prism dimerization (Figure 2.10, row 1). Successfully dimerized prisms should contain 2 cholesterol anchor points to the bilayer. If only a single DNA-cholesterol anchor is displaced, the remaining anchor may continue to hold the assembly on the bilayer. Figure 2.10 rows 2 and 3 show the results of performing a single anchor displacements on the dimerized DNA cages. When either

TP-A or TP-B is addressed with its specific anchor displacement strand, we see that the beads remain fluorescent in both label channels. Quantitative analysis, Figure 2.11, carried out for sample populations of at least 50 beads shows that the ratio of Cy3:Cy5 fluorescence is maintained, in agreement with the continued presence of the prism dimer that is now singly anchored.

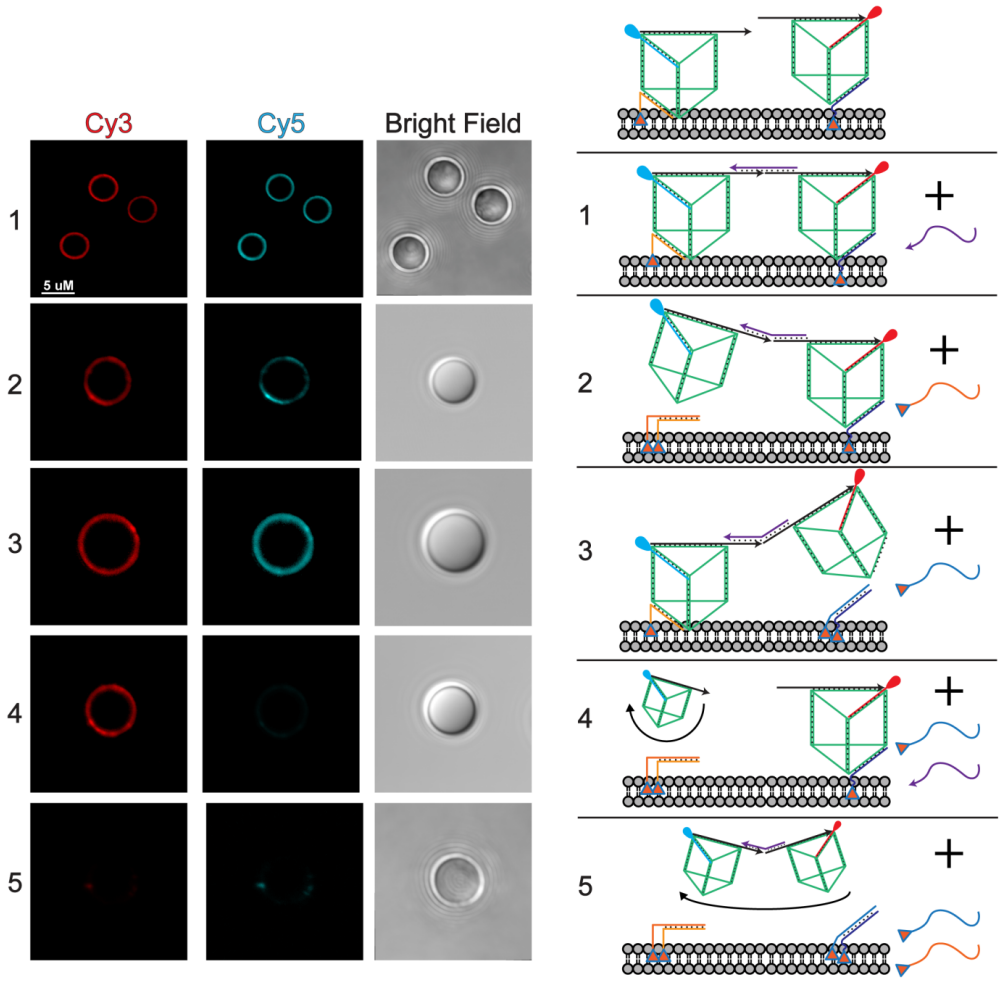

Figure 2.10: Confocal fluorescent images of dimerization and lift-off of the prisms on the bilayer: 1- Control sample TP-A(Cy5) + TP-B(Cy3) with linker, 2-Displace TP-A (Cy5), 3-Displace TP-B (Cy3), 4-Displace TP-B (Cy3) and add the linker displacement strand to break the dimer, 5-Displace dimer prisms by adding both cholesterol erasing strands.

If the resulting prism dimer is singly anchored, then addition of the linker displacement strand should dissociate it into the two prism monomers, thus liberating the non-anchored prism component, which can be removed upon washing. Figure 2.10 row 4 shows the reaction sequence in which the anchor of TP-A is first displaced, followed by linker displacement. Indeed, only the Cy3 fluorescence for TP-B remains on the beads, consistent with dissociation of the prism dimer into monomers and removal of TB-P after washing.

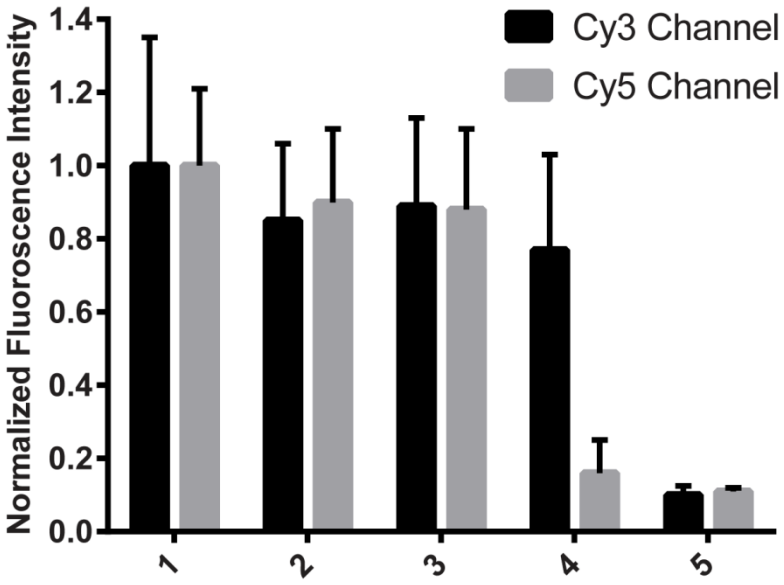

Figure 2.11: Normalized fluorescence intensity measurements for rows 1 to 4 from Figure 2.12.

The dimerized prism can only be lifted off into the supernatant when DNA-cholesterol anchor displacement strands for both component prisms are added (Figure 2.10 row 5). Quantitative analysis shows only a residual (10%) fluorescence remaining on the beads in either Cy3 or Cy5 channels (Figure 2.11). The supernatant was collected after bead centrifugation. PAGE analysis indeed reveals the formation of a prism dimer, which can be separated into the two prism monomers upon displacement of the linking strand.

Following the removal of our dimerized product (Figure 2.10, row 5) the supernatant was collected and analyzed using fluorescence scanning of PAGE (Figure 2.12, lane 9). Lanes 1-3 and 4-6 in

Figure 2.12 correspond to the fluorescently labeled respective prism populations, TP-A (Cy5 blue) and TP-B (Cy3 red). Dimerized prism assemblies, lanes 7-10, therefore appear as pink bands indicative of prism co-localization. This analysis is complicated by the fact that after multiple washing-centrifugation cycles, the supernatant contains some non-gel penetrating components (possibly some cholesterol-DNA anchors that have formed micellar aggregates), which may also affect the gel mobility of the other DNA components. Nevertheless, a diffuse band in the region associated with the prism dimer is apparent (lane 9), and this dimer band disappears after displacement of the linking strand, with concomitant appearance of the monomeric prism, lane 10. We carried out a control experiment, in which we generated a similar prism dimer in solution under the same conditions as the bilayer dimerization (1 hour at room temperature). A parallel dimer band which reverts to monomers upon displacement of the linking strand is observed, Figure 2.12 lanes 7, 8 with solution dimerization. Thus, gel analysis of the supernatant provides additional evidence for on-bilayer dimerization of the prisms and removal when two anchor displacement strands are added.

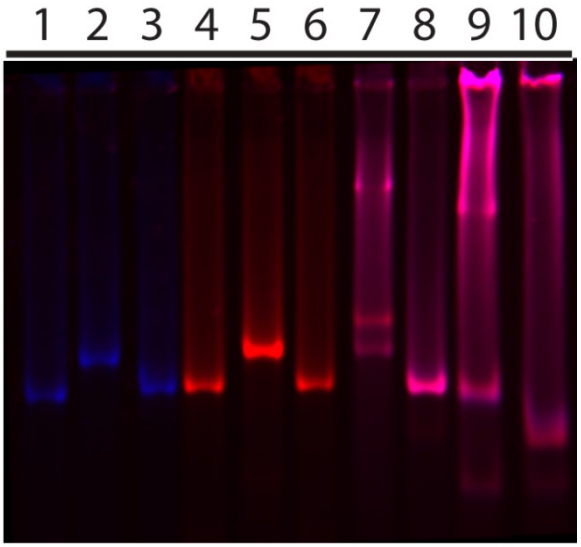

Figure 2.12: Lane 1: represents fully loaded TP-A (Cholesterol anchor, Cy5 tag, and sticky-end overhang), lane 2: addition of the linker, lane 3: displacement of the dimerizing linker strand on a TP-A, lane 4: TP-B (Cholesterol anchor, Cy3 tag, and sticky-end overhang), lane 5: addition of the linker to TP-B, lane 6: displacement of the dimerizing linker strand on TP-B. Lane 7: in solution dimerization of TP-A and

TP-B following addition of the linker strand, lane 8: dimer disassembly following displacement of the linking strand. Lane 9: on bilayer dimerization of TP-A and TP-B following addition of the linker strand, lane 10: dimer disassembly on bilayer following displacement of the linking strand.

2.4 Conclusion

These experiments show that amphiphilic DNA cages can retain their dynamic behavior when associated with a supported bilayer membrane environment. The anchored DNA cage can load and selectively unload three different DNA-fluorophores on its top face via strand displacement. On the other hand, displacement of the cage from the bottom prism face requires functionalization of the erasing strand with a cholesterol group. This addition renders the erasing strand more soluble within the bilayer. It is thus able to adopt a favorable orientation with which to access the toehold region for displacement.

The DNA scaffolds are also tunable in terms of their orientation within a bilayer environment. This parameter is controlled by positioning multiple cholesterol anchors on the two faces of the DNA cage, thus changing its orientation within the SSLBMs. The resulting embedded cages are less susceptible to DNase I degradation, suggesting that access of anchored cages to proteins is tunable through site-specific modification of the cages themselves. This finding introduces new strategies to protect DNA cages from protein binding and nuclease degradation, when used in drug delivery applications.

Finally, we demonstrate the successful association of two different prisms by hybridization on-bilayer. The resulting dimer prism can only be released from the bilayer when both of its anchored prisms components are displaced, and stays associated with the bilayer if only one of its components is displaced.

The DNA cage used here is the simplest 3D object that we can form via our clip-by-clip assembly.[30] We show that this 3D-assembly method is highly modular, allowing us to combine up to eight clipping strands into octameric prisms, which contain 16 asymmetric ss regions available for hybridization with various DNA conjugates (unpublished material). Unlike DNA origami

constructs, the DNA cages appear to be intimately coupled to the lipid bilayer, which sterically blocks access to one or more of their sites. This will have interesting consequences on their ability for tunable cellular penetration and protein binding.

Overall, this approach allows stable association of DNA cages with lipid bilayers, thereby controlling their orientation and accessibility within the membrane. The bilayer has also been used to template the dimerization of DNA cages and these assembled structures can be selectively released and collected for analysis. These events will potentially allow programmable dynamic control of protein binding, cell signaling, drug delivery, and optical properties on lipid bilayers using a modular, easy to construct and DNA-economic methodology.

2.5 Experimental Section

2.5.1 General Information

Gel Red™ was purchased from VWR. Acetic acid, tris(hydroxymethyl)-aminomethane (Tris), and urea were used as purchased from Aldrich. Acetic acid and boric acid were purchased from Fisher Scientific and used without further purification. Nucleosides (dA, dC, dG and T) and universal 1000Å LCAA-CPG supports with loading densities between 25-40 μmol/g and reagents used for automated DNA synthesis were purchased through Bioautomation Corporated. Size-exclusion columns (sephadex G-25, DNA grade) were purchased from Glen Research. 1×TAMg buffer is composed of 45 mM Tris and 12.6 mM $Mg(OAc)2{\cdot}6H_2O$. The pH of the 1×TAMg buffer was adjusted to 8 using glacial acetic acid.

2.5.2 Synthesis of Oligonucleotides and Modified DNA Conjugates.

Standard automated oligonucleotide phosphoramidite solid-phase synthesis was performed on a Mermade MM6 synthesizer from Bioautomation. Gel electrophoresis experiments were carried out on an acrylamide 20 × 20 cm vertical Hoefer 600 electrophoresis unit. Annealing of all structures was conducted using an Eppendorf Mastercycler Pro. DNA quantification was performed using a BioTek Synergy HT microplate reader.

All fluorescent labels, terminal amines and cholesterol modifications are purchased from Glen Research (with the exception of Alexa488) and used directly in manual off-column phosphoramidite coupling reactions or as ready to use pre-functionalized controlled pore glass (CPG) columns from which the oligonucleotide can be directly grown. The three fluorophores used to label oligonucleotides are the cyanine derivatives Cy3 and Cy5, and Alexa488. These dyes are chosen for their well separated excitation and emission spectra. Cy3 and Cy5 are manually inserted at the 5' position of the 26mer DNA strands. Alexa488 is purchased from Life Technologies as a succinimidyl ester (NHS ester), and coupling to DNA proceeds via an amine handle which is inserted at the 3' end of the DNA strand. The 3' cholesterol modification is available as a pre-functionalized CPG column while the 5' cholesterol is manually added as a phosphoramidite through off-column coupling procedures. All samples are purified and characterized using denaturing polyacrylamide gel electrophoresis (PAGE). Quantification of DNA and DNA-conjugates is performed using UV absorbance measurements at 260 nm.

DNA synthesis is performed on a 1 μmole scale, starting from a universal 1000 Å LCAA-CPG solid-supports. Coupling efficiency is monitored after removal of the dimethoxytrityl (DMT) 5′-OH protecting groups. The two cyanine derivatives Cy3™ and Cy5™, the cholesterol (Chol), and amine (NH) phosphoramidites, as well as the cholesterol modified CPG, are purchased from Glen Research. Cy3, Cy5, and NH phosphoramidites are initially diluted with acetonitrile (ACN) to a concentration of 0.1 M in a glove box. For DNA couplings, approximately 10-fold excess of each phosphoramidite is used in comparison to DNA. For off-column couplings, an equal volume of ethylthiotetrazole (0.1M in acetonitrile, Glen Research) is combined with each phosphoramidite and manually coupled on the DNA solid support with an extended reaction time of 15 minutes. After coupling, supports are removed from the glove box and returned to the DNA synthesizer for oxidation, capping and deblock steps. The cholesterol phosphoramidite is coupled in a similar fashion, however this compound was initially dissolved in dichloromethane (DCM). All sequences, modified and unmodified, are fully deprotected in concentrated ammonium hydroxide (60 oC/12 hours). The Alexa488™ modification is used as a succinimidyl ester (NHS ester), and coupling to the amine modified oligonucleotide is performed post synthesis and purification as per supplier protocols.

Table 2.2: Oligonucleotides prepared via solid-phase synthesis. The TTTT represents a short non-base pairing spacer that is inserted within each strand and serves as the vertices of the assembled 3D structures. Non-nucleoside phosphoramidites Cy3™, Cy5™, Chol, and NH/Alexa488™ are inserted selectively into individual sequences as indicated.

Number	Name	Sequence (5′ → 3′)
1	**DP1**	TCGCTGAGTATTTTGCCTGGCCTTGGTCCATTTGTTTTGCAAGTGTGGGCAC GCACACTTTT CGCACCGCGACTGCGAGGACTTTTCACAAATCTG
2	**Pol7-DP3**	CACTGGTCAGTTTTCCACCAGCTAGATGTTGAAGTTTTTACTCAGCGACAGA TTTGTGTTTT CGCTCTTCTATACTGGCGGATTTTGGTTTGCTGA
3	**HA4**	CCACACTTGCTTTTGTCGACACAGTAGCAGTGTGTTTTCTGACCAGTGTCAG CAAACCTTTTCCATGACGATGCACTACATGTTTTGTGTGCGTGC
4	**Pol1-DP3Top-DP1Bot**	TCGCTGAGTATTTTCCACCAGCTAGATGTTGAAGTTTTGCAAGTGTGGGCAC GCACACTTTTCGCACCGCGACTGCGAGGACTTTTCACAAATCTG
5	**Pol4-Int.Cy3-DP3**	CCACACTTGCTTTTCCACCAGCTAGATGTTGAAGT-**Cy3**-TTCTGACCAGT GTCAGCAAACCTTTTCGCTCTTCTATACTGGCGGATTTTGTGTGCGTGC
6	**Pol1-(TOP-(DP1BOT)-BOT-(DP3BOT)**	TCGCTGAGTATTTTCGCACCGCGACTGCGAGGACTTTTGCAAGTGTGGGCA CGCACACTTTTCGCTCTTCTATACTGGCGGATTTTCACAAATCTG
7	**Pol7-(TOP-(DP1TOP)-BOT-(DP3BOT)**	CACTGGTCAGTTTTGCCTGGCCTTGGTCCATTTGTTTTTACTCAGCGACAGA TTTGTGTTTTCGCTCTTCTATACTGGCGGATTTTGGTTTGCTGA
8	**DP1-Top-Alexa488**	CAAATGGACCAAGGCCAGGC-**NH- Alexa488**

9	**DP3-Top-Cy5**	**Cy5**-CTTCAACATCTAGCTGGTGGTCTTGA
10	**HA4-Top-Cy3**	**Cy3**- CTCTAGCACACTGCTACTGTGTCGAC
11	**DP1-Bot-Chol**	GTCCTCGCAGTCGCGGTGCGAGTTGA-**Chol**
12	**DP1-Bot-Chol-T10**	GTCCTCGCAGTCGCGGTGCGAGTTGATTTTTTTTTT-**Chol**
13	**DP3-Bot-Chol-T10**	CTTCAACATCTAGCTGGTGGTCTTGATTTTTTTTTT-**Chol**
14	**DS- DP1-Top-Alexa488**	TCTAGTGCCTGGCCTTGGTCCATTTG
15	**DS- DP3-Top-Cy5**	TCAAGACCACCAGCTAGATGTTGAAG
16	**DS- HA4-Top-Cy3**	GTCGACACAGTAGCAGTGTGCTAGAG
17	**DS- DP1-Bot-Chol**	TCAACTCGCACCGCGACTGCGAGGAC
18	**DS- DP1-Bot-Chol**	**Chol**-TCAACTCGCACCGCGACTGCGAGGAC
19	**DS-DP3-Bot-Chol**	**Chol**-CGGATTCGCTCTTCTATACTGGCGGA
20	**DP1-3'over**	CAAATGGACCAAGGCCAGGC CTGATAGCAGCTCGT
21	**DP1-5'over**	ACCAGTCGATGTACGCAAATGGACCAAGGCCAGGC
22	**DP1-Linker**	TGACCACGTACATCGACTGGTTTTACGAGCTGCTATCAG

23	**DP1-Linker Comp**	CTGATAGCAGCTCGTAAAACCAGTCGATGTACGTGGTCA

All 96mer crude products are purified on an 8% polyacrylamide/8M urea polyacrylamide gel (PAGE; up to 20 OD260 of crude DNA per gel) at constant current of 30 mA for 2 hours (30 min. at 250V followed by 1.5 hr at 500V), using the 1x TBE buffer. Following electrophoresis, the gels are placed on a fluorescent TLC plate wrapped in plastic wrap and illuminated with a UV lamp (254nm). The bands are excised, and the gel pieces are crushed and incubated in 12 mL of sterile water at 60 ºC for 12-16 hours. Samples are then dried to 1 mL, desalted using size exclusion chromatography (Sephadex G-25 columns, Glen Research), and quantified (OD260) using UV-Vis spectroscopy. Smaller strands (<50 base pairs) are purified using a 15% PAGE mixture and running conditions of 30 min at 250V followed by 45 min at 500V, followed by the same work up.

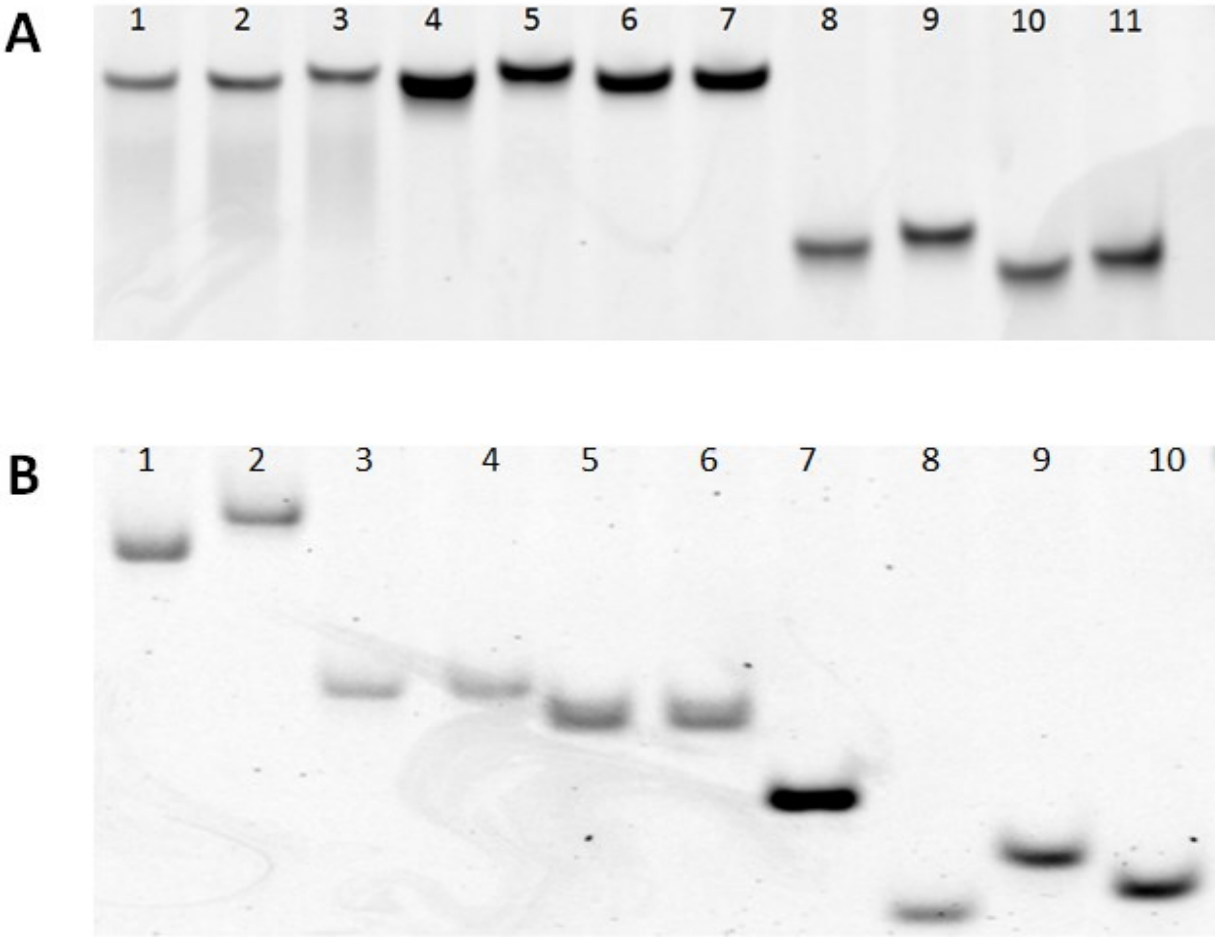

Figure 2.13: Denaturing PAGE Analysis of synthesized oligonucleotides. (A) Denaturing PAGE (8%, 1xTBE) gel ran for 30 minutes at 250V and then 1 hr at 500 V; Lane 1-1, Lane 2- 2, Lane 3- 3, Lane 4- 4, Lane 5- 5, Lane 6- 6, Lane 7- 7, Lane 8 – 20, Lane 9- 21, Lane 10- 22, Lane 11- 23. (B) Denaturing PAGE (12%, 1xTBE) gel ran for 30 minutes at 250V and then 1 hr at 500 V; Lane 1-12, Lane 2-13, Lane 3-18, Lane 4-19, Lane 5-10, Lane 6-9, Lane 7-8, Lane 8-15, Lane 9-15, Lane 10-16, Lane 11-17.

2.5.3 Assembly and Characterization of 3D DNA Cages

In general, equimolar amounts of each of the three scaffold clip strands (1 – 3) are combined in 1xTAMg buffer at a final 3D concentration of 0.250 μM. Functional strands (fluorescent tags and cholesterol anchors) are added in slight excess of 1:1.2 equivalents to ensure full loading of the

cage structure. Samples are then subjected to an annealing protocol whereby strands are brought to 95 ºC for 5 minutes and cooled back to 4 ºC over 4 hours. Regions of symmetry are introduced for binding of multiple DNA-cholesterol conjugates for the enzyme accessibility experiments using the clipping strands numbered 4, 6, and 7 (Table 2.2). These modified clipping strands are added as necessary for organization of up to 3 cholesterol functionalized strands. Clipping strand 5 contains an internalized Cy3 positioned within a vertex region for the enzyme accessibility experiments.

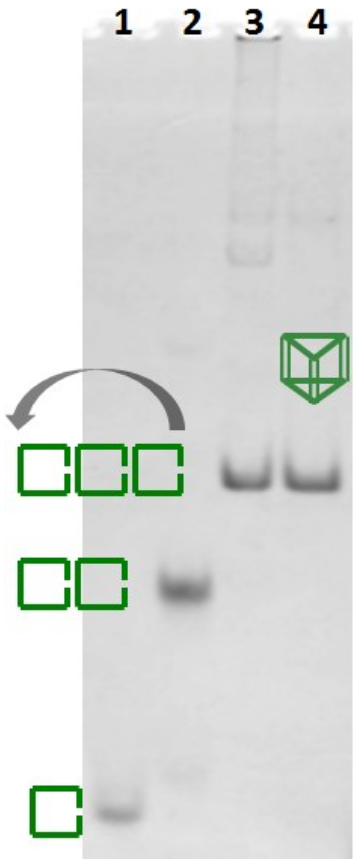

Figure 2.14: Native PAGE Analysis of TP assembly. Native PAGE (6%, all samples are assembled in 1xTAMg) gel ran for 3 hours at 250V. Lanes 1 to 3 are RT additions of component strands and lane 4 is the annealed final product; Lane 1: Strand 1, Lane 2: Strand 1 + 2, Lane 3: Strands 1 + 2 + 3, Lane 4: Strands 1 + 2 + 3 (Annealed).

2.5.4 Preparation of Bilayer Coated Beads

Spherically supported bilayers (SSLBMs) are generated by mixing a solution of 5 μm silica beads (Bangs Laboratories) at a concentration of 9×10^6 particles/mL in PBS buffer, with an equal volume of small unilamellar lipid vesicles (SUVs) solution in the same buffer for 30 minutes. The bead-vesicle solution is then washed by centrifugation (3x at 7000 rpm for 10 minutes) and the resulting pellet is re-suspended in 1x TAMg buffer. For the formation of DOPC SUVs, a chloroform solution of DOPC (1 mg/mL) is dried overnight under vacuum, and the resulting lipid film is then hydrated using PBS through vortex mixing, followed by sonication in a bath sonicator for 5-10 minutes.

In general, 60 μL of a 250 nM solution of annealed DNA cages are combined with 60 μL of the bilayer coated bead solution and 380 μL of 1xTAMg buffer for a total volume of 500 μL. The bead/DNA solution is shaken gently and incubated for 15 minutes at RT and is then washed by centrifugation (1x at 7000 rpm for 10 minutes) and the resulting pellet is re-suspended in 1x TAMg. The washing steps allow for the removal of any unbound DNA cage or DNA-conjugate. The 60 μL of 250 nM DNA prisms we are adding to the incubation represents approximately 15×10^{-12} mols which is an excess of about 5x the number of prisms which could theoretically be accommodated at the surface. The higher value ensures maximum coverage of the bilayer surface with the DNA scaffold. Working with concentrations in the nM range ensures unwanted aggregations from cholesterol mediated self-assembly.

The amount of fully assembled DNA cage incubated with the SSLBMs is determined based on the available molecular area of the total number of bilayer coated beads present in an incubation mixture. Each bead is 5 μm in diameter and the bilayer itself is approximately 5 nm in thickness. To simplify the calculation, the approximate surface area is determined using the 5 μm bead diameter only. The formula for the area of a sphere is $A = 4\pi r^2$, which gives a calculated value of 78.5 μm^2/bead. Therefore by using 60 μL of a 9×10^6 beads/mL stock solution we generate 4.24×10^7 μm^2 total available area. Each edge of our prism is 20 bp in length which is approximately equal to 7 nm in length. The triangular prism face of a DNA cage will thus occupy an area of 2.12×10^{-5} μm^2 assuming a rigid construct. Dividing the total available surface area by the area of

a single prism face we calculate that approximately 2.00×10^{12} triangular prisms (or 3.32×10^{-12} mols of prisms) can theoretically be accommodated at the surface of the beads available.

2.5.5 Bilayer Loading Quantification

Bilayer loading efficiency is determined using Cy5 fluorescence intensity signal. In these experiments the SSLBs are prepared and then coated with a DNA prism assembled with a cholesterol anchor and a Cy5 label. Samples are allowed to incubate and are then washed twice to ensure removal of any unbound prism scaffold. The cholesterol anchor displacing strand is then added to the washed mixture and incubated at RT for 1 hr. The supernatants are then collected and spin concentrated to a volume of approximately 20μL. These samples are then loaded on native PAGE (Figure 2.15 lanes 7, 9, 11) next to a series of wells containing increasing amounts of a known concentration of Cy5-labeled DNA scaffold as a calibration curve (Figure 2.15 lanes 1 to 5). Once the gel run is complete, we scan for Cy5 fluorecence intensity using a ChemiDoc fluorescent imager (Bio-Rad). The Image Lab (Bio-Rad) software is then used for quantification of the band associated with the collected DNA material using the band intensity from the calibration samples. After a second wash of the DNA/beads solution, the supernatants did not show any measurable fluorescence intensity, indicating that the incorporated DNA assemblies are stable within the SSLBMs.

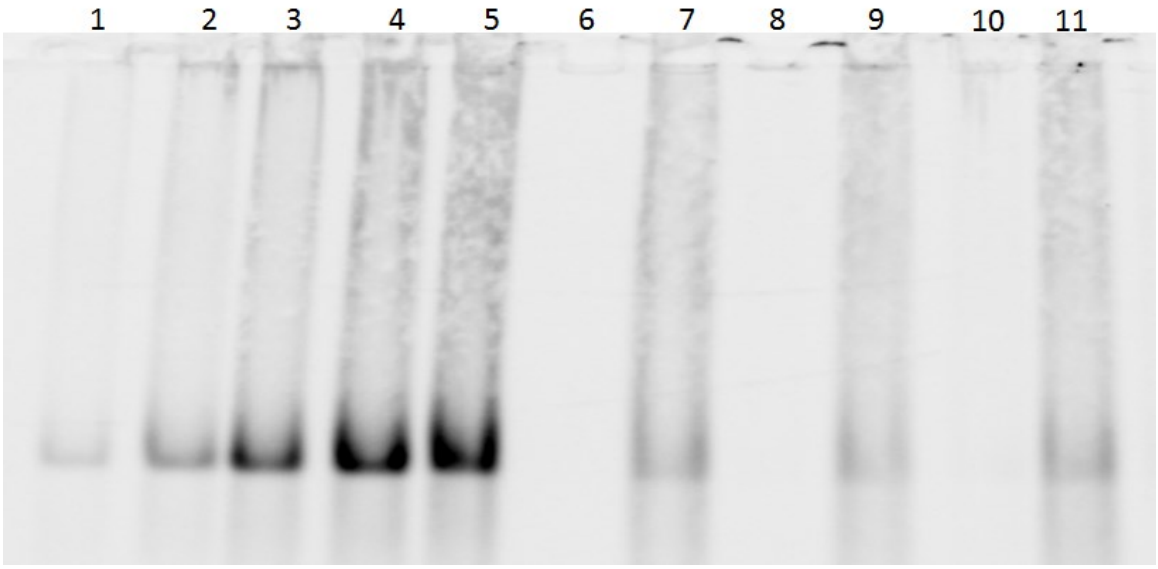

Figure 2.15: Native PAGE Analysis of bilayer released DNA prisms. Native PAGE (6%, 1xTAM) gel ran for 2.5 hrs at 250V; Lanes 1 – 5 represent the calibration curve using a 0.25 μM solution with volumes of 2, 4, 6, 8, and 10 μL respectively. Lanes 7, 9, and 11 represent the spin concentrated supernatant following the addition of the cholesterol anchor displacing strand.

2.5.6 Confocal Microscopy

Images are obtained using either one or a combination of the following optical settings (i) λex 488 nm/ λem LP > 505 nm (single channel imaging) or λem BP 505−550 nm (multi-channel imaging), (ii) λex 543 nm/ λem LP > 565 nm (single channel imaging) or λem BP 550−615 nm (multi-channel imaging), and (iii) λex 633 nm/ λem LP > 685 nm, depending on the fluorescent tag(s) selection. The acquired intensity images are checked to avoid detector saturation and loss of offsets by carefully adjusting the laser power and detector gain. The obtained confocal images and 3D stacks are not subject to any post-acquisition image processing. For each sample, a minimum of 50 beads are imaged.

2.5.7 FRAP Experiments

The experiment proceeds by imaging DOPC SSLBMs containing either BODIPY® FL-C5 or Alexa488 functionalized DNA cages. The fluorescent lipid analog BODIPY® FL-C5 (4,4-difluoro-5,7-dimethyl-4-bora-3a,4a,diaza-s-indacene-3-pentanoic acid) is purchased from Molecular Targeting Technologies (Pennsylvania, USA). A Zeiss LSM710 confocal laser scanning microscope is used with a 63X/1.4 oil-immersion objective and a 488 nm argon ion laser (25 mW). As seen in Figure 2.16, a FRAP circular bleach spot, a reference spot and a third background spot (not shown here) are used for data collection and subsequent analysis. The circular spots have a radius of 1.3 μm and the image size was 4.89 μm x 3.60 μm. Laser intensity of 100% is used for bleaching and a maximum of 10% for imaging. Five images are captured prior to FRAP bleaching in order to measure the initial average intensity, followed by 10 consecutive bleach iterations. In order to minimize the total scan time only the circular FRAP, reference and background spots are imaged. This allows a reduction of the total experiment time, and calculation of a more reliable fluorescence recovery time and diffusion coefficient. At least 50 post-bleaching images are collected, each acquired with a scan time of 247 ms. FRAP data for each experiment are normalized to their respective initial pre-bleaching fluorescence intensity. After accounting for background fluorescence and bleaching caused by imaging, a FRAP average curve is constructed from the whole data set (50 separate experiments). The FRAP curve is then fitted, assuming the presence of one diffusive species, to a one component fit model with the equation $f(t) = A(1-e^{-\tau t})$ where A is the ratio of mobile to immobile species and τ is the "characteristic" diffusion time required to recover 50% of original fluorescence intensity. A lower limit of the diffusion coefficient D can be calculated from the equation $D \geq 0.224w^2/\tau$ where w is the radius of the photobleached area.[47] The observed recovery half time corresponds to the fastest recovery time that can be measured with the experimental parameters accessible to the confocal set up used for these measurements. Therefore the calculated diffusion coefficient value must be considered as a lower limit for the prism diffusion coefficient rather than an absolute value. All data processing and fitting are performed using KaleidaGraph (Synergy software).

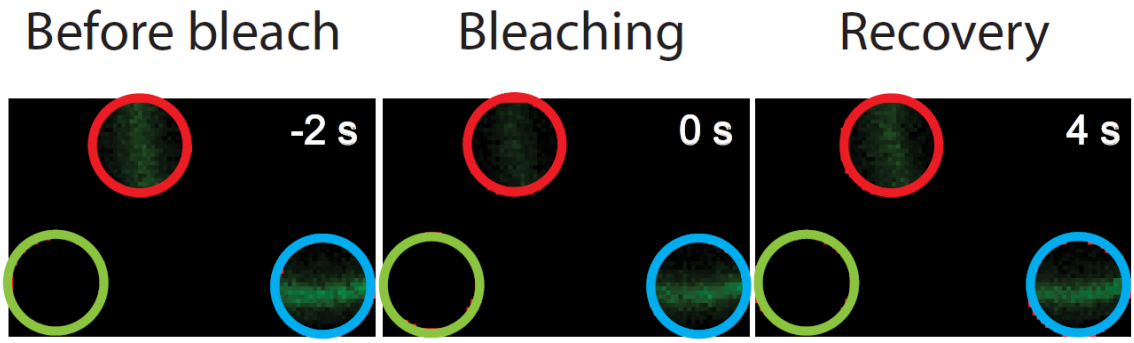

Figure 2.16: Experimental set up for FRAP data collection. Images of BODIPY labeled DOPC bilayer coated SSLBM before and after bleaching a 1.3 μm diameter circular spot (shown in red). The same size circular spot is applied for collecting reference and background fluorescence signals during the FRAP experiments (indicated in blue and green, respectively). Each image involved collecting fluorescence data from the three highlighted circular spots only.

2.5.8 In Solution Hybridization and Displacement of Fluorescent Labels and Cholesterol Anchors on the DNA Cage

This PAGE analysis shows the accumulation of the displaced components from the scaffold as seen at the bottom of the gel. This series of bands corresponds to the same set of samples as in Figure 2.2.

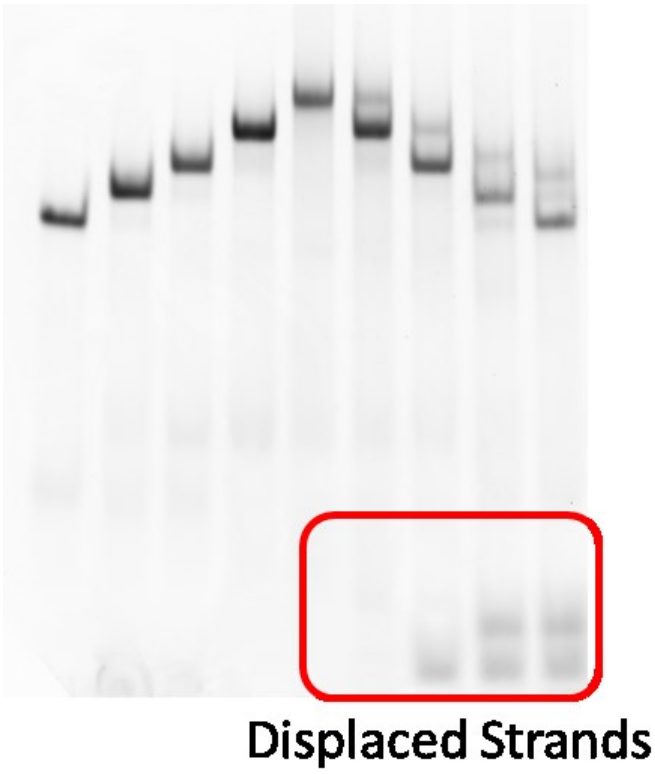

Figure 2.17: Native PAGE. This PAGE analysis shows the stepwise addressability of the triangular DNA scaffold and its disassembly via strand displacement. The boxed region highlights the displaced duplexed strands. Lane 1: TP, lane 2: previous + Cy3, lane 3: previous + Cy5, lane 4: previous + Alexa488, lane 5: previous +cholesterol anchor, lane 6: displace cholesterol anchor, lane 7: displace Alexa488, lane 8: displace Cy5, lane 9: displace Cy3.

2.5.9 Membrane Integrity Control

This figure shows the fluorescence microscopy for SSLBMs prepared using the fluorescent DOPC analog (BODIPY) and then further labeled using a Cy3 functionalized prism scaffold. The image shows homogeneous coverage of the bead with the labeled bilayer, as well as with the Cy3 labeled prism. This indicates the beads are completely covered in both a lipid bilayer and an outer shell of DNA cages.

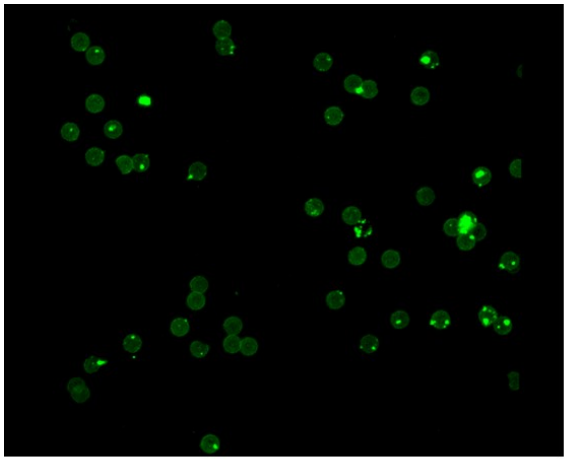

BODIPY labeled bilayer

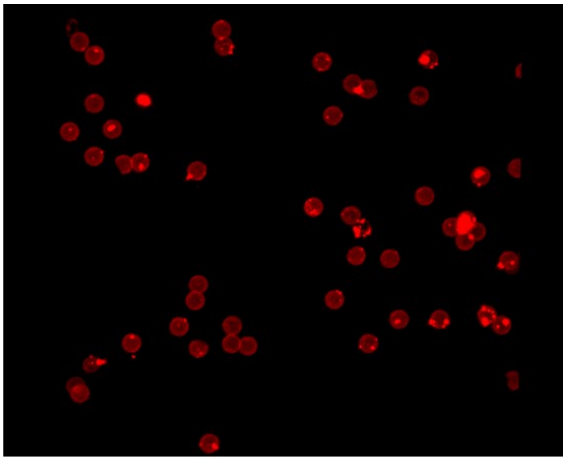

Cy3 labeled prism on bilayer

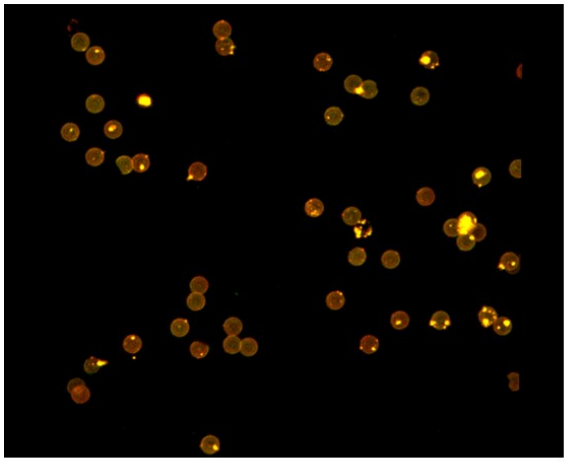

Fluorescent Overlay

Figure 2.18: Membrane integrity and coverage. Top right, shows the fluorescence channel for the BODIPY labeled bilayer. Top left, shows the same beads through the Cy3 channel. Bottom, shows the overlay of the two channels and confirms co-localization of the bilayer and the labeled prisms.

2.6 References

(1) Börjesson, K.; Wiberg, J.; El-Sagheer, A. H.; Ljungdahl, T.; Mårtensson, J.; Brown, T.; Nordén, B.; Albinsson, B. *ACS Nano* **2010**, *4*, 5037-5046.

(2) Howorka, S. *Langmuir* **2013**, *29*, 7344-7353.

(3) Kwak, M.; Herrmann, A. *Chem. Soc. Rev.* **2011**, *40*, 5745-5755.

(4) van der Meulen, S. A. J.; Leunissen, M. E. *J. Am. Chem. Soc.* **2013**, *135*, 15129-15134.

(5) He, H.-Z.; Chan, D. S.-H.; Leung, C.-H.; Ma, D.-L. *Nucleic Acids Res.* **2013**, *41*, 4345-4359.

(6) Leung, C.-H.; Chan, D. S.-H.; He, H.-Z.; Cheng, Z.; Yang, H.; Ma, D.-L. *Nucleic Acids Res.* **2012**, *40*, 941-955.

(7) Ma, D.-L.; He, H.-Z.; Chan, D. S.-H.; Leung, C.-H. *Chem. Sci.* **2013**, *4*, 3366-3380.

(8) Ma, D.-L.; He, H.-Z.; Leung, K.-H.; Zhong, H.-J.; Chan, D. S.-H.; Leung, C.-H. *Chem. Soc. Rev.* **2013**, *42*, 3427-3440.

(9) Hung, Y.-C.; Lin, T.-Y.; Hsu, W.-T.; Chiu, Y.-W.; Wang, Y.-S.; Fruk, L. *Opt. Mater.* **2012**, *34*, 1208-1213.

(10) Jones, M. R.; Osberg, K. D.; Macfarlane, R. J.; Langille, M. R.; Mirkin, C. A. *Chem. Rev.* **2011**, *111*, 3736-3827.

(11) Pal, S.; Dutta, P.; Wang, H.; Deng, Z.; Zou, S.; Yan, H.; Liu, Y. *J. Phys. Chem. C* **2013**, *117*, 12735-12744.

(12) Young, K. L.; Ross, M. B.; Blaber, M. G.; Rycenga, M.; Jones, M. R.; Zhang, C.; Senesi, A. J.; Lee, B.; Schatz, G. C.; Mirkin, C. A. *Adv. Mater.* **2014**, *26*, 653-659.

(13) Keum, J.-W.; Ahn, J.-H.; Bermudez, H. *Small* **2011**, *7*, 3529-3535.

(14) Li, J.; Pei, H.; Zhu, B.; Liang, L.; Wei, M.; He, Y.; Chen, N.; Li, D.; Huang, Q.; Fan, C. *ACS Nano* **2011**, *5*, 8783-8789.

(15) Schüller, V. J.; Heidegger, S.; Sandholzer, N.; Nickels, P. C.; Suhartha, N. A.; Endres, S.; Bourquin, C.; Liedl, T. *ACS Nano* **2011**, *5*, 9696-9702.

(16) Walsh, A. S.; Yin, H.; Erben, C. M.; Wood, M. J. A.; Turberfield, A. J. *ACS Nano* **2011**, *5*, 5427-5432.

(17) Hamblin, G. D.; Carneiro, K. M. M.; Fakhoury, J. F.; Bujold, K. E.; Sleiman, H. F. *J. Am. Chem. Soc.* **2012**, *134*, 2888-2891.

(18) Fakhoury, J. J.; McLaughlin, C. K.; Edwardson, T. W.; Conway, J. W.; Sleiman, H. F. *Biomacromolecules* **2014**, *15*, 276-282.

(19) Park, S. Y.; Lytton-Jean, A. K. R.; Lee, B.; Weigand, S.; Schatz, G. C.; Mirkin, C. A. *Nature* **2008**, *451*, 553-556.

(20) Banchelli, M.; Betti, F.; Berti, D.; Caminati, G.; Bombelli, F. B.; Brown, T.; Wilhelmsson, L. M.; Nordén, B.; Baglioni, P. *J. Phys. Chem. B* **2008**, *112*, 10942-10952.

(21) Beales, P. A.; Vanderlick, T. K. *J. Phys. Chem. B* **2009**, *113*, 13678-13686.

(22) Chung, M.; Boxer, S. G. *Langmuir* **2011**, *27*, 5492-5497.

(23) Chan, Y.-H. M.; van Lengerich, B.; Boxer, S. G. *Biointerphases* **2008**, *3*, FA17-FA21.

(24) Stengel, G.; Zahn, R.; Höök, F. *J. Am. Chem. Soc.* **2007**, *129*, 9584-9585.

(25) Li, C. Y.; Wood, D. K.; Hsu, C. M.; Bhatia, S. N. *Lab Chip* **2011**, *11*, 2967-2975.

(26) Burns, J. R.; Stulz, E.; Howorka, S. *Nano Lett.* **2013**, *13*, 2351-2356.

(27) Langecker, M.; Arnaut, V.; Martin, T. G.; List, J.; Renner, S.; Mayer, M.; Dietz, H.; Simmel, F. C. *Science* **2012**, *338*, 932-936.

(28) Woller, J. G.; Hannestad, J. K.; Albinsson, B. *J. Am. Chem. Soc.* **2013**, *135*, 2759-2768.

(29) Schade, M.; Knoll, A.; Vogel, A.; Seitz, O.; Liebscher, J.; Huster, D.; Herrmann, A.; Arbuzova, A. *J. Am. Chem. Soc.* **2012**, *134*, 20490-20497.

(30) Suzuki, Y.; Endo, M.; Yang, Y.; Sugiyama, H. *J. Am. Chem. Soc.* **2014**, *136*, 1714-1717.

(31) Johnson-Buck, A.; Jiang, S.; Yan, H.; Walter, N. G. *ACS Nano* **2014**, *8*, 5641-5649.

(32) Langecker, M.; Arnaut, V.; List, J.; Simmel, F. C. *Acc. Chem. Res.* **2014**, *47*, 1807-1815.

(33) Czogalla, A.; Petrov, E. P.; Kauert, D. J.; Uzunova, V.; Zhang, Y.; Seidel, R.; Schwille, P. *Faraday Discuss.* **2013**, *161*, 31-43.

(34) Conway, J. W.; McLaughlin, C. K.; Castor, K. J.; Sleiman, H. *Chem. Commun.* **2013**, *49*, 1172-1174.

(35) Lo, P. K.; Karam, P.; Aldaye, F. A.; McLaughlin, C. K.; Hamblin, G. D.; Cosa, G.; Sleiman, H. F. *Nature Chem.* **2010**, *2*, 319-328.

(36) Bayerl, T. M.; Bloom, M. *Biophys. J.* **1990**, *58*, 357-362.

(37) Mornet, S.; Lambert, O.; Duguet, E.; Brisson, A. *Nano Lett.* **2005**, *5*, 281-285.

(38) Tanaka, M.; Sackmann, E. *Nature* **2005**, *437*, 656-663.

(39) Argyo, C.; Weiss, V.; Bräuchle, C.; Bein, T. *Chem. Mater.* **2014**, *26*, 435-451.

(40) Gopalakrishnan, G.; Thostrup, P.; Rouiller, I.; Lucido, A. L.; Belkaïd, W.; Colman, D. R.; Lennox, R. B. *ACS Chem. Neurosci.* **2010**, *1*, 86-94.

(41) Schwille, P.; Diez, S. *Crit. Rev. Biochem. Mol. Biol.* **2009**, *44*, 223-242.

(42) Troutier, A.-L.; Ladavière, C. *Adv. Colloid Interface Sci.* **2007**, *133*, 1-21.

(43) Gopalakrishnan, G.; Rouiller, I.; Colman, D. R.; Lennox, R. B. *Langmuir* **2009**, *25*, 5455-5458.

(44) Silvius, J. *Lipid-protein interactions* **1982**, *2*, 239-281.

(45) Börjesson, K.; Lundberg, E. P.; Woller, J. G.; Nordén, B.; Albinsson, B. *Angew. Chem., Int. Ed.* **2011**, *50*, 8312-8315.

(46) Woller, J. G.; Börjesson, K.; Svedhem, S.; Albinsson, B. *Langmuir* **2012**, *28*, 1944-1953.

(47) Soumpasis, D. M. *Biophys. J.* **1983**, *41*, 95-97.

Preface

Chapter 2 examined the dynamic properties of DNA cages anchored on spherically supported lipid bilayers. In Chapter 3, we continue the work towards interfacing DNA nanotechnology and lipid bilayers. The work presented herein aims to combine the programmability of DNA with the long range self-assembly of lipid membranes, to create selectively patterned extended DNA networks. Towards this end we have used a three-point star DNA tile motif, which assembles into a hexagonal network, modified with a centrally positioned hydrophobic anchor to direct tile networks onto lipid bilayers. We examine three structurally varied hydrophobic anchors on both pure and mixed saturated/unsaturated lipid bilayers, which exhibit significantly different interactions due to the hydrophobic packing of DNA-anchors within the bilayer. We are able to demonstrate selective deposition of the tile networks onto the lipid bilayers and as well as variable network morphology linked to the anchor structure and membrane packing.

Chapter 3

DNA Tile Networks on Supported Lipid Bilayers: Long-Range Assembly and Selective Patterning

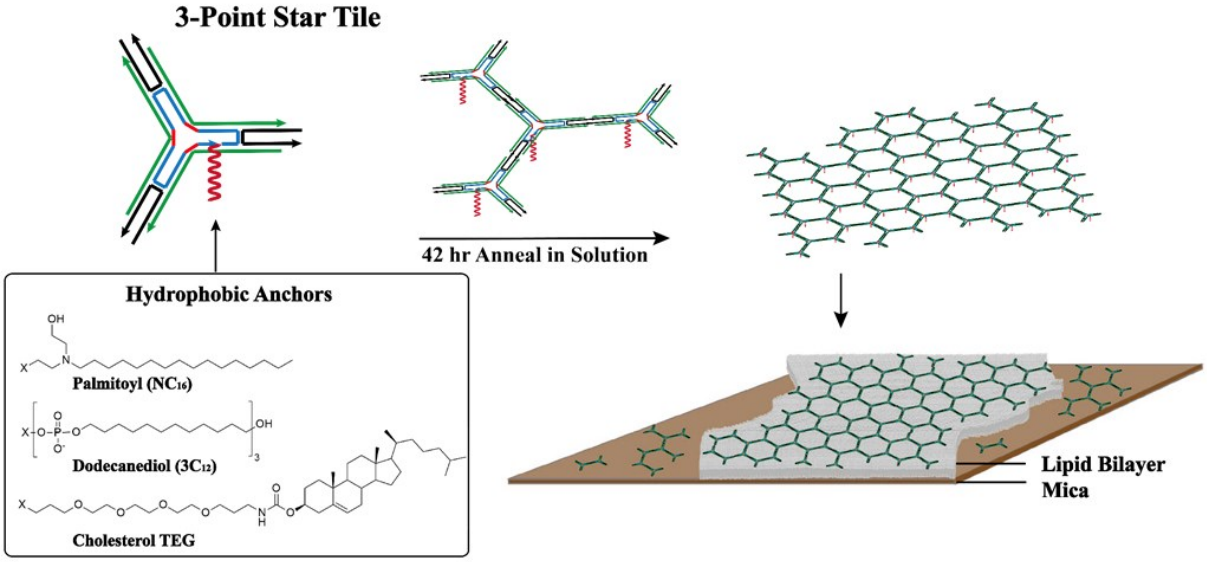

The majority of this chapter has been has been submitted to JACS and is under review (February 2015) as "DNA Tile Networks on Supported Lipid Bilayers: Long-Range Assembly and Selective Patterning", Justin Conway, Nicole Avakyan, John Chu Chia Hsu, Donatien de Rochambeau, Maciej Barlog, Hassan S. Bazzi, Hanadi F. Sleiman.

3.1 Abstract

DNA tile networks based on a three point star (3PS) motif have been modified with hydrophobic anchors (cholesterol, a palmitoyl analogue, and a hydrophobic polymer), deposited on saturated/unsaturated supported lipid bilayers and imaged using atomic force microscopy (AFM). This study focuses on examining the combination of several modes of self-assembly within modified tile networks: (1) Watson-Crick base pairing of modified tile networks in solution, (2) amphiphilic organization of tile networks on lipid bilayers, and (3) hydrophobic anchor aggregation. When the hydrophobically modified tiles are deposited on lipid bilayers best matching their anchor properties, they exhibit long-range, relatively defect-free hexagonal network patterns. This occurs for cholesterol tiles on unsaturated lipid bilayers, and palmitoyl analogue tiles on saturated lipid bilayers. These bilayer-supported DNA patterns can be generated with as little as 20% anchor labeling, outlining the ease and scalability of this approach. In contrast, other lipid-anchor combinations result in disruption of the Watson-Crick base pairing to generate different morphologies (herringbone-like patterns, small aggregates). When mixed saturated-unsaturated lipid bilayers are generated, the tiles are able to target a specific lipid domain based on their anchor. This produces spatially segregated DNA hexagonal networks, as well as different bilayer-supported DNA patterns side-by-side. These results can be used to begin interfacing extended network organizations of oligonucleotides, nanoparticles and proteins with biologically relevant membrane systems or other soft surface materials for applications in cellular recognition, drug delivery, plasmonics and light harvesting.

3.2 Introduction

DNA has emerged as an excellent material for the construction of scaffolds that accurately organize nanomaterials,[1-4] proteins or antibodies.[5-7] These DNA platforms are found predominantly as networks of origami tiles[8,9] or as extended 2D tile-based assemblies.[10-15] Of these approaches, 2D tile-based networks have the advantage of requiring far fewer strands thereby simplifying their application and scalability. DNA nanotechnology represents a bottom-up assembly scheme to create functional materials, however the generation of large DNA scaffolds is still a challenge[16]. On the other hand, lipid self-assembly into bilayers or vesicles exhibit long range ordering over 100 μm, but lack the programmability of DNA scaffolds. It would therefore

be of particular interest to combine these two self-assembly methods through the introduction of hydrophobic groups that would interface DNA tile networks with extended lipid bilayers. Lipid bilayers are a highly ordered but dynamic material[17-20] and provide an ideal environment to direct DNA nanostructures to surfaces while maintaining their native structures. A number of DNA nanostructures have been anchored to lipid bilayer membranes, including DNA origami[17,18,21-23] discrete DNA scaffolds[24-30] and 3D-DNA cage structures.[19] In all previous examples, the structures were pre-formed and robust, and were not expected to be disrupted or reorganized by the underlying bilayer membrane.

On the other hand, tile assemblies are held together by relatively weak interactions using short sticky-ends and can potentially undergo reorganization on lipid bilayers. If the two non-covalent interactions, DNA tile base-pairing and DNA-bilayer interactions are engineered to work synergistically, this can result in long-range ordered DNA nanostructures on lipid bilayer surfaces. These materials will be useful for applications in protein patterning,[4] drug delivery,[31-33] cell signaling as well as nanophotonics and light harvesting.[2,3,34]

Lipid bilayers can introduce an additional level of patterning for DNA networks. In a mixed lipid system, lipids with different packing constraints will partition into phase separated domains typically differentiated by saturated and unsaturated hydrophobic carbon chains.[35,36] It would thus be interesting to examine whether DNA tile networks with different hydrophobic anchors can be directed to a particular lipid domain within a mixed lipid system.

We here report the preparation of a DNA three-point star (3PS) tile motif [10-12] that is modified with hydrophobic anchors, and investigate its self-assembly on lipid bilayer membranes of different composition. (Figure 3.1) Three different anchors are examined: (i) cholesterol (Chol), (ii) a new palmitoyl analogue (NC_{16}) and (iii) a length-controlled polymer containing dodecane diol repeat units ($3C_{12}$). Two different lipid bilayer compositions, composed of an unsaturated (DOPC) and a saturated variant (DPPC), are considered (DOPC: 1,2-dioleoyl-sn-glycero-3-phosphocholine; DPPC: 1,2-dipalmitoyl-sn-glycero-3-phosphocholine).

A number of findings arise from the combination of the two types of non-covalent interactions described above. First, when anchor affinity to the lipid bilayer is optimally balanced with base-pairing, such as in the case of cholesterol to DOPC, or palmitoyl analogue to DPPC, we observe

long-range and relatively defect-free hexagonal assemblies anchored on the bilayer. Interestingly, this effect can be achieved using a reduced number (20%) of functionalized tiles (80% unfunctionalized). This outlines an economic and scalable method to create highly ordered DNA surfaces on dynamic bilayers. Secondly, when mixed bilayers are generated, the tiles segregate on their 'matched' bilayer domain, and form similar hexagonal patterns to those in the pure bilayers. This results in phase-separated domains with different DNA composition and patterning. On the other hand, sticky-ended tiles whose anchors do not efficiently pack within the bilayer, or blunt-ended DNA tiles that cannot associate via Watson-Crick base-pairing do not form these hexagonal surfaces. Instead, self-recognition via the hydrophobic effect induces them in some cases to assemble into new motifs, such as networks resembling herringbone structures or nanofibers. This balance between DNA hybridization and hydrophobic assembly may lead to the development of useful nanostructures for therapeutic or diagnostic applications. Furthermore, the fluid nature of unsaturated bilayers may allow for error correction within the network and fewer defects over an increased area. In addition, the properties of the hydrophobic anchors direct networks to particular domains and play a major role in their deposition and morphology. This combination of orthogonal self-assembly methods can be used to increase the size range of DNA self-assembled structures without the need to use a large number of DNA sequences.[37-39]

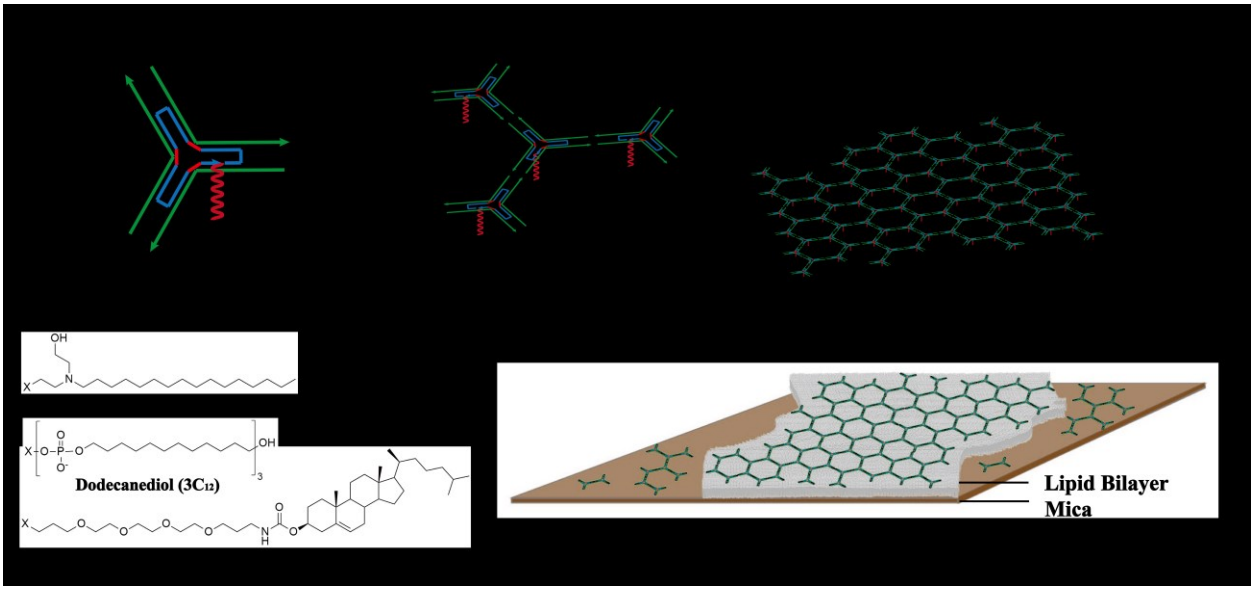

Figure 3.1: (A) Tile design and hydrophobic anchor structure, (B) tile assembly into network, (C) network deposition onto a lipid bilayer surface.

3.3 Results and Discussion

The DNA three point star (3PS) has been shown by Mao[10,11] to form extended 2D networks with hexagonal packing on mica surfaces. This tile structure, assembled using 3 different DNA strands, orients three short sticky-ended self-complementary units at 120° angles. Deposition of the tiles onto a hydrophobic medium like a lipid bilayer requires modifying the 3PS with a hydrophobic anchor. We introduce this anchor group in the central strand of the tile (Figure 3.1A), so as not to perturb sticky-end association. The tile network was originally designed to compensate for the inherent curvature within each tile unit over extended assemblies by alternating the tile face up and down.[12] The tile anchors are most likely small enough to thread through the center of the structure in order to orient themselves towards the bilayer from either tile face. Blunt-ended tiles have been shown to exhibit non-specific end-stacking leading to partially assembled networks as reported elsewhere.[40,41] We have synthesized them as a control structure to determine if the hydrophobic anchoring unit generates any distinct tile aggregation in the absence of Watson-Crick base pairing.

We have modified the original 3PS tile motif with three different types of hydrophobic groups as indicated in Figure 3.1. Cholesterol (Chol) was introduced as a commercially available phosphoramidite derivative with a short triethylene glycol spacer. The palmitoyl analogue NC_{16} is a new molecule, which was synthesized as its mono-dimethoxytrityl (DMT) phosphoramidite derivative from N-dodecyl bis-ethanol (Experimental Section 3.5.4). It is of note that the final NC_{16} modification has a tertiary amine group which will likely be protonated, potentially influencing its electrostatic interactions with the phosphatidyl zwitterionic lipid head groups. Finally, the polymer-DNA conjugate with three consecutive C_{12} ($3C_{12}$) modifications was synthesized by sequential solid-phase coupling of three dodecanediol dimethoxytrityl phosphoramidite molecules to the DNA strand end.[38,42] All products were characterized using denaturing polyacrylamide gel electrophoresis (PAGE), reverse-phase high-performance liquid chromatography (RP-HPLC) and mass spectrometry (MS) (Experimental Section 3.5.3 and 3.5.5).

The assembly of the hydrophobically modified 3PS tiles is examined using non-denaturing PAGE analysis. Both unmodified and modified tiles containing the different anchors hybridize correctly (Experimental Section 3.5.3). The tile networks are assembled in solution using a 42 hr annealing step from 75-10˚C and then deposited on mica-supported lipid bilayer surfaces for imaging by atomic force microscopy (AFM) in fluid (Experimental Section 3.5.7). For bilayer preparation, the synthetic phospholipids DOPC and DPPC are chosen as examples of unsaturated and saturated lipids respectively. As a mixture, they are known to phase separate because of the structural differences in their respective alkyl tails.[35,36,43] Vesicles of each lipid are prepared by rehydration of dried lipid films with sonication and show a particle size distribution between 50-90 nm by DLS (Experimental Seciton 3.5.6). Bilayer samples are prepared via vesicle deposition on a freshly cleaved mica surface.[18,44] The supported bilayers of DOPC and DPPC show heights of 3.7 nm and 5.2 nm respectively as measured by AFM, which is good agreement with previous studies (see Experimental section 3.5.10).[45] These differences in height arise from the lipid packing differences in alkyl tail groups containing varying degrees of saturation.

In a first experiment, we prepare and anneal the unmodified 3PS tiles in solution, deposit them on a bare mica surface and image them using liquid AFM, Figure 3.2A. The sticky-ended tiles form well-defined hexagonal arrays when deposited on mica, as previously shown.[10,11] When the unmodified networking tile is deposited on bilayer coated mica, the extended network is disrupted.

We observe small localized regions of network patches exclusively on the mica surface with DOPC (Figure 3.2B). With DPPC, we observe the same patches on the bare mica, but the tiles also deposit non-specifically on the bilayer (Figure 3.2C). Non-specific deposition of DNA onto bilayers through electrostatic interactions has been shown elsewhere[18]. The bilayer appears textured but with little hexagonal or long-range order. The control blunt-ended tile shows partially formed network structures, likely through end π-π stacking for all three surfaces, but these do not deposit on any of the lipid bilayers (Experimental Section 3.5.8).

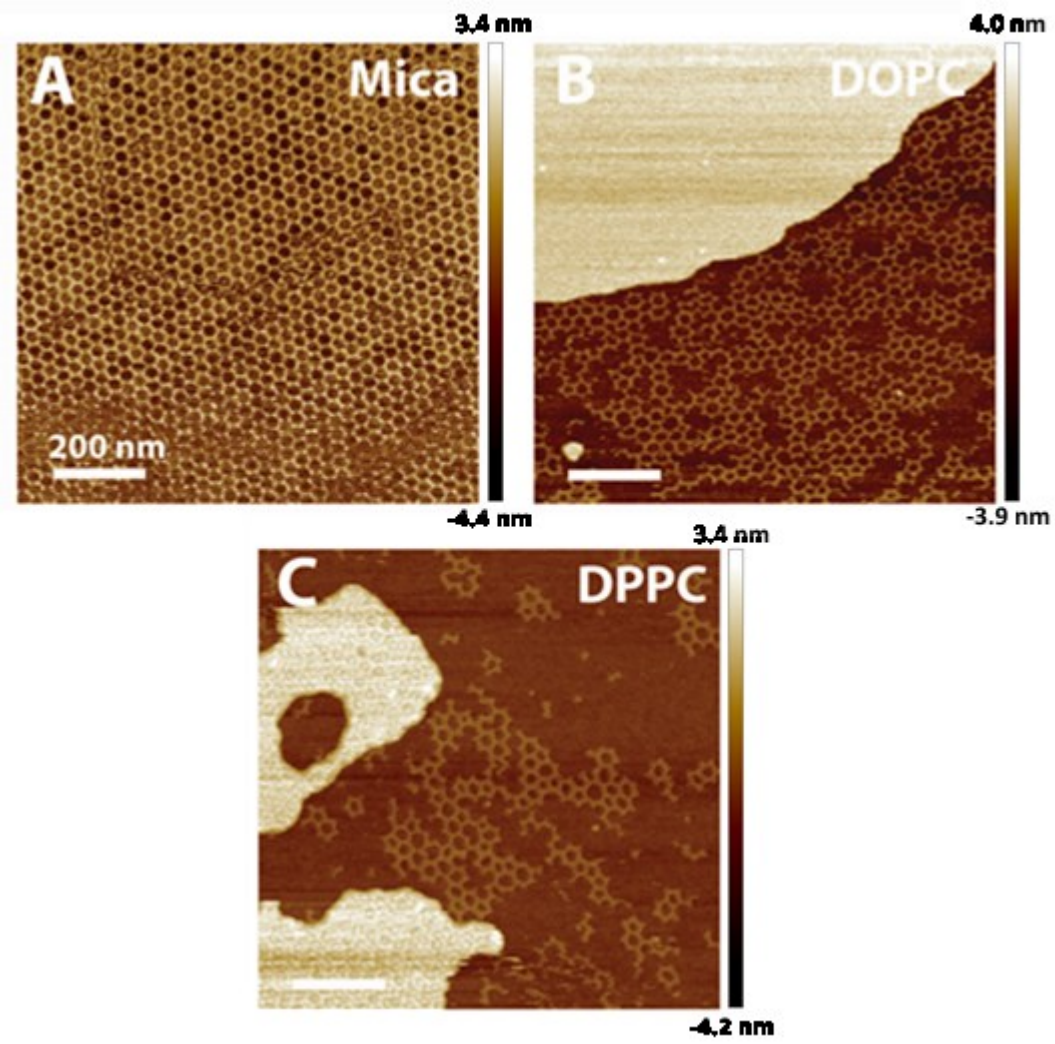

Figure 3.2: Liquid AFM images for unmodified networking tiles on bare mica (A), DOPC (B) and DPPC (C). Scale bars – 200 nm.

The cholesterol, NC_{16}, and $3C_{12}$ modified tile networks are next investigated to determine whether the hydrophobic modifications would direct the tile networks to either of the supported lipid bilayer domains. When deposited on a mica surface, the cholesterol and NC_{16} modified tiles are observed to remain capable of forming networks (Figures 3.3A/3.4A), however the formed structures have significantly more defects and holes in the hexagonal network, in comparison to the unmodified tile networks. Network formation in this case is disrupted by the hydrophobic modification, likely because the tiles do not adhere as uniformly to the mica surface, or because of hydrophobic aggregation between anchor units.

Next, we examine the deposition of cholesterol modified tile networks on DOPC coated mica. In contrast with the results on mica alone, the cholesterol tiles land almost exclusively on the bilayer surface and form highly ordered, extended hexagonal patterns supported by the bilayer (Figure 3.3B). Defect-free features are noted over long distances. The cholesterol-tile is further investigated to determine if the network could be directed onto DOPC using fewer anchoring cholesterol modifications. This is accomplished by including only 20% of cholesterol modified central strand (80% unmodified central strand) to the networking tile mixture during the one-pot 42 hour anneal. When this partially labeled tile system is deposited on a DOPC bilayer, the network is again successfully directed onto the lipid surface exclusively (Figure 3.3C). The network is now held to the bilayer by fewer anchoring units, but interestingly, long-range, relatively defect-free assembly persists. We did not note any significant accumulation of tiles on the bare mica: this argues against segregation of the unmodified tiles together into assembled structures that display a higher affinity to the bare mica regions as in Figure 3.2. Thus, fewer modified strands are necessary to achieve network formation and deposition on a bilayer, illustrating the scalability and ease of this approach which correlates well with similar[46].

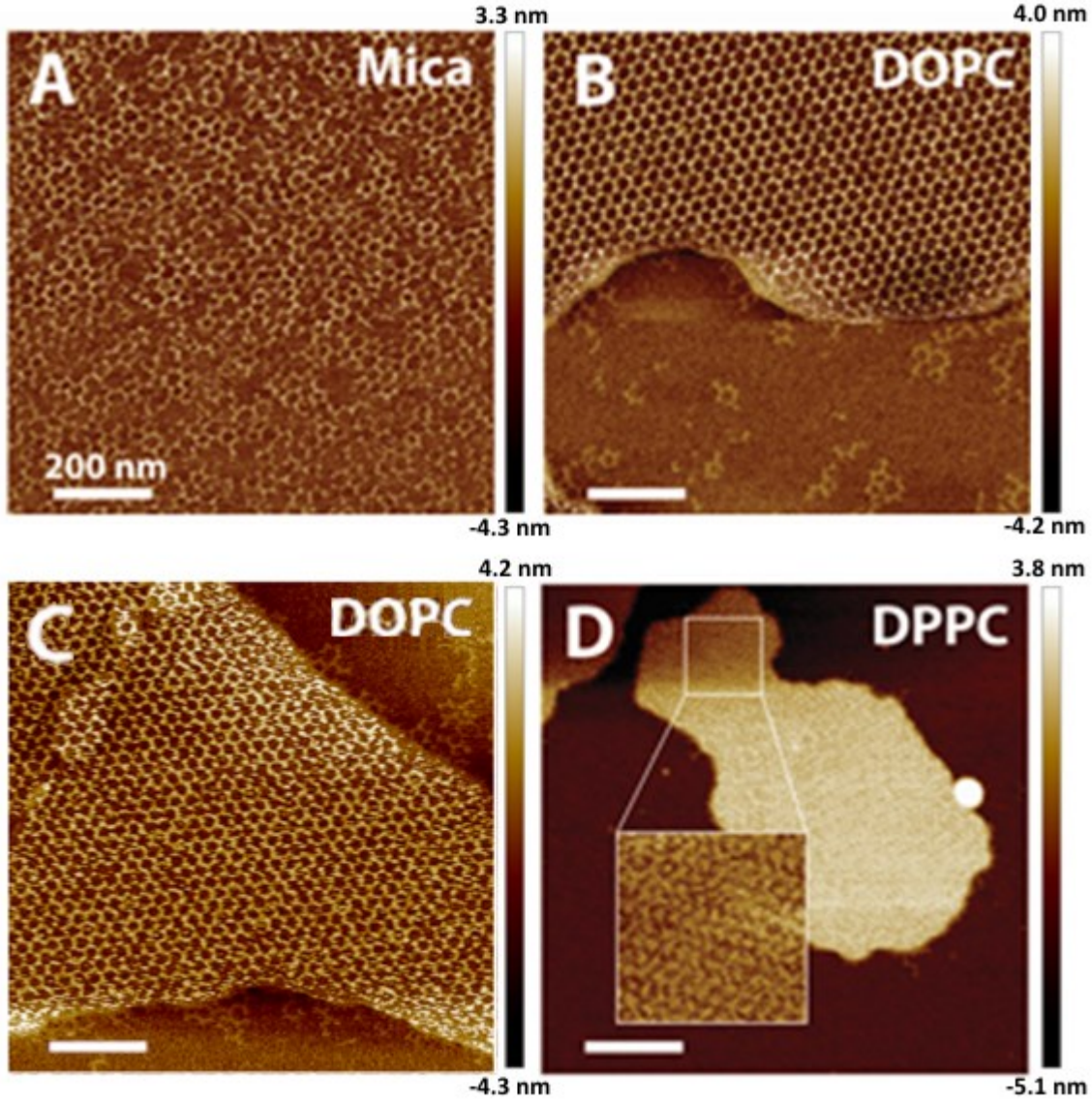

Figure 3.3: Liquid AFM images in fluid for cholesterol networking tiles on bare mica (A), DOPC (B), 20% cholesterol-modified networks on DOPC (C) and DPPC (D). Image (C) shows the deposition of tile networks containing only 20% cholesterol labeled tiles (80% unmodified tiles). Scale bars – 200 nm. Inset is a 400 nm cross-section.

When assembled cholesterol-tiles are deposited on DPPC coated mica (Figure 3.3D), the network morphology is significantly altered. In this case, a patterned structure does form on the lipid bilayer, but it is not hexagonal. Instead, it exhibits some resemblance to a closely packed, herringbone structure. Cholesterol is known to have high affinity to saturated lipid domains.[20,36]

In addition, the orientation of cholesterol within a lipid bilayer is dependent on lipid unsaturation.[47,48] Although determination of the occupied surface area for the two networks on DOPC or DPPC over a defined size would yield evidence for a differences in tile packing density, the lack of a defined structure within the herringbone-like networks prevents precise analysis. However, a comparative close-up of the two networks empirically suggests a significantly greater density of bilayer associated networked material in the case of the herringbone-like networks (Figure 3.4). A height analysis of the respective bilayers with a deposited cholesterol tile network, indicates an average height of 2.2 nm for DOPC and 6.2 nm for DPPC. Comparing these values to the pure bilayer height measurements however may not be valid, as cholesterol is known to alter the lipid alkyl chains packing which will change the bilayer height[49].

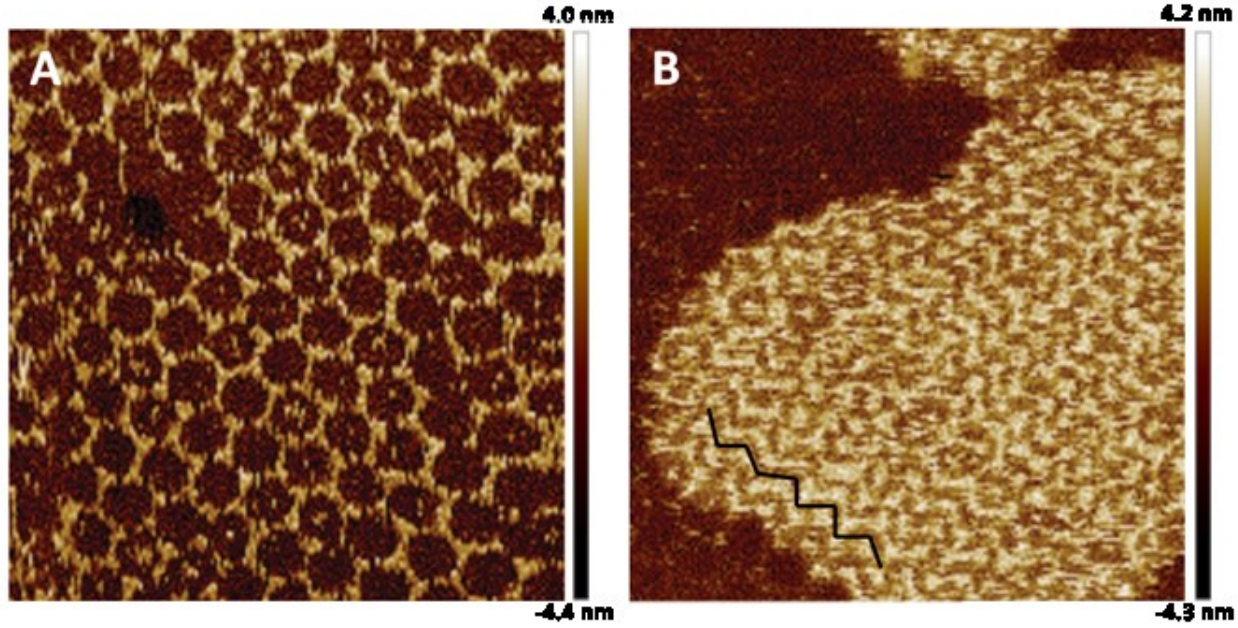

Figure 3.4: Cholesterol-modified tile networks landed on, (A) DOPC, which generates a hexagonal network, and (B) DPPC, which generates a network resembling a herringbone pattern (the black line is added to as a visual guide). Images are 300 nm.

We suggest several possible sources for these observations. As is shown in the literature, cholesterol has a higher preference for saturated lipids[36,46,50]. This can possibly result in higher packing density for the tiles, generating steric crowding of the cholesterol tile networks on DPPC bilayers, which may disrupt the hexagonal network pattern and lead to the observed morphology.

Figure 3.4B supports this theory as the DPPC bilayers show a higher density of bilayer associated network material relative to DOPC. It has also been shown that cholesterol exhibits different orientations within saturated/unsaturated bilayers[47-49]. These different anchor orientations may also contribute to the deformation of the hexagonal network. Finally, incorporation of cholesterol into DOPC/DPPC bilayers has been shown to increase the bilayer thickness, which may also affect the network organization[49]. The source of the herringbone-like formation remains currently under study. One experiment that would be particularly useful for elucidating the cause of this morphology would be to prepare the 80:20 mixture of unmodified to cholesterol-modified networked tiles and deposit them on DPPC. These networks contain a greatly reduced number of cholesterol anchors therefore, if the herringbone-like network persists under these conditions it may not be linked to steric crowding of the anchor at the bilayer surface.

The next set of experiments involve the assembly of the NC_{16} (palmitoyl-analogue) tiles on supported bilayers. Palmitoyl units are known to associate strongly with saturated bilayers, moreover it has been shown that at least two palmitoyl chains are needed to anchor a DNA construct on bilayer membranes.[20,43,51] When the NC_{16} tile network is pre-assembled then deposited on DOPC supported bilayers, the bilayer surface (observed as the brighter yellow region) appears covered in small aggregates ranging from 1.5 - 5 nm in height (Figure 3.5B). The small assemblies are distributed across the extended bilayer surface. This observed behaviour is consistent with possible phase separation of the NC_{16} chains to minimize contact within the DOPC environment, and subsequent disruption of their Watson-Crick base-pairing. Some tile assemblies with distorted features also appear on the mica surface. On the other hand, when the palmitoyl tiles are deposited on DPPC, a highly extended, relatively defect-free hexagonal network is formed exclusively on the DPPC surfaces (Figure 3.5C). Many of the hexagonal structures in the NC_{16} networks deposited on DPPC exhibit a centrally located feature. It is unclear if this feature is part of the DNA nanostructure or a protrusion from the underlying bilayer material. The identity of this feature is currently being investigated. One possible experiment that could be used to address this question involves re-designing the tile unit to contain extended arms terminated in the normal sticky ends. In this way the assembled hexagonal network should still form however the diameter of the hexagon would be increased. If the central feature is part of the DNA nanostructure, the increase in hexagon cavity size may reduce the crowding that causes it to form.

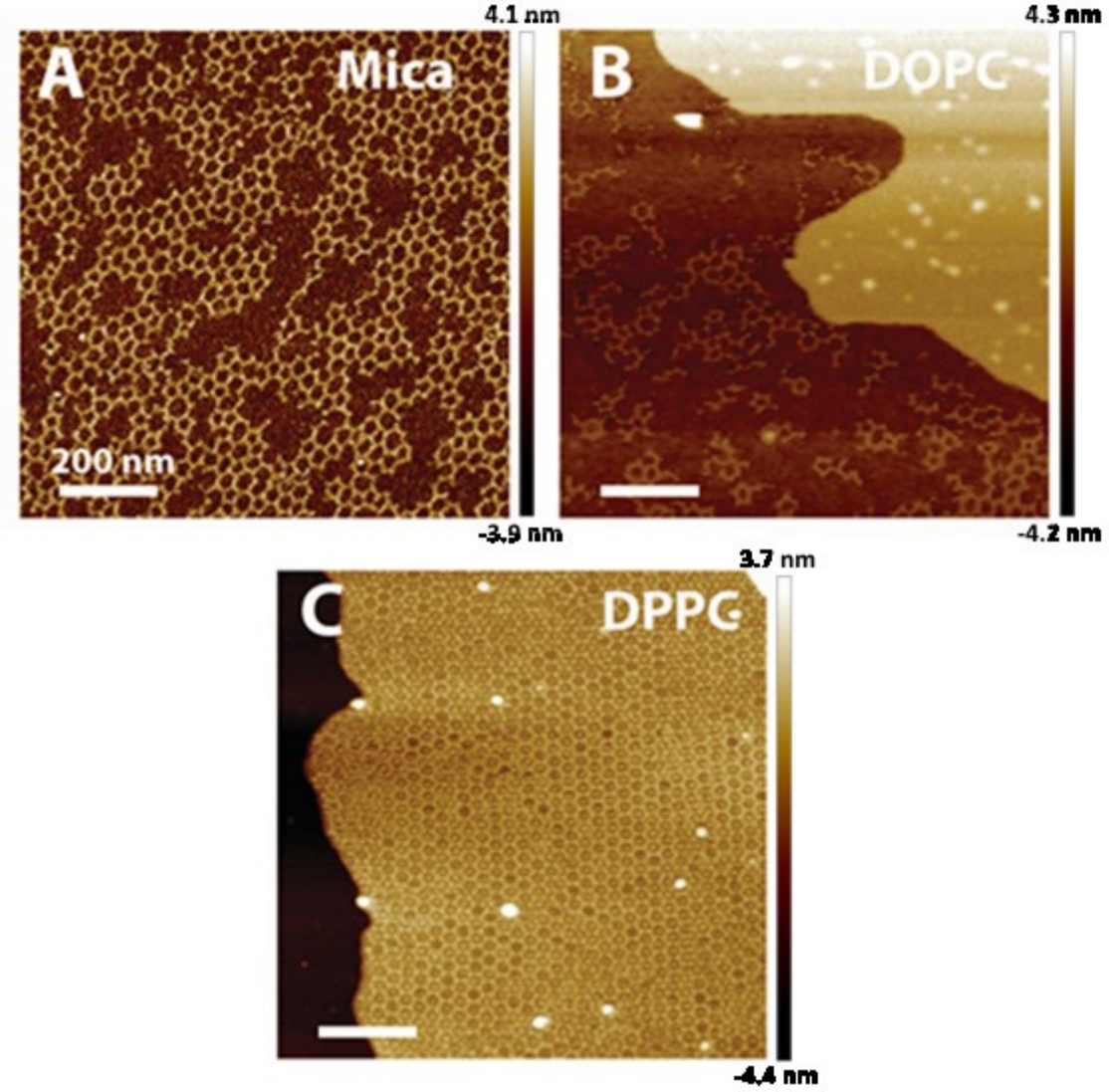

Figure 3.5: Liquid AFM images for the NC_{16}-modified networking tiles on mica (A), DOPC (B), and DPPC (C). Scale bars – 200 nm.

Fast Fourier transform (FFT) analysis is used to quantify the registry of the hexagonally packed tile networks based on the periodicity (Figure 3.6). This analysis compares the spacing periodicity and generates the repeating distance value between features in a particular direction. The hexagonal pattern periodicity for the networks formed by the unmodified network on mica, the cholesterol-modified network on DOPC and the NC_{16}-modified tile on DPPC are shown in Figure 3.6. The samples show similar values for the periodicity observed in three axes, with the cholesterol-tile networks on DOPC showing a slightly higher value possibly linked to the bilayer

anchor packing interactions or membrane fluidity. This indicates that the cholesterol and NC_{16}-modified networks retain the same high degree of precise positioning as observed in the original design. This demonstrates that the fidelity of Watson-Crick base-pairing is maintained when the anchor group has a strong affinity with the bilayer and is well-accommodated within the lipid bilayer.

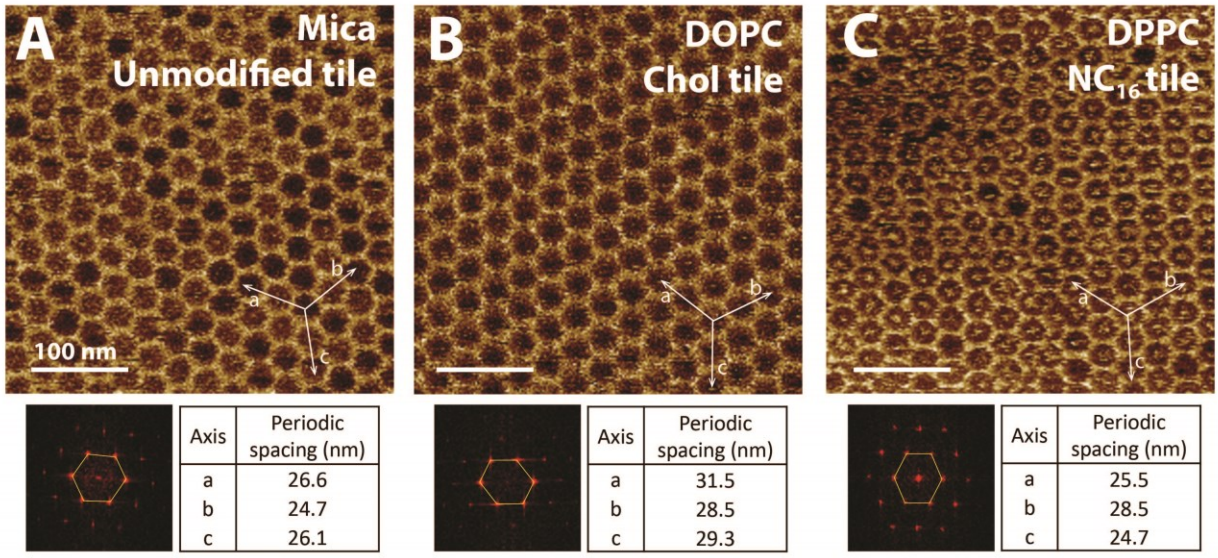

Axis	Periodic spacing (nm)
a	26.6
b	24.7
c	26.1

Axis	Periodic spacing (nm)
a	31.5
b	28.5
c	29.3

Axis	Periodic spacing (nm)
a	25.5
b	28.5
c	24.7

Figure 3.6: Fast Fourier Transform (FFT) of images of network forming tiles on the different surfaces to analyze the network periodic spacing. Unmodified tiles on mica (A), cholesterol-modified (Chol) tiles on DOPC (B) and NC_{16}-modified tiles on DPPC (C). Inserts show corresponding 2D Fourier transform patterns. Scale bars – 100 nm.

These results suggest that by selecting the appropriate hydrophobic anchor, specific bilayers can be targeted for network deposition. We therefore designed an experiment in which vesicles were prepared from DPPC:DOPC mixtures. In this mixed lipid system, the two types of lipids phase separate leading to the formation of enriched lipids domains. Based on the results we have shown, we expect that a cholesterol tile will show hexagonal arrays on the DOPC domains while the palmitoyl tile will form these patterns on DPPC domains exclusively. Our experiment use a lipid ratio of 70:30 DPPC:DOPC for vesicle preparation.[36] These samples were deposited on mica and show extended bilayer surfaces of 5 nm in height. Phase separation observed by AFM is shown in Figure 3.7A. DPPC domains are found to be 0.7 nm higher than the DOPC domains, which is in

good agreement with literature values[35,52] and the relative amount of DPPC area to that of DOPC correlates well to the lipid mixture composition.

Pre-assembled cholesterol tile networks are deposited on the 70:30 DPPC:DOPC mixed bilayer. The tile networks are observed to have two different modes of assembly on each respective lipid domain (Figure 3.7B). In this image the dark area corresponds to the DOPC enriched domain, and a clear hexagonal packing can be observed, which resembles our previous result (Figure 3.3). The brighter regions are the DPPC enriched domains, and these surfaces show the clear registry of an alternating herringbone-like pattern (Figure 3.7B).

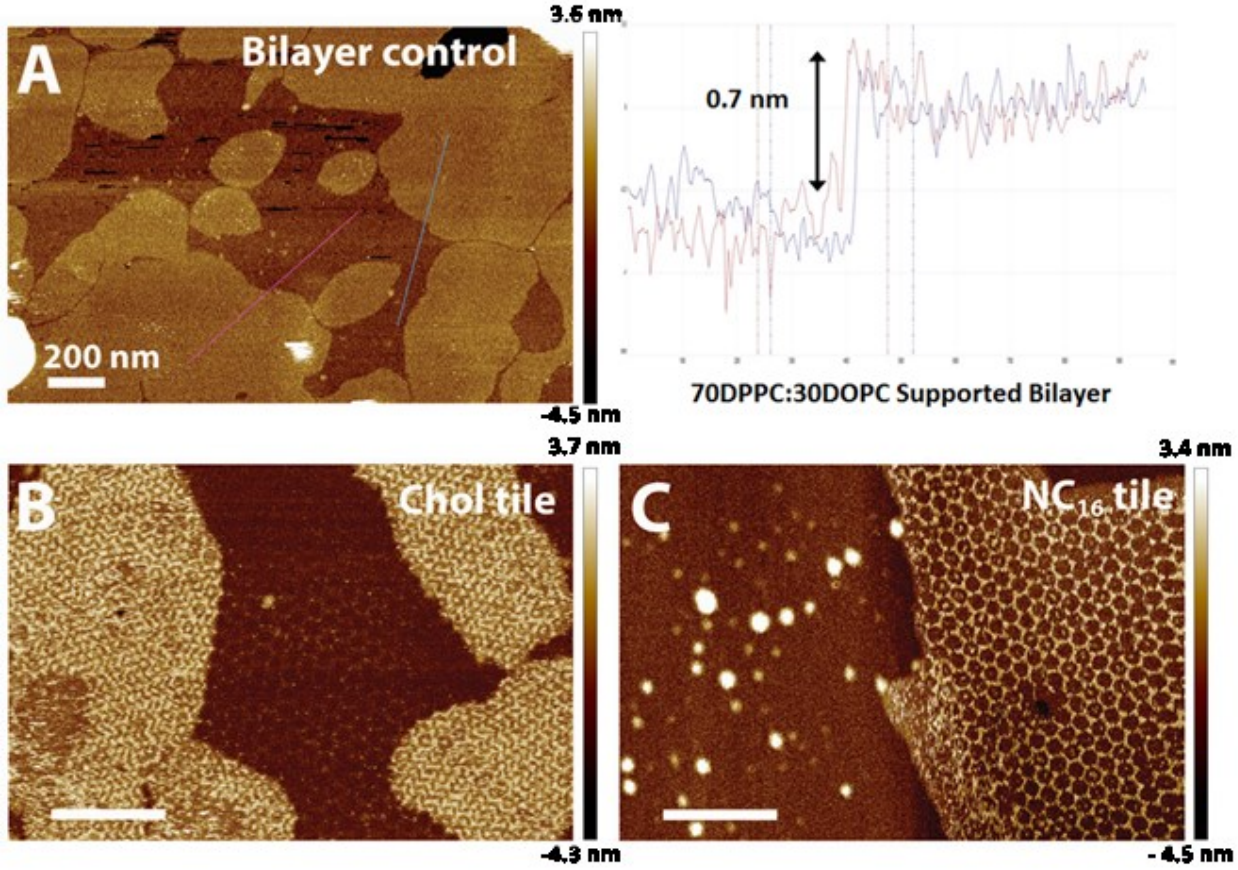

Figure 3.7: Liquid AFM images for the deposition of cholesterol/NC_{16}-modified networking tiles on mixed lipid bilayers (70:30 DPPC:DOPC): (A) mixed bilayer control (no DNA tiles), with height measurements indicated as the marked lines across the AFM image (B) cholesterol-modified networking tiles, (C) NC_{16}-modified networking tiles. Scale bars – 200 nm.

The AFM results for NC_{16} tile networks deposited on the mixed bilayer are shown in Figure 3.7C. Large bilayer domains coated in networked material with the same hexagonal packing previously seen for NC_{16} tile networks are observed (Figure 3.7C). In these images the higher region corresponds to DPPC and confirm targeted network deposition exclusively on these saturated domains. The darker region is the DOPC enriched domain and we see a similar morphology to the NC_{16} tile networks deposited on DOPC alone (Figure 3.5). The patterned and bare regions of bilayer are confirmed as actual bilayer and not mica by noting the diagnostic 3-5 nm (depending on the lipid) step along all edges of the extended mixed bilayer (see Experimental Section 3.5.10).

Thus, bilayer-tile interactions not only determine the self-assembly outcome of DNA tiles, but can also spatially direct these networks to different domains. Liposome-anchored spherical nucleic acids are shown to efficiently silence gene expression and are promising therapeutic tools.[53] It will be interesting to create liposome supported nucleic acids tiles such as the ones described here, and examine the effect of patterning and lipid-selective interactions on their therapeutic efficiency. Moreover, different hydrophobic anchors on tiles may direct these structures to different cellular membrane domains and can be used to finely tune cellular recognition processes.

The last type of tile we examined is modified with $3C_{12}$. This anchoring unit consists of three repeats of dodecane diol separated by phosphate groups (Figure 3.1A). This polymer has been previously used by our group to form scaffolded micelle structures for potential therapeutic and light-harvesting applications.[38] Its hydrophobic self-assembly requires the presence of divalent cations, such as Mg^{2+} to offset the repulsions between the phosphate groups that separate the C_{12} chains. On bare mica, the $3C_{12}$-modified networking tiles form hexagonal networks, but these are shorter-ranged and include a large number of defects, consistent with steric factors introduced by the central hydrophobic oligomer (Figure 3.8A). On the other hand, the $3C_{12}$-modified networked tiles deposited on DOPC and DPPC do not show hexagonally ordered material, and very little misassembled network is seen on the surrounding mica regions (Experimental Section 3.5.8 Figure 3.25). This suggests that in the presence of lipid bilayers the $3C_{12}$ modified tile networks are significantly disrupted, possibly through non-specific hydrophobic aggregation.

As a control experiment, we examine the assembly of blunt-ended DNA tiles that should not exhibit Watson-Crick base-pairing to form hexagonal networks (see Experimental Section 3.5.8).

Unmodified blunt ended tiles show non-specific end-to-end association, and prefer to deposit on bare mica, rather than on bilayer surfaces. The cholesterol and NC_{16} substituted blunt-ended tiles generate misassembled materials, and show some preferential deposition on compatible surfaces (e.g., cholesterol-tile prefers DOPC rather than bare mica).

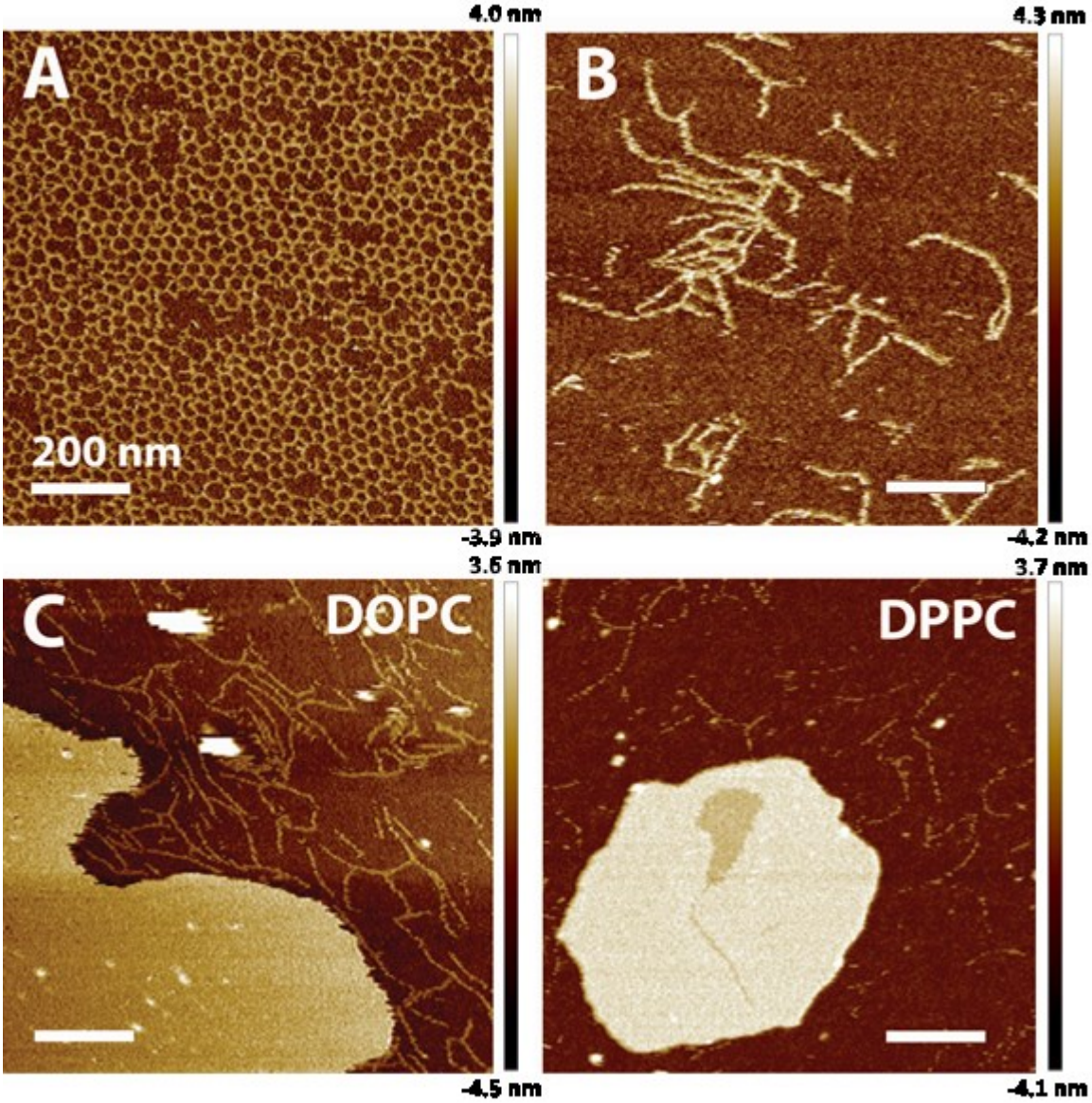

Figure 3.8: Liquid AFM images in fluid for $3C_{12}$ modified tiles: (A) networking tile on mica, (B) blunt-ended tile on mica, (C) blunt-ended tile on DOPC and DPPC. Scale bars – 200 nm.

In contrast, the blunt-ended $3C_{12}$ tile gave a distinct nanofiber structure, rather than the previously observed misassembled networks, when deposited on bare mica. These filaments were observed to have a height of 2.2 ± 0.1 nm (Figure 3.8B). The formation of these fibers is likely a result of a self-assembly mode dominated by the hydrophobic packing of the $3C_{12}$ anchor in the absence of the DNA sticky-ends. This central hydrophobic anchor minimizes contact with the aqueous medium by associating with hydrophobic polymeric anchors of the other tiles, possibly creating a fiber with parallel tiles where the core is a hydrophobic domain and the corona is the 3PS DNA portion. A proposed structure for the assembly is shown in Figure 3.9. On DPPC or DOPC-coated mica, these filaments are also observed, but appeared exclusively on the surrounding mica, rather than the lipid bilayers (see Experimental Section 3.5.8 Figure 3.26), suggesting a hydrophilic exterior. Thus, the bilayers do not disrupt the hydrophobic packing of the DNA tiles, and their DNA exterior preferentially interacts with the bare mica surfaces.

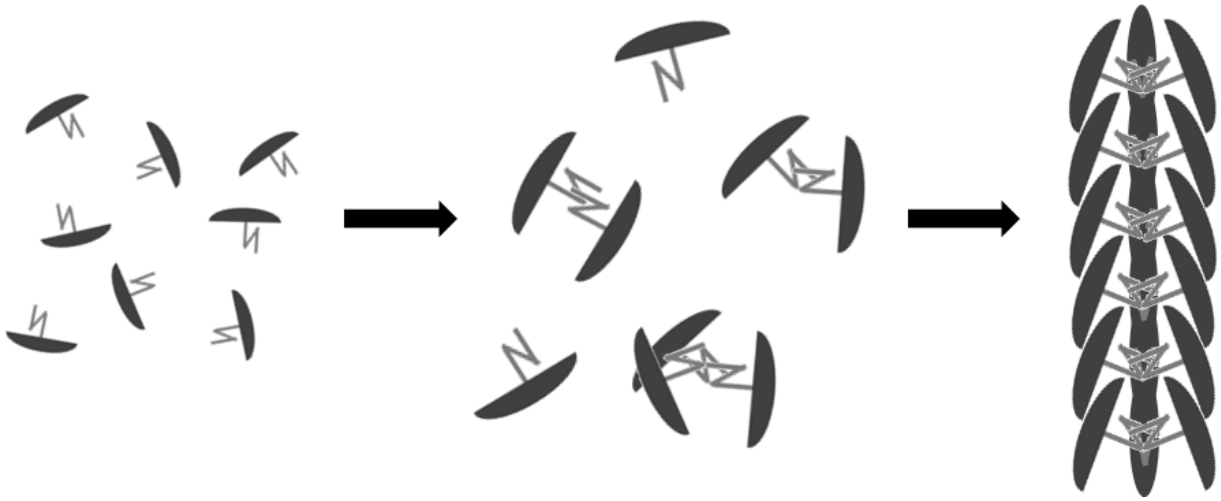

Figure 3.9: A proposed representation of the assembled filamentous structure for blunt ended $3C_{12}$ modified tiles. The DNA 3 point star tile portion is represented by the dark grey umbrella and the $3C_{12}$ chains are the lighter gray strands. Filamentous material may be formed through hydrophobic aggregation of the $3C_{12}$ chains. The size of the tile head group relative to the hydrophobic anchor drives the formation of the filamentous structure.

3.4 Conclusion

In conclusion, we have examined the interaction of hydrophobically modified DNA tile networks with supported bilayer environments and the interplay of Watson-Crick base-pairing with hydrophobic interactions. This study has resulted in a number of observations: (1) when the anchor binds well to the bilayer through compatible bilayer packing, Watson-Crick base-pairing can be maintained. This occurs for cholesterol tiles with DOPC and palmitoyl analogue (NC_{16}) tiles with DPPC. (2) As little as 20% cholesterol labeling of the tiles can result in high-fidelity assembly on supported DOPC bilayers. (3) The tile assembly is selective to its bilayer with matched properties: when mixed DOPC:DPPC bilayers are generated, the cholesterol tile forms hexagonal patterns on the DOPC-enriched domains, while the palmitoyl analogue associates with DPPC-enriched domains. (4) Cholesterol-tiles on DPPC show a close-packed structure resembling a herringbone motif, instead of the hexagonal pattern, likely as a result of altered interactions with DNA-anchor and the bilayer. (5) On the other hand, tiles which do not bind strongly to the bilayer do not show any ordering on these surfaces. Interestingly, blunt-ended tiles modified with a dodecane diol oligomer ($3C_{12}$) assemble into nanofibers as a result of hydrophobic self-recognition. (6) It was shown that by combining DNA network structures with lipid self-assembly, the long range ordering of DNA can be significantly increased.

Thus, ordered DNA networks can be selectively anchored onto their matched lipid bilayers without disruption of the Watson-Crick base-pairing that holds them together. DNA networks landed on fluid bilayers such as DOPC may be able to diffuse in two-dimensions allowing for potential error correction between network domains. This can lead to larger extended networks with fewer defects. It would also be of particular interest to study how the tethered networks affect the biophysical properties of lipid bilayers such as fluidity or phase transition. The materials created here can find applications in a number of areas, such as oligonucleotide therapeutics, patterned surfaces for selective cell recognition, templates for light-harvesting units, as well as long range ordered, and fluid surfaces to interface DNA nanostructures with solid substrates for materials applications.

3.5 Experimental Section

3.5.1 General

The staining solution Gel Red™ is purchased from VWR. Acetic acid, tris(hydroxymethyl)-aminomethane (Tris) and urea are used as purchased from Aldrich for buffer preparations. Boric acid and acetic acid are purchased from Fisher Scientific and used as received. All nucleosides (dA, dC, dG and T), as well as the universal 1000Å LCAA-CPG supports with loading densities between 25-40 μmol/g, and reagents used for automated DNA synthesis are purchased through Bioautomation Corporated. Desalting, size-exclusion columns (Sephadex G-25, DNA grade) are purchased from Glen Research. The 1×TAMg buffer consists of 45 mM Tris and 12.6 mM Mg(OAc)2·6H2O; the pH of the 1×TAMg buffer is adjusted to 8 using glacial acetic acid.

3.5.2 Synthesis of Oligonucleotides and Modified DNA Conjugates

A Mermade MM6 synthesizer from Bioautomation is used for standard automated oligonucleotide phosphoramidite solid-phase synthesis. All gel electrophoresis experiments are carried out using an acrylamide 20 × 20 cm vertical Hoefer 600 electrophoresis kit. Annealing of all structures is conducted using an Eppendorf Mastercycler Pro. Quantification of DNA and DNA-conjugates is performed using UV absorbance measurements at 260 nm performed using a Thermo Scientific NanoDrop Lite.

Cholesterol (Chol) and dodecanediol (C12) modifications are purchased from Glen Research and used directly in manual off-column phosphoramidite coupling reactions or as ready to use pre-functionalized controlled pore glass (CPG) columns from which the oligonucleotide can be directly grown (3’ cholesterol). All unmodified samples are purified and characterized using denaturing polyacrylamide gel electrophoresis (PAGE).

DNA synthesis is performed on a 1 μmol scale, starting from a universal 1000 Å CPG solid-supports. Coupling efficiency is monitored after removal of the dimethoxytrityl (DMT) 5′-OH protecting groups. For off-column couplings, an equal volume of ethylthiotetrazole (0.1M in acetonitrile, Glen Research) is combined with each phosphoramidite and manually coupled on the DNA solid support with an extended reaction time of 15 minutes in the glove box. After coupling,

supports are removed from the glove box and returned to the DNA synthesizer for oxidation, capping and deblock steps. All sequences, modified and unmodified, are fully deprotected in concentrated ammonium hydroxide (60 ^{o}C/24 hours).

Table 3.1: Oligonucleotides are prepared via solid-phase synthesis. The three-point-star motif component strands (S1, S2, S3A, S3B) are designed by the Mao group. Non-nucleoside phosphoramidites cholesterol (Chol), palmitoyl (NC_{16}), and dodecane trimer ($3C_{12}$) are inserted selectively into individual sequences as indicated in either the 3' or 5' position.

Number	Name	Sequence (5′ → 3′)
1	**S1**	AGGCACCATCGTAGG TTT CTTGCCAGGCACCATCGTAGG TTT CTTGCCAGGCACCATCGTAGG TTT CTTGCC
2	**S2**	ACTATGCAACC TGCCTGGCAAG CCTACGATGG ACACGGTAACG
3	**S3A (Blunt)**	CGTTACCGTGTGGTTGCATAGT
4	**S3B (Network)**	CGCG CGTTACCGTGTGGTTGCATAGT CATG
5	**S1_Chol**	AGGCACCATCGTAGG TTT CTTGCCAGGCACCATCGTAGG TTT CTTGCCAGGCACCATCGTAGG TTT CTTGCC-**Chol**
6	**S1_NC_{16}**	**NC_{16}**-AGGCACCATCGTAGG TTT CTTGCCAGGCACCATCGTAGG TTT CTTGCCAGGCACCATCGTAGG TTT CTTGCC
7	**S1_$3C_{12}$**	AGGCACCATCGTAGG TTT CTTGCCAGGCACCATCGTAGG TTT CTTGCCAGGCACCATCGTAGG TTT CTTGCC-**C_{12}-C_{12}-C_{12}**

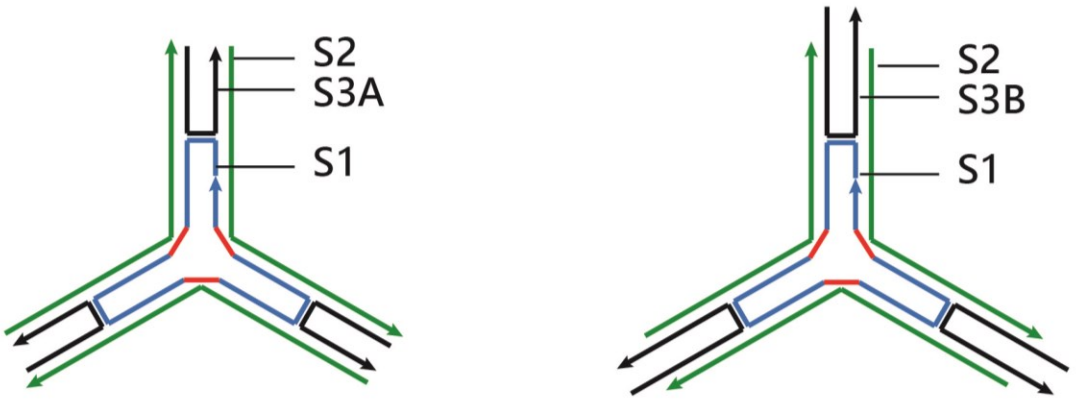

Figure 3.10: Unmodified tile. Left, blunt tile. Right, networking tile.

All crude DNA products are purified on 8% polyacrylamide/8M urea polyacrylamide denaturing gel (PAGE; up to 20 OD260 of crude DNA per gel) at constant current of 30 mA for 2 hours (30 min. at 250V followed by 1.5 hr at 500V), using 1x TBE buffer. DNA products are excised from gels by visualizing the bands on a fluorescent TLC plate wrapped in plastic wrap and illuminated with a UV lamp (254 nm). The gel pieces are crushed and incubated in 12 mL of sterile water at 60 ºC for 12-16 hours. Samples are then dried to 1 mL, desalted using size exclusion chromatography (Sephadex G-25), and quantified (OD260) using UV-Vis spectroscopy. Smaller strands (<50 base pairs) are purified using a 15% PAGE mixture and running conditions of 30 min at 250V followed by 45 min at 500V, followed by the same work up.

3.5.3 Assembly and Characterization of Modified Three-Point Star Tiles

All component strands are run on denaturing PAGE to determine their purity. As seen in Figure 3.9, strands show a single discreet band corresponding to the intended DNA strand. To prepare all eight tile variations (unmodified, cholesterol, NC_{16}, $3C_{12}$ with networking or blunt ends) strands S1 (central strand), S2 (tile arms), and S3 (sticky/blunt ends) are combined at a molar ratio of 1:3:3 in 1xTAMg buffer for a final tile concentration of 0.5 μM. All hydrophobic modifications are positioned at the 3'/5' ends of S1. S3 has two variations: S3A, which is the blunt end, and S3B, which is the networking sticky ends. Tiles are composed of the combinations of strands shown in Table 3.2.

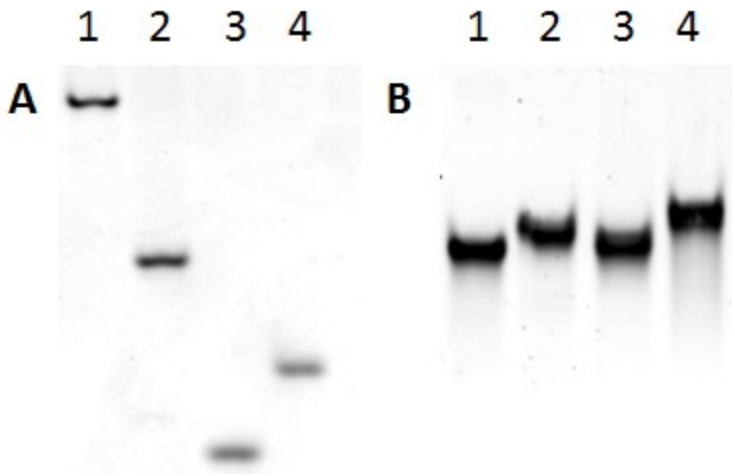

Figure 3.11: (A) Denaturing PAGE analysis of DNA strands. Denaturing PAGE (12%, 1xTBE) gel ran for 30 minutes at 250V and then 1 hr at 500 V; Lane 1-S1, Lane 2- S2, Lane 3- S3A, Lane 4- S3B. (B) Denaturing PAGE Analysis of modified S1 strands Denaturing PAGE (12%, 1xTBE) gel ran for 30 minutes at 250V and then 1 hr at 500 V; Lane 1-S1, Lane 2- S1-NC_{16}, Lane 3- S1-Cholesterol, Lane 4- S1-$3C_{12}$.

Table 3.2: Strand combinations for tile assemblies. Strands are combined at the ratio of 1(S1):3(S2):3(S3).

Tile	**Strands**
Blunt Unmodified tile	1, 2, 3
Networking Unmodified tile	1, 2, 4
Blunt Cholesterol tile	5, 2, 3
Networking Cholesterol tile	5, 2, 4
Blunt NC_{16} tile	6, 2, 3
Networking NC_{16} tile	6, 2, 4
Blunt $3C_{12}$ tile	7, 2, 3
Networking $3C_{12}$ tile	7, 2, 4

All tile constructs are characterized by native PAGE to confirm correct assembly. Tiles are sequentially constructed in 1xTAM and subjected to a quick annealing protocol from 95ºC to 4ºC over 2 hours (this protocol is only applied to PAGE samples described here). A slight excess of strands S2 and S3 are used to promote tile assembly. PAGE is performed for each tile sample at 250V in 6% native PAGE for 2.5 to 3 hours (Figures 3.12-3.16). All samples that are prepared for deposition on bilayer are similarly prepared but annealed from 75ºC to 10ºC over 42 hours to maximize network formation.

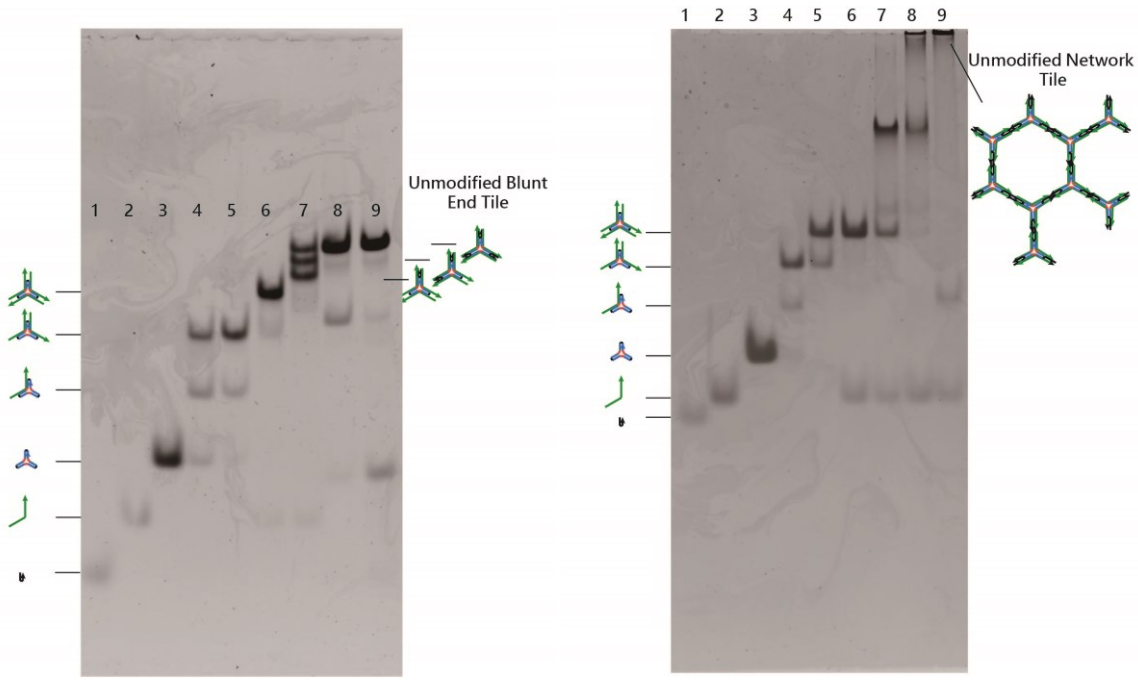

Figure 3.12: Native PAGE analysis of DNA tile assembly. 6% Native PAGE run for 2.5 to 3 hours at 250V. (Left) Assembly of blunt unmodified tile. Lane 1: S3A, Lane 2: S2, Lane 3: S1, Lane 4: S1 + S2 (1 : 1.2 molar ratio), Lane 5: S1 + S2 (1 : 2.4), Lane 6: S1 + S2 (1 : 3.6), Lane 7: S1 + S2 + S3A (1 : 3.6 : 1.2), Lane 8: S1 + S2 + S3A (1 : 3.6 : 2.4), Lane 9 final product: S1 + S2 + S3A (1 : 3.6 : 3.6). (Right) Assembly of network unmodified tile. All the lanes contain the same strand combinations as the left gel except that all the S3A strands are replaced with S3B.

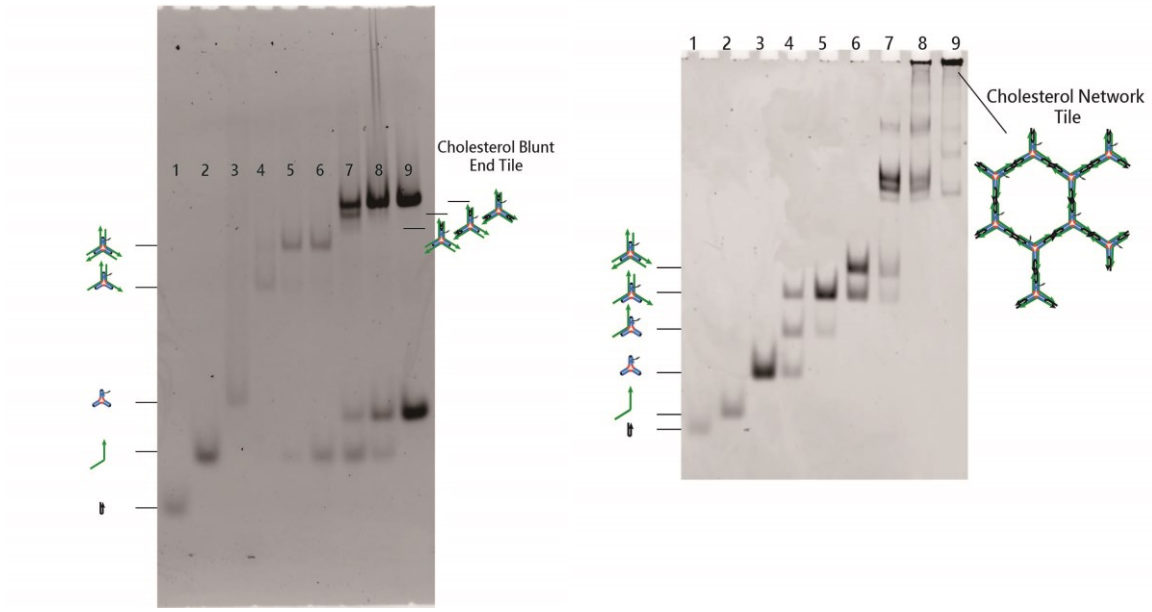

Figure 3.13: Native PAGE analysis of cholesterol tile assembly. 6% Native PAGE run for 2.5 to 3 hours at 250V. (Left) Assembly of blunt cholesterol modified tile. Lane 1: S3A, Lane 2: S2, Lane 3: S1-Cholesterol, Lane 4: S1-Cholesterol + S2 (1 : 1.2 molar ratio), Lane 5: S1-Cholesterol + S2 (1 : 2.4), Lane 6: S1-Cholesterol + S2 (1 : 3.6), Lane 7: S1-Cholesterol + S2 + S3A (1 : 3.6 : 1.2), Lane 8: S1-Cholesterol + S2 + S3A (1 : 3.6 : 2.4), Lane 9 final product: S1-Cholesterol + S2 + S3A (1 : 3.6 : 3.6). (Right) Assembly of network cholesterol modified tile. All lanes contain the same strand combinations as the left gel except that all S3A strands are replaced with S3B.

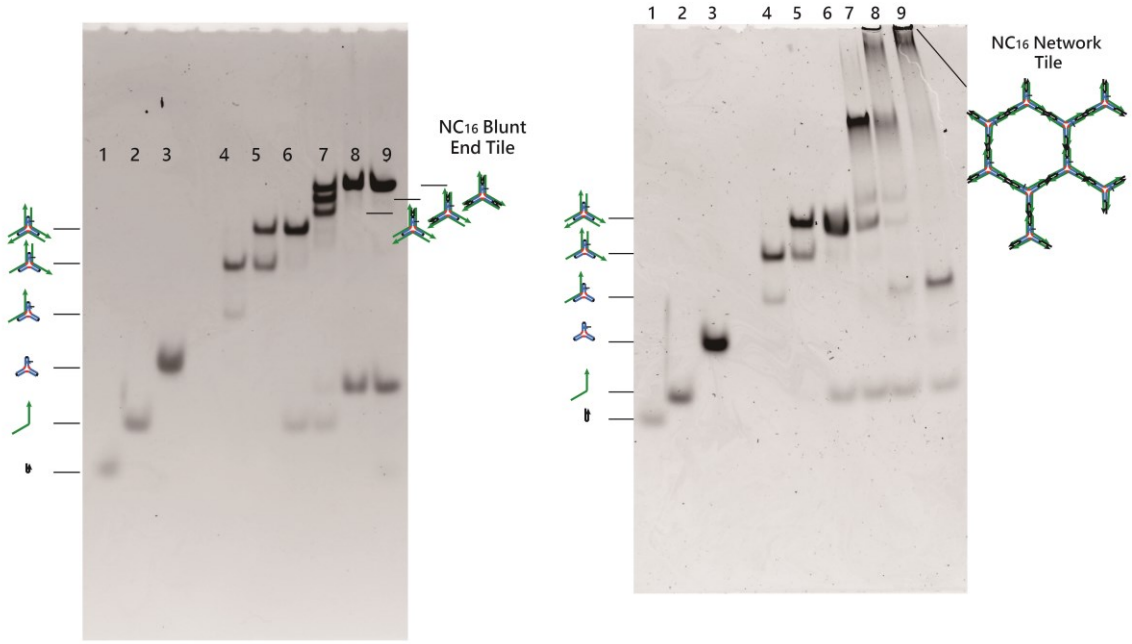

Figure 3.14: Native PAGE analysis of NC_{16} tile assembly. 6% Native PAGE run for 2.5 to 3 hours at 250V. (Left) Assembly of a blunt NC_{16} modified tile. Lane 1: S3A, Lane 2: S2, Lane 3: S1-NC_{16}, Lane 4: S1-NC_{16} + S2 (1 : 1.2 molar ratio), Lane 5: S1-NC_{16} + S2 (1 : 2.4), Lane 6: S1-NC_{16} + S2 (1 : 3.6), Lane 7: S1-NC_{16} + S2 + S3A (1 : 3.6 : 1.2), Lane 8: S1-NC_{16} + S2 + S3A (1 : 3.6 : 2.4), Lane 9 final product: S1-NC_{16} + S2 + S3A (1 : 3.6 : 3.6). (Right) Assembly of a network NC_{16} modified tile. All lanes contain the same strand combinations as the left gel except that all the S3A strands are replaced with S3B.

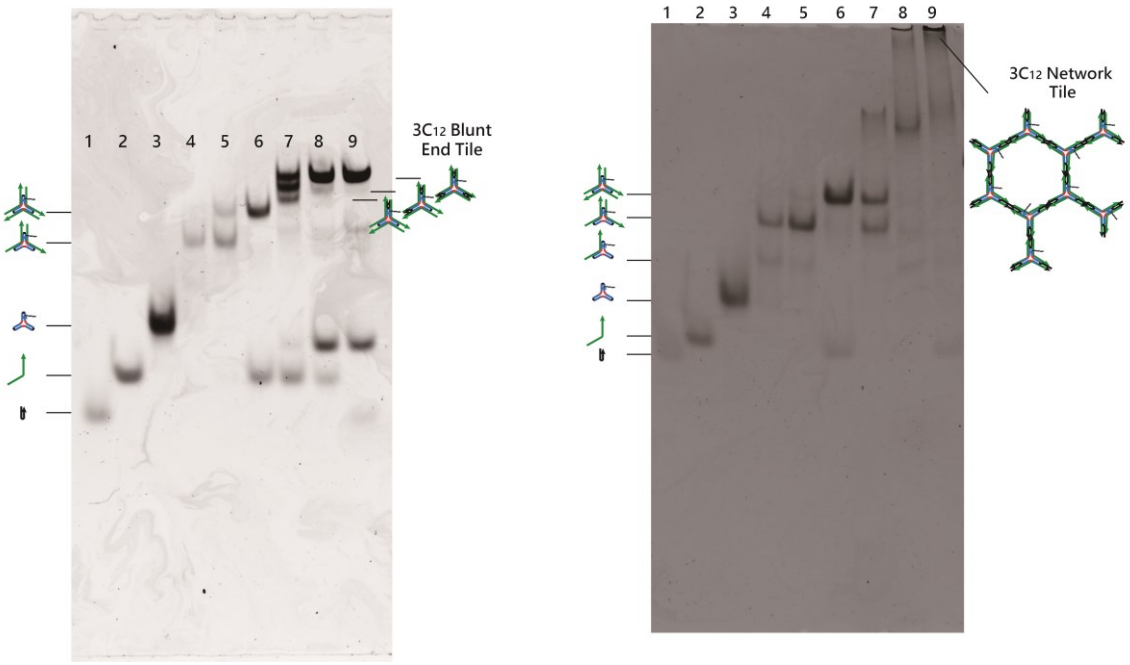

Figure 3.15: Native PAGE analysis of $3C_{12}$ tile assembly. 6% Native PAGE run for 2.5 to 3 hours at 250V. (Left) Assembly of a blunt $3C_{12}$ modified tile. Lane 1: S3A, Lane 2: S2, Lane 3: S1-$3C_{12}$, Lane 4: S1-3C12+ S2 (1 : 1.2 molar ratio), Lane 5: S1-$3C_{12}$+ S2 (1 : 2.4), Lane 6: S1-$3C_{12}$+ S2 (1 : 3.6), Lane 7: S1-$3C_{12}$+ S2 + S3A (1 : 3.6 : 1.2), Lane 8: S1-$3C_{12}$+ S2 + S3A (1 : 3.6 : 2.4), Lane 9 final product: S1-$3C_{12}$+ S2 + S3A (1 : 3.6 : 3.6). (Right) Assembly of a network $3C_{12}$ modified tile. All the lanes contain the same strand combinations as the left gel except that the S3A strands are replaced with S3B.

3.5.4 Preparation of Palmitoyl (NC_{16}) modified S1 strand

Synthesis of Palmitoyl (NC_{16}) Anchor:

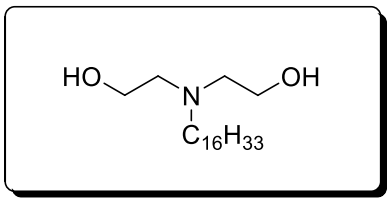

2,2'-(hexadecylazanediyl)diethanol:

The synthesis is adapted from Boukli et al.[54] 2,2'-(hexadecylazanediyl)diethanol: Diethanolamine (3.8 g, 36 mmol) and 1-Hexadecylbromide (9.19 g, 30 mmol) are added to dried RBF charged with $KHCO_3$ (6.02 g, 60 mmol) and KI (0.5 g, 3 mmol) than mixed in dry acetonitrile (80 mL). The reaction mixture is heated under reflux for 3 hours, cooled down and the solvent removed under vacuum. Residues are taken in dichloromethane (100 mL) and washed with water (3 x 100 mL). Organic layer is dried with $MgSO_4$ and solvent removed under vacuum to obtain a yellow oil solidifying fast on standing, forming orange waxy solid as a pure product in quantitative yield (9.82 g).

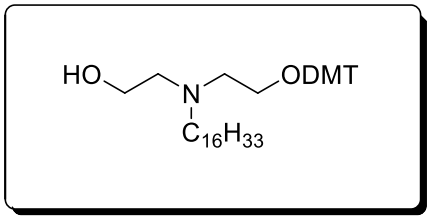

2-((2-(bis(4-methoxyphenyl)(phenyl)methoxy)ethyl)(hexadecyl)amino)ethanol:

2,2'-(hexadecylazanediyl)diethanol (3 g, 9.1 mmol) is dissolved in a mixture of dry CH_2Cl_2 (20 mL) and dry triethylamine (4 mL) at RT. 1 equivalent of DMT chloride (3.08 g, 9.1 mmol) is added dropwise and the reaction mixture changed colour from pink to yellow in 30 minutes. It is stirred in RT for 2 more hours. The solvent is evaporated and the resulting yellow oily residue is purified by chromatography on triethylamine pre-treated silica gel with slow gradient of EtOAc/Hexane (0-15%) to obtain the product as a sticky yellow oil: 1.32 g, 23% (pure fractions).

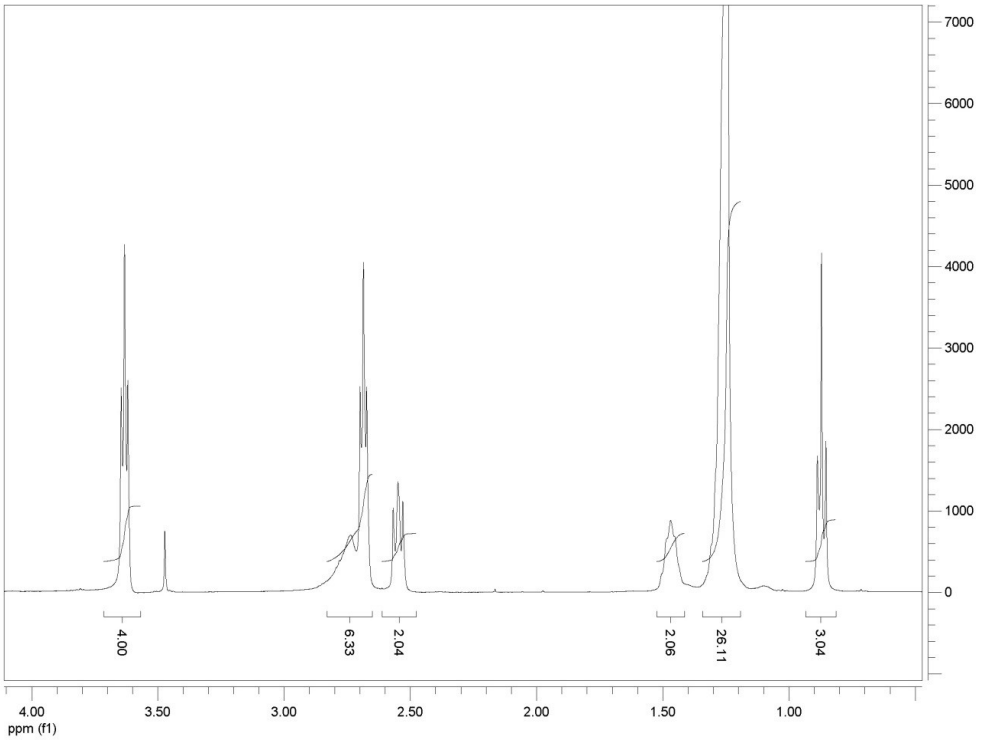

Figure 3.16: 2,2'-(hexadecylazanediyl)diethanol (Top) 1H NMR (400 MHz, CDCl3) δ 0.87 (t, J = 7.0 Hz, 3H), 1.15-1.36 (m, 26H), 1.36-1.54 (br. m, 2H), 2.55 (t, J = 7.6 Hz, 2H), 2.69 (t, J = 5.4 Hz, 4H), 2.74 (br. s, 2H), 3.63 (t, J = 5.4 Hz, 4H).

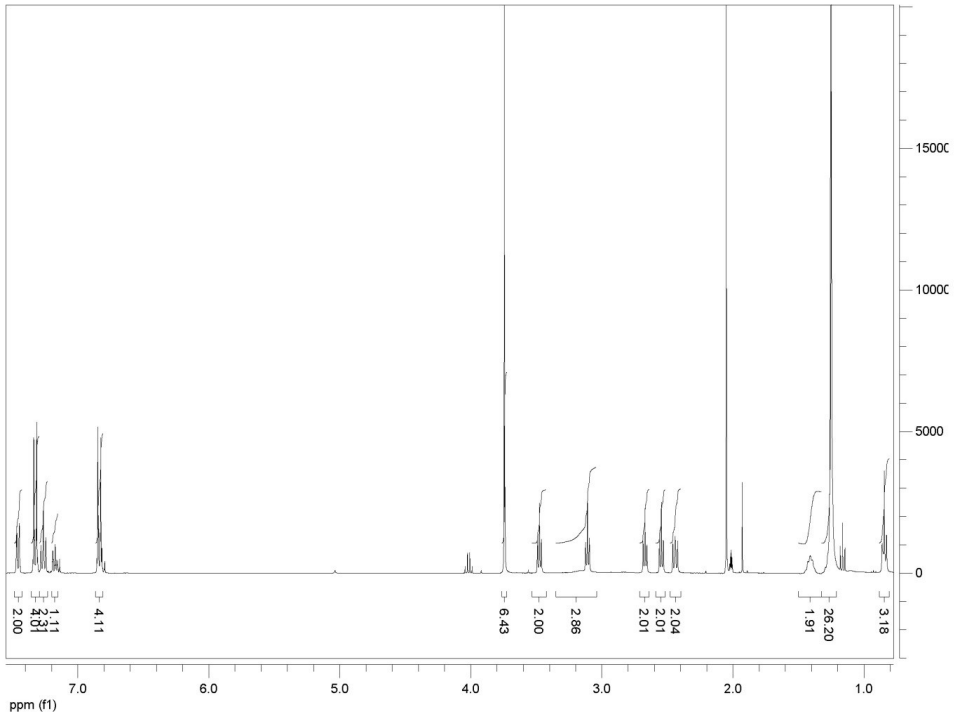

Figure 3.17: 2-((2-(bis(4-methoxyphenyl)(phenyl)methoxy)ethyl)(hexadecyl)amino)ethanol. (Top) 1H NMR (400 MHz, Acetone-d6) δ 0.84 (t, J = 7.0 Hz, 3H), 1.25 (br. s, 26H), 1.41 (br. m, 2H), 2.44 (t, J = 7.4 Hz, 2H), 2.55 (t, J = 6.0 Hz, 2H), 2.69 (t, J = 5.9 Hz, 2H), 3.11 (t, J = 5.9 Hz, 2H), 3.17 (br. s, 1H), 3.48 (t, J = 6 Hz, 2H), 3.74 (s, 6H), 6.82 - 7.47 (DMT, 13H).

3.5.5 Synthesis and Coupling of Palmitoyl (NC_{16}) Phosphoramidite:

Synthesis of NC16 phosphoramidite:

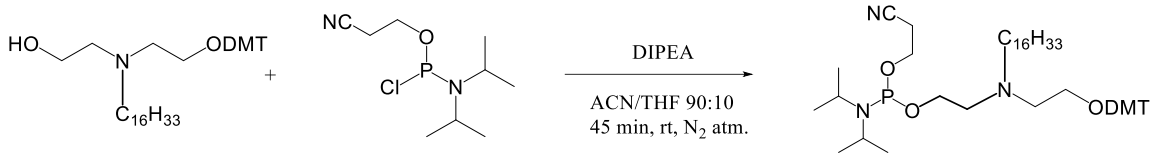

Figure 3.18: General synthesis scheme for NC_{16} phosphoramidite.

Diisopropylethylamine and N,N-Diisopropylamino cyanoethyl phosphonamidic-Cl are respectively purchased from Sigma-Aldrich and ChemGenes. In a 20 mL oven-dried round bottom

flask, monoprotected alcohol NC_{16} (31.6 mg, 0.050 mmol) is dissolved in a dry mixture of acetonitrile/tetrahydrofurane 90:10 (500 µl) under an inert atmosphere. Diisopropylethylamine (8.7 µL, 0.050 mmol, 1 eq.) and N,N-Diisopropylamino cyanoethyl phosphonamidic-Cl (10.0 µL, 0.045 mmol, 0.9 eq.) are added sequentially. The reaction is stirred at room temperature under an inert atmosphere during 45 minutes. Yield is found to be higher than 80% through 31P NMR (δ=147.4 ppm relative to phosphoric acid). The main by-product is suspected to be the hydrolysed N,N-Diisopropylamino cyanoethyl phosphonamidic-Cl due to trace moisture.

Coupling of NC_{16} phosphoramidite at the 5' end of DNA:

After DNA synthesis, CPG columns are removed from the synthesizer. Under a nitrogen atmosphere, the coupling is performed using off-column coupling: the crude mixture solution (200 µl, 0.1 M) is mixed with the ETT activator solution (200µL, 0.25 M) and is manually mixed through the CPG using a syringe. After twenty minutes, the solution is removed from the columns and the strands are cycled through the capping, oxidation and deblocking steps on the automated DNA synthesizer.

Strands are deprotected in a 50:50 mixture 28% aqueous ammonium hydroxide solution/methylamine (40 wt. % in water) for 3 hours at 60°C. The crude solution is collected from the solid support and concentrated under reduced pressure at 60°C. This crude solid is re-suspended in 1 mL Millipore water. Sephadex G-25 column desalting and filtration using 0.22µm centrifugal filter are then used prior to HPLC purification. The resulting solution is quantified by absorbance at 260 nm.

HPLC Analysis and Purification of Palmitoyl (NC_{16}) Phosphoramidite:

Solvents (0.22 µm filtered): 50mM Triethylammonium acetate (TEAA) buffer (pH 7.5) and HPLC grade acetonitrile. Elution gradient: 3-50% acetonitrile over 30 minutes at 60°C. Column: Hamilton PRP-1 5 µm 100 Å 2.1 x 150 mm. For each separation approximately 0.5 OD260 of crude strand is injected in a volume of 30µL in Millipore water. Detection is carried out using a diode-array detector, monitoring absorbance at 260 nm. Yield is found to be higher than 25%.

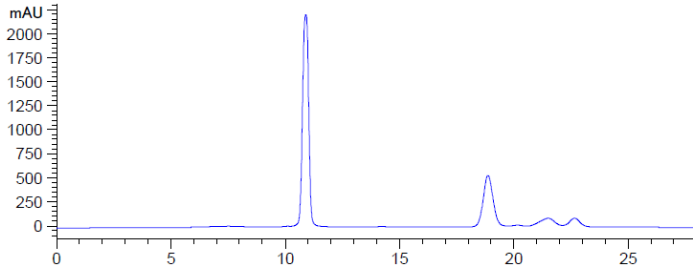

Figure 3.19: Crude HPLC trace (UV detection, λ=260 nm). First peak is due to unmodified DNA, second one is the expected product.

3.5.6 Mass Spectrometry of modified S1 strands

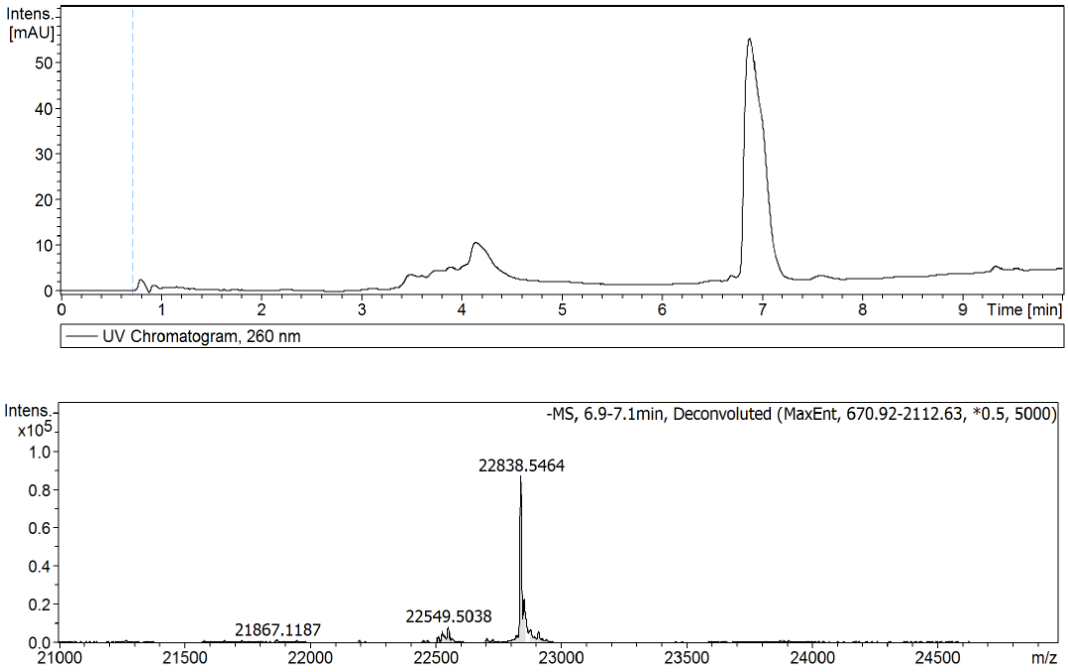

Figure 3.20: LC-MS spectra for the cholesterol modified S1 strand. (Top) LC, (Bottom) MS, measured peak 22838 m/z, expected peak 22839 m/z.

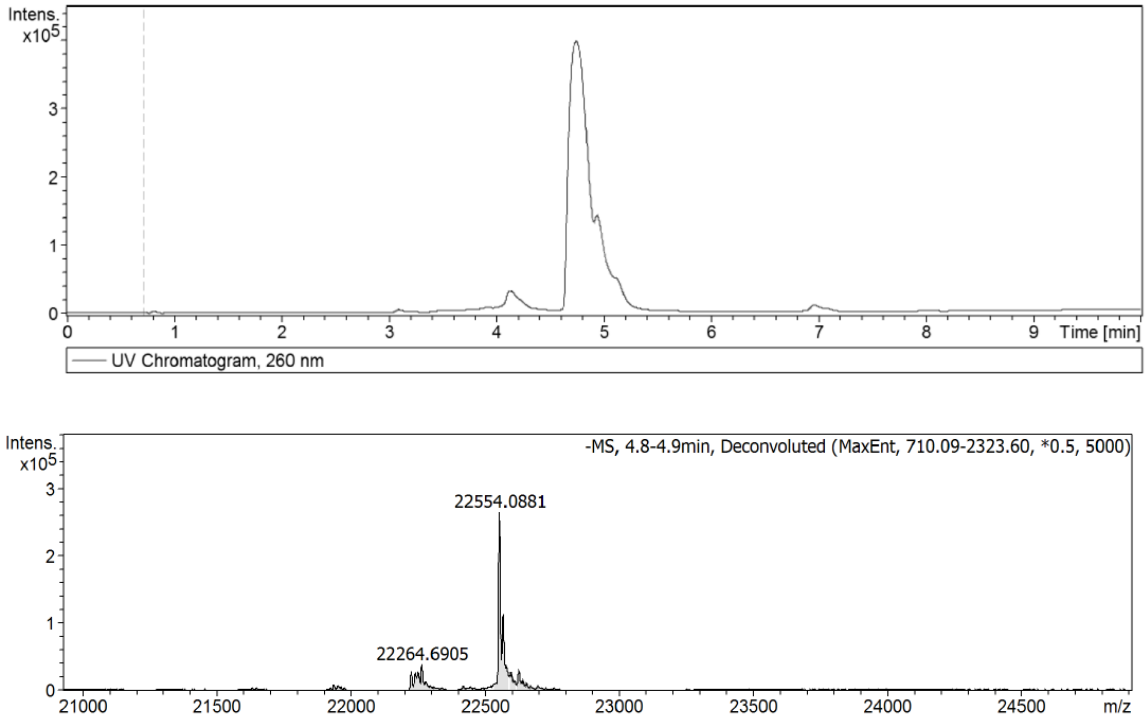

Figure 3.21: LC-MS spectra for the NC16 modified S1 strand. (Top) LC, (Bottom) MS, measured peak 22554 m/z, expected peak 22555 m/z.

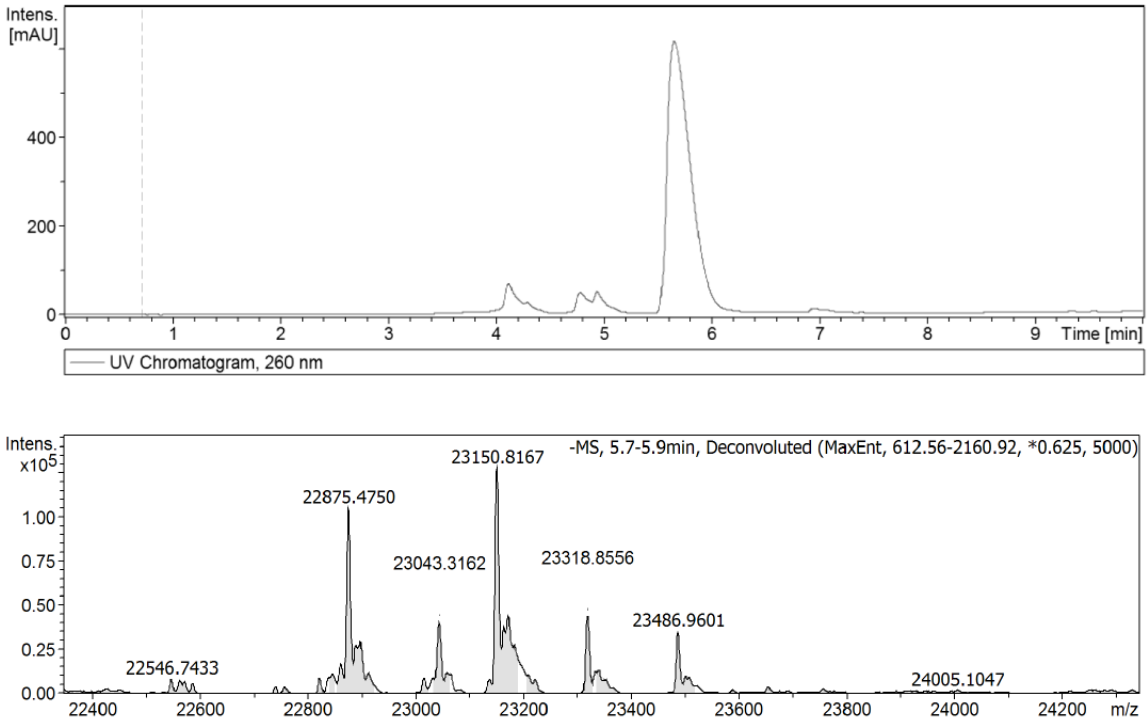

Figure 3.22: LC-MS spectra for the 3C12 modified S1 strand. (Top) LC, (Bottom) MS, measured peak 22875 m/z, expected peak 22872 m/z.

3.5.7 Lipid Vesicle Preparation

Lipid vesicles are prepared by adding 200 uL of a 25 mg/mL lipid stock solution in chloroform (Avanti Polar Lipids) to a round bottom flask. The chloroform is evaporated under vacuum, leaving an even layer of dried down lipid material on the flask wall. The flask is then left overnight under vacuum. The dried down film is resuspended in 5 mL of 1xPBS, vigorously vortexed for 5 minutes, and sonicated with gentle heating for 30 minutes. This lipid solution is then directly used for preparation of AFM samples. DLS results show a vesicle population of 57.4 ± 12.2 nm.

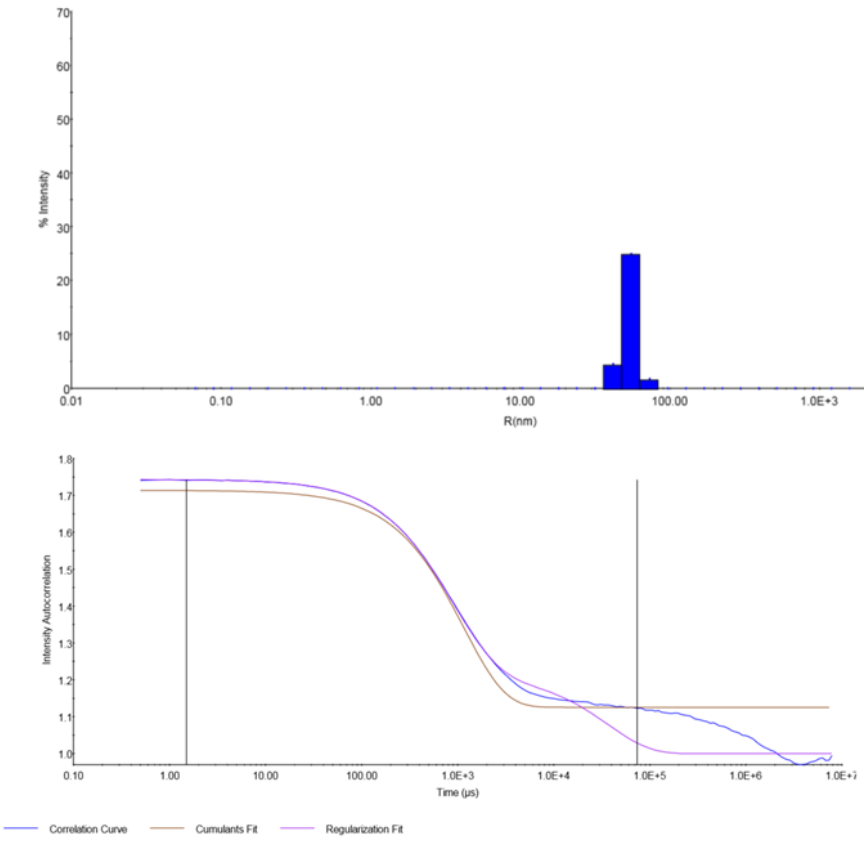

Figure 3.23: (Top) The bar graph shows the measured hydrodynamic radius of the prepared vesicles. (Bottom) Correlation curves for the DLS data.

3.5.8 AFM Sample Preparation and Imaging conditions

Vesicle solutions are used directly on mica. In these experiments the supported bilayers are deposited on freshly cleaved mica by adding 20 uL of a 1 mg/mL vesicle solution with 20 uL of 1xTAMg at RT. DOPC solutions on mica are incubated at RT for 20 minutes, while DPPC solutions and DOPC:DPPC mixtures are incubated for 1 hour before imaging or deposition of tile samples. The surface is then washed with 30 uL of 1xTAM. Next, 2-5 uL of the 0.5 µM assembled tile stock is applied to the mica surface and given 2 minutes to deposit. Finally, 15 uL of 1xTAM is added to the surface and this sample is imaged by AFM in fluid with the addition of another 60 uL 1xTAM to the fluid cell (MTFML fluid cell, Bruker)

Topography images are acquired at ambient conditions using a MultiMode 8 microscope with a Nanoscope V controller (Bruker) in ScanAsyst mode. Silicon nitride levers with a nominal spring constant of 0.1 N/m, resonant frequency of 38 kHz and a tip radius of 2 nm are used (MSNL-E, Bruker). The cantilevers are calibrated in solution using the thermal tune method. Images are captured at scan rates between 0.5 and 1.5 Hz at a resolution of 512 x 512 pixels. The z limit is set at 1 μm and the peak force amplitude at 50 nm. The peak force setpoint is set automatically by the software. Images are processed using Nanoscope Analysis 1.40 software.

3.5.9 Additional Liquid AFM Images

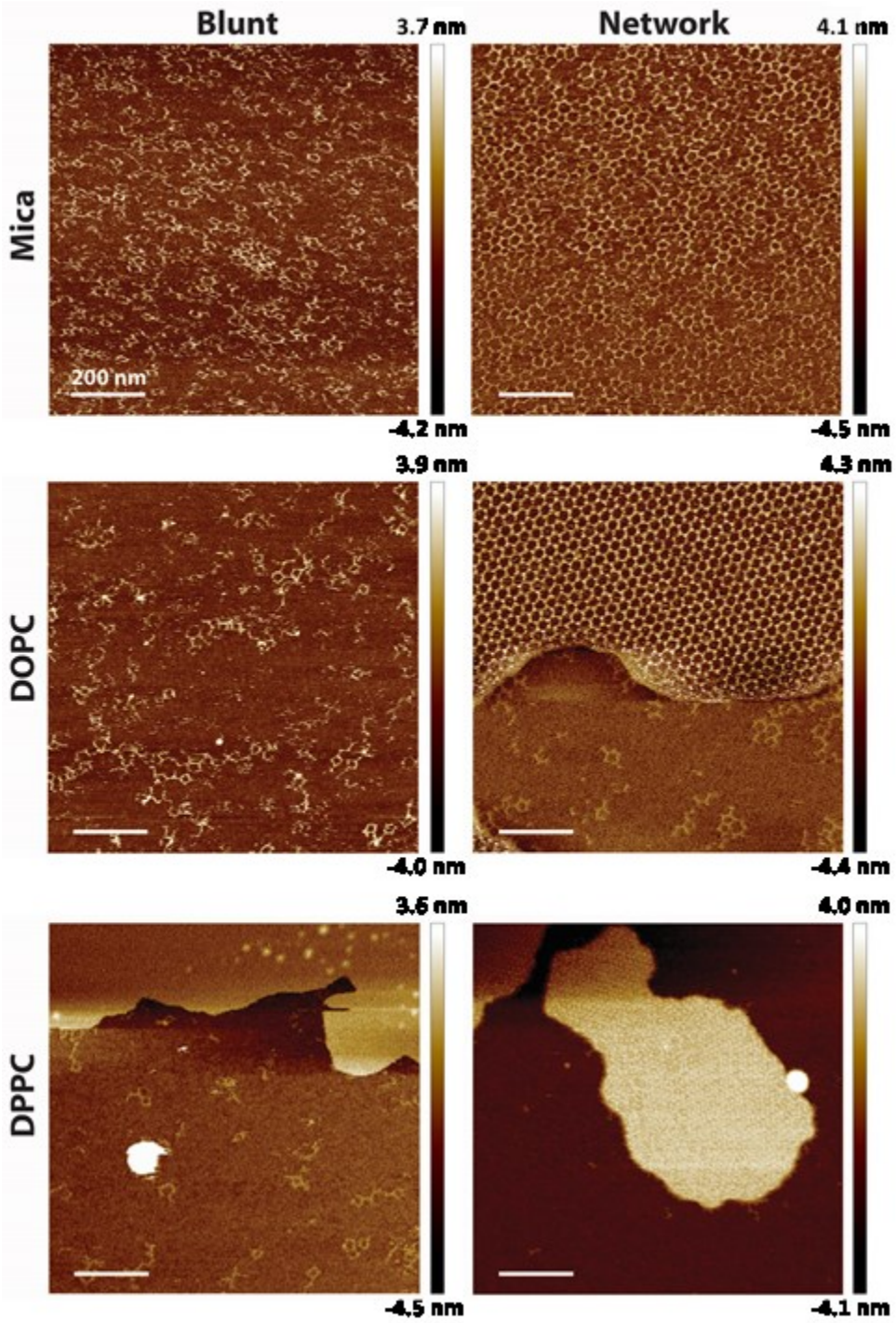

Figure 3.24: AFM in fluid of cholesterol modified tiles: (Left) blunt ended tiles on mica, DOPC, and DPPC (Right) networking, sticky ended tiles on mica, DOPC, and DPPC.

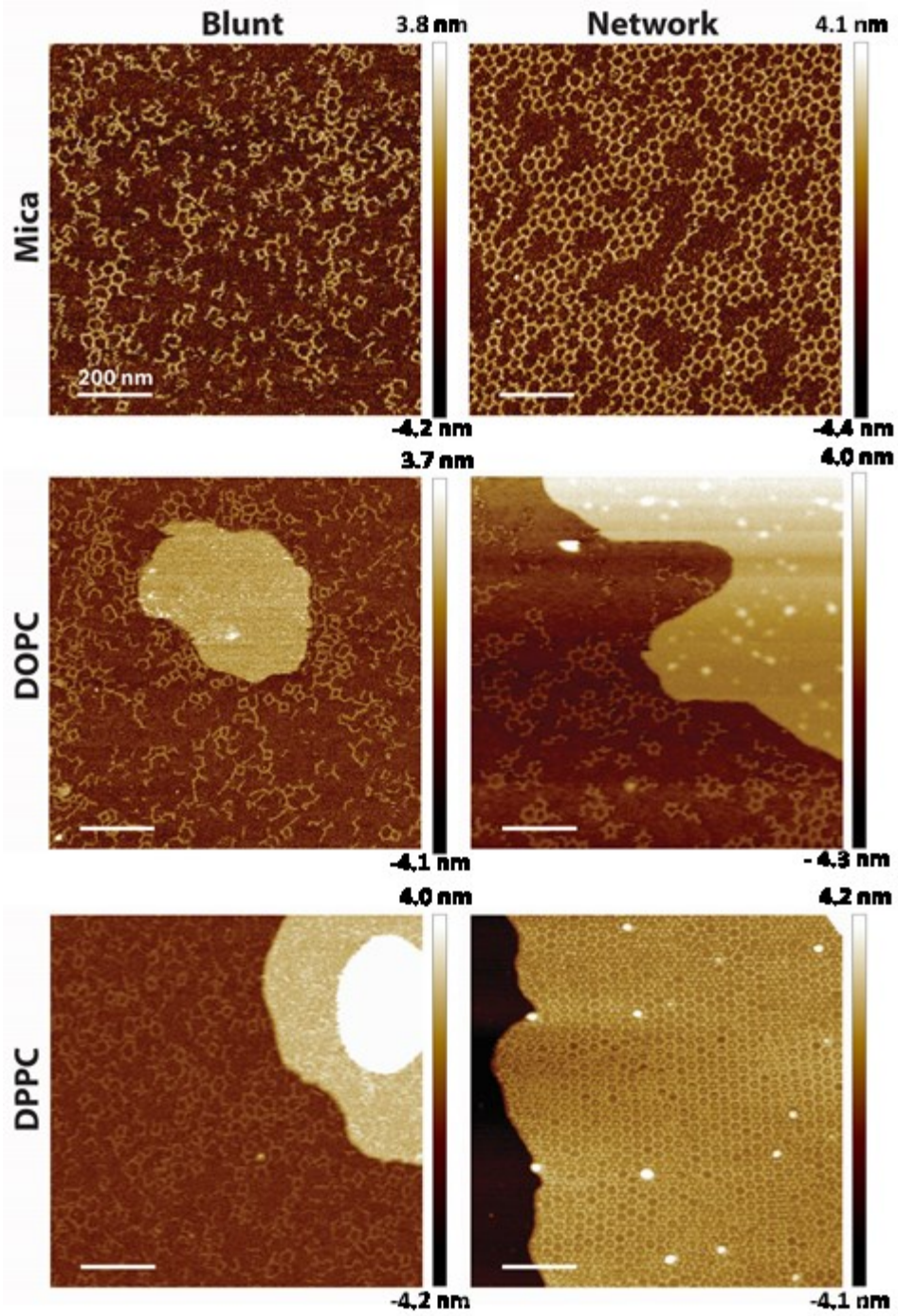

Figure 3.25: AFM in fluid of NC_{16} modified tiles: (Left) blunt ended tiles on mica, DOPC, and DPPC (Right) networking, sticky ended tiles on mica, DOPC, and DPPC.

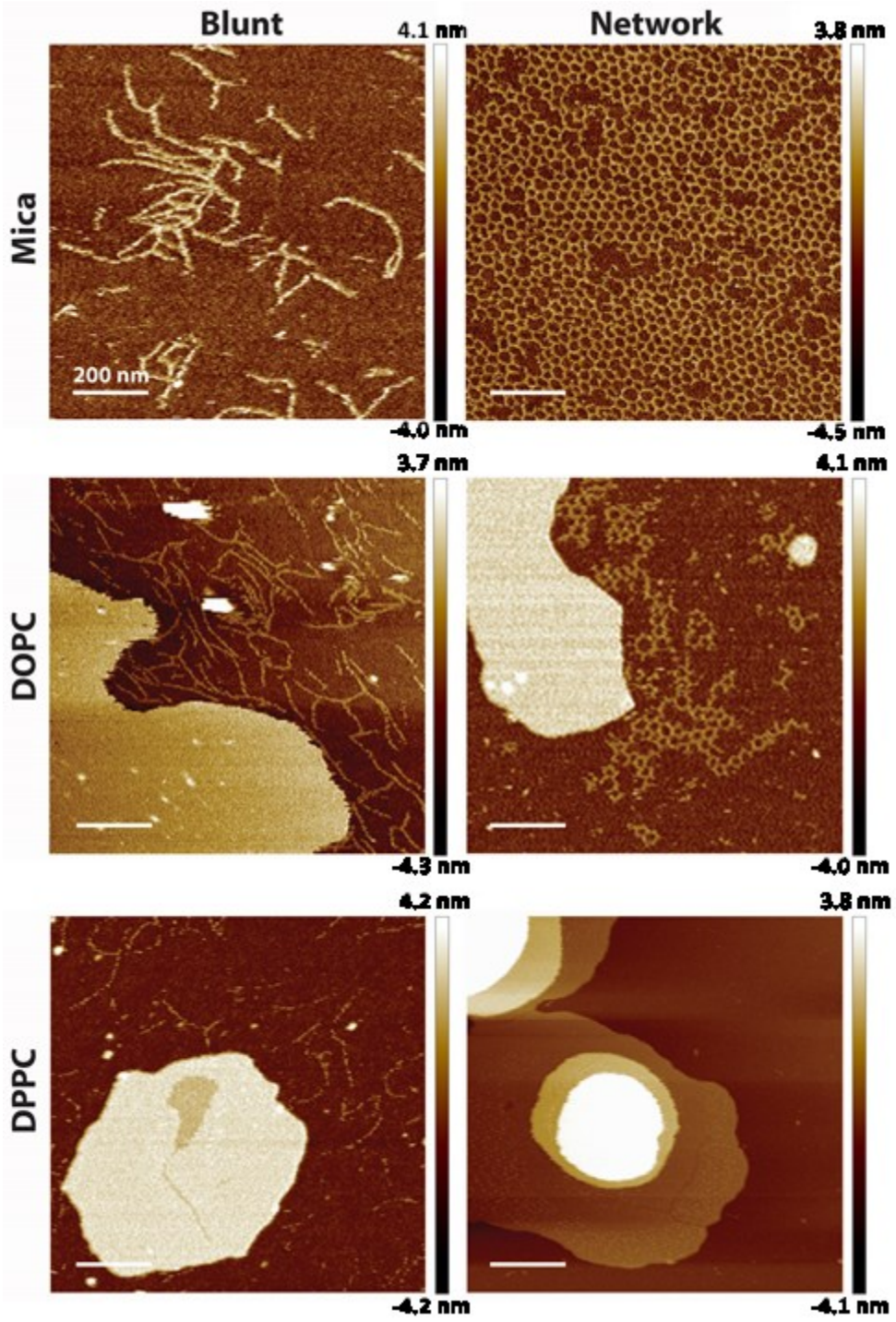

Figure 3.26: AFM in fluid of $3C_{12}$ modified tiles: (Left) blunt ended tiles on mica, DOPC, and DPPC (Right) networking, sticky ended tiles on mica, DOPC, and DPPC.

3.5.10 AFM Images of Supported Bilayers

The supported bilayers formed using DOPC, DPPC, and the DOPC:DPPC mixture were deposited on mica substrates and imaged using AFM in fluid. Figures 3.25/3.26 show the AFM measurements for the two bilayers. Bilayers of DOPC and DPPC are shown to have a height of 3.7 nm and 5.2 nm respectively which is comparable with expected values. Furthermore, due to the different packing constraints of these lipids, it is expected that the DOPC bilayer should be lower than the DPPC bilayer as the unsaturated oleoyl chains prevent efficient chain packing. This correlates to each lipid occupying a greater molecular area and therefore are not able to pack tightly together in a more upright position such as that of the DPPC lipids under similar conditions. Figure 3.27 shows the AFM images for the phase separated mixture of DOPC and DPPC. This AFM image reveals a height difference between the two lipid domains of 0.7 nm which is within error of what would be expected for the difference between the two individual bilayer height measurements.

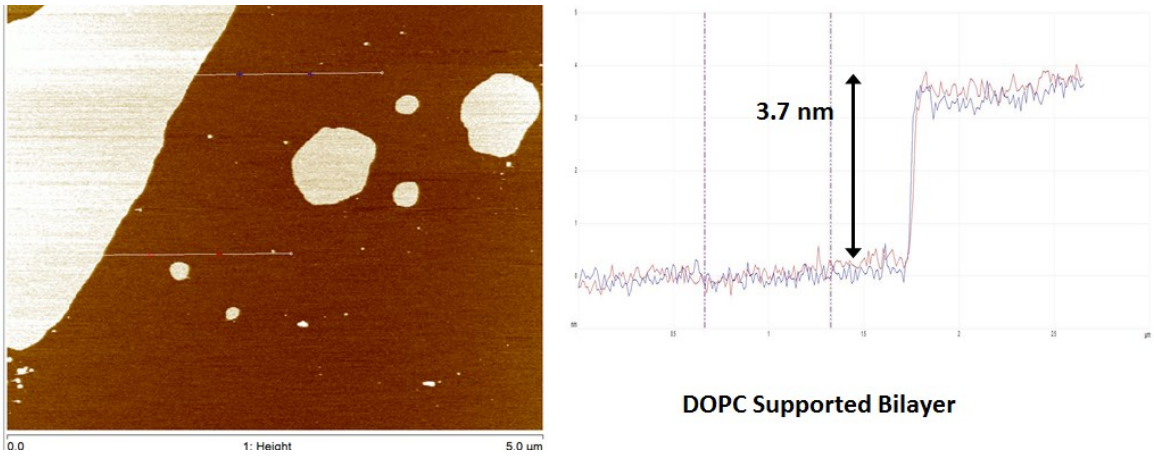

Figure 3.27: (Left) AFM in fluid of DOPC bilayer, (Right) height measurements, which correspond to the marked lines across the AFM image.

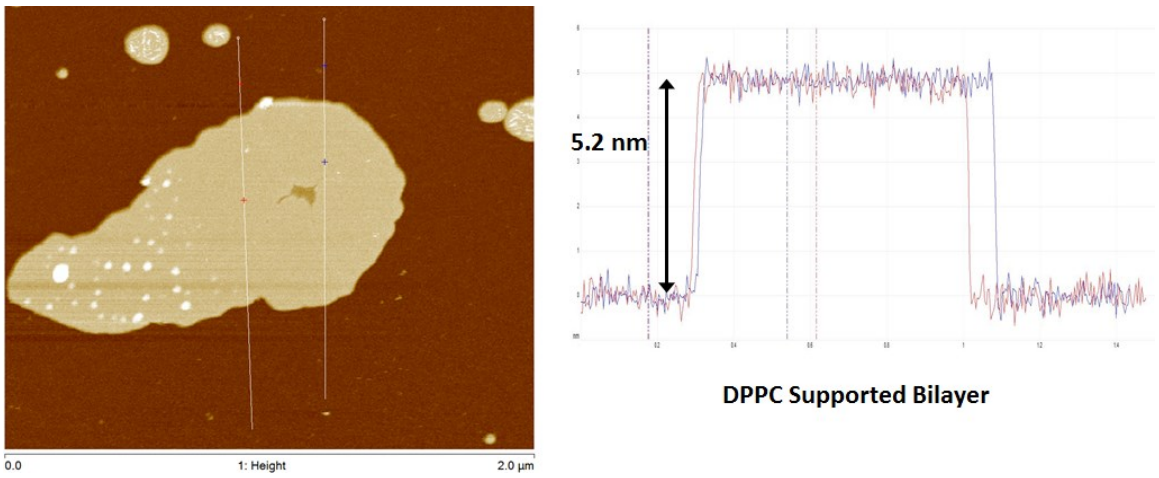

Figure 3.28: (Left) AFM in fluid of DPPC bilayer, (Right) height measurements, which correspond to the marked lines across the AFM image.

3.6 References

(1) Le, J. D.; Pinto, Y.; Seeman, N. C.; Musier-Forsyth, K.; Taton, T. A.; Kiehl, R. A. *Nano Lett.* **2004**, *4*, 2343.

(2) Zhang, J.; Liu, Y.; Ke, Y.; Yan, H. *Nano Lett.* **2006**, *6*, 248.

(3) Sharma, J.; Ke, Y.; Lin, C.; Chhabra, R.; Wang, Q.; Nangreave, J.; Liu, Y.; Yan, H. *Angew. Chem., Int. Ed.* **2008**, *47*, 5157.

(4) Howorka, S. *Langmuir* **2013**, *29*, 7344.

(5) Park, S. H.; Yin, P.; Liu, Y.; Reif, J. H.; LaBean, T. H.; Yan, H. *Nano Lett.* **2005**, *5*, 729.

(6) He, Y.; Tian, Y.; Ribbe, A. E.; Mao, C. *J. Am. Chem. Soc.* **2006**, *128*, 12664.

(7) Chhabra, R.; Sharma, J.; Ke, Y.; Liu, Y.; Rinker, S.; Lindsay, S.; Yan, H. *J. Am. Chem. Soc.* **2007**, *129*, 10304.

(8) Rothemund, P. W. K. *Nature* **2006**, *440*, 297.

(9) Nangreave, J.; Han, D.; Liu, Y.; Yan, H. *Curr. Opin. Chem. Biol.* **2010**, *14*, 608.

(10) He, Y.; Chen, Y.; Liu, H.; Ribbe, A. E.; Mao, C. *J. Am. Chem. Soc.* **2005**, *127*, 12202.

(11) He, Y.; Mao, C. *Chem. Commun.* **2006**, 968.

(12) He, Y.; Ye, T.; Su, M.; Zhang, C.; Ribbe, A. E.; Jiang, W.; Mao, C. *Nature* **2008**, *452*, 198.

(13) Tian, C.; Zhang, C.; Li, X.; Hao, C.; Ye, S.; Mao, C. *Langmuir* **2013**, *30*, 5859.

(14) Seeman, N. C. *Annu. Rev. Biochem.* **2010**, *79*, 65.

(15) Aldaye, F. A.; Palmer, A. L.; Sleiman, H. F. *Science* **2008**, *321*, 1795.

(16) Marchi, A. N.; Saaem, I.; Vogen, B. N.; Brown, S.; LaBean, T. H. *Nano Lett.* **2014**, *14*, 5740.

(17) Johnson-Buck, A.; Jiang, S.; Yan, H.; Walter, N. G. *ACS Nano* **2014**, *8*, 5641.

(18) Suzuki, Y.; Endo, M.; Yang, Y.; Sugiyama, H. *J. Am. Chem. Soc.* **2014**, *136*, 1714.

(19) Conway, J. W.; Madwar, C.; Edwardson, T. G.; McLaughlin, C. K.; Fahkoury, J.; Lennox, R. B.; Sleiman, H. F. *J. Am. Chem. Soc.* **2014**, *136*, 12987.

(20) Schade, M.; Berti, D.; Huster, D.; Herrmann, A.; Arbuzova, A. *Adv. Colloid Interface Sci.* **2014**, *208*, 235.

(21) Langecker, M.; Arnaut, V.; Martin, T. G.; List, J.; Renner, S.; Mayer, M.; Dietz, H.; Simmel, F. C. *Science* **2012**, *338*, 932.

(22) Czogalla, A.; Kauert, D. J.; Seidel, R.; Schwille, P.; Petrov, E. P. *Nano Lett.* **2015**, *15*, 649.

(23) Burns, J. R.; Göpfrich, K.; Wood, J. W.; Thacker, V. V.; Stulz, E.; Keyser, U. F.; Howorka, S. *Angew. Chem., Int. Ed.* **2013**, *52*, 12069.

(24) Banchelli, M.; Betti, F.; Berti, D.; Caminati, G.; Bombelli, F. B.; Brown, T.; Wilhelmsson, L. M.; Nordén, B.; Baglioni, P. *J. Phys. Chem. B* **2008**, *112*, 10942.

(25) Woller, J. G.; Börjesson, K.; Svedhem, S.; Albinsson, B. *Langmuir* **2011**, *28*, 1944.

(26) Börjesson, K.; Lundberg, E. P.; Woller, J. G.; Nordén, B.; Albinsson, B. *Angew. Chem., Int. Ed.* **2011**, *50*, 8312.

(27) Lundberg, E. P.; Feng, B.; Saeid Mohammadi, A.; Wilhelmsson, L. M.; Nordén, B. *Langmuir* **2012**, *29*, 285.

(28) Dave, N.; Liu, J. *ACS Nano* **2011**, *5*, 1304.

(29) Gissot, A.; Oumzil, K.; Patwa, A.; Barthelemy, P. *New Journal of Chemistry* **2014**, *38*, 5129.

(30) Dong, Y.; Sun, Y.; Wang, L.; Wang, D.; Zhou, T.; Yang, Z.; Chen, Z.; Wang, Q.; Fan, Q.; Liu, D. *Angew. Chem., Int. Ed.* **2014**, *53*, 2607.

(31) Bujold, K. E.; Fakhoury, J.; Edwardson, T. G. W.; Carneiro, K. M. M.; Briard, J. N.; Godin, A. G.; Amrein, L.; Hamblin, G. D.; Panasci, L. C.; Wiseman, P. W.; Sleiman, H. F. *Chem. Sci.* **2014**, *5*, 2449.

(32) Kwak, M.; Herrmann, A. *Chem. Soc. Rev.* **2011**, *40*, 5745.

(33) Patwa, A.; Gissot, A.; Bestel, I.; Barthelemy, P. *Chem. Soc. Rev.* **2011**, *40*, 5844.

(34) Dutta, P. K.; Levenberg, S.; Loskutov, A.; Jun, D.; Saer, R.; Beatty, J. T.; Lin, S.; Liu, Y.; Woodbury, N. W.; Yan, H. *J. Am. Chem. Soc.* **2014**, *136*, 16618.

(35) Lawrence, J. C.; Saslowsky, D. E.; Michael Edwardson, J.; Henderson, R. M. *Biophys. J.* **2003**, *84*, 1827.

(36) Connell, S. D.; Smith, D. A. *Mol. Membr. Biol.* **2006**, *23*, 17.

(37) Edwardson, T. G. W.; Carneiro, K. M. M.; McLaughlin, C. K.; Serpell, C. J.; Sleiman, H. F. *Nature Chem.istry* **2013**, *5*, 868.

(38) Serpell, C. J.; Edwardson, T. G. W.; Chidchob, P.; Carneiro, K. M. M.; Sleiman, H. F. *J. Am. Chem. Soc.* **2014**, *136*, 15767.

(39) Woo, S.; Rothemund, P. W. K. *Nature Chem.* **2011**, *3*, 620.

(40) Maffeo, C.; Luan, B.; Aksimentiev, A. *Nucleic Acids Res.* **2012**, *40*, 3812.

(41) Nakata, M.; Zanchetta, G.; Chapman, B. D.; Jones, C. D.; Cross, J. O.; Pindak, R.; Bellini, T.; Clark, N. A. *Science* **2007**, *318*, 1276.

(42) Edwardson, T. G. W.; Carneiro, K. M. M.; Serpell, C. J.; Sleiman, H. F. *Angew. Chem., Int. Ed.* **2014**, *53*, 4567.

(43) Schade, M.; Knoll, A.; Vogel, A.; Seitz, O.; Liebscher, J.; Huster, D.; Herrmann, A.; Arbuzova, A. *J. Am. Chem. Soc.* **2012**, *134*, 20490.

(44) Bayerl, T. M.; Bloom, M. *Biophys. J.* **1990**, *58*, 357.

(45) Jass, J.; Tjärnhage, T.; Puu, G. *Biophys. J.* **2000**, *79*, 3153.

(46) Beales, P. A.; Vanderlick, T. K. *J. Phys. Chem. B* **2009**, *113*, 13678.

(47) Marrink, S. J.; de Vries, A. H.; Harroun, T. A.; Katsaras, J.; Wassall, S. R. *J. Am. Chem. Soc.* **2007**, *130*, 10.

(48) Harroun, T. A.; Katsaras, J.; Wassall, S. R. *Biochemistry* **2008**, *47*, 7090.

(49) Drolle, E.; Kučerka, N.; Hoopes, M. I.; Choi, Y.; Katsaras, J.; Karttunen, M.; Leonenko, Z. *Biochimica et Biophysica Acta (BBA) - Biomembranes* **2013**, *1828*, 2247.

(50) Veatch, S. L.; Polozov, I. V.; Gawrisch, K.; Keller, S. L. *Biophys. J.* **2004**, *86*, 2910.

(51) Loew, M.; Springer, R.; Scolari, S.; Altenbrunn, F.; Seitz, O.; Liebscher, J.; Huster, D.; Herrmann, A.; Arbuzova, A. *J. Am. Chem. Soc.* **2010**, *132*, 16066.

(52) Mingeot-Leclercq, M.-P.; Deleu, M.; Brasseur, R.; Dufrene, Y. F. *Nat. Protocols* **2008**, *3*, 1654.

(53) Banga, R. J.; Chernyak, N.; Narayan, S. P.; Nguyen, S. T.; Mirkin, C. A. *J. Am. Chem. Soc.* **2014**, *136*, 9866.

(54) Boukli, L.; Touaibia, M.; Meddad-Belhabich, N.; Djimdé, A.; Park, C.-H.; Kim, J.-J.; Yoon, J.-H.; Lamouri, A.; Heymans, F. *Bioorg. Med. Chem.* **2008**, *16*, 1242.

Preface

Chapter 4 discusses our work towards developing serum stable DNA prism cages. The stability of 3D DNA nanostructures in biological environments such as serum is affected by two main factors, (1) non-buffered conditions with lowered stabilizing Mg^{2+} concentration and (2) the presence of nucleases which digest oligonucleotides. The research presented herein uses a fetal bovine serum assay to assess the stability of several modified DNA cages. We have used a combination of folding topology and 5'/3' end synthetic insertions to improve the serum stability. A fully ligated triangular prism is synthesized for comparison. The cage structure formation is also highly modular, and can be extended to larger polygon based prisms through the insertion of extra clip strands. This allows a researcher to introduce single stranded binding regions for further functionalization as is needed for a particular system.

Chapter 4

DNA Nanostructure Serum Stability: Greater Than the Sum of its Parts

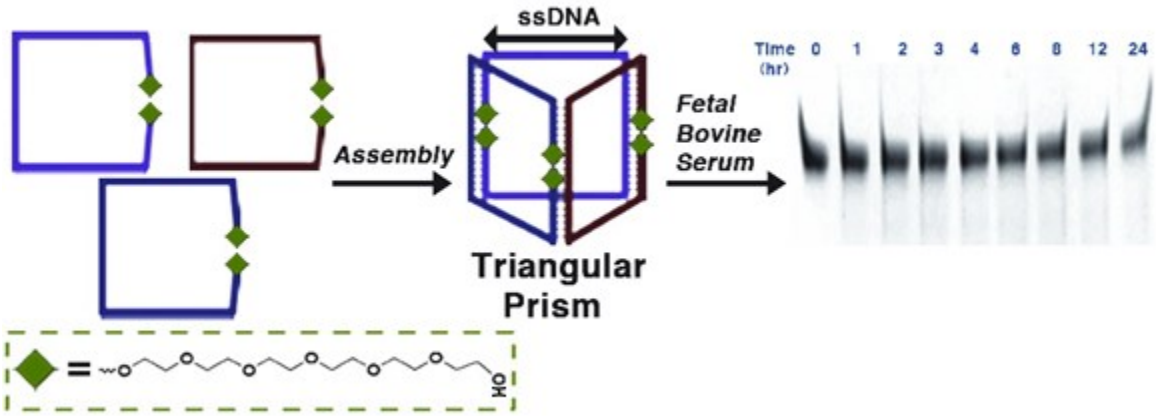

The majority of this chapter has been published as, ”DNA Nanostructure Serum Stability: Greater Than the Sum of its Parts,” J. W. Conway, C. K. McLaughlin, K. J. Castor & H. F. Sleiman, Chem. Comm. 2013, 49, 1172-1174.

4.1 Abstract

One of the major challenges limiting the use of DNA in biological systems is its susceptibility for serum nuclease degradation. We describe herein, simple chemical modifications to oligonucleotide ends with hexaethylene glycol and hexanediol that are shown to significantly increase nuclease resistance under serum conditions. The modified oligonucleotides are used to construct DNA prismatic cages in a single step and in quantitative yield. These cages further stabilize their strands towards nucleases, with lifetimes of 62 hours in serum. The cages contain a large number of single-stranded regions for functionalization, illustrating their versatility for biological applications such as drug delivery vehicles or imaging agents.

4.2 Introduction

DNA cages hold tremendous potential to encapsulate and selectively release therapeutic drugs, and can provide useful tools to probe the size and shape dependence of nucleic acid delivery.[1-3] These structures have been shown to site-specifically present ligands, small molecule drugs or antisense/siRNA motifs, in order to increase their therapeutic efficiency.[4-10] One of the major barriers towards their *in vivo* applications is the susceptibility of their strands towards nuclease degradation. A number of chemical strategies have been used to block nuclease digestion of oligonucleotides and improve potency, such as the use of a phosphorothioate backbone, 2′-*O*-methyl, locked nucleic acids, and short hybrid gapmers.[11,12] However, the synthesis of these oligonucleotides is often complicated and expensive, driving the need for simple modifications to enhance serum stability and address *in vivo* bio-distribution.

As an alternative to chemical modification of short oligonucleotides, advances in DNA nanotechnology have shown that the folding of DNA into a tetrahedral structure improves both serum stability and uptake[13-15]. However, beyond this tetrahedron example, there exists no general platform to assemble 3D DNA scaffolds that limits susceptibility to nuclease degradation and maximizes geometrically well-defined regions for additional functionalization.

Herein we report simple, commercially available end-modifications to the component strands of a DNA nanostructure, which confer a significant increase in serum stability for both the individual

strands and their self-assembled objects. We use these modified oligonucleotides to construct DNA cages using a modular 'clip-by-clip' design strategy, in a single step and in quantitative yields. The resulting DNA cages can be generated with a customized number of single-stranded binding regions. We examine the effect of DNA-end modifications on nuclease susceptibility. Even in single-stranded form, these modifications stabilize their component strands towards nucleases, with mean lifetimes as long as 62 hours in 10 % (v/v) fetal bovine serum (FBS). Finally, we show the ligation of these single-stranded cages into topologically interesting catenane 'necklaces', with mean lifetimes in serum of ~200 hours.

4.3 Results and Discussion

We first developed a simple method to assemble three unmodified DNA strands into a triangular prism (TP, Figure 4.1A). The component strands ('clips') are 96-mer oligonucleotides, which contain 20 base edges, separated by short non-pairing thymine (T4) vertices (Figure 4.1C). These strands are designed to assemble using a 'clip-by-clip' approach, in which each DNA strand represents a single clip or prism face[16]. As strands assemble into a 3D object, each clip hybridizes to the back edge of the next clip, and in the case the triangular prism, the third clip is complementary to the first clip's back edge. Overall, this one-pot assembly strategy generates a DNA cage structure with 6 single stranded edges, rapidly and in quantitative yield, as analysed by polyacrylamide electrophoresis (PAGE) under native conditions (Figure 4.1B). This clip-based assembly strategy has been extended to form a series of rectangular prisms with different geometries (triangular, cube, pentagonal prisms) for the introduction of ss binding regions[17].

Strands are synthesized with their respective modifications and purified as described below (Experimental Section 4.5.3). The three 5′/3′ modifications include: hexaethylene glycol (HEG), hexane diol (C6) and phosphate (P) (Figure 4.1C). The HEG and C6 modifications are hydrophilic/hydrophobic molecules used in DNA nanotechnology[1] and are commercially available as phosphoramidites for automated DNA synthesis. Phosphorylation allows us to explore enzymatic ligation of structures (see Experimental Section 4.5.7). The synthetic modifications do not appear to affect clip self-assembly, as seen by the single band in the native polyacrylamide gel electrophoresis (PAGE) analysis of each strand series (Figure 4.1B). Assembled triangular prism

samples are prepared as described below (Experimental Section 4.5.4).

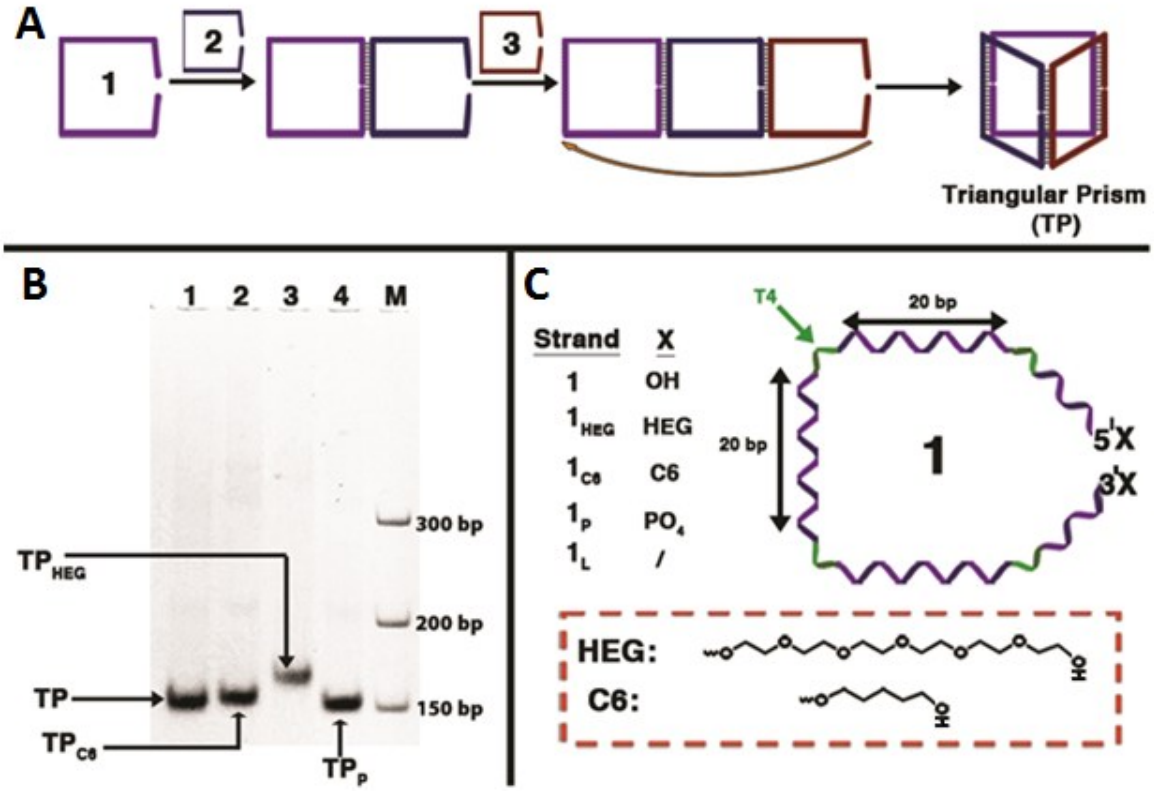

Figure 4.1: (A) Schematic representation of the 1-pot assembly of triangular prisms (TP) from 'clip' strands 1-3. (B) Native PAGE (6%) characterization of all fully assembled DNA TPs; Lane 1 – TP, Lane 2 – TP_{HEG}, Lane 3 – TP_{C6}, Lane 4 - TP_P and Lane M – molecular weight marker (C) Schematic representation of a single clip, highlighting edge length, vertex composition and 5′/3′ end modifications. (L=ligated)

Structural characterization of the triangular prism is performed using a combination of dynamic light scattering (DLS) and atomic force microscopy (AFM). DLS experiments are performed to determine the size of each 3D DNA structure in solution. Each structure is analysed with DLS measurements. DLS of the ss prism TP shows a near monodisperse particle population with a hydrodynamic radius of 5.3 ± 0.4 nm (Figure 4.2A), which is close to what would be expected for a DNA cage with a 20 base pair edge (~7 nm).

AFM is used to determine the height of the DNA prisms deposited on mica. AFM shows collapsed circular objects with height values of 0.7 ± 0.4 nm (Figure 4.2B). A number of previous studies

have shown that the height of a DNA double helix, measured by AFM is consistently lower than the expected 2 nm. In many experiments, the largest observed heights are in fact ~0.5 nm. Moreno-Herrero et al.[18] showed that this was due to a ~0.8 nm thick salt layer on mica, in which DNA strands are embedded. Chen et al have recently suggested that these discrepancies are also due to tip-induced deformation of the soft DNA molecules under AFM imaging conditions, and to inconsistent-imaging dynamics, in which the cantilever oscillates in the attractive regime on substrate background but in the repulsive regime on the target sample[19]. Thus, previous AFM studies of double-stranded DNA show significantly lower heights than 2 nm. Keeping these effects in mind, as well as the previously described distortion of these structures on the mica surface upon drying, the heights observed here are reasonable, and consistent with previous measurements[20].

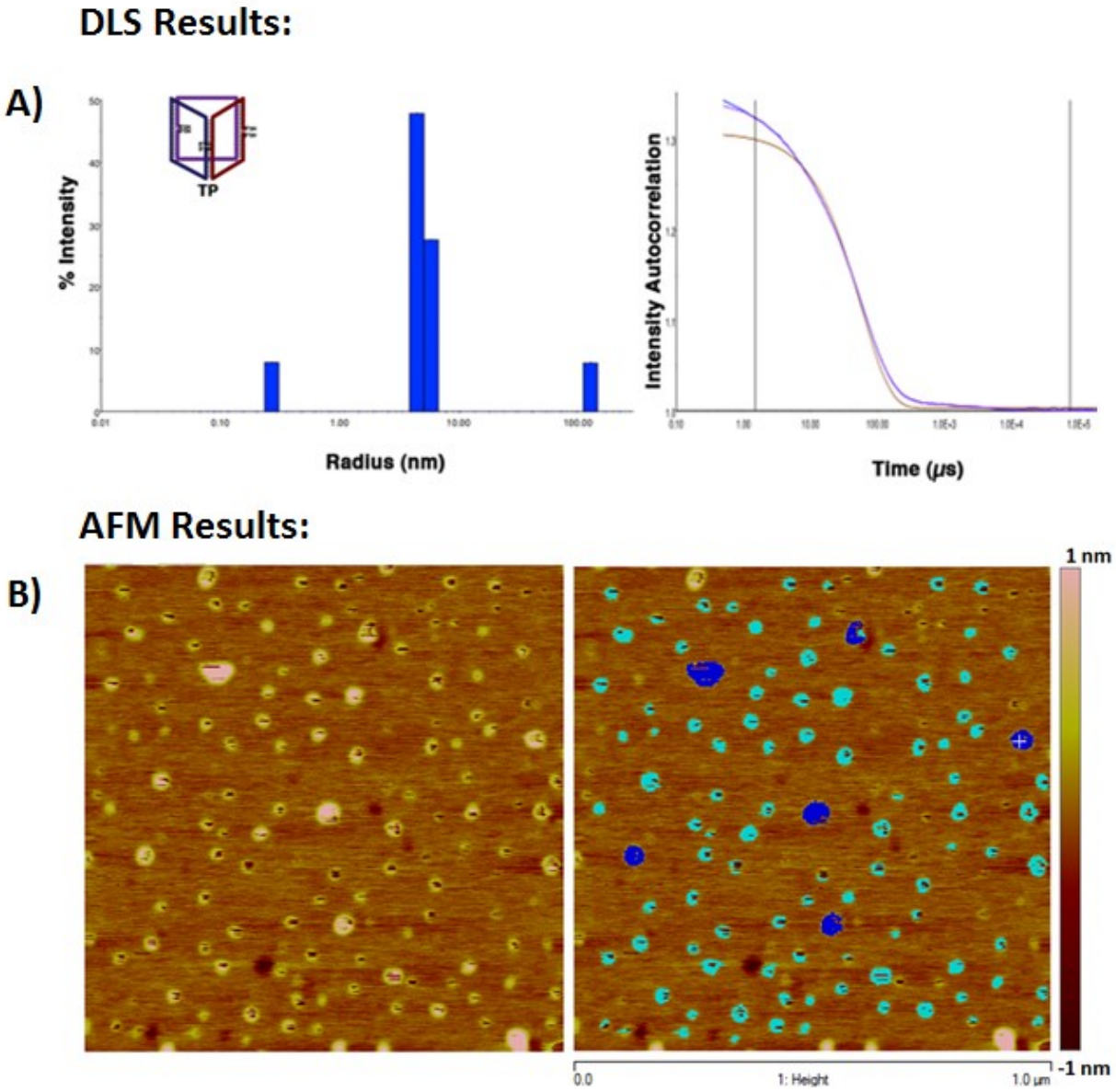

Figure 4.2: DLS and AFM results (A): DLS regularization distribution histogram and associated correlation function for TP. % PD observed was 14 %. Small peaks likely due to buffer components and maybe a small amount of intermolecular dimer. AFM (B): Height analysis of TP; pale blue color indicates particles included for statistical analysis, dark blue color indicates particles that were excluded. DLS and AFM were performed on preformed TPs in 1xTAM buffer.

UV absorption spectra at 260 nm is used to monitor the thermal denaturation of the prims and determine if the 5'/3' end modifications at the clipping regions destabilize the structure relative to

the unmodified control. The melting curves (Figure 4.3) obtained for TP, TP_{HEG} and TP_{C6} are all quite broad, likely due in part to the sequence asymmetry within each duplex region of the structure. Results show that chemical modifications at the 5'/3' terminal positions do not drastically alter the melting profiles obtained relative to the unmodified control; they do however result in slight destabilization. Reported values beneath Figure 4.3 are an average of three measurements with less than 5% error.

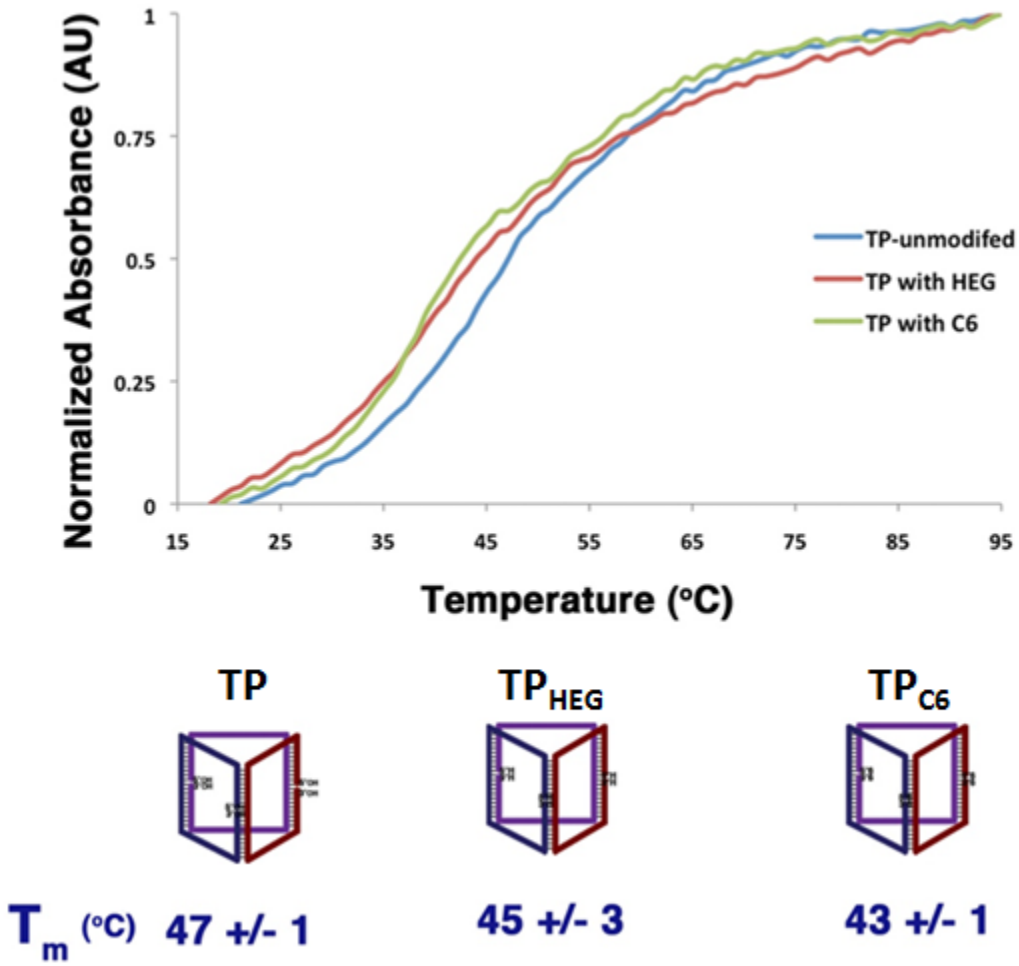

Figure 4.3: Thermal denaturation studies on TP, TP_{HEG} and TP_{C6}, (triplicate measurements).

The ssDNA regions within TP are designed to be sequence asymmetric, such that each region can be individually addressed by addition of the corresponding 20mer complement strand, yielding

fully double-stranded structures (Figure 4.4A). This will be particularly useful for site-specific loading of the DNA cage with multivalent components for targeting, stability or therapeutic applications. Native PAGE analysis (Figure 4.4B) shows that the ssTP can be addressed in a sequential manner to ultimately yield the fully loaded dsTP. This asymmetric sequence arrangement within the 3D DNA structure also allows for a multitude orientational variations useful for examining structure dependent interactions.

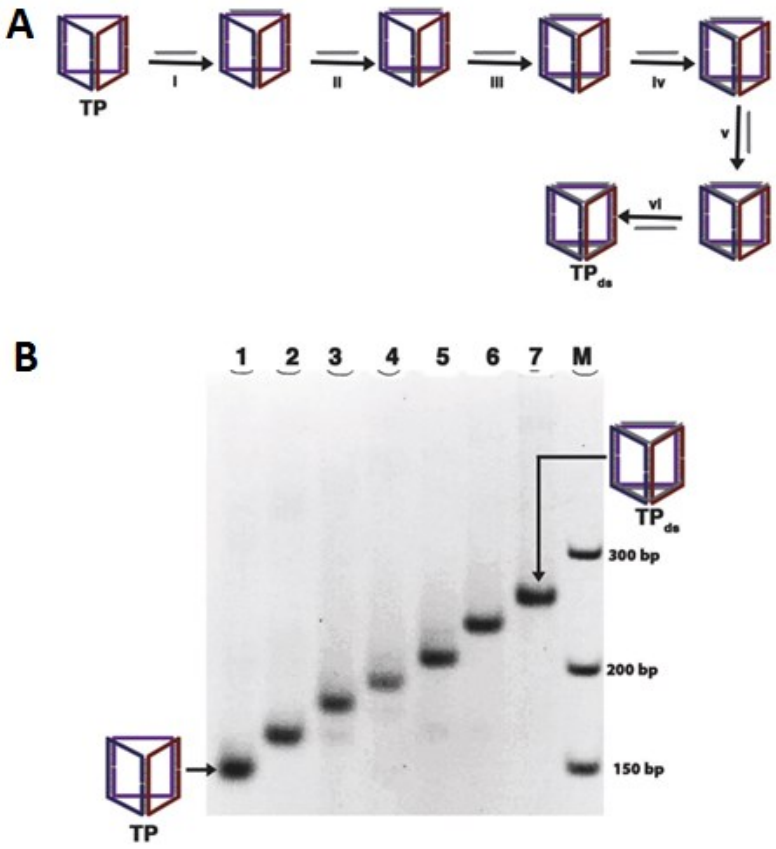

Figure 4.4: Availability of single-stranded regions in TP to hybridization. (A) Schematic representation for the stepwise addition of 20mer complement strands (i – vi) to each single-stranded region of ssTP to generate fully double-stranded structure dsTP. (B) Native PAGE (6%, 1 x TAM, 250V, 60 mA, 5 hr, RT) analysis of dsTP formation; Lane 1-TP, Lane 2- TP/1-TOP, Lane 3- TP/1-TOP/1-BOT, Lane 4- TP/1-TOP/1-BOT/2-TOP, Lane 5- TP/1-TOP/1-BOT/2-TOP/2-BOT, Lane 6- TP/1-TOP/1-BOT/2-TOP/2-BOT/3-TOP, Lane 7- TP/1-TOP/1-BOT/2-TOP/2-BOT/3-TOP/3-BOT (TPds) and Lane M - base-pair marker.

In biological media, DNA is degraded by a variety of nucleases in an unselective fashion.[21] We use fetal bovine serum (FBS) as our experimental media, which contains a mixture of nucleases and proteins, and has previously been employed to represent biological conditions for investigating DNA stability[22,23] Recent studies have shown that a fully double-stranded DNA tetrahedron imparts improved nuclease resistance to its component DNA strands (mean lifetime 42 hours).[24] This is attributed to a reduction in binding affinity to these enzymes, and/or the rigidity of its DNA strands, which prevents distortion that may be required for catalysis. The triangular prism constructed here possesses stretches of single-stranded DNA, and as such would be more readily distorted.

In general, single strands are mixed with FBS (10% v/v) in Dulbecco's modified Eagle's medium (DMEM) at 400 nM and incubated at 37°C. Aliquots are collected over a 24 h period and digestion products are analysed by denaturing (PAGE) (Figure 4.5). Results show that the unmodified strand, 1, was digested after only 1 hr, indicating minimal resistance to enzymatic attack. Strand 1_P (Figure 4.5B), phosphorylated at the 5'/3' ends already shows improvement over the control but, there are clear, higher mobility degradation bands that can be seen as early as 5 hrs due to enzymatic digestion. Remarkably, strands 1_{C6} and 1_{HEG} (Figure 4.2C/D) show significantly increased stability with almost no observable degradation bands after 24 hrs of degradation, which is comparable to the ligated control (Figure 4.2E). Nuclease resistance in FBS over 24 h is frequently reported for only heavily modified DNA[12] further highlighting the usefulness and applicability of our HEG/C6 5′ and 3′ additions. The greatest improvement is seen for hexaethylene glycol substituted 1_{HEG}, which shows a mean lifetime of 28 hours, as opposed to < 1 h for the unmodified clip strand. The hexanediol modified strand 1_{C6} also shows a considerable increase in lifetime, although not to the extent observed with HEG protection.

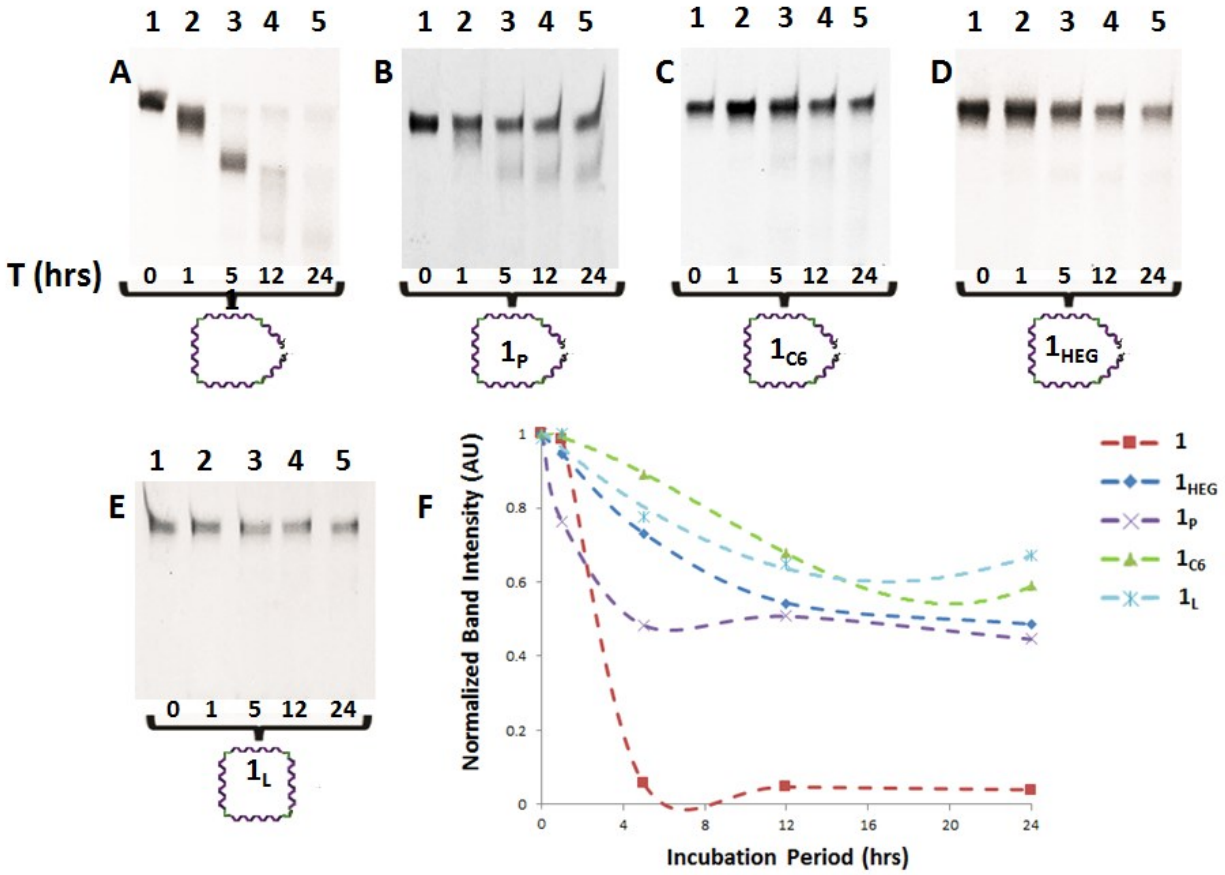

Figure 4.5: Denaturing PAGE (8%, 1 x TBE, 250V → 30 min, 500 V → 1 hr, 15 mA, RT) analysis of FBS degradation assay products for ss individual clipping strands collected over a 24 hr period,: (A) 1 unmodified control, (B) 1_P phosphate modified strand, (C) 1_{C6} hexane diol modified strand, (D) 1_{HEG} hexaethylene glycol modified strand, (E) 1_L ligated control strand, (F) Graphical overlay of the decrease in band intensity monitored for each strand. Trend lines added to guide reader (not fitted data).

The intensity of the PAGE bands corresponding to each time point are analysed with Image J to obtain intensity values that can be plotted and used to graphically demonstrate the serum lifetime of each strand (Figure 4.5F). The data is well described by exponential decay (Equation 1). Integrating and rearranging Equation 1 generates Equation 2, which is used to fit our data and extract a decay constant (λ). The decay constant is inversely related to the lifetime (τ) (Equation 3), and is reported for FBS degradation comparisons. The half-life $t_{1/2}$ = lifetime (τ) x ln2. Data interpretation using exponential decay analysis was used for comparison with other groups[25]; the

mean lifetime values derived from this analysis are directly related to changes in band intensity. We acknowledge that the lifetime values derived from exponential decay interpretation contain intrinsic fitting errors reflected by the R^2 value (Table 4.1). The single strand FBS serum stability assay results analysed using exponential decay fitting are summarized in Table 4.1. As shown, unmodified strand **1** undergoes quick degradation of the full 96mer strand within a 2 hr incubation window. Each of the modified strands, 1_{HEG}, 1_{C6}, 1_P, and 1_L, show marked improvements to stability in serum nucleases.

Equation 1: $\frac{dN}{dt} = -\lambda N$

Equation 2: $N(t) = N_o\, e^{-\lambda t}$

Equation 3: $\tau = \frac{1}{\lambda}$

N: band intensity

No: initial band intensity

λ: decay constant (hrs-1)

τ: lifetime (hrs)

t: time (hrs)

Table 4.1: Summary of exponential decay analysis for all single clips and 3D assembled structures.

	ss Clips			**TP Denaturing**			**TP Native**		
Sample	λ (hrs^{-1})	R^2	τ (hrs)	λ (hrs^{-1})	R^2	τ (hrs)	λ (hrs^{-1})	R^2	τ (hrs)
Unmod.	0.275	0.756	3.63	0.055	0.973	18.18	0.494	0.987	2.02
HEG	0.051	0.989	19.61	0.016	0.945	62.50	0.065	0.818	15.38
C6	0.075	0.988	13.33	0.018	0.872	55.56	0.287	0.835	3.48
PO4	0.136	0.966	7.35	0.044	0.961	22.73	0.696	0.946	1.44
LIG	0.037	0.954	27.03	na	na	na	0.005	0.637	200.00

We are also interested in examining whether the introduction of simple functional groups on the nicked ends of the clip strands can provide increased nuclease resistance to folded prismatic structures. FBS digestion of prisms are examined and monitored by both denaturing and native PAGE, which allows analysis of how the individual strands and the full prism are protected using folding topology compared to the fully assembled structure.

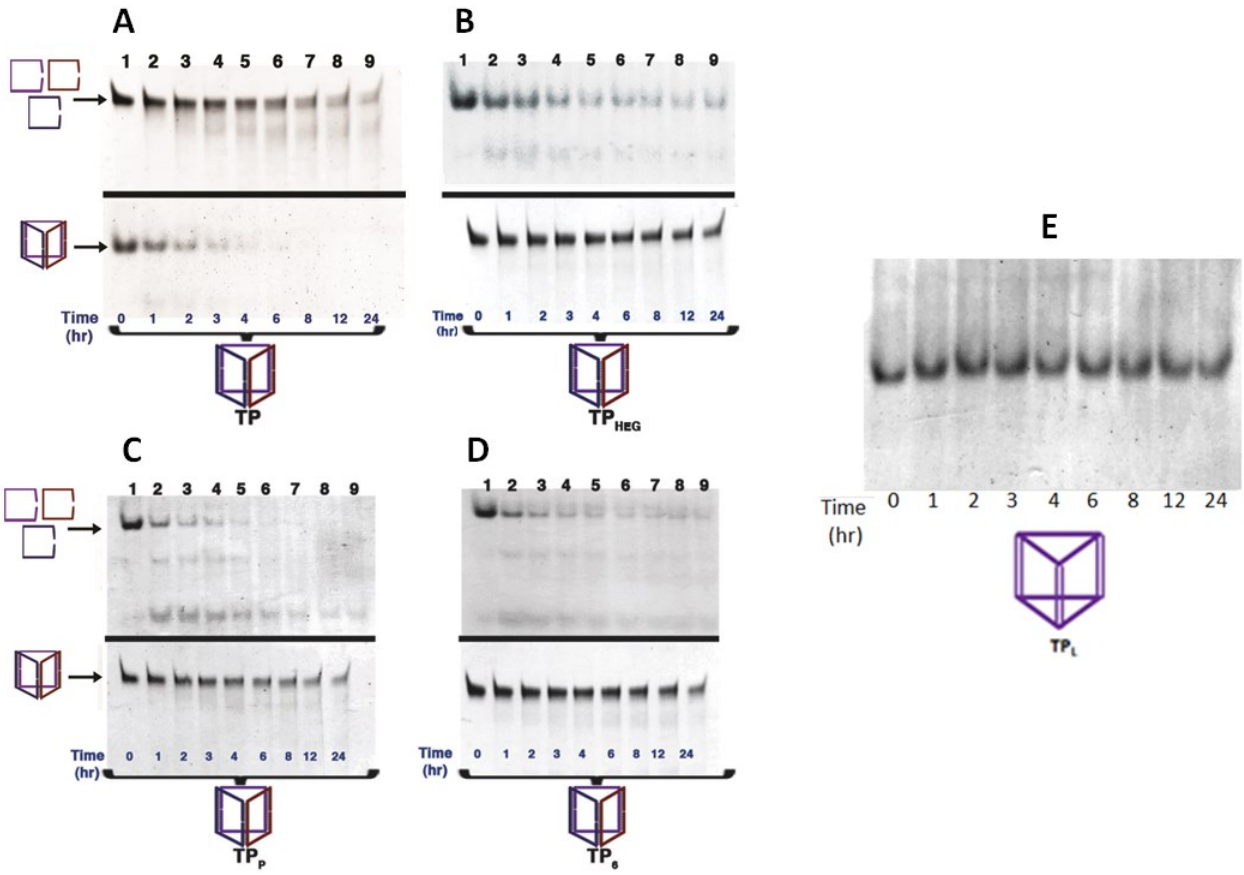

Figure 4.6: Analysis of DNA prism degradation following FBS assay. Each sample is analyzed using both denaturing PAGE (8%, 1 x TBE, 250V → 30 min, 500 V → 1 hr, 15 mA, RT) (top gels) and native PAGE (6%, 1 x TAM, 250V, 60 mA, 3 hr, RT) (bottom gels), samples are assembled as described, mixed with the FBS serum media (Experimental Section 4.5.5), and aliquots are collected over 24 hrs: (A) unmodified TP, (B) TP_{HEG}, (C) TP_P, (D) TP_6, (E) TP_L, the fully ligated control, which should display the highest nuclease resistance since it has no 5'/3' ends for exonuclease recognition.

The fully assembled prisms are subjected to FBS digestion assays and samples are collected to compare band intensities. The denaturing PAGE analysis of all TP structures (Figure 4.6-top gel of each gel pair) show significant stabilization imparted by the folded topology for its three component strands (which co-migrate under these conditions), compared to the single strand experiments (Figure 4.5). Normalized band intensities are used to account for small variations in experimental volumes. Band intensities are plotted with respect to time, and fit well to first order exponential decay (Figure 4.7). This analysis shows much slower degradation for all structures relative to the single strand experiments. Of particular interest, denaturing PAGE analysis indicates that both TP_{HEG} and TP_{C6} show marked increases in nuclease resistance (Figure 4.7A and Table 4.1). TP_{C6} shows an increase in lifetime from 13 hr for the single strand, to 55 hr when folded into the prism. TP_{HEG} shows an increase in the mean lifetime from 28 h for single strands to 62 h when they are self-assembled. Despite the presence of many single-stranded DNA stretches and of three nicked junctions in a TP, packaging the component strands into a prismatic structure introduces substantial stabilization towards nucleases.

We next analyse the FBS digestion profile of prisms by PAGE under native conditions (Figure 4.6-bottom gel of each gel pair). This provides information on how long the DNA cage itself persists as a 3D-object in serum, and is important for encapsulation-based DNA delivery schemes. This analysis shows mean lifetimes of the folded structure no longer than 3.5 hr for all cages except the TP_{HEG} and TP_L. Native PAGE analysis shows significantly longer persistence of the TP_{HEG} modified DNA cage in serum (Figure 4.7B and Table 4.1), which exhibits a mean lifetime of ~15 hrs compared to 2 hr for the unmodified prism. Similarly interpreted native FBS studies on a comparable DNA tetrahedron reveal a lifetime of 6 hrs.[7] Thus, simple end-modification can impart significant stabilization of DNA cages towards nuclease degradation.

Ligated samples are prepared by first synthesizing 5'phosphorylated prism clip strands. The strands are combined and annealed to form the triangular prism scaffold which is then incubated with T4 ligase (see Experimental Section 4.5.7). The ligated triangular is purified using denaturing PAGE and desalted before use. The ligated structures are incubated with FBS and analysed, and show the greatest resistance with a mean lifetime of 39 hours for the single ligated clips 1_L, and of 200 hours for ligated prism TP_L (Figure 4.7B and Table 4.1). While these stabilities are substantial,

it is of note that the facile introduction of hexaethylene glycol end-substitutions in TP_{HEG}, is sufficient to give improved serum stabilization. This ligated prism is formally a [4]-catenane 'necklace', and represents a unique example of a closed catenated object formed using a minimum number of ligations (Experimental section 4.5.7). It is distinct from other ligated DNA cages[26-28] because it possesses a large number of single-stranded regions.

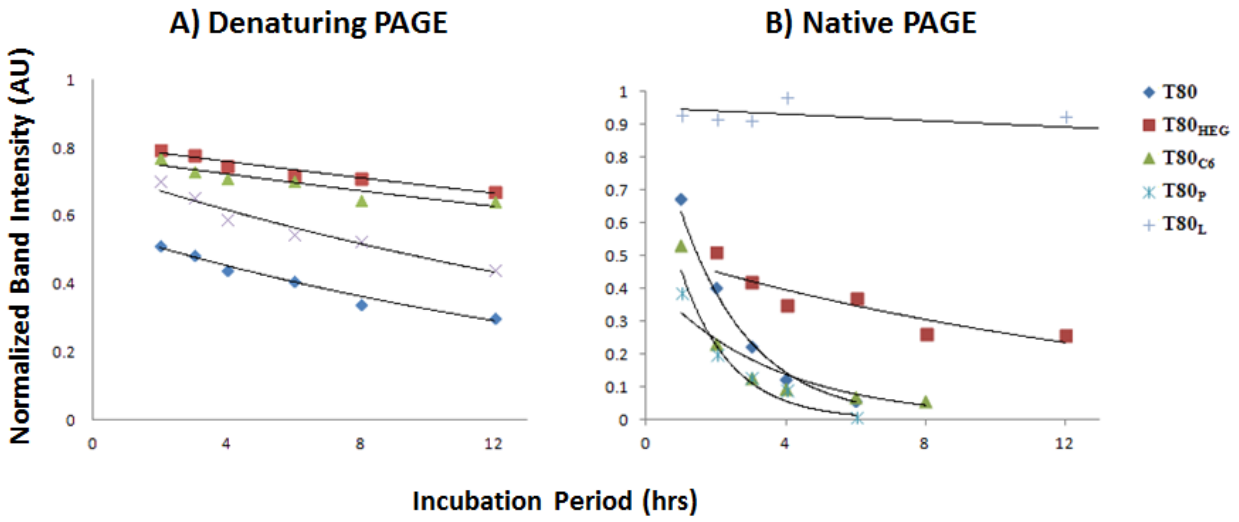

Figure 4.7: Graphical overlay of the decrease in band intensity monitored for each triangular prism. (A) Denaturing PAGE results, (B) native PAGE results.

The additional nuclease stabilization imparted by the prismatic cage is noteworthy, considering its single-stranded character and intrinsic flexibility. Interestingly, serum incubation of control DNA structures that are the permanently open, linear trimer analogues to our cages led to their rapid digestion (Experimental Section 4.5.6). This directly implies that the strands in this cage are protected by the topological folding of DNA into a condensed 3D-structure. Recent studies by Schatz, Nguyen and Mirkin support the stabilization of DNA aggregates by ion-cloud sharing of their parallel duplexes.[29,30] Our triangular prisms possess three parallel DNA duplexes that can possibly induce compaction via ion-cloud sharing. In contrast to TP_{HEG}, native PAGE analysis shows that TP_{C6} and TP_P do not persist in their intact form in serum, an observation which we are further investigating (Figure 4.7 and Table 4.1).

4.4 Conclusion

In summary, the small end-modifications examined here are shown to significantly improve the nuclease resistance of single DNA strands. Assembled DNA prisms confer even greater serum stability to their component strands, even though they contain large stretches of single-stranded DNA. These synthetic end modifications are available commercially at a comparably low cost and are easily coupled using standard DNA synthesis. Such DNA scaffolds offer the potential combination of improved serum stability, simplicity of functionalization for therapeutic functionality, and in the case of ligated prisms, the ability to be used as versatile components of molecular machines.

4.5 Experimental Section

4.5.1 General

StainsAll®, acetic acid, tris(hydroxymethyl)-aminomethane (Tris), formamide and urea are used as purchased from Aldrich. Acetic acid and boric acid are purchased from Fisher Scientific and used without further purification. Nucleoside (dA, dC, dG and T) derivatized and universal 1000Å CPG supports with loading densities between 25-40 μmol/g and reagents used for automated DNA synthesis are purchased through Bioautomation Corporated. Size-exclusion columns (sephadex G-25, DNA grade) are purchased from Glen Research. Fetal bovine serum (FBS) and phosphate buffered saline (PBS) are purchased from Wisent Corporated. 1xTBE buffer is composed of 0.09M Tris and Boric acid (TB) and 2 mM EDTA with a pH ~8.3. 1xTAM buffer is composed of 45 mM Tris and 12.6 mM Mg(OAc)2·6H2O. The pH of the 1xTAMg buffer is adjusted to 8 using glacial acetic acid. Dulbecco's Modified Eagle Medium (DMEM) is purchased from Invitrogen. The T4 DNA Ligase (400,000 units/ml) is purchased from New England BioLabs.

4.5.2 Instrumentation

Standard automated oligonucleotide solid-phase synthesis is performed on a Mermade MM6 synthesizer from Bioautomation. Gel electrophoresis experiments are carried out on an acrylamide

20 X 20 cm vertical Hoefer 600 electrophoresis unit. Annealing of all structures is conducted using an Eppendorf Mastercycler Pro. DNA quantification is performed using a BioTek Synergy HT microplate reader.

4.5.3 Solid Phase Synthesis of 3D DNA 'Clip' Strands

General Procedure for Solid-Phase DNA Synthesis: DNA synthesis is performed on a 1 μmole scale, starting from the required nucleotide modified or universal 1000 Å CPG solid-supports. Coupling efficiency is monitored after removal of the dimethoxytrityl (DMT) 5′-OH protecting groups. The hexaethylene glycol (HEG) and hexane diol (C6) phosphoramidites are purchased from ChemGenes Inc. Phosphoramidites HEG and C6 are initially diluted with dichloromethane (DCM) to a concentration of 0.1 M in a glove box. For DNA couplings, approximately 10-fold excess of each phosphoramidite is used in comparison to DNA. For off-column couplings, an equal volume of ethylthiotetrazole (0.1M in acetonitrile, Glen Research) is combined with each phosphoramidite and manually coupled on the DNA solid support with an extended reaction time of 10 minutes. After coupling, supports are removed from the glove box and returned to the DNA synthesizer for oxidation, capping and deblock steps. The chemical phosphorylation reagent (P, Glen Research, cat # 10-1900) is coupled in a similar fashion, however this compound is initially dissolved in acetonitrile. All sequences, modified and unmodified, are fully deprotected in concentrated ammonium hydroxide (25 ^{o}C/1.5 hours followed by 60 ^{o}C/2 hour).

Table 4.2: Oligonucleotides prepared via solid-phase synthesis. The TTTT represents a short non-base pairing thymidine spacer that is inserted within each strand and ends up near the junction points (or hybridization regions) of assembled 3D structures. Non-nucleoside phosphoramidites hexaethylene glycol (HEG), 1,6-hexanediol (C6) and chemical phosphorylation reagent (P) are inserted selectively into individual sequences as indicated.

Name	Sequence (5′ → 3′)
1	TCGCTGAGTA**TTTT**GCCTGGCCTTGGTCCATTTG**TTTT**GCAAGTGTGGGCA CGCACAC**TTTT**CGCACCGCGACTGCGAGGAC**TTTT**CACAAATCTG
2	CACTGGTCAG**TTTT**CCACCAGCTAGATGTTGAAG**TTTT**TACTCAGCGACAG ATTTGTG**TTTT**CGCTCTTCTATACTGGCGGA**TTTT**GGTTTGCTGA
3	CCACACTTGC**TTTT**GTCGACACAGTAGCAGTGTG**TTTT**CTGACCAGTGTCA GCAAACC**TTTT**CCATGACGATGCACTACATG**TTTT**GTGTGCGTGC
1_H	**(HEG)**TCGCTGAGTA**TTTT**GCCTGGCCTTGGTCCATTTG**TTTT**GCAAGTGTG GGCACGCACAC**TTTT**CGCACCGCGACTGCGAGGAC**TTTT**CACAAATCTG (**HEG)**
2_H	**(HEG)**CACTGGTCAG**TTTT**CCACCAGCTAGATGTTGAAG**TTTT**TACTCAGCG ACAGATTTGTG**TTTT**CGCTCTTCTATACTGGCGGA**TTTT**GGTTTGCTGA **(HEG)**
3_H	**(HEG)**CCACACTTGC**TTTT**GTCGACACAGTAGCAGTGTG**TTTT**CTGACCAGT GTCAGCAAACC**TTTT**CCATGACGATGCACTACATG**TTTT**GTGTGCGTGC **(HEG)**
1_6	**(C6)**TCGCTGAGTA**TTTT**GCCTGGCCTTGGTCCATTTG**TTTT**GCAAGTGTGG GCACGCACAC**TTTT**CGCACCGCGACTGCGAGGAC**TTTT**CACAAATCTG**(C6)**
2_6	**(C6)**CACTGGTCAG**TTTT**CCACCAGCTAGATGTTGAAG**TTTT**TACTCAGCGA CAGATTTGTG**TTTT**CGCTCTTCTATACTGGCGGA**TTTT**GGTTTGCTGA**(C6)**

3_6	**(C6)**CCACACTTGC**TTTT**GTCGACACAGTAGCAGTGTG**TTTT**CTGACCAGTG TCAGCAAACC**TTTT**CCATGACGATGCACTACATG**TTTT**GTGTGCGTGC**(C6)**
1_P	**P**TCGCTGAGTA**TTTT**GCCTGGCCTTGGTCCATTTG**TTTT**GCAAGTGTGGGC ACGCACAC**TTTT**CGCACCGCGACTGCGAGGAC**TTTT**CACAAATCTG
2_P	**P**CACTGGTCAG**TTTT**CCACCAGCTAGATGTTGAAG**TTTT**TACTCAGCGACA GATTTGTG**TTTT**CGCTCTTCTATACTGGCGGA**TTTT**GGTTTGCTGA
3_P	**P**CCACACTTGC**TTTT**GTCGACACAGTAGCAGTGTG**TTTT**CTGACCAGTGTC AGCAAACC**TTTT**CCATGACGATGCACTACATG**TTTT**GTGTGCGTGC
1-TOP	CAAATGGACCAAGGCCAGGC
1-BOT	GTCCTCGCAGTCGCGGTGCG
2-TOP	CTTCAACATCTAGCTGGTGG
2-BOT	TCCGCCAGTATAGAAGAGCG
3-TOP	CACACTGCTACTGTGTCGAC
3-BOT	CATGTAGTGCATCGTCATGG
C1	TCGCTGAGTA**TTTT**TCAACTGCTC**TTTT**GCAAGTGTGGGCACGCACAC**TTT T**TCAACTGCTC**TTTT**CACAAATCTG
C2	CTATCGGTAG**TTTT**TCAACTGCTC**TTTT**TACTCAGCGACAGATTTGTG**TTT T**TCAACTGCTC**TTTT**CAACTAGCGG
C3	CACTGGTCAG**TTTT**TCAACTGCTC**TTTT**CTACCGATAGCCGCTAGTTG**TTT T**TCAACTGCTC**TTTT**GGTTTGCTGA

C4	CCACACTTGC**TTTT**TCAACTGCTC**TTTT**CTGACCAGTGTCAGCAAACC**TTT T**TCAACTGCTC**TTTT**GTGTGCGTGC
B	CAGATTTGTGTACTCAGCGA

Purification: Each of the 96mer crude products is purified on an 8% polyacrylamide/8M urea polyacrylamide gel (PAGE; up to 20 OD_{260} of crude DNA per gel) at constant current of 30 mA for 2 hours (30 min at 250V followed by 1.5 hr at 500V), using the 1x TBE buffer. Following electrophoresis, the plates are wrapped in plastic and placed on a fluorescent TLC plate and illuminated with a UV lamp (254 nm). The bands are quickly excised, and the gel pieces are crushed and incubated in 12 mL of sterile water at 60 ^{o}C for 12-16 hours. Samples are then dried to 1 mL, desalted using size exclusion chromatography (Sephadex G-25 columns, Glen Research), and carefully quantified (OD_{260}) using UV-Vis spectroscopy. Smaller strands (1-TOP, 1-BOT, 2-TOP, 2-BOT, 3-TOP and 3-BOT) are purified using a 15% PAGE mixture and running conditions of 30 min at 250V followed by 45 min at 500V.

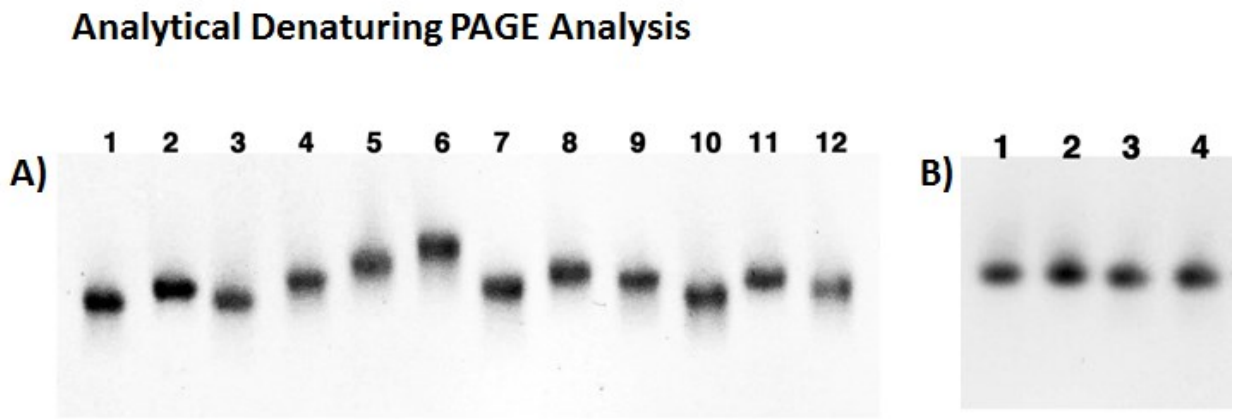

Figure 4.8: Denaturing PAGE Analysis of synthesized oligonucleotides. Denaturing PAGE (8%, 1xTBE, gels run for 30 minutes at 250V and then 1 hr at 500 V); Gel (A): Lane 1-1, Lane 2- 2, Lane 3- 3, Lane 4- 1_H, Lane 5- 2_H, Lane 6- 3_H, Lane 7- 1_6, Lane 8 – 2_6, Lane 9- 3_6, Lane 10- 1_P, Lane 11- 2_P and Lane 12- 3_P. Gel (B): Lane 1-C1, Lane 2- C2, Lane 3- C3, Lane 4- C4.

4.5.4 Assembly and Characterization of 3D DNA Structure TP

In general, equimolar amounts of each of the three strands (1 – 3) are combined in 1xTAM buffer at a final 3D concentration of 1.25 μM. Samples are then subjected to a simple annealing protocol whereby strands are brought to 95 ºC for 5 minutes and cooled back to 4 ºC over 4 hours. Table S2 shows each of the individual strand combinations used to assemble triangular prisms TP, TP_H, TP_6 and TP_P, which are analyzed (native PAGE) in manuscript Figure 4.1B. To limit the amounts of magnesium used in the degradation studies, DNA structures TP, TP_H, TP_6 and TP_P are additionally concentrated using microcon centrifugal filtration devices (30K MWCO). Before concentration, filter devices are washed with autoclaved Milli-Q water (2 x 450 μL) by centrifugation at 13,400 rpm and 4 °C for 8 minutes. Each sample is then centrifuged (13,400 rpm, 10 minutes, 4 °C). The final volumes for each sample are adjusted with 1xTAM buffer to give overall 3D concentrations of 25 - 30 μM.

Table 4.3: Strands combinations used to prepare each 3D triangular prismatic structure.

Structure	Component strands	[3D] for annealing (μM)
TP	1, 2, 3	1.25
TP_{HEG}	1_{HEG}, 2_{HEG}, 3_{HEG}	1.25
TP_{C6}	1_{C6}, 2_{C6}, 3_{C6}	1.25
TP_P	1_P, 2_P, 3_P	1.25
M	C1, B	1.25
D	C1, C4, B	1.25
T	C1, C4, C3, B	1.25

DLS Experiments:

DLS measurements of the unmodified TP structure are performed on a DynaPro99 (Protein Solution/Wyatt) instrument operating at 24 °C and using a laser wavelength of 824 nm. Samples are diluted to a concentration of 5 μM and 14 μL is used for measurements.

AFM Experiments:

AFM samples are measured using a Multimode microscope equipped with the Nanoscope IIIa controller (Digital Instruments, Santa Barbara, CA). AFM silicon probes (model AC160TS from Asylum Research) with resonance frequency ~200-400 kHz and spring constant ~12-103 N/m or RTSEP NanoProbe tips (Veeco, Santa Barbara, CA) with resonance frequency 200-400 kHz, spring constant ~20-80 N/m (tip radius < 10 nm) are used. Images are analysed using NanoScope® (DI) and worked up using a 3rd order plane fit which corrects for sample tilt. DNA samples are diluted to 25 nM with Millipore water, and 3 uL of this solution is applied to freshly cleaved mica. After 60s the mica surface is washed with 50-60 uL of water which is wicked away using filter paper. AFM samples are dried under air for 30 min and put under vacuum for 12 hours.

The deposited TPs are dried overnight, therefore 3D structures are expected to be collapsed and distorted, leading to the ring-like structures. Particles included in the height analysis can be selected with a height filter using the Nanoscope software (light blue selection Figure 4.2B). Structures that are clearly unrelated (larger aggregates) can be excluded from the selection (dark blue selection Figure 4.2B). The Nanoscope software then generates the particle analysis table included below based on this selection.

Table 4.4: Summary of AFM particle analysis for height and diameter of TP.

Parameter	**Mean**	**Minimum**	**Maximum**	**Sigma**
Total Count	120.0	120.0	120.0	0.0
Density (/nm^2)	120.0	120.0	120.0	0.0
Height (pm)	709.8	229.5	2672.1	397.1
Area (nm^2)	522.4	95.4	2998.4	415.9
Diameter (nm)	24.2	11.0	61.8	8.9

Thermal Denaturation Experiments:

UV absorption spectra (normalized A260 vs. temperature) were recorded with a Varian CaryBio 300 UV/Vis spectrometer equipped with a temperature controller. Samples were initially prepared as described in section S-IV and concentrated to 25-35 μM. Structures TP, TP_{HEG} and TP_{C6} (375 pmol/structure) were then each diluted with 1xTAM buffer up to a total volume of 100 μL. To each of these samples was added 1.4 mL PBS buffer (Wisent), bringing the total volume to 1.5 mL and [3D] = 250 nM, which provide enough material to perform denaturation studies in triplicate (0.5 mL/run). The temperature of the denaturation experiments ranged from 10 - 95 ºC and was performed with a temperature ramp of 1.0 ºC/min. Thermal denaturation temperatures (T_m) were determined after buffer blank subtraction from the first derivatives maximum of the normalized absorbance vs. temperature curve (Figure 4.3).

4.5.5 Stability Studies in Fetal Bovine Serum (FBS)

For initial degradation studies, DNA strands are concentrated to a stock solution of 40 μM in 1xTAM buffer. As an example, strand **1** (40 μM, 2 μL) is first diluted with DMEM media (88 μL). To this mixture is added a fresh sample of undiluted FBS (10 μL) with slight mixing to make the overall % of FBS 10% (v/v). An aliquot is immediately taken out (10 μL), formamide (5 μL) added and then stored at -4 °C as the t =0 hr time point. The remaining sample is then incubated at 37 °C and similar aliquots are removed and treated as described above at time points of 1, 5, 12 and 24 hr. Digested products are analysed by denaturing PAGE (8%, 15 mA, 250V → 30 min followed by 500V → 1 hr).

For degradation studies on each 3D structure, stock solutions between 25 - 35 μM in 1xTAM buffer are prepared (see section S-IV). As an example, TP ([3D] = 32.3 uM, 1.24 μL) is first diluted with 1xTAM (0.76 uL) and DMEM media (88 μL). The additional 1xTAM maintains the concentration of magnesium used within each degradation assay. To this mixture is then added undiluted FBS (10 μL) with slight mixing to make the overall % of FBS 10% (v/v). An aliquot is immediately taken out (10 μL) and either glycerin:EDTA(50 mM) (4 μL:1μL) or formamide (5 μL) added and stored at -4 °C as the t =0 hr time points. The remaining sample is then incubated

at 37 °C and similar aliquots are removed and treated as described above at time points of 1, 2, 3, 4, 6, 8, 12 and 24 hr. Digested products are then analyzed by either native or denaturing PAGE.

4.5.6. Linear Open Ladder Structure: Characterization and FBS Analysis

As outlined in the manuscript, a number of linear structures are prepared so as to compare degradation profiles with those obtained for the 3D DNA objects (Figure 4.9A). Each linear structure is closed via hybridization to 20mer, strand b (same annealing conditions as 3D cages). Unlike TP, the three-component trimer T is unable to close back onto the unhybridized end of the structure. As shown in Figure 4.9B, linear structures M, D and T are formed in excellent yields.

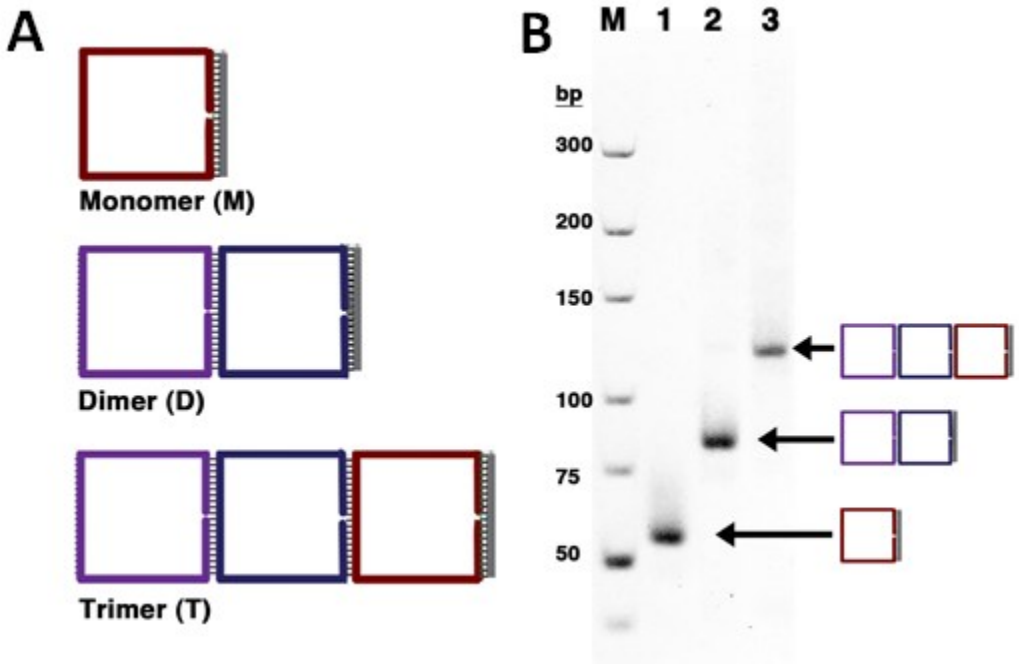

Figure 4.9: Design and analysis of linear structures. (A) Schematic representaion of linear structures monomer (M), dimer (D) and trimer (T). (B) Native PAGE (6%, 1 x TAM, 250V, 60 mA, 3 hr, RT); Lane M – marker, Lane 1-M, Lane 2- D and Lane 3-T.

All of the degradation assay results obtained for structures M, D and T (Figure 4.10) reveal rapid digestion of the closed structures within only one hour. It would appear that these variants contain

nicked junctions that are far more accessible to nuclease digestion. Especially in the case of direct linear analog T (Figure 4.10C), rapid degradation of the structure occurs, which is in contrast to the longevity observed for closed 3D structure TP. It is still unclear as to what factors contribute to the inherent stability observed for some of the 3D structures. Further investigations are underway to better elucidate the structural basis of this nuclease stability.

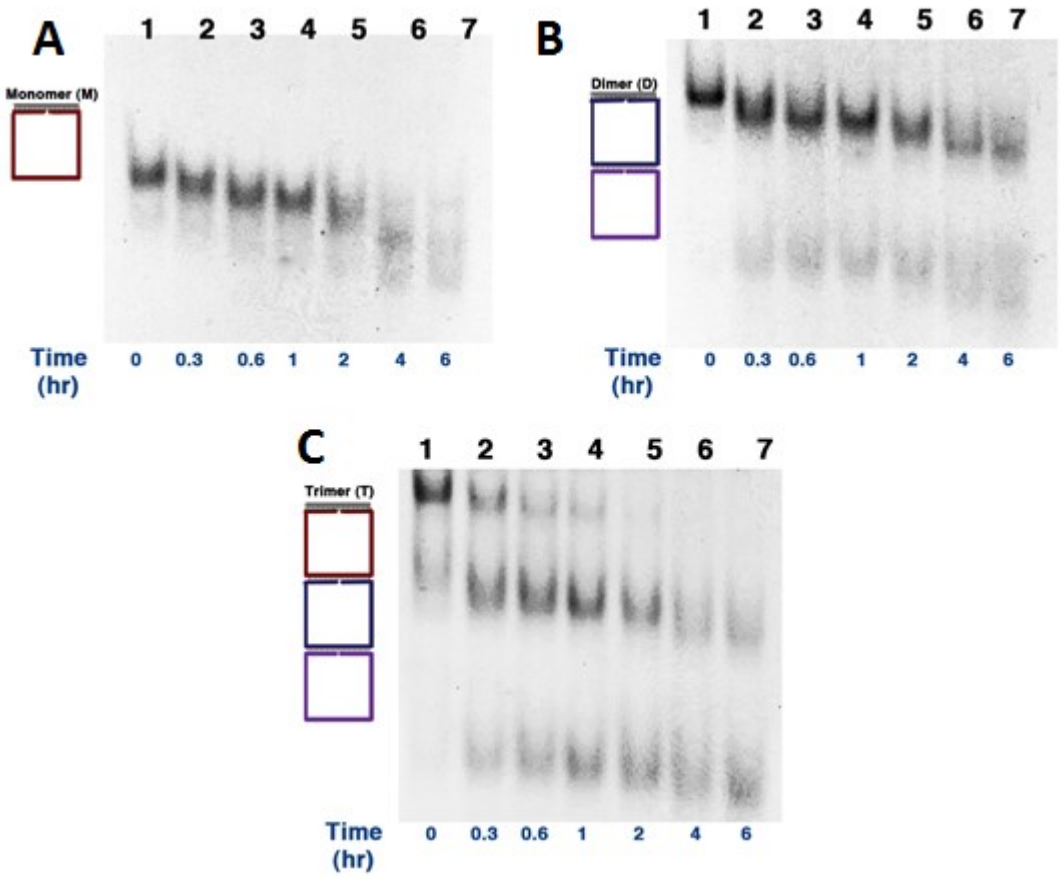

Figure 4.10: Typical degradation assay results for linear DNA structures M, D and T. Native PAGE (6%, 1 x TAM, 250V, 60 mA, 3 hr, RT) analyses are performed for each structure. Time points where samples are removed from the FBS mixture are indicated on each gel: (A) M, (B) D and (C) T.

4.5.7. Characterization of Ligated Structures

All samples are ligated following supplier experimental conditions (New England Biolabs). All nicked regions targeted for ligation (see Fig. 4.11) were first prepared with the complement strands

or assembled into the target 3D triangular prism for a final concentration of 5 uM (single clip or assembled TP) in 1xTAM; T4 ligase and the ligation buffer are then added to the solution and samples are incubated 8-12 hours at room temperature. Samples are heated to 90°C for 10 min. to inactivate the enzyme, quickly cooled to RT and then incubated with Exo VII, which digests unligated DNA (4 hrs, 37 °C). Ligated products are isolated using denaturing PAGE gel excision, extraction and desalting. Successful ligation of intended products is confirmed using Exo VII digestion (4 hrs, 37 °C) and 8% denaturing PAGE (Figure 4.11).

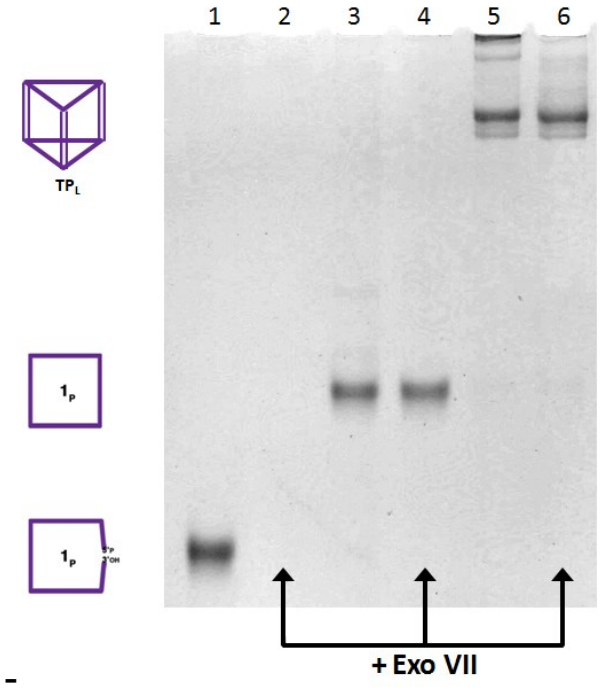

Figure 4.11: Preparation and digestion controls for ligated samples. Denaturing (8%, 1 x TBE, , 250V → 30 min, 500V → 1hr, 15 mA, RT).

4.6 References

(1) McLaughlin, C. K.; Hamblin, G. D.; Sleiman, H. F. *Chem. Soc. Rev.* **2011**, *40*, 5647-56.

(2) Torring, T.; Voigt, N. V.; Nangreave, J.; Yan, H.; Gothelf, K. V. *Chem. Soc. Rev.* **2011**, *40*, 5636-46.

(3) Fu, J.; Liu, M.; Liu, Y.; Yan, H. *Acc. Chem. Res.* **2012**, *45*, 1215-26.

(4) Chang, M.; Yang, C. S.; Huang, D. M. *ACS Nano* **2011**, *5*, 6156-6163.

(5) Bhatia, D.; Surana, S.; Chakraborty, S.; Koushika, S. P.; Krishnan, Y. *Nat. Commun.* **2011**, *2*.

(6) Keum, J. W.; Ahn, J. H.; Bermudez, H. *Small* **2011**, *7*, 3529-3535.

(7) Li, J.; Pei, H.; Zhu, B.; Liang, L.; Wei, M.; He, Y.; Chen, N.; Li, D.; Huang, Q.; Fan, C. *ACS Nano* **2011**, *5*, 8783-9.

(8) Lee, H.; Lytton-Jean, A. K.; Chen, Y.; Love, K. T.; Park, A. I.; Karagiannis, E. D.; Sehgal, A.; Querbes, W.; Zurenko, C. S.; Jayaraman, M.; Peng, C. G.; Charisse, K.; Borodovsky, A.; Manoharan, M.; Donahoe, J. S.; Truelove, J.; Nahrendorf, M.; Langer, R.; Anderson, D. G. *Nature Nanotech.* **2012**, *7*, 389-93.

(9) Douglas, S. M.; Bachelet, I.; Church, G. M. *Science* **2012**, *335*, 831-4.

(10) Liu, X.; Xu, Y.; Yu, T.; Clifford, C.; Liu, Y.; Yan, H.; Chang, Y. *Nano Lett.* **2012**, *12*, 4254-9.

(11) Deleavey, G. F.; Damha, M. J. *Chem Biol* **2012**, *19*, 937-54.

(12) Watts, J. K.; Corey, D. R. *J Pathol* **2012**, *226*, 365-79.

(13) Keum, J.-W.; Ahn, J.-H.; Bermudez, H. *Small* **2011**, *7*, 3529-3535.

(14) Walsh, A. S.; Yin, H.; Erben, C. M.; Wood, M. J. A.; Turberfield, A. J. *ACS Nano* **2011**, *5*, 5427-5432.

(15) Li, J.; Pei, H.; Zhu, B.; Liang, L.; Wei, M.; He, Y.; Chen, N.; Li, D.; Huang, Q.; Fan, C. *ACS Nano* **2011**, *5*, 8783-8789.

(16) McLaughlin, C. K.; Hamblin, G. D.; Hanni, K. D.; Conway, J. W.; Nayak, M. K.; Carneiro, K. M.; Bazzi, H. S.; Sleiman, H. F. *J Am Chem Soc* **2012**, *134*, 4280-6.

(17) Serpell, C. J.; Edwardson, T. G. W.; Chidchob, P.; Carneiro, K. M. M.; Sleiman, H. F. *J. Am. Chem. Soc.* **2014**, *136*, 15767-15774.

(18) Moreno-Herrero, F.; Colchero, J.; Baró, A. M. *Ultramicroscopy* **2003**, *96*, 167-174.

(19) Chen, L.; Yu, X.; Wang, D. *Ultramicroscopy* **2007**, *107*, 275-280.

(20) Zhang, C.; Tian, C.; Li, X.; Qian, H.; Hao, C.; Jiang, W.; Mao, C. *J. Am. Chem. Soc.* **2012**, *134*, 11998-12001.

(21) Uhlmann, E.; Ryte, A.; Peyman, A. *Antisense Nucleic Acid Drug Dev* **1997**, *7*, 345-50.

(22) Wahlestedt, C.; Salmi, P.; Good, L.; Kela, J.; Johnsson, T.; Hokfelt, T.; Broberger, C.; Porreca, F.; Lai, J.; Ren, K.; Ossipov, M.; Koshkin, A.; Jakobsen, N.; Skouv, J.; Oerum, H.; Jacobsen, M. H.; Wengel, J. *PNAS* **2000**, *97*, 5633-8.

(23) Deleavey, G. F.; Watts, J. K.; Alain, T.; Robert, F.; Kalota, A.; Aishwarya, V.; Pelletier, J.; Gewirtz, A. M.; Sonenberg, N.; Damha, M. J. *Nucleic Acids Res.* **2010**, *38*, 4547-4557.

(24) Keum, J. W.; Bermudez, H. *Chem. Commun.* **2009**, 7036-8.

(25) Keum, J.-W.; Bermudez, H. *Chem. Commun.* **2009**, 7036-7038.

(26) Chen, J. H.; Seeman, N. C. *Nature* **1991**, *350*, 631-3.

(27) Goodman, R. P.; Schaap, I. A.; Tardin, C. F.; Erben, C. M.; Berry, R. M.; Schmidt, C. F.; Turberfield, A. J. *Science* **2005**, *310*, 1661-5.

(28) Bhatia, D.; Mehtab, S.; Krishnan, R.; Indi, S. S.; Basu, A.; Krishnan, Y. *Angew. Chem. Int. Ed.* **2009**, *48*, 4134-7.

(29) Lytton-Jean, A. K. R.; Gibbs-Davis, J. M.; Long, H.; Schatz, G. C.; Mirkin, C. A.; Nguyen, S. T. *Adv. Mater.* **2009**, *21*, 706-709.

(30) Eryazici, I.; Prytkova, T. R.; Schatz, G. C.; Nguyen, S. T. *J. Am. Chem. Soc.* **2010**, *132*, 17068-17070.

Chapter 5

Conclusion

5.1 Conclusions and Perspectives

The underlying theme of the research presented in this thesis is the study of new ways in which DNA nanotechnology can be interfaced with biological systems. These studies are possible because of the ability to covalently link DNA to synthetic molecules, which act as bridges to other orthogonal self-assembling materials or as nuclease protecting groups. Towards this end, we have developed new strategies for dynamic bilayer labeling with both 3D cages and 2D networks, and used variable hydrophobic anchors to drive switch morphologies. Towards applications using DNA cages for drug delivery, we have demonstrated simple modifications and topological folding for serum stability and investigated the use of multivalent targeting motifs (Appendix 1). The findings of this work are summarized below, along with a discussion about how these findings may be used for future applications.

In Chapter 2, it is shown that a 3D DNA cage could be anchored to a spherically supported lipid bilayer membrane and reversibly loaded with 3 different fluorophores. It is also shown that the prism face in closest contact with the lipid bilayer could also be reversibly addressed using a cholesterol modified toehold displacing strategy. Finally using fluorescence recovery after photobleaching, it is demonstrated that DNA assemblies freely diffuse within the bilayer, and that by positioning multiple cholesterol modified strands on opposing faces, the prism becomes more deeply embedded within the bilayer and less accessible to nuclease degradation. Furthermore, the spherically supported lipid bilayer membrane supports are substantially more robust than comparable vesicles, rendering improved handling and isolation for characterisation. They could therefore be used as a modular platform for loading bilayer anchored DNA devices or as part of a model system for biological studies.

The spherically supported lipid bilayer membrane system developed here is useful may be particular useful for sensor based applications as it can be loaded with several reporter molecules. Similar to logic based sensors, individual reporting molecules or combinations thereof, could be used to create powerful diagnostic tools. This scaffold is highly modular, and extra clip faces can easily be added to introduce more single-stranded binding regions to increasing the number of reporter molecules (for signal intensity or diversity), add targeting motifs or even therapeutics.

The spherically supported lipid bilayer membrane also presents an interesting approach towards protecting nucleic acid based therapeutics from serum nuclease degradation. Towards this end, a prism could be designed to hybridize variable numbers of anchoring DNA-cholesterol conjugates which will control how deeply it is embedded within the bilayer and consequently how accessible to nuclease degradation it is. The DNA construct itself could contain stretches of therapeutic oligonucleotide or act as a scaffold to mount both gene silencing strands and the cholesterol anchors. The solid bead center itself could also be replaced with spherical mesoporous material which could also encapsulate small drug molecules. Finally, as was demonstrated by Lennox et al, these spherically supported lipid bilayer membranes can be used to stimulate neuro-regenerative properties by varying the lipid composition. Combining a modular DNA scaffold at the bilayer interface with variable positioning of modified strands could allow similar studies to investigate organizations of different chemical motifs for improving cellular regeneration.

Chapter 3 further extended our experiments interfacing DNA and lipid self-assembly to expand DNA networks towards longer range organization. In this work we demonstrate how a network forming 3 point star (3PS) tile motif can be directed onto supported lipid bilayers without network disruption. This work demonstrated how different hydrophobic anchors can be covalently attached to the 3PS to selectively deposited tile networks on bilayers of DOPC or DPPC and phase separated 40DOPC:60DPPC mixtures (DOPC: 1,2-dioleoyl-sn-glycero-3-phosphocholine; DPPC: 1,2-dipalmitoyl-sn-glycero-3-phosphocholine). Most significant of these findings is the switchable network morphologies observed for the different pairings of DNA tile anchor structure and the lipid bilayer phase behaviour. The cholesterol-tile is shown to form the expected hexagonal packing on DOPC bilayers but switches to a herringbone-like morphology on DPPC bilayers. The NC_{16}-tile in contrast, only shows hexagonal packing on the DPPC bilayers and no distinct morphologies on the DPPC. Moreover, when these respective tile networks are deposited on a

30DOPC:70DPPC mixture the dual morphologies (or absence of) are observed over phase separated regions. This observation highlights the importance of matching the DNA-lipidic anchor structure with the alkyl chain packing constraints within lipid bilayers to control deposition interactions.

Modification of the tiles using a $3C_{12}$ polymer motif exhibits switchable morphologies between filamentous material and the 2D hexagonal network. The switching for these samples is induced by using either blunt or sticky ended tiles. In these samples when tiles are assembled with blunt ends we observed the non-specific aggregation into long filaments, likely driven to form as the hydrophobic component buries itself to minimize contact with the aqueous medium. With the addition of the sticky ends during network formation, the hexagonal network formation dominates.

One of the major findings of this work lies in the selective deposition of modified tile networks on lipids with different phase behaviour. If the tile networks are designed with single-stranded binding regions, many different DNA-conjugated molecules can be selectively patterned onto the network domains, which could be useful for creating arrays of light harvesting complexes or protein/enzymes. In this way, each phase separated lipid domain could be modified with different functional components. The selective deposition on bilayers could also be applied to fundamental research into lipid phase behaviour, such as examining the effects of the tethering network on phase transition temperatures and lipid mixing studies. Using a fluid bilayers such as DOPC, may allow for error correction within the tile network, leading to defect-free, longer range assembly relative to existing solid substrate deposited networks. This may also be useful towards creation of micro-circuitry patterns. Alternatively, the amphiphilic network material could be used as a system for loading micellar or vesicular aggregates with a DNA closed network shell. The tiles in this strategy could be further modified with diagnostic or therapeutic functionality.

One aspect of the tile based research of particular interest is the use of the sequence-controlled polymers NC_{16} and $3C_{12}$ in combination with DNA nanotechnology. Although both of these molecules are hydrophobic, they exhibit significantly different morphologies from the combination of two orthogonal self-assembly modes. Using phosphoramidite chemistry, polymer components can be added in a precise, sequential manner with DNA added to the sequence in any desired position relative to the polymer[1]. These strategies yield block copolymer constructs, and

as such different polymers could be combined in varied lengths or architectures (brush, comb, or linear) with DNA for the creation of new functional materials. The polymer DNA conjugates can be extended for use in all aspects of DNA nanotechnology from tiles to origami, or even metal coordinated complexes to develop new ways of combining orthogonal self-assembly methods.

Another major finding from both the research in chapters 2 and 3, is the ability to use the hierarchical self-assembling systems to greatly extend the organizational range of DNA nanotechnology into the micrometer range. The solid substrate in either of these research chapters defines the size and shape of the supported bilayer, which allows many options for system design using this technology. Substrate supported bilayers can be loaded with either 3D DNA cages or 2D networks and functionalized with any complementary DNA-conjugate of interest. This could be directly used to create biomimetic models, as well as detection or drug delivery devices. The 3D DNA cage is of particular interest for these applications as it is readily loaded with organized, multivalent components on two levels (close to the bilayer or above it).

Chapter 4 shows that DNA prism serum stability can be significantly increased using a combination of small 5'/3' synthetic end modifications and folded 3D topology. This strategy would be advantageous as it significantly reduces the need for modified nuclease resistant nucleotides, which are often expensive and synthetically challenging. Most significant from this research is the single-stranded clip nuclease resistance using the hexaethylene glycol (HEG) or hexanediol (C6) capping ends relative to the unmodified clip, which is quickly digested. Fetal bovine serum studies on the 3D cages formed through modified clips indicate that although both the HEG and C6 show even greater nuclease resistance due to the folded topology, the HEG prism retains its folded native prism state the longest in serum. Future work will investigate how the hydrophobic end modifications are destabilizing the prism structure. The ligated prism showed the greatest serum stability, which highlights the need to stabilize the nicked regions towards nucleases. The ligation strategy used also demonstrates a facile way of forming a closed ligated DNA cage

The strategy presented here for forming serum stable drug delivery capsules is also advantageous as the scaffold contains single-stranded regions with can be loaded with therapeutics or targeting motifs, such as aptamers or DNA-peptide conjugates. Not only can several multivalent additions

be hybridized to the structure, but the scaffold itself can be modulated to a cube, pentagonal or even octagonal prism simply by creating a new DNA clip with the correct sequence. This allows the researcher the ability to put several chemically distinct DNA-conjugates in a precise arrangement to benefit cellular targeting, uptake, nuclease resistance and bio-distribution.

The collection of experimental studies presented herein reflects our efforts towards developing new strategies to interface DNA nanotechnology with biological systems, for both chemical biology and materials applications. Presently DNA nanotechnology is being applied for therapeutic purposes such as gene silencing or developing medical devices and to study biological systems such as cellular communication or multivalent protein interactions. These emerging strategies will benefit from the research platforms shown here, as examples of how DNA structures can be designed to interact with biological membranes and survive serum environments.

5.2 List of Publications

1. McLaughlin C.K., Hamblin G.D., Hänni K.D., **Conway J.W.**, Nayak M.K., Carneiro K.M., Bazzi H.S., Sleiman H.F.. *Three-dimensional organization of block copolymers on "DNA-minimal" scaffolds*. J Am Chem Soc. 2012, 134(9):4280-4286.
2. **Conway J.W.**, McLaughlin C.K., Castor K.J., Sleiman H.F. *DNA nanostructure serum stability: greater than the sum of its parts*. Chem. Commun., 2013, 49, 1172-1174.
3. **Conway J.W.**, Madwar C., Edwardson T.G., McLaughlin C.K., Fahkoury J. J., Lennox R.B., Sleiman H.F. *Dynamic behavior of DNA cages anchored on spherically supported lipid bilayers*. J. Am. Chem. Soc. 2014, 136 (37), 12987–12997.
4. Fakhoury J.J., McLaughlin C.K., Edwardson T.W., **Conway JW**, Sleiman H.F. *Development and characterization of gene silencing DNA cages.* Biomacromolecules 2014, 15, 276–282.
5. **Conway J. W.**, Avakyan N., Hsu J.C., de Rochambeau D., Barlog M., Bazzi H.S., Sleiman H.F. *DNA Tile Networks on Supported Lipid Bilayers: Long-Range Assembly and Selective Patterning*. Submitted .

5.3 References

(1) Edwardson, T. G. W.; Carneiro, K. M. M.; Serpell, C. J.; Sleiman, H. F. *Angew. Chem., Int. Ed.* **2014**, *53*, 4567-4571.

Chapter 6

Appendix 1: Orientational Dependence of Multivalent Aptamers

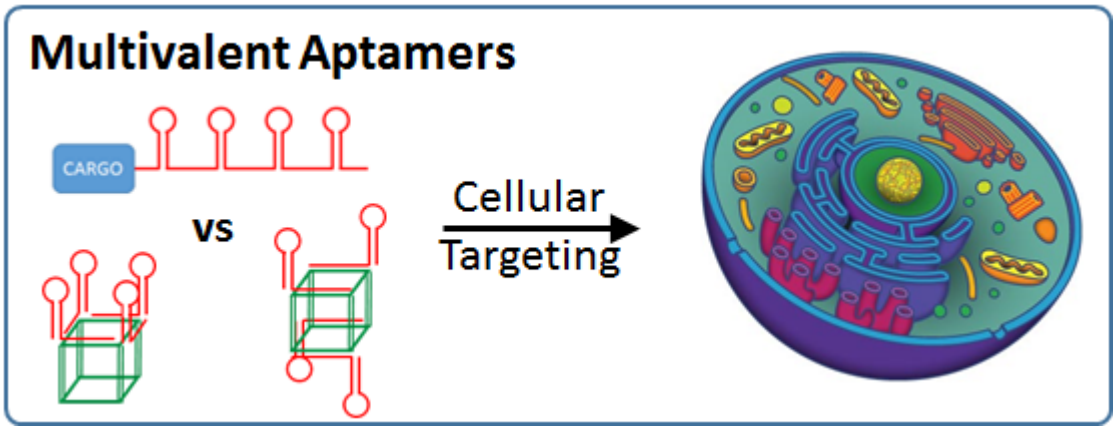

6.1 Abstract

Aptamers are gaining significant attention as targeting motifs for diagnostic strategies and therapeutic applications. Although aptamers have been included in a variety of assemblies for these purposes, they are generally designed as a mono-conjugates, which can be used as individual molecules or non-specific aggregated assemblies like micelles[1]. Aptamers interact with their targets through specific non-covalent structural affinity, however there are very few examples which examine the 3D presentation of multivalent aptamer assemblies to their targets. We have therefore employed a cubic DNA scaffold to investigate the dependence of aptamer recognition on precise numbers of aptamers organized with distinct 3D orientations. Our system is based on the TD05 aptamer developed elsewhere[2] which specifically targets B-cell surface receptors. Fluorescently labeled cubic scaffolds are self-assembled with variable aptamer presentations, incubated with the cell lines, and imaged using confocal microscopy. Results indicate that binding affinity increases as the number of aptamers increases, and exhibit a topological preference for certain aptamer orientations relative to linear repeating controls.

6.2 Introduction

Aptamers are self-complementary oligonucleotides that fold into distinct shapes and exhibit highly specific non-covalent interactions with a target molecule such as a protein[3,4]. They are similar to antibodies in their targeted behaviour, but have several advantages, making them highly attractive as targeting functional groups. Aptamers are oligonucleotides and can be routinely synthesized in many labs, with facile modifications through synthetic base pairs. They can also be generated for a wide variety of applications through a technique termed systematic evolution of ligands by exponential enrichment (SELEX) as described elsewhere[3,4]. In general, this selection process is performed using immobilized targets and polymerase chain reaction (PCR) enrichment, eliminating the need for complex biological strategies as for antibodies. Although aptamers are routinely synthesized and developed for specific targets, they exhibit lower affinity and selectively compared to antibodies.

There presently exists a large aptamer library for a wide selection of targets. Many groups have used covalently modified aptamers to add both therapeutic functionality and to increase cellular

uptake. These modifications typically consist of antisense oligonucleotides (ASO) or small interfering RNA (siRNA) as drug payloads and a lipidic motif such as cholesterol or tocopherol[5,6]. These molecules have been used to deliver therapeutics as monodisperse units or aggregated assemblies such as micelles. The presentation of aptamers in these instances is either as a 1:1 (aptamer-target) or an aptamer saturated system such as an aggregated micelle (containing many molecules) to a single target. Either of these all or nothing strategies may impede optimal aptamer to target binding, through steric hindrance (target crowding) or incomplete target interaction (bivalent binding locations). It is therefore particularly interesting to use discrete orientations of aptamers to find a compromise between these existing strategies.

Previous work has used a linear repeating array of aptamers to investigate aptamer binding affinity[2]. This work applied a previously developed TD05 aptamer targeting B-cell receptors, to create 1 to 4 covalently linked aptamers separated by a hexaethylene glycol (HEG) spacing unit (Figure 6.1), in a linear arrangement. It was found that as the number of aptamers increased, so too did the observed binding affinity. *In vivo* experiments have also shown that monomeric TD05 binds circulating IgM, however the tetrameric aptamer binds selectively to the membrane bound B-cell recptors. While this demonstrates a significant improvement for targeting, the lack of specific geometric presentation within the aptamer assembly, limits interpretation of the organizational dependence in 3D. Protein targets are globular in nature with highly specific folded structures, therefore creating structured arrangements of aptamers may lead to increased targeting and binding affinity. Furthermore, proteins have been shown to often contain primary and secondary binding sites[7], a modular platform for orthogonal aptamer placement may generate DNA structures with greater target specificity.

DNA nanostructures have been used as scaffolds to position aptamers. Multivalent placement of aptamers has been previously examined using ligated circular arrangements[8]. These studies revealed improved target affinity using an increasing number of aptamer motifs within a single circular structure. DNA origami has also been used to study the distance dependence for optimal bivalent aptamer binding[9]. An addressable DNA 3D geometry for precise placement of multivalent aptamer components may therefore improve binding affinity and selectivity.

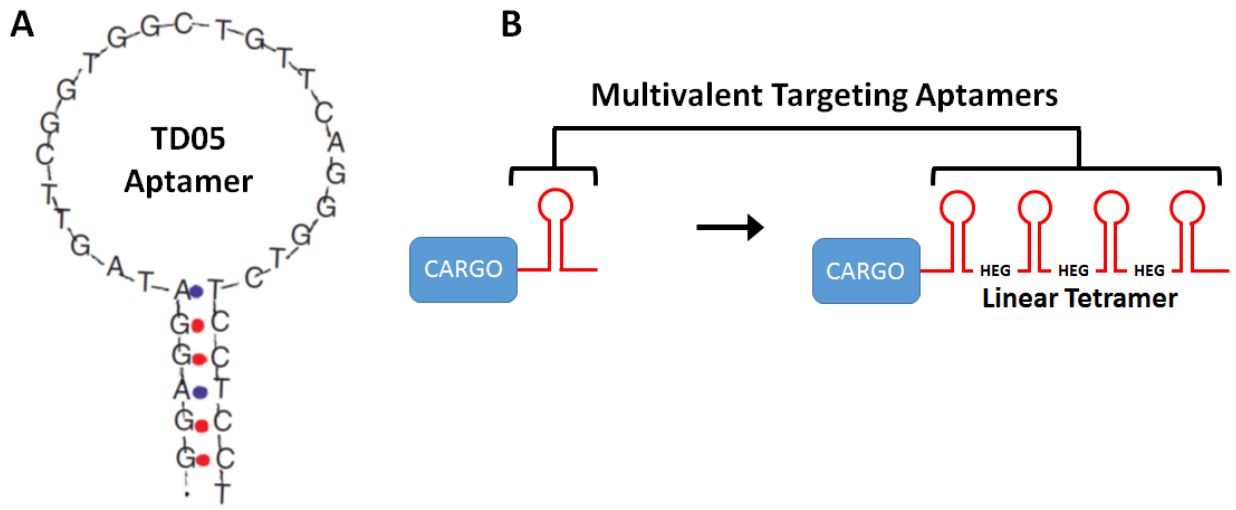

Figure 6.1: (A) Schematic representation of TD05. (B) Linear tetramer of TD05

We herein describe the design and synthesis of a cubic DNA scaffold, self-assembled from four strands that contains eight single stranded (ss) binding regions. The TD05 aptamer has been synthesized with a 20 nucleotide (nt) extension complementary to the ss regions on the cube, which allows for the placement of up to 8 aptamers with variable positioning. These samples are fluorescently labeled and incubated with different cell lines to determine how 3D multivalent aptamer presentation affects targeting.

6.3 Results and Discussion

The cubic DNA scaffold is designed from four 96mer strands that self-assemble via a clip-by-clip folding motif as previously described[10] (Figure 6.2A). The ss regions are arranged on the top and bottom faces of the cubic scaffold, which allows for loading of aptamers in either a face-centered crown orientation or a less hindered opposing face orientation (Figure 6.2C). In this way we can compare the targeting affinity of cubic scaffolds loaded with up to 4 aptamers in all possible 3D arrangements to a previously reported linear tetramer of aptamers[2], separated by hexaethylene glycol (HEG) spacing units.

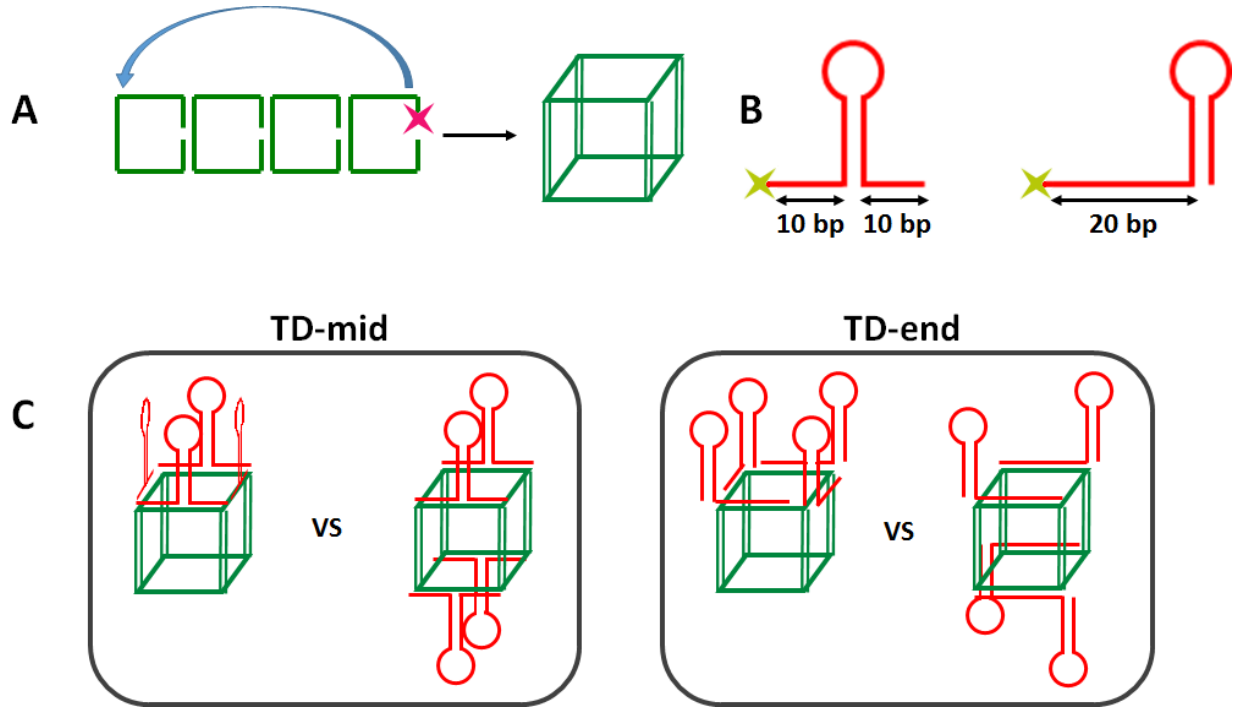

Figure 6.2: (A) Design of clip-by-clip motif to form a cube scaffold. (B) Position of aptamers relative to the binding region for TD-end and TD-mid (C) Schematic showing positional variations of the 4 aptamers. For imaging purposes, a clipping strand and the aptamer are labeled with the fluorescent tags Cyanine 3 (Cy3) and Cyanine 5 (Cy5) respectively. Fluorophore labels are indicated by the magenta and yellow four point stars.

Aptamers are intrinsically self-complementary oligonucleotides, therefore when designing the scaffold we used two different aptamer structures to suppress cross-linking between the strands when confined in close proximity. The two variations of aptamers are synthesized containing different organizations of the cube binding regions. The first sample, TD-end, contains the 20mer complementary binding region followed by 2 non-pairing thymine (2T) and the aptamer itself (39 nts). The second strand, TD-mid, has a sequence designed with the first half (10 nts) of the cube binding region, a 2T spacer, the aptamer itself, followed by a second 2T spacer and then the remaining half of the complementary binding region (Figure 6.2B). The TD-end sample is suspected to potentially exhibit cross-linking between the bound units as the aptamer motif is in a flexible position. Alternatively, within the TD-mid samples, the aptamer is sandwiched within the

two 10mer binding regions. This architecture prevents aptamer cross-linking, however introduces the possibility of cross-linking the cube scaffolds during the assembly.

Samples are synthesized, purified and assembled using a 1-pot annealing step as described below (Experimental Section 6.2). These samples are then analysed by native polyacrylamide gel electrophoresis (PAGE) to determine proper self-assembly. The number of aptamers bound to a scaffold is controlled by introducing symmetrical binding sites into each clipping strand. In this way four different scaffolds are used to bind 1 to 4 aptamers respectively. The cube and the aptamers are both labeled with different fluorophopres (Cy3/Cy5) to allow determination of co-localization at the cellular target. The cube is labeled by fluorescently modifying a single clip with a tag, which is then folded into the cubic structure with the remaining three strands.

Product self-assembly is examined using native PAGE to determine how both TD-end/mid interact with the DNA cage, shown in Figure 6.3. The assembly of TD-end is examined for loading of oppositely bound and facially centered organizations (Figure 6.2A and B respectively). The scaffold loaded with aptamers on opposing faces shows a stepwise shift towards lower band mobilities as 1 to 4 TD-end aptamers are bound (Figure 6.3A). TD-end was next loaded on the cube scaffold in four positions located on the same face. We again observe a stepwise shift towards lower band mobility however, we also begin to observe bands corresponding to misassembled material. The misassembled material is especially prevalent in the orientations placing two aptamers on adjacent edge lengths. Comparing lanes 3 and 4 in Figure 6.3B, the aptamers are bound on opposite and adjacent edges respectfully. While lane 3 shows reasonable assembly, the more sterically crowded sample in lane 4 shows increased band smearing indicating misassembled products. This is observed in the case of 3 aptamers as well (Figure 6.3 B, lane 5). Binding of 4 units appears to saturate the binding sites thereby rigidifying the structure and potentially limiting the cross-talk, as seen by the prominent lowest mobility band. There is however a significant amount of misassembled material remaining in lane 6. TD-mid is also examined in this way, and is found to cleanly assemble on the DNA structure in the opposite edge binding pattern (Figure 6.3C) with little observed cross-linked cube assemblies. This is likely the result of the of the aptamer portion, essentially a hairpin structure, limiting the flexibility between the two 10mer cube binding regions. The characterization of the same face binding orientation of TD-mid is still under way.

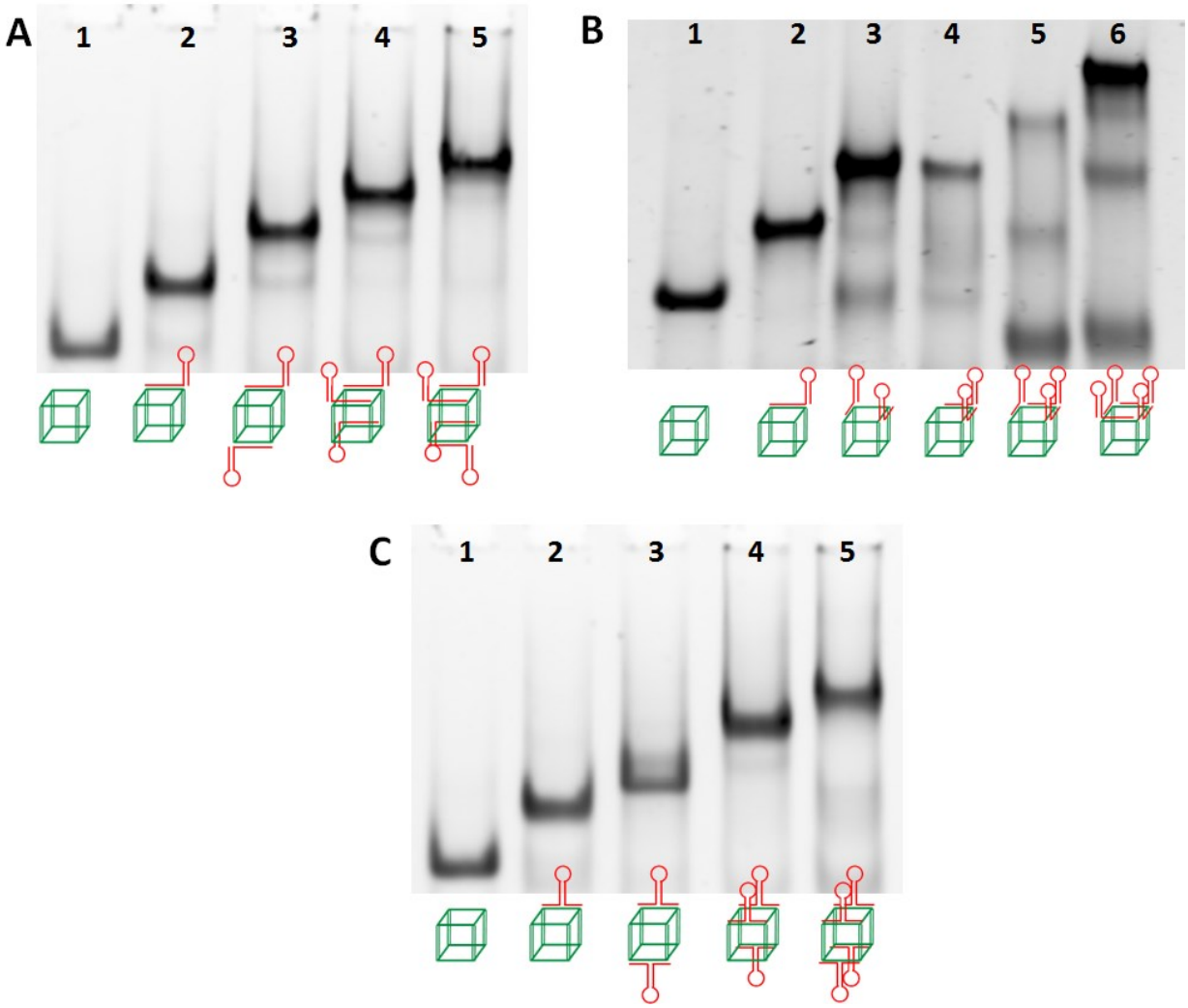

Figure 6.3: Native PAGE anaylsis of aptamer binding: (A) TD-end bound to cube scaffold at opposite edge positions. (B) TD-end bound to cube scaffold on the same face. (C) TD-mid bound to cube scaffold at opposite edge positions. Preliminary data only.

Cube scaffolds are loaded with a varied number of aptamers and incubated with Ramos cells, which are known to express B-cell surface receptors. The samples are then imaged using confocal fluorescence microscopy. Figure 6.4 shows the results for the co-localization experiments using both labeled scaffolds and aptamers. Although the empty cube scaffold (Figure 6.4, row 1) images indicate non-specific interactions with the cells membranes, increasing the number of TD-end aptamers bound to the scaffold results in an increase in the Cy3 fluorescence intensity due to

increased cubes at the surface. Figure 6.4, row 4 exhibits the highest fluorescence intensity and corresponds to the scaffold loaded with 4 aptamers in a face-centered crown formation. The overlay image of this sample also indicates co-localization of the aptamers and scaffold components. A labeled aptamer monomer is incubated at an equivalent concentration relative to the cube with 4 aptamers and showed significantly lower intensity. This may indicate that aptamer interactions with the bilayer are increased when organized on a scaffold, although non-specific scaffold interactions must be considered. Other groups have reported similar non-specific electrostatic interactions between DNA and the lipid head groups[11,12]. These preliminary experiments have only been performed for the TD-end sample to date.

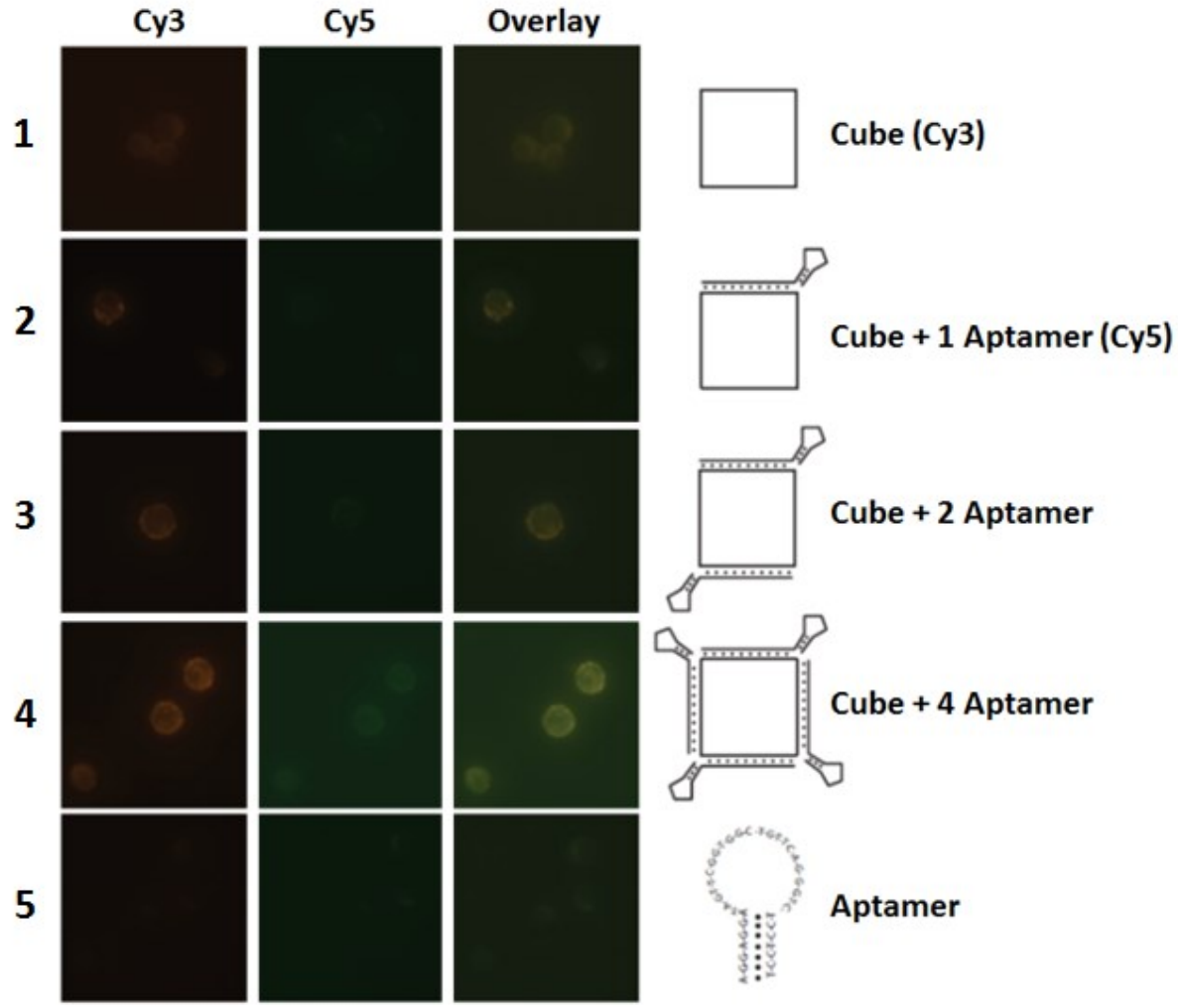

Figure 6.4: Confocal fluorescence images for co-localization of the cube scaffold and TD-end aptamer assemblies.

The next experiments compare the effects of 3D orientation on aptamer binding affinity relative to linear repeating organizations (Figure 6.5). As a control for binding affinity assays, a linear aptamer dimer and tetramer are synthesized. The synthesis of these strands includes the 39 bp aptamer repeats separated by HEG spacers Figure 6.1B (1HEG for the dimer and 3HEGs for tetramer) and a terminal 5'Cy3, purified by denaturing PAGE (see Experimental Section 6.6.2). Yields of the tetrameric aptamer are significantly low due to the oligonucleotide length, this further supports the need to explore other means of multivalent presentation.

Samples are prepared as described and imaged using confocal fluorescence microscopy. In these experiments all constructs are designed with only a single Cy3 modification for comparison and are performed only for the TD-end modification. Most significant, the cube with 4 aptamers (Figure 6.5, row 3) bound shows a much greater fluorescence intensity that the linear tetramer control (Figure 6.5, row 6). This indicates an increase in binding affinity for the aptamers when organized into a crown motif on a single cube face. Comparison between the cube with 2 aptamers (Figure 6.5, row 2) and the dimer control do not exhibit any notable difference in intensity. The empty scaffold and aptamer monomer show faint fluorescence. A negative control was performed on HeLa cells which do not express B-cell receptors, with no observed fluorescent accumulation.

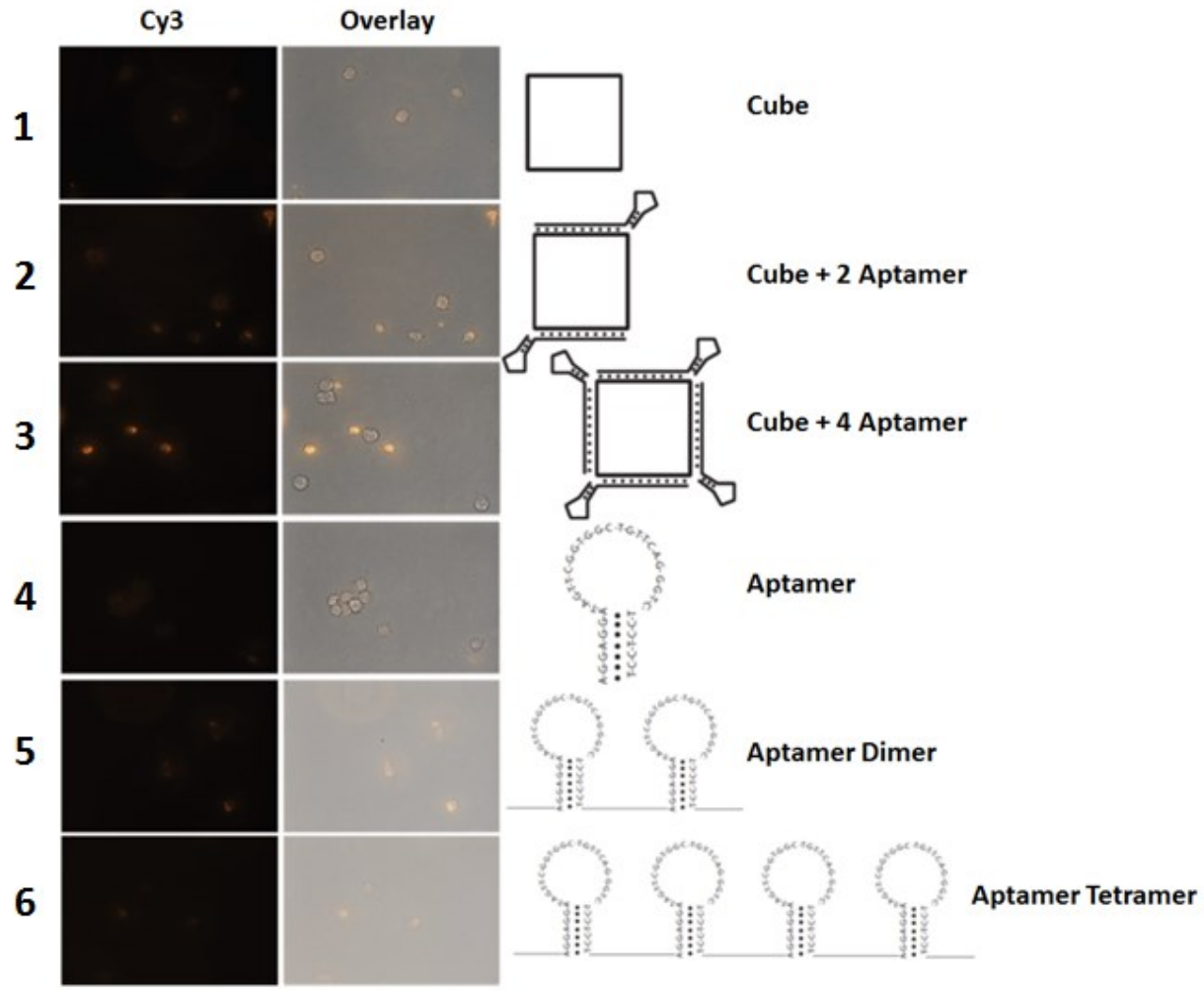

Figure 6.5: Confocal fluorescence images for comparison of the binding affinity for 3D oriented aptamers versus that of the linear repeating assemblies.

6.4 Conclusions

Our results indicate that the organization of 4 aptamers onto a single face of a cubic scaffold significantly increases their binding affinity relative to a linear tetramer repeat control. Furthermore, the scaffolds and aptamers appear to remain intact when they interact with the bilayer, which is essential for any cargo carrying application. The 3D orientation of multivalent aptamers could be used to organize different combinations of bi-valent aptamers to examine new ways of increasing targeting. Furthermore, the 3D scaffolds could be used to organize aptamers

during SELEX experiments to drive selection of synergistically functioning aptamers. As indicated these are preliminary results and there remains investigating both the interactions of opposing face aptamer orientations as well as increasing the number of loaded aptamers to 8 (1 for each single stranded scaffold edge). The TD-mid aptamers are also currently being studied. These findings may be useful for the creation of improved detection and drug carrying applications.

6.5 Experimental Section

6.5.1 General Information

Gel Red™ was purchased from VWR. Acetic acid, tris(hydroxymethyl)-aminomethane (Tris), and urea were used as purchased from Aldrich. Acetic acid and boric acid were purchased from Fisher Scientific and used without further purification. Nucleosides (dA, dC, dG and T) and universal 1000Å LCAA-CPG supports with loading densities between 25-40 μmol/g and reagents used for automated DNA synthesis were purchased through Bioautomation Corporated. Size-exclusion columns (sephadex G-25, DNA grade) were purchased from Glen Research. 1×TAMg buffer is composed of 45 mM Tris and 12.6 mM Mg(OAc)2·6H2O. The pH of the 1×TAMg buffer was adjusted to 8 using glacial acetic acid.

6.5.2 Synthesis and Purification of Oligonucleotides and Modified DNA Conjugates.

Standard automated oligonucleotide phosphoramidite solid-phase synthesis was performed on a Mermade MM6 synthesizer from Bioautomation. Gel electrophoresis experiments were carried out on an acrylamide 20 × 20 cm vertical Hoefer 600 electrophoresis unit. Annealing of all structures was conducted using an Eppendorf Mastercycler Pro. DNA quantification was performed using a BioTek Synergy HT microplate reader.

All fluorescent label modifications are purchased from Glen Research and used directly in manual off-column phosphoramidite coupling reactions. The fluorophores used to label oligonucleotides are the cyanine derivatives Cy3 and Cy5. These dyes are chosen for their well separated excitation and emission spectra. Cy3 and Cy5 are manually inserted at the 5’ position of the DNA strands.

All samples are purified and characterized using denaturing PAGE. Quantification of DNA and DNA-conjugates is performed using UV absorbance measurements at 260 nm.

DNA synthesis is performed on a 1 μmole scale, starting from a universal 1000 Å LCAA-CPG solid-supports. Coupling efficiency is monitored after removal of the dimethoxytrityl (DMT) 5′-OH protecting groups. The cyanine derivatives Cy3 and Cy5 are initially diluted with acetonitrile (ACN) to a concentration of 0.1 M in a glove box for off-column manual coupling. For off-column couplings, equal volumes of 200 uL of activator, ethylthiotetrazole (0.1M in acetonitrile, Glen Research) and phosphoramidite solution are added to the CPG and manually flushed through the DNA solid support with an extended reaction time of 15 minutes. After coupling, supports are removed from the glove box and returned to the DNA synthesizer for oxidation, capping and deblock steps. All sequences, modified and unmodified, are fully deprotected in concentrated ammonium hydroxide (60 ^{o}C/12 hours).

Table 6.1: Oligonucleotides prepared via solid-phase synthesis. The TTTT represents a short non-base pairing spacer that is inserted within each strand and serves as the vertices of the assembled 3D structures. Non-nucleoside phosphoramidites Cy3™, Cy5™, Chol, and NH/Alexa488™ are inserted selectively into individual sequences as indicated.

Number	Name	Sequence (3′ → 5′)
1	**P1-TOP(DP1)-BOT(DP3)**	TCGCTGAGTA TTTT GCCTGGCCTT GGTCCATTTG TTTT GCAAGTGTGG GCACGCACAC TTTT CCACCAGCTA GATGTTGAAG TTTT CACAAATCTG
2	**P1-TOP(DP3)-BOT(DP3)**	TCGCTGAGTA TTTT CCACCAGCTA GATGTTGAAG TTTT GCAAGTGTGG GCACGCACAC TTTT CCACCAGCTA GATGTTGAAG TTTT CACAAATCTG
3	**P2-TOP(DP1)-BOT(DP3)**	CTATCGGTAG TTTT GCCTGGCCTT GGTCCATTTG TTTT TACTCAGCGA CAGATTTGTG TTTT CCACCAGCTA GATGTTGAAG TTTT CAACTAGCGG

4	**P2-TOP(DP1)-BOT(DP1)**	CTATCGGTAG TTTT GCCTGGCCTT GGTCCATTTG TTTT TACTCAGCGA CAGATTTGTG TTTT GCCTGGCCTT GGTCCATTTG TTTT CAACTAGCGG
5	**P3-TOP(DP1)-BOT(DP3)**	CACTGGTCAG TTTT GCCTGGCCTT GGTCCATTTG TTTT CTACCGATAG CCGCTAGTTG TTTT CCACCAGCTA GATGTTGAAG TTTT GGTTTGCTGA
6	**P3-TOP(DP3)-BOT(DP3)**	CACTGGTCAG TTTT CCACCAGCTA GATGTTGAAG TTTT CTACCGATAG CCGCTAGTTG TTTT CCACCAGCTA GATGTTGAAG TTTT GGTTTGCTGA
7	**P4-TOP(DP1)-BOT(DP3)**	CCACACTTGC TTTT GCCTGGCCTT GGTCCATTTG TTTT CTGACCAGTG TCAGCAAACC TTTT CCACCAGCTA GATGTTGAAG TTTT GTGTGCGTGC-**Cy3**
8	**P4-TOP(DP1)-BOT(DP1)**	CCACACTTGC TTTT GCCTGGCCTT GGTCCATTTG TTTT CTGACCAGTG TCAGCAAACC TTTT GCCTGGCCTT GGTCCATTTG TTTT GTGTGCGTGC**-Cy3**
9	**TD-end**	CAAATGGACCAAGGCCAGGC TT AGGAGGATAGTTCGGTGGCTGTTCAGGGTCTCCTCCT-**Cy5**
10	**TD-mid**	CAAATGGACC TT AGGAGGATAGTTCGGTGGCTGTTCAGGGTCTCCTCCT TT AAGGCCAGGC-**Cy5**
11	**TD-Dimer**	AGGAGGATAGTTCGGTGGCTGTTCAGGGTCTCCTCCT-**HEG-** AGGAGGATAGTTCGGT GGCTGTTCAGGGTCTCCTCCT-**Cy3**
12	**TD-Tetramer**	AGGAGGATAGTTCGGTGGCTGTTCAGGGTCTCCTCCT-**HEG-** AGGAGGATAGTTCGGTGGC

		TGTTCAGGGTCTCCTCCT-**HEG** AGGAGGATAGTTCGGTGGCTGTTCAGGGTCTCCTCCT- **HEG-** AGGAGGATAGTTCGGTGGCTGTTCAGGGTCTCCTCCT- **Cy3**

All 96mer crude products are purified on an 8% polyacrylamide/8M urea polyacrylamide gel (PAGE; up to 20 OD260 of crude DNA per gel) at constant current of 30 mA for 2 hours (30 min. at 250V followed by 1.5 hr at 500V), using the 1x TBE buffer. Following electrophoresis, the gels are placed on a fluorescent TLC plate wrapped in plastic wrap and illuminated with a UV lamp (254nm). The bands are excised, and the gel pieces are crushed and incubated in 12 mL of sterile water at 60 ºC for 12-16 hours. Samples are then dried to 1 mL, desalted using size exclusion chromatography (Sephadex G-25 columns, Glen Research), and quantified (OD260) using UV-Vis spectroscopy. Smaller strands (<50 base pairs) are purified using a 15% PAGE mixture and running conditions of 30 min at 250V followed by 45 min at 500V, followed by the same work up.

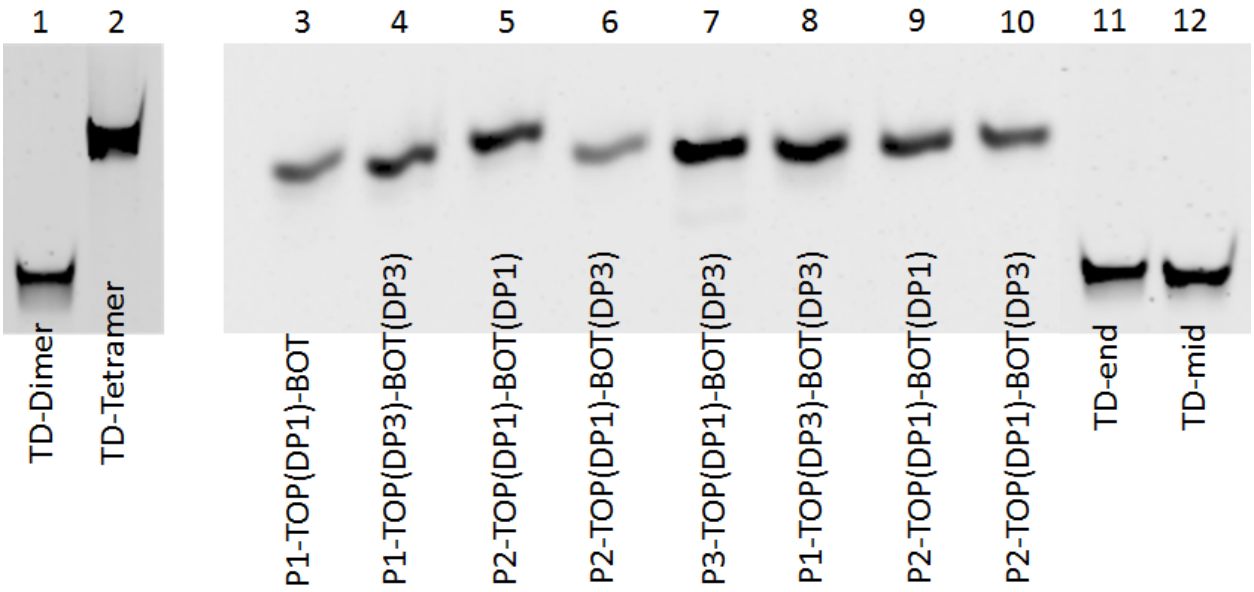

Figure 6.6: Denaturing PAGE (8%, 1xTBE) analysis of synthesized oligonucleotides, gel ran for 30 minutes at 250V and then 1 hr at 500 V; lane 1-11, lane 2-12, lane 3-1, lane 4-2, lane 5-3, lane 6-4, lane 7-5, lane 8–6, lane 9-7, lane 10-8, lane 11-9, lane 12-10 (the numbers correspond to the strand number in Table 6.1).

6.5.3 Assembly of 3D DNA Cages

Equimolar amounts of each of the four scaffold clip strands (1 – 4) are combined in 1xTAMg buffer for a final 3D concentration of 0.250 μM. Aptamer strands are added in slight excess of 1:1.2 equivalents to ensure full loading of the cage structure. Samples are then subjected to an annealing protocol whereby strands are brought to 95 ºC for 5 minutes and cooled back to 4 ºC over 4 hours. Regions of symmetry are introduced for binding of multiple aptamers.

6.5.4 Cellular Incubation and Confocal Microscopy Procedures

Ramos (Burkitt's lymphoma) and HeLa (adenocarcinoma) cells were seeded at a density of $5x10^5$ in 8-well slides. After 1 hour cells were incubated with Cube-Aptamer constructs, add 50 uL of each sample (1 uM stock final 0.1 uM), total volume 400 uL, at 4°C or 37°C for 1 or 3 hours. Subsequently, cells were fixed with 2% paraformaldehyde/1X PBS. Cells were then washed with

1X PBS and mounted with Prolong Gold (Invitrogen, USA) and cured overnight at 4°C. Images were recorded using a Zeiss AxioImager and using the Zen software (Zeiss, USA).

6.6 References

(1) Wu, Y.; Sefah, K.; Liu, H.; Wang, R.; Tan, W. *PNAS* **2010**, *107*, 5-10.

(2) Mallikaratchy, P. R.; Ruggiero, A.; Gardner, J. R.; Kuryavyi, V.; Maguire, W. F.; Heaney, M. L.; McDevitt, M. R.; Patel, D. J.; Scheinberg, D. A. *Nucleic Acids Res.* **2011**, *39*, 2458-2469.

(3) Wilson, D. S.; Szostak, J. W. *Annu. Rev. Biochem.* **1999**, *68*, 611-647.

(4) Svobodová, M.; Pinto, A.; Nadal, P.; O' Sullivan, C. K. *Anal. Bioanal. Chem.* **2012**, *404*, 835-842.

(5) Wolfrum, C.; Shi, S.; Jayaprakash, K. N.; Jayaraman, M.; Wang, G.; Pandey, R. K.; Rajeev, K. G.; Nakayama, T.; Charrise, K.; Ndungo, E. M.; Zimmermann, T.; Koteliansky, V.; Manoharan, M.; Stoffel, M. *Nat Biotech* **2007**, *25*, 1149-1157.

(6) Nishina, K.; Unno, T.; Uno, Y.; Kubodera, T.; Kanouchi, T.; Mizusawa, H.; Yokota, T. *Mol. Ther.* **2008**, *16*, 734-740.

(7) Ge, L.; Jin, G.; Fang, X. *Langmuir* **2012**, *28*, 707-713.

(8) Di Giusto, D. A.; King, G. C. *J. Biol. Chem.* **2004**, *279*, 46483-46489.

(9) Rinker, S.; Ke, Y.; Liu, Y.; Chhabra, R.; Yan, H. *Nat. Nanotechnol.* **2008**, *3*, 418-422.

(10) Edwardson, T. G. W.; Carneiro, K. M. M.; McLaughlin, C. K.; Serpell, C. J.; Sleiman, H. F. *Nature Chem.* **2013**, *5*, 868-875.

(11) Suzuki, Y.; Endo, M.; Yang, Y.; Sugiyama, H. *J. Am. Chem. Soc.* **2014**, *136*, 1714-1717.

(12) Langecker, M.; Arnaut, V.; List, J.; Simmel, F. C. *Acc. Chem. Res.* **2014**, *47*, 1807-1815.